

QUANTITATIVE ANALYSIS OF METAL NANOPARTICLE LIGAND SHELLS

by

Ashley Marie Smith

B. A., Washington & Jefferson College, 2011

Submitted to the Graduate Faculty of

The Kenneth P. Dietrich School of Arts and Sciences in partial fulfillment

of the requirements for the degree of

Doctor of Philosophy

University of Pittsburgh

2017

UNIVERSITY OF PITTSBURGH
DIETRICH SCHOOL OF ARTS AND SCIENCES

This dissertation was presented

by

Ashley Marie Smith

It was defended on

March 23, 2017

and approved by

Dr. Nathaniel L. Rosi, Professor, Department of Chemistry

Dr. Alexander Star, Professor, Department of Chemistry

Dr. Leanne M. Gilbertson, Assistant Professor, Department of Engineering

Dissertation Advisor: Dr. Jill E. Millstone, Associate Professor, Department of Chemistry

Copyright © by Ashley Marie Smith

2017

QUANTITATIVE ANALYSIS OF METAL NANOPARTICLE LIGAND SHELLS

Ashley Marie Smith, Ph.D.

University of Pittsburgh, 2017

Nanoparticles (NPs) are used in an increasingly large number of applications ranging from coatings to sensing. Gold (Au) NPs, in particular, are emerging as some of the most well-studied and versatile particle types due to their facile synthesis, high stability, and wide range of morphologies. For these and all colloidal NPs, the surface chemistry can significantly impact physical properties and performance in downstream applications. The first step in leveraging this tunability is to develop analytical approaches to describe surface chemical features. Here, we introduce analytical approaches and resulting chemical insights that allow one to quantify, predict, and control the extent of ligand exchange on a range inorganic NPs.

We present data to establish the dynamic range, chemical resolution, and substrate generality of our NMR-based ligand quantification approach. First, we determine ligand density values for thiolated single-moiety ligand shells. We then use these data to describe ligand exchange behavior with a second, thiolated molecule to identify trends in AuNP functionalization efficiency as a function of ligand properties and exchange methodologies. Finally, we use our quantification method to analyze a diversity of particle shapes, sizes, and compositions.

In the studied systems, several trends emerge that ultimately serve as design rules for the generation of well-controlled ligand shells on metal NPs. In particular, we find that AuNPs functionalized with thiolated molecules exhibit a range of exchange efficiencies that strongly depend on the structure of the existing ligand shell. Further, we demonstrate that ligand

incorporation into the final ligand shell varies based on the strength of the ligand binding moiety and binding affinity to the AuNP, with stoichiometric loading more closely achieved in cases where the ligands have a weaker affinity for the NP as well as with ligands that exhibit limited intermolecular interactions. Finally, we discuss the ligand loading trends in relation to particle size, composition, and shapes to probe how these aspects of particle morphology may or may not influence the ligand loading. Taken together, the reported results provide advances in the fundamental understanding of mixed ligand shell formation and are important for the use of AuNPs in a variety of applications.

TABLE OF CONTENTS

ACKNOWLEDGEMENTS	XXXI
1.0 LIGAND DENSITY QUANTIFICATION ON COLLOIDAL INORGANIC NANOPARTICLES.....	1
1.1 INTRODUCTION	1
1.2 GENERAL CONSIDERATIONS FOR LIGAND QUANTIFICATION.....	3
1.2.1 Core Considerations	3
1.2.1.1 Particle Concentration and Surface Area Calculation.....	4
1.2.1.2 Core Morphology	5
1.2.2 Ligand Property Considerations.....	6
1.3 THERMOGRAVIMETIC ANALYSIS (TGA).....	10
1.4 OPTICAL SPECTROSCOPY.....	15
1.4.1 Photoluminescence (PL) Spectroscopy	16
1.4.1.1 Fluorescently-labelled Ligands	16
1.4.1.2 “Turn on” Fluorescent Indicators.....	18
1.4.1.3 Optically Active Ligands	19
1.4.2 Absorption Spectroscopy	20
1.4.2.1 Ligands Tagged with Optically Active Labels.....	20
1.4.2.2 Plasmonic NPs	21

1.4.2.3	Optically Active Indicators	23
1.5	ATOMIC SPECTROSCOPY	26
1.6	NUCLEAR MAGNETIC RESONANCE (NMR) SPECTROSCOPY	28
1.6.1	“Off particle” NMR Analysis	30
1.6.2	“On Particle” NMR Analysis.....	34
1.7	VIBRATIONAL SPECTROSCOPY	40
1.7.1	Raman Spectroscopy	40
1.7.2	Infrared Spectroscopy	41
1.8	ELECTROSPRAY-DIFFERENTIAL MOBILITY ANALYSIS (ES-DMA)	42
1.9	PH TITRATIONS.....	44
1.10	X-RAY PHOTOELECTRON SPECTROSCOPY (XPS).....	45
1.11	SUMMARY AND OUTLOOK.....	46
2.0	QUANTITATIVE ANALYSIS OF THIOLATED LIGAND EXCHANGE ON GOLD NANOPARTICLES MONITORED BY ¹ H NMR SPECTROSCOPY.....	48
2.1	INTRODUCTION	48
2.2	EXPERIMENTAL.....	50
2.2.1	Materials and Methods	50
2.2.2	AuNP Synthesis.....	51
2.2.3	UV-vis-NIR Analysis of AuNPs	52
2.2.4	TEM Analysis of AuNPs for Size Determination	52
2.2.5	Synthesis of PEGSeCN	52
2.2.6	Ligand Exchange of Citrate-capped AuNPs	53

2.2.7	Ligand Exchange of Citrate-capped AuNPs in Organic Solvents.....	56
2.2.8	Ligand Exchange of Citrate-capped AuNPs in Salt Solutions	56
2.2.9	Ligand Exchange of Citrate-capped AuNPs at Various Temperatures ...	57
2.2.10	ICP-MS Analysis	57
2.2.11	ICP-OES Analysis of PEGSeCN	58
2.2.12	¹ H NMR Analysis.....	59
2.2.13	Minimum Ligand Footprint and Ligand Excess Determination	59
2.3	RESULTS AND DISCUSSION	61
2.3.1	Ligand Quantification Method.....	61
2.3.2	Ligand Concentration and Incubation Time	68
2.3.3	Ligand Densities in Single-Moiety Ligand Shells	73
2.3.4	Influence of Ligand Chain Length on Ligand Loading	76
2.3.5	Influence of Salt and Temperature on Ligand Loading Density.....	81
2.4	CONCLUSION	84
3.0	QUANTITATIVE EVALUATION OF LIGAND BACKFILLING AND CO-LOADING ON GOLD NANOPARTICLE FUNCTIONALIZATION.....	86
3.1	INTRODUCTION	86
3.2	EXPERIMENTAL.....	87
3.2.1	Materials and Methods	87
3.2.2	AuNP Synthesis.....	88
3.2.3	UV-vis-NIR Analysis of AuNPs	89
3.2.4	TEM Analysis of AuNPs for Size Determination	89
3.2.5	Initial Ligand Exchange of Citrate-capped AuNPs.....	90

3.2.6	Backfilling of PEGSH-capped AuNPs with a Second Thiolated Ligand..	91
3.2.7	Backfilling of PEGNH ₂ -capped AuNPs with a Second Aminated Ligand	92
3.2.8	Backfilling of Mercaptoalkanoic Acid-capped Particles with PEGSH.....	92
3.2.9	Backfilling of Aminoalkanoic Acid-capped Particles with PEGNH ₂	93
3.2.10	Backfilling of MUA-capped Particles with MUPA and MUPA-capped Particles with MUA.....	93
3.2.11	Co-loading of Ligands on AuNPs.....	94
3.2.12	ICP-MS Analysis	95
3.2.13	¹ H NMR Analysis.....	95
3.3	RESULTS AND DISCUSSION.....	96
3.3.1	Quantification of Thiolated Mixed Ligand Shells	99
3.3.2	Influence of Existing Thiolated Ligand Shell on Ligand Exchange Efficiency.....	101
3.3.3	Co-loading of Thiolated and Aminated Ligands on AuNPs	104
3.3.4	Backfilling of Thiolated and Aminated Ligands on AuNPs	107
3.3.5	Examining the Factors that Dictate Final Ligand Shell Composition	112
3.4	CONCLUSION	116
4.0	EXPANDING LIGAND SHELL DESIGN RULES TO PHOSPHINES AND TERNARY THIOL SYSTEMS.....	118
4.1	INTRODUCTION	118
4.2	EXPERIMENTAL.....	119
4.2.1	Materials and Methods	119
4.2.2	AuNP Synthesis.....	120

4.2.3	Absorption Spectroscopy	120
4.2.4	Transmission Electron Microscopy (TEM).....	121
4.2.5	Initial Ligand Exchange of Citrate-capped AuNPs.....	121
4.2.6	Backfilling of BSPP-capped AuNPs with a Thiolated or Aminated Ligand	122
4.2.7	Sequential Addition of Three Ligands.....	122
4.2.8	Inductively Coupled Plasma Mass Spectrometry (ICP-MS).....	123
4.2.9	¹ H NMR Spectroscopy.....	124
4.3	PHOSPHINE LIGANDS.....	125
4.3.1	Introduction	125
4.3.2	Phosphine Ligand Densities.....	125
4.3.3	Ligand Shell Quantification of BSPP-containing Mixed Ligand Shells.	128
4.3.4	Ongoing and Future Work	131
4.4	TERNARY LIGAND SHELLS.....	132
4.4.1	Introduction	132
4.4.2	Selection of Three Ligands.....	133
4.4.3	Sequential Addition of Three Thiolated Ligands	133
4.4.4	Ongoing and Future Work	136
4.5	CONCLUSION	136
5.0	ESTABLISHING METHOD GENERALITY: APPLYING LIGAND QUANTIFICATION TO VARIOUS NP SIZES, SHAPES, AND COMPOSITIONS.....	137
5.1	INTRODUCTION	137
5.2	EXPERIMENTAL.....	138

5.2.1	Materials and Methods	138
5.2.2	Synthesis of 4-DPPBA-Terminated AuNPs.....	139
5.2.3	Synthesis of Citrate-Capped AgNPs	140
5.2.4	Synthesis of Citrate-capped AuNPs	141
5.2.5	Synthesis of PVP-capped AgNPs.....	141
5.2.6	Au Nanoprism Synthesis	142
5.2.7	Purification of Au Nanoprisms.....	143
5.2.8	Ligand Exchange of Citrate-Capped AgNPs	143
5.2.9	Ligand Exchange of Citrate-Capped AuNPs	144
5.2.10	Ligand Exchange of PVP-Capped AgNPs.....	145
5.2.11	Ligand Exchange of Au Nanoprisms	146
5.2.12	ICP-MS of AuNPs	147
5.2.13	ICP-MS of AgNPs.....	147
5.2.14	Ligand Quantification/Ligand Density Determination by ¹ H NMR.....	148
5.3	RESULTS AND DISCUSSION	149
5.3.1	NP Size Effects	149
5.3.2	NP Composition	152
5.3.3	NP Shape	155
5.4	CONCLUSION	157
APPENDIX A		158
APPENDIX B		172
APPENDIX C		194
APPENDIX D.....		200

BIBLIOGRAPHY..... 213

LIST OF TABLES

Table 1. Compilation of ligand densities (in units of ligands/nm ²) reported by papers reviewed in chapter 1.....	8
Table 2. Conditions for synthesis of AuNPs with different diameters.	51
Table 3. Ligand densities for 13 and 30 nm AuNPs (average size ± standard deviation) functionalized with PEGSH, MUA, or MOA, where the errors represent standard error for at least 20 trials.	74
Table 4. Comparison of the number of ligands and the ligand densities for BSPP- and 4-DPPBA-capped AuNPs after 24 hours at a 50x ligand excess with respect to NP surface area.	126

LIST OF FIGURES

- Figure 1. Scheme representing three key regions of small molecule capping ligands: 1. the particle binding moiety, 2. an intra-molecular region, and 3. a terminal group. *N. B.* Components in regions 2 and 3 can also interact with the NP surface under certain conditions (*vide infra*). 7
- Figure 2. Number of PEGSH ligands on 15 nm AuNPs as a function of PEGSH molecular weight, showing that ligand density decreases as ligand chain length increases; inset plots “grafting” (i.e. ligand) density as a function of PEGSH molecular weight. Modified from ref. 63 with permission from The Royal Society of Chemistry. 13
- Figure 3. Scheme illustrating the quantitative analysis of oligonucleotide-functionalized AuNPs of various core diameters. Here, AuNPs are functionalized with fluorescein-labelled oligonucleotides in the presence of salt, purified, and then exposed to DTT, which removes the ligands from the NP surface. The released ligands are then quantified using photoluminescence spectroscopy. Adapted with permission from ref. 100. Copyright 2006 American Chemical Society..... 18
- Figure 4. Ligand exchange of the α -AlW₁₁O₃₉⁹⁻ cluster-capped AuNPs with MUA. (A) Absorption spectra of the AuNP LSPR during the ligand exchange, and (B) plot of the change in LSPR absorbance at the initial λ_{max} of 526 nm as a function of added MUA concentration. Adapted with permission from ref. 52. Copyright 2012 American Chemical Society..... 22

Figure 5. Scheme demonstrating 4 different techniques for the quantitative characterization of NH₂PEGSH on AuNPs: (i) a fluorescamine photoluminescence assay, (ii) a ninhydrin-based absorption spectroscopy method, (iii) fluorescein labelling of terminal amines on the appended ligand, and (iv) Cu²⁺ labelling of terminal amines, an ICP-MS method. Techniques (i) and (ii) quantify ligand density, whereas (iii) and (iv) quantify the amino groups available for functionalization. Adapted with permission from ref. 98. Copyright 2012 American Chemical Society..... 25

Figure 6. Scheme of a typical off particle NMR analysis. Here, NP conjugates are digested for quantification by ICP-MS, while the released ligands are quantified by ¹H NMR. Adapted with permission from ref. 54. Copyright 2015 American Chemical Society. 32

Figure 7. Ligands/nm² as a function of NP diameter for ZnO NPs. Particle ligand densities are lower than predicted for a self-assembled monolayer (SAM) of DDA ligands on a flat ZnO surface. Adapted with permission from ref. 142. Copyright 2014 American Chemical Society. 38

Figure 8. Scheme for ligand exchange of citrate-capped AuNPs. 54

Figure 9. Comparison of PEGSH footprint measured from particles analyzed immediately after purification, analyzed after purification and subsequent incubation overnight in base (phosphate buffer, 10 mM, pH = 10), and analyzed after purification and subsequent incubation overnight in pure water, where error bars represent standard error of at least 5 trials. No significant difference is observed between the sets of AuNPs. 55

Figure 10. Representative molecule for minimum ligand occupation area of alkane thiol ligands on a flat gold surface (A) and corresponding calculation for ligand “diameter” based on the estimated geometry (B)..... 61

Figure 11. Representative UV-vis-NIR spectra for 13 nm (A) and 30 nm (B) NPs and corresponding TEM images, (C) and (D). Insets are histograms for 13 nm and 30 nm NPs generated from measurements of at least 200 NPs. Scale bars are 100 nm..... 63

Figure 12. Sample calibration curve obtained for PEGSH by plotting integrated ratios of PEGSH/ACN against the concentration of PEGSH. PEGSH protons used for this analysis are highlighted in red. 64

Figure 13. Representative ¹H NMR spectra of PEGSH on-particle (red line) and off-particle (blue line) in D₂O for 13 nm AuNPs. Line broadening observed with the on-particle spectrum can obscure accurate quantification..... 66

Figure 14. Plots of PEGSH footprint on the AuNP surface as a function of time in excess PEGSH (50×) for 13 nm (A) and 30 nm (B) AuNPs. Results indicate that ligand loading reaches a steady state (with standard errors of < 10% for at least 5 trials) on the timescale of minutes under the conditions tested..... 69

Figure 15. Plots of MUA footprint on the NP surface as a function of AuNP time in excess MUA (50x) for 13 nm (A) and 30 nm (B) AuNPs, where error bars represent the standard error of at least 5 trials. Results indicate that ligand loading reaches a plateau on the timescale of 2-3 hours under the conditions tested..... 70

Figure 16. Plots of MOA footprint on the NP surface as a function of AuNP time in excess MOA (50x) for 13 nm (A) and 30 nm (B) AuNPs, where error bars represent the standard error of at least 5 trials. Results indicate that ligand loading reaches a plateau on the timescale of 2-3 hours under the conditions tested..... 70

Figure 17. Graphs displaying PEGSH footprint as a function of PEGSH excess with respect to NP surface area after 4 hours for 13 nm (A) and 30 nm (B) AuNPs. Results indicate that

maximum loading under the conditions evaluated reaches a steady state at an excess above 20× (with standard errors of < 10% for at least 5 independent trials)..... 71

Figure 18. Graphs displaying MUA ligand footprint as a function of MUA excess with respect to surface area after 4 hours for 13 nm (A) and 30 nm (B) AuNPs, where error bars represent the standard error of at least 5 trials. Results indicate that loading reaches a consistent value at a ligand excess above 20x..... 72

Figure 19. Graphs displaying MOA ligand footprint as a function of MOA excess with respect to surface area after 4 hours for 13 nm (A) and 30 nm (B) AuNPs, where error bars represent the standard error of at least 5 trials. Results indicate that loading reaches a consistent value at an excess above 20x..... 72

Figure 20. Surface curvature as a function of particle diameter. The figure illustrates that for particles with diameters larger than 10 nm, change in curvature as a function of particle diameter decreases dramatically. 75

Figure 21. Plots of PEGSH footprint on 13 nm AuNPs as a function of time in excess PEGSH (50×) (A) and PEGSH excess with respect to surface area after 4 hours (B) for different MWs of PEGSH, where error bars represent the standard error of at least 5 trials. Results indicate that loading reaches a consistent value at a ligand excess above 20x and above 4 hours under the conditions tested..... 77

Figure 22. Graph of number of PEGSH ligands per particle as a function of PEGSH chain length, where error bars represent the standard error of at least 5 trials. Shorter polymer chains have fewer ligands per particle than longer chains. 78

Figure 23. Graph of number of mercaptoalkanoic ligands per particle as a function of chain length, where error bars represent the standard error of at least 5 trials. 79

Figure 24. Graph of number of MUA ligands per particle in various solvents, where error bars represent the standard error of at least 3 trials. No significant difference is observed in ligand loading in organic solvents. 80

Figure 25. Graph of number of mercaptoalkanoic ligands per particle as a function of chain length, where error bars represent the standard error of at least 5 trials. The shorter ligands have a higher ligand density..... 81

Figure 26. Plot of the number of PEGSH ligands per particle as a function of salt identity. The identity of the salt impacted the PEGSH loading on the basis of ionic radius. 82

Figure 27. Plot of the number of PEGSH ligands as a function of NaCl concentration. Increased loading is only observed for the 1 kDa PEGSH, likely due to the longer chain lengths with the 2 kDa and 5 kDa PEGSH..... 83

Figure 28. Plot of the number of PEGSH ligands as a function of PEGSH excess at various temperatures. No significant change in ligand loading is observed at elevated or decreased temperatures..... 84

Figure 29. Scheme depicting the two types of ligand addition used in this study to form mixed thiolated ligand shells on AuNPs. An analogous process is used to form aminated mixed ligand shells. 98

Figure 30. Plot of PEGNH₂ (gray triangles), AUA (blue circles), and AOA (green squares) densities on the NP surface as a function of AuNP incubation time in presence of the aminated ligand for 13 nm AuNPs where the error bars represent standard error of at least 5 trials. Results indicate that ligand loading is consistent for all the time points studied after 4 hours. 98

Figure 31. Comparison of the ligand loading values for PEGSH with AOA (A) and PEGNH₂ with MOA (B) for 13 nm AuNPs. In both cases of combining a short chain amine with a longer

thiol and combining a short chain thiol with a longer amine, the thiol dominates the ligand shell in all three systems of backfilling and co-loading. 99

Figure 32. Comparison of the amount of PEGSH displaced upon secondary ligand exchange with a smaller thiolated ligand of various chain lengths and terminal functional groups, where error bars represent standard error for at least 20 trials. Gray = PEGSH, burgundy = AUT, blue = MUA, green = MOA, and peach = MPA. 100

Figure 33. Comparison of the amount of MUA or MOA displaced upon secondary ligand addition with either PEGSH or MPA, where error bars represent standard error for at least 15 trials. The first bar in each series represents the homogeneous ligand shell of MUA (blue bar) or MOA (green bar). Blue = MUA, green = MOA, peach = MPA, and gray = PEGSH (same color scheme as in Figure 32). 102

Figure 34. Scheme depicting two possible pathways of secondary ligand addition. 103

Figure 35. Comparison of the percent loadings of MUA (A, B), MOA (C, D), or MHA (E, F) in the final ligand shell when co-loaded with PEGSH, where error bars represent the standard error of at least 5 trials. 105

Figure 36. Comparison of the percent loadings of AUA (A, B), AOA (C, D), or AHA (E, F) in the final ligand shell when co-loaded with PEGNH₂, where error bars represent the standard error of at least 5 trials. 106

Figure 37. Comparison of single ligand loading of PEGSH and various MAAs (A) and of ligand loading when co-loading at a 50:50 ratio of PEGSH with a MAA, MAAs backfilled with PEGSH, and PEGSH backfilled with each MAA (B-D), where error bars represent standard error of at least five trials. 109

Figure 38. Comparison of single ligand loading of PEGNH₂ and the AAAs (A), and of ligand loading when co-loading at a 50:50 ratio of PEGNH₂ with each AAA, AAAs backfilled with PEGNH₂, and PEGNH₂ backfilled with each AAA (B-D), where error bars represent standard error of at least five trials. 111

Figure 39. Comparison of similar ligand loading between two 11-carbon MAA analogues with backfilling and 50:50 co-loading (A), as well as various co-loading ratios (C, D) and two PEGSH analogues with backfilling and 50:50 co-loading (B), as well as various co-loading ratios (E, F), where the error bars represent standard error of at least five trials. 114

Figure 40. Plots of the BSPP ligand density as a function of time at a 50x ligand excess (A) and incubation in various ligand excesses for 16 hours (B). Results indicate that ligand loading reaches a steady state after approximately 8 hours and at a ligand excess of 30x. 127

Figure 41. Plots of the total number of ligands for BSPP particles as well as when they are co-loaded with thiolated ligands (A) or aminated ligands (B). Markedly different ligand shells are obtained by changing the identity of the co-loaded ligand. 129

Figure 42. Plots of the total number of ligands for BSPP particles when they are backfilled with either thiolated (A) or aminated ligands (B). 130

Figure 43. Plots of the total number of ligands for AuNPs when thiolated (A) or aminated (B) ligand shells are backfilled with BSPP. 131

Figure 44. Representative ¹H NMR spectrum of three component ligand shells in D₂O after AuNP digestion. Labelled peaks correspond to peaks used for ligand quantification compared to the integrated intensity of the ACN peak. 134

Figure 45. Graphs depicting the ligand incorporation for two different backfilling sequences: PEGSH backfilled with MOA backfilled with MPA (A) and MOA backfilled with MPA backfilled with PEGSH (B). 135

Figure 46. Total number of ligands per particle before and after the AuNPs underwent ligand exchange with thiolated ligands. Error bars represent the standard error of at least three measurements..... 151

Figure 47. PEGSH ligand density plotted against time (A) and ligand density versus PEGSH excess with respect to surface area (B) for AuNPs (gray squares) and AgNPs (red circles) originally functionalized with citrate after ligand exchange with PEGSH. Error bars represent the standard error of at least five independent trials. 153

Figure 48. PEGSH ligand density plotted against time (A) and ligand density versus PEGSH excess with respect to surface area (B) for AgNPs originally functionalized with citrate (red), 5 mM 10 kDa PVP (black), and 5 mM 40 kDa PVP (purple) after ligand exchange with PEGSH. Error bars represent the standard error of at least five independent trials. 154

Figure 49. PEGSH ligand density plotted against time (A) and ligand density versus PEGSH excess with respect to surface area (B) for AuNPs (blue triangles) and AgNPs (black squares) functionalized with PVP followed by ligand exchange with PEGSH. Error bars represent the standard error of at least three independent trials. 155

Figure 50. Flowchart depicting the process for calculating the number of gold atoms per particle for ligand density determination for pseudospherical particles. 158

Figure 51. Flowchart depicting the process for calculating the number of ligands per particle for ligand density determination for pseudospherical particles..... 159

Figure 52. Flowchart depicting the process for ligand density determination for pseudospherical particles. 159

Figure 53. Representative calibration curves obtained for AUT (A), MUA (B), MOA (C), and MPA (D) by plotting integrated ratios of specific protons from each respective ligand/ACN against the concentration of that ligand to yield the equation for the line that will generate the unknown concentrations for each ligand. 160

Figure 54. Representative ^1H NMR spectra of PEGSeCN (red) and PEGSH (blue). The discrepancy in the peak at 3.1 ppm (for the PEGSH) and 2.68 ppm (for the PEGSeCN) is due to the location of the protons on the carbon adjacent to either the sulfur (in PEGSH) or the selenium (in PEGSeCN)..... 161

Figure 55. Representative ^1H NMR spectrum of PEGSH in D_2O with its labeled structure corresponding to plotted ^1H NMR peak locations. For calculation of PEGSH concentration, Peak A is integrated and compared to the integrated intensity of the ACN peak. 162

Figure 56. Representative ^1H NMR spectrum of AUT in D_2O with its labeled structure corresponding to plotted ^1H NMR peak locations. For calculation of AUT concentration, Peak C is integrated and compared to the integrated intensity of the ACN peak. Peaks from both the thiol and amine protons are not observed, as they exchange with the surrounding deuterated medium. 163

Figure 57. Representative ^1H NMR spectrum of MUA in D_2O with its labeled structure corresponding to plotted ^1H NMR peak locations. For calculation of MUA concentration, Peak D is integrated and compared to the integrated intensity of the ACN peak. 164

Figure 58. Representative ^1H NMR spectrum of MOA in D_2O with its labeled structure corresponding to plotted ^1H NMR peak locations. For calculation of MOA concentration, Peak D is integrated and compared to the integrated intensity of the ACN peak. 165

Figure 59. Representative ^1H NMR spectrum of MPA in D_2O with its labeled structure corresponding to plotted ^1H NMR peak locations. For calculation of MPA concentration, Peaks A and B (due to peak overlap) are integrated and compared to the integrated intensity of the ACN peak..... 166

Figure 60. Representative ^1H NMR spectrum of PEGSeCN acquired in D_2O 167

Figure 61. ^1H - ^1H Nuclear Overhauser Effect Spectroscopy (NOESY) of 13 nm AuNPs capped with PEGSH and ligand exchanged with MUA acquired with a 400 ms mixing time. MUA does not show any cross peaks with the PEGSH ligand, consistent with a segregated ligand shell architecture consisting of MUA and PEGSH domains. The formation of thiolated, small-molecule islands that are segregated from the original PEGSH shell are consistent with a cooperative binding mechanism for ligand exchange. The peaks at 4.7 ppm in the indirect dimension result from incomplete water suppression. The positive artifacts (red) on the PEGSH diagonal are residual T_1 noise that could not be completely removed. 168

Figure 62. UV-vis spectra for all 13 nm PEGSH-functionalized AuNPs before and after secondary ligand addition (A). No significant change in particle size is observed (average \pm standard deviation) (B). 169

Figure 63. UV-vis spectra for all 30 nm PEGSH-functionalized AuNPs before and after secondary ligand addition (A). No significant change in particle size is observed (average \pm standard deviation) (B). 169

Figure 64. UV-vis spectra for all 13 nm MUA-functionalized AuNPs before and after secondary ligand addition (A). No significant change in particle size is observed (average \pm standard deviation) (B)..... 170

Figure 65. UV-vis spectra for all 30 nm MUA-functionalized AuNPs before and after secondary ligand addition (A). No significant change in particle size is observed (average \pm standard deviation) (B)..... 170

Figure 66. UV-vis spectra for all 13 nm MOA-functionalized AuNPs before and after secondary ligand addition (A). No significant change in particle size is observed (average \pm standard deviation) (B)..... 171

Figure 67. UV-vis spectra for all 30 nm MOA-functionalized AuNPs before and after secondary ligand addition (A). No significant change in particle size is observed (average \pm standard deviation) (B)..... 171

Figure 68. Representative UV-vis-NIR spectrum for 13 nm NPs (A) and corresponding TEM image (B). Inset is a histogram for 13 nm NPs generated from measurements of at least 200 NPs. 172

Figure 69. Representative ^1H NMR spectrum of PEGSH after AuNP digestion. For calculation of PEGSH concentration, the labeled peak is integrated and compared to the integrated intensity of the ACN peak..... 173

Figure 70. Representative ^1H NMR spectrum of MUA after AuNP digestion. For calculation of PEGSH concentration, the labeled peak is integrated and compared to the integrated intensity of the ACN peak..... 174

Figure 71. Representative ^1H NMR spectrum of MOA after AuNP digestion. For calculation of PEGSH concentration, the labeled peak is integrated and compared to the integrated intensity of the ACN peak..... 175

Figure 72. Representative ^1H NMR spectrum of MHA after AuNP digestion. For calculation of PEGSH concentration, the labeled peak is integrated and compared to the integrated intensity of the ACN peak..... 176

Figure 73. Representative ^1H NMR spectrum after digestion of co-loaded AuNPs with PEGSH and MUA. For calculation of ligand concentrations, the peaks labeled PEGSH and MUA are integrated and compared to the integrated intensity of the ACN peak. 177

Figure 74. Representative ^1H NMR spectrum after digestion of backfilled AuNPs with MOA backfilled with PEGSH. For calculation of ligand concentrations, the peaks labeled PEGSH and MOA are integrated and compared to the integrated intensity of the ACN peak..... 178

Figure 75. Representative ^1H NMR spectrum of PEGNH₂ after AuNP digestion. For calculation of PEGNH₂ concentration, the labeled peak is integrated and compared to the integrated intensity of the ACN peak. 179

Figure 76. Representative ^1H NMR spectrum of AUA after AuNP digestion. For calculation of AUA concentration, the labeled peak is integrated and compared to the integrated intensity of the ACN peak..... 180

Figure 77. Representative ^1H NMR spectrum of AOA after AuNP digestion. For calculation of AOA concentration, the labeled peak is integrated and compared to the integrated intensity of the ACN peak..... 181

Figure 78. Representative ^1H NMR spectrum of AHA after AuNP digestion. For calculation of AHA concentration, the labeled peak is integrated and compared to the integrated intensity of the ACN peak..... 182

Figure 79. Representative ^1H NMR spectrum after digestion of co-loaded AuNPs with PEGNH₂ and AOA. For calculation of ligand concentrations, the peaks labeled PEGNH₂ and AOA are integrated and compared to the integrated intensity of the ACN peak. 183

Figure 80. Representative ^1H NMR spectrum after digestion of backfilled AuNPs with AUA backfilled with PEGNH₂. For calculation of ligand concentrations, the peaks labeled PEGNH₂ and AUA are integrated and compared to the integrated intensity of the ACN peak..... 184

Figure 81. Representative ^1H NMR spectrum of MUPA after AuNP digestion. For calculation of MUPA concentration, the labeled peak is integrated and compared to the integrated intensity of the ACN peak..... 185

Figure 82. Representative ^1H NMR spectrum after digestion of MUPA and MUA co-loaded AuNPs. For calculation of ligand concentrations, the peaks labeled MUA and MUPA are integrated and compared to the integrated intensity of the ACN peak. 186

Figure 83. Representative ^1H NMR spectrum of biotinPEGSH after AuNP digestion. For calculation of biotinPEGSH concentration, the labeled peak is integrated and compared to the integrated intensity of the ACN peak..... 187

Figure 84. Representative ^1H NMR spectrum after digestion of biotinPEGSH and PEGSH co-loaded AuNPs. For calculation of ligand concentrations, the peaks labeled biotinPEGSH and PEGSH are integrated and compared to the integrated intensity of the ACN peak. 188

Figure 85. Graph of the total number of ligands on PEGSH AuNPs backfilled with MUA as a function of time for 13 nm AuNPs, where the error bars represent the standard error of at least 5

trials. Results indicate that ligand loading reaches consistent values on the timescale of 2-3 hours under the conditions tested..... 189

Figure 86. Graph of the total number of ligands on MUA AuNPs backfilled with PEGSH as a function of time for 13 nm AuNPs, where the error bars represent the standard error of at least 5 trials. Results indicate that ligand loading reaches consistent values on the timescale of 2-3 hours under the conditions tested..... 190

Figure 87. Graphs of the total number of ligands on MUA AuNPs backfilled with MPA as a function of time for 13 nm AuNPs, where the error bars represent the standard error of at least 5 trials. Results indicate that ligand loading reaches consistent values on the timescale of 2-3 hours under the conditions tested..... 191

Figure 88. UV-vis-NIR spectra for all 13 nm AuNPs before and after ligand exchange from citrate to a thiolated ligand (A), after co-loading with two thiolated ligands (B), after backfilling PEGSH-capped particles with a secondary thiolated ligand (C), and after backfilling with PEGSH from other thiolated ligand-capped particles (D). 192

Figure 89. UV-vis-NIR spectra for all 13 nm AuNPs before and after ligand exchange from citrate to an aminated ligand (A), after co-loading with two aminated ligands (B), after backfilling PEGNH₂-capped particles with a secondary aminated ligand (C), and after backfilling with PEGNH₂ from other aminated ligand-capped particles (D). 193

Figure 90. Representative ¹H NMR spectrum after digestion of BSPP-capped AuNPs. For calculation of ligand concentrations, the peak labeled BSPP is integrated and compared to the integrated intensity of the ACN peak..... 195

Figure 91. Representative ^1H NMR spectrum after digestion of BSPP and PEGSH co-loaded AuNPs. For calculation of ligand concentrations, the peaks labeled BSPP and PEGSH are integrated and compared to the integrated intensity of the ACN peak. 196

Figure 92. Representative ^1H NMR spectrum after digestion of BSPP and MOA co-loaded AuNPs. For calculation of ligand concentrations, the peaks labeled BSPP and MOA are integrated and compared to the integrated intensity of the ACN peak. 197

Figure 93. Representative ^1H NMR spectrum after digestion of BSPP and PEGNH₂ co-loaded AuNPs. For calculation of ligand concentrations, the peaks labeled BSPP and PEGNH₂ are integrated and compared to the integrated intensity of the ACN peak. 198

Figure 94. Representative ^1H NMR spectrum after digestion of BSPP and AOA co-loaded AuNPs. For calculation of ligand concentrations, the peaks labeled BSPP and AOA are integrated and compared to the integrated intensity of the ACN peak. 199

Figure 95. Representative ^1H NMR spectrum of 4-DPPBA after digestion of the AuNPs with its labeled structure corresponding to plotted ^1H NMR peak locations. For the calculation of 4-DPPBA concentration, Peaks A-E (due to peak overlap) are integrated and compared to the integrated intensity of the ACN peak..... 201

Figure 96. Representative ^1H NMR spectrum of TGA-exchanged AuNPs following digestion with aqua regia with its labeled structure corresponding to plotted ^1H NMR peak locations. Due to overlap of the impurity peak (+) with the ACN internal standard peak, isopropanol (IPA) is used as an internal standard. The impurity peak (*) is residual polymeric material (glycerol) from the molecular weight cut-off filters..... 202

Figure 97. Representative ^1H NMR spectrum of MPA-exchanged AuNPs following digestion in aqua regia with its labeled structure corresponding to plotted ^1H NMR peak locations. For the

calculation of MPA concentration, Peaks A and B are integrated and compared to the integrated intensity of the ACN peak..... 203

Figure 98. Representative ^1H NMR spectrum of MBuA-exchanged AuNPs following digestion in aqua regia with its labeled structure corresponding to plotted ^1H NMR peak locations. For the calculation of MBuA concentration, Peak B is integrated and compared to the integrated intensity of the ACN peak..... 204

Figure 99. Representative ^1H NMR spectrum of MHA-exchanged AuNPs following digestion in aqua regia with its labeled structure corresponding to plotted ^1H NMR peak locations. For the calculation of MHA concentration, Peak B is integrated and compared to the integrated intensity of the ACN peak. 205

Figure 100. Representative ^1H NMR spectrum of MOA-exchanged AuNPs following digestion in aqua regia with its labeled structure corresponding to plotted ^1H NMR peak locations. For the calculation of MOA concentration, Peak D is integrated and compared to the integrated intensity of the ACN peak. 206

Figure 101. Representative ^1H NMR spectrum of MUA-exchanged AuNPs following digestion in aqua regia with its labeled structure corresponding to plotted ^1H NMR peak locations. For the calculation of MUA concentration, Peak D is integrated and compared to the integrated intensity of the ACN peak. 207

Figure 102. Representative ^1H NMR spectrum of PEGSH-exchanged AgNPs following particle digestion in nitric with its labeled structure corresponding to plotted ^1H NMR peak locations. For the calculation of PEGSH concentration, peak A is integrated and compared to the integrated intensity of the IPA doublet peak at 1.17 ppm..... 208

Figure 103. Representative ^1H NMR spectrum of PEGSH-exchanged AuNPs following particle digestion with its labeled structure corresponding to plotted ^1H NMR peak locations. For the calculation of PEGSH concentration, peak A is integrated and compared to the integrated intensity of the ACN peak..... 209

Figure 104. Representative ^1H NMR spectrum of AUT-exchanged Au prisms following digestion with aqua regia with its labeled structure corresponding to plotted ^1H NMR peak locations. For calculation of AUT concentration, Peak D is integrated and compared to the integrated intensity of the ACN peak. 210

Figure 105. Representative ^1H NMR spectrum of MUA-exchanged Au prisms following digestion with aqua regia with its labeled structure corresponding to plotted ^1H NMR peak locations. The peak labelled with (*) indicates trace amounts of residual CTAB remaining after the ligand exchange. For calculation of MUA concentration, Peak B is integrated and compared to the integrated intensity of the ACN peak..... 211

Figure 106. Representative ^1H NMR spectrum of MMPA-exchanged Au prisms following digestion with aqua regia with its labeled structure corresponding to plotted ^1H NMR peak locations. For calculation of MMPA concentration, Peak C is integrated and compared to the integrated intensity of the ACN peak..... 212

LIST OF EQUATIONS

Equation 1	65
Equation 2	65

ACKNOWLEDGEMENTS

I would first like to thank my advisor, Jill Millstone. Throughout my graduate studies, she has encouraged and supported me to become a better scientist and individual. She has provided a steady source of inspiration to complete better experiments, approach tasks in creative ways, and expand my knowledge in science and leadership. I will always be incredibly grateful for having Jill as my advisor and the wide range of opportunities that she has allowed me to explore.

I would next like to thank all of the past and present members of the Millstone lab, whose friendship and encouragement have made my graduate experience more fulfilling. I consider myself lucky to have had the opportunity to work with all of you and get to know you as friends. I would especially like to thank Katie Johnston, Scott Crawford, and Dr. Chris Andolina for their friendship and the many fruitful conversations about both science and life outside of it. I also need to thank Professors Carol Fortney and Ericka Huston for their wise advice and the opportunities to expand my teaching skills.

Finally, I would like to thank my family and Chris Marvin. Throughout the last six years, Chris has been both an unwavering support and my best friend. My parents, sister, and the rest of my family have given me the love and encouragement necessary to help me get to where I am today. I will always be grateful for everything you have given me and for always being there.

1.0 LIGAND DENSITY QUANTIFICATION ON COLLOIDAL INORGANIC NANOPARTICLES

(Portions of this work were previously published and reprinted with permission from Smith, A. M.; Johnston, K. A.; Crawford, S. E.; Marbella, L. E.; Millstone, J. E., *Analyst*. **2017**, *142*, 11-29. Copyright 2017, The Royal Society of Chemistry.)

1.1 INTRODUCTION

Nanoparticles (NPs) demonstrate a myriad of new and potentially useful properties that deviate from those observed in their bulk or molecular counterparts. A key component of these structure-function relationships is the surface chemistry of the NPs. Surface chemistry is defined by both the crystallographic features of the particle surface as well as the ligands appended to it. Here, ligands refer to species adsorbed to the NP surface and can range from monoatomic ions to large macromolecules. Ligands can be used to control the growth of the particle,¹⁻³ to provide stability to particles once formed,⁴⁻⁶ and also to direct their functionality.⁷⁻¹² For example, ligands may influence charge transfer in NP-based devices¹³ or targeting in biological systems.¹⁴ On extended solid surfaces, correlations between surface ligand architectures and the function of the material have been well-documented,¹⁵⁻¹⁷ in no small part because of the thorough characterization of the ligand architecture itself.¹⁸⁻²¹ However, the study and use of ligand arrangements on colloidal

inorganic NPs present unique (and sometimes deceptively mundane) challenges including polydispersity in NP samples, determination of NP surface area, and purification of particle conjugates from unbound ligands.

The analytical methods used to assess NP ligand architectures depend on the questions one asks about the ligand shell structure. Three fundamental aspects of this structure are the identity of the constituent ligands, the quantity of each ligand type, and the spatial arrangement of those ligands, both with respect to each other and to the NP core. Therefore, a crucial first step towards understanding and leveraging NP surface chemistry is to describe each of these architectural features, the most basic of which is the quantity of ligands appended to the NP surface. Ligand quantification studies may be used in a variety of ways including to assess as-synthesized particle ligand densities, ligand densities after post-synthetic modification (e.g. ligand exchange), or following particle exposure to, or operation in, various environments.^{22, 23} Ligand identification and quantification then provides a robust foundation from which to study additional features of the NP ligand shell including aspects of its arrangement and dynamics,^{24, 25} as well as NP efficacy in downstream applications, including drug delivery^{26, 27} and heterogeneous catalysis.^{28, 29}

Here, we review techniques that determine NP ligand density, focusing on methods that yield a quantitative ligand analysis (i.e. an absolute ligand density as opposed to relative ligand ratios). In Section 1.2, we outline characteristics of both the NP and the ligand that inherently influence particle ligand densities as well as the analytical methods used to evaluate them. We then discuss the implementation of these approaches in detail, with the discussion divided into sections based on the analytical approach. Thermogravimetric analysis, the first widely implemented technique for ligand quantification, is discussed in Section 1.3. Subsequently, we

highlight various spectroscopic methods, including optical (Section 1.4), atomic (Section 1.5), nuclear magnetic resonance (Section 1.6), and vibrational (Section 1.7) spectroscopies. We also include brief reviews of niche or emerging techniques including electrospray-differential mobility analysis (Section 1.8), pH-based methods (Section 1.9), and X-ray photoelectron spectroscopy (Section 1.10). We have summarized the ligand density results of the highlighted studies in the table below (Table 1). In order to facilitate comparisons between methods, we report all ligand densities in units of ligands/nm², using information contained in the specific reports to make unit conversions when necessary.

1.2 GENERAL CONSIDERATIONS FOR LIGAND QUANTIFICATION

An ideal method to quantify ligands on a particle surface would be to isolate an individual NP and count ligands directly bound to that structure only. However, since techniques have not yet been developed to characterize particles in such detail, all current analytical methods for determining particle ligand densities involve analysis of the bulk colloid in some way. Below, we outline general considerations when quantifying ligands on a NP surface, including characteristics of the NP core (Section 1.2.1) and ligand shell (Section 1.2.2).

1.2.1 Core Considerations

Measurements of NP concentration and core morphology strongly influence the accuracy of ligand density determination because both parameters are needed to determine the total surface area of the particle sample. This total surface area is then used to extract ligand density values.

1.2.1.1 Particle Concentration and Surface Area Calculation

In order to determine particle ligand densities, the general approach is to divide the total amount of ligands measured by the total amount of particle surface area measured. This method of ligand density determination is necessary because single particle ligand counting is not yet feasible (*vide supra*). Therefore, although we focus here on quantification of NP ligands, quantification of particle ligand densities also critically depends on the measurement of total particle surface area. Surface area can be determined directly using methods such as gas sorption approaches³⁰⁻³⁴ or may be determined indirectly by calculating surface area from NP core concentrations and average particle dimensions (where dimensions may be determined by techniques including transmission electron microscopy (TEM), scanning electron microscopy (SEM), or dynamic light scattering (DLS)).

However, whether particle surface area is measured directly or indirectly, particle concentration must also be determined in order to quantify per particle ligand densities. There are multiple methods to measure NP core concentrations. Two of the most common approaches are absorption spectroscopy and atomic spectroscopies such as inductively coupled plasma mass spectrometry/atomic emission spectroscopy (ICP-MS/AES). For absorption spectroscopy measurements, absorbance of the NP sample at a specific wavelength is recorded. Then, using the particle molar extinction coefficient at this wavelength, the particle concentration can be determined.³⁵⁻³⁸ Absorption spectroscopy, especially in the solution phase, has several advantages including the ability to perform measurements *in situ* (e.g. assessing NP concentration as a function of ligand exchange or modification reactions). However, because each NP has an extinction coefficient (at a given wavelength) that varies as a function of NP size, shape, and surface chemistry, dispersity in these parameters influences the calculated NP

concentration when using a single average extinction coefficient. Polte and co-workers have conducted a detailed study of these dispersity-induced errors, including particle size variation, NP surface modification, and metal oxidation state.³⁹

Unlike absorption measurements, ICP-MS/AES measures the total number of atoms of interest in the NP sample. Then, the atom concentrations are combined with experimentally determined NP sizes and shapes to derive the total surface area of the sample. Therefore, ICP-MS/AES approaches have the same shortcomings introduced by NP dispersity as discussed above.⁴⁰⁻⁴³ However, ICP-MS/AES measures atom concentration directly and is unparalleled in atom detection sensitivity regardless of NP size, surface chemistry, or oxidation state (detection limits vary depending on instrument, experimental conditions, and analyte of interest but can range as low as parts-per-trillion for Au detected with high resolution ICP-MS).⁴⁴

Taken together, each NP surface area determination approach ultimately assumes an average particle size and shape and determines a total particle surface area from those values. As a result, the error in calculated ligand density is fundamentally limited by the dispersity of the particle sample in terms of both size and shape, regardless of the method selected (see Appendix A for sample calculation methodology).

1.2.1.2 Core Morphology

Even if single particle ligand counting was possible, different surface features can be exhibited within a single particle and each unique surface will likely have a distinct ligand density for any given ligand of interest. NP properties that may produce this heterogeneity include core composition, size, and shape. Particle size and shape influence parameters such as the population of exposed crystal facets and surface radii of curvature, which can influence inter-ligand interactions. Composition also influences the population of exposed Miller planes (and

corresponding surface atom densities) for any given particle, and ligands may arrange differently depending on these features.^{45, 46} Further, in multi-element NPs (e.g. alloyed or metal chalcogenide NPs), ligand binding and arrangements will vary depending on which atoms are present at the NP surface and the affinity of the ligand for each atom (or site) type.⁴⁷⁻⁴⁹ It is important to note that in the ligand quantification approaches discussed here, facet- or atom-specific ligand quantification is not resolved, although recent nuclear magnetic resonance (NMR) studies have shown promise for determining these details.⁵⁰

Finally, particle core properties not only influence intrinsic ligand binding motifs, they also impact the selection of analytical approaches for evaluating those motifs. For example, in certain absorption spectroscopy techniques, ligand-dependent shifts in particle optical features such as localized surface plasmon resonances (LSPRs) are exploited.^{51, 52} For these techniques, particles must be of both a composition and a size that exhibit spectroscopically discernible LSPRs, among other factors. Likewise, the composition of the NPs may impact the use of techniques such as ICP-MS/AES, where challenges including spectral interferences between analyte elements can occur.

1.2.2 Ligand Property Considerations

While a wide variety of chemical moieties may act as NP ligands, organic small molecules are some of the most common and are the most widely studied with respect to quantification. These ligands have three key regions (Figure 1). First is the particle binding moiety (e.g. -SH, -PR₃, -NH₂) which is directly appended to the NP surface. The density of ligands on the surface of a NP is fundamentally limited by the space this functional group occupies.⁵³⁻⁵⁵ The second region is the intra-molecular portion, and there is a wide array of chemical functionalities that can be

present at this site. Interactions between adjacent intra-molecular regions (i.e. inter-molecular interactions) can also influence ligand density limits via factors such as steric effects and noncovalent interactions. Last, there is the solvent-facing portion of the molecule. Each region, and/or all regions in concert, may influence not only the fundamental limits on the physical space occupied by the ligands but also the dynamics of these ligands in ligand exchange equilibria,^{56, 57} surface ligand migration (i.e. translational motion),^{58, 59} and ligand conformation with respect to the surface (e.g. tilt, cant, or intra-ligand conformers).⁶⁰⁻⁶²

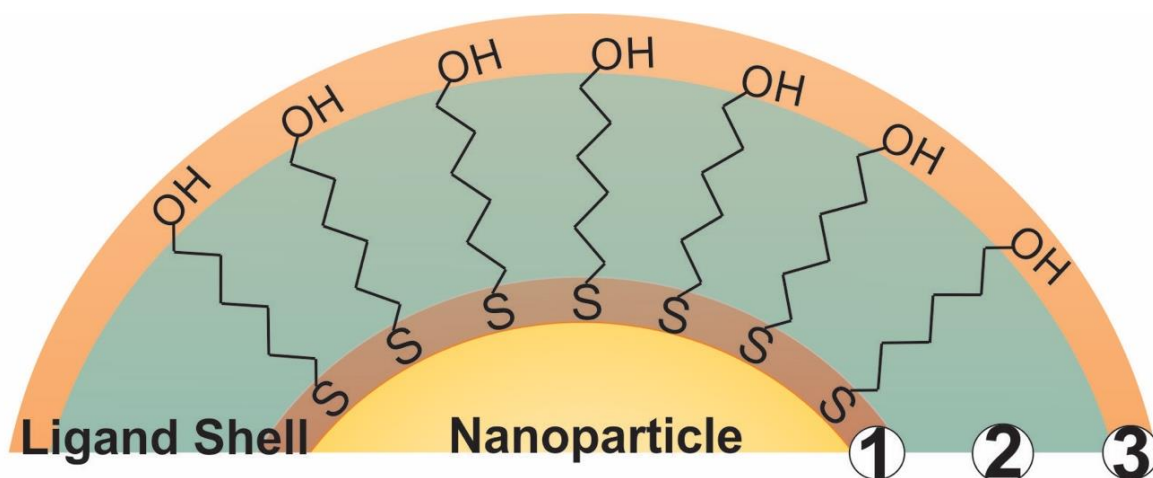


Figure 1. Scheme representing three key regions of small molecule capping ligands: 1. the particle binding moiety, 2. an intra-molecular region, and 3. a terminal group. *N. B.* Components in regions 2 and 3 can also interact with the NP surface under certain conditions (*vide infra*).

All of these dynamic factors can play key roles in the accuracy of any given ligand quantification approach. For example, in preparing NP-ligand conjugates for quantification analysis (and typically, for subsequent applications), the conjugates must be washed thoroughly in order to remove any unbound or non-specifically bound ligands from solution. However, if the

ligands are not strongly associated with the particle, such as trisodium citrate on AuNPs,¹⁵ the on-particle ligand density will be modified during the purification steps, and accurate ligand quantification may not be possible with current capabilities.

These ligand dynamics also impact variation in ligand density from sample to sample as a function of several factors. First, variability can occur from ligand dissociation during particle washing procedures as mentioned above. Second, ligand adsorption is a dynamic process, and therefore depending on how long the sample is exposed to excess ligand, some variability is expected. Consequently, it is helpful to analyze ligand density by conducting both a binding isotherm study as well as a time-based quantification study at constant ligand excess, in order to assess whether consistent ligand loading values are achieved during the functionalization procedure selected. In this report, standard errors or deviations in ligand density values are included for all cases where they are available from the original report.

Table 1. Compilation of ligand densities (in units of ligands/nm²) reported by papers reviewed in chapter 1.

Particle Type	Ligand Identity	Reported NP Size ^a (nm)	Packing Density (Ligands/nm ²)	Quantification Technique	Source
Ag	MUA	4.5 ± 1.3	6.4	TGA	88
	1 kDa PEGSH	25.4 ± 2.1	2.11 ± 0.06	NMR	130
Au	MPA	5	6.7	ICP-OES	120
	MPA	13.2 ± 1.4	6.26 ± 0.59	ICP-MS	119
	Thioctic acid	11.6 ± 1.0	1.72	XPS	155
	DDT	5.6	4.67	TGA	77
	MUA/DPPBA	1.8 ± 0.4	5.50 ± 0.88	NMR	25
	MUA	2.4 ± 0.5	14	pH	150
	MUA	12.6 ± 1.2	4.97	XPS	154
	MUA	13 ± 1	4.5 ± 0.1	NMR	54
	MUA	13.8 ± 0.9	4.68 ± 0.05	UV-vis	52
	tetradecanethiol	2.0 ± 0.8	5.81 ± 0.14	TGA	66
	tetradecanethiol	3.9 ± 0.5	4.35	TGA	71
	EG ₄ -SH	3.4	4.17	TGA	75
	HS(CH ₂) ₁₁ -(EG) ₆ -OH	1.3 ± 0.3	3.8 ± 0.7	XPS	153

Particle Type	Ligand Identity	Reported NP Size ^a (nm)	Packing Density (Ligands/nm ²)	Quantification Technique	Source
Au	1 kDa PEGSH	60	1.4	IR	23
	2 kDa PEGSH	5.7 ± 2	2.38	TGA	67
	2 kDa PEGSH	4.9 ± 1.0	7.04 ± 2.97	TGA	68
	2 kDa PEGSH	11.7 ± 1.4	2.25 ± 0.01	TGA	64
	2.1 kDa PEGSH	15 ± 1.8	3.93	TGA	63
	5 kDa PEGSH	2.8 ± 1	2.88	TGA	79
	1 kDa NH ₂ PEGSH	16.9 ± 0.26	0.36 ± 0.05	TGA	74
	3 kDa PEGNH ₂	50 [‡]	2.21 ± 0.18	UV-vis	98
	0.6 kDa TA-PEG-Mal	10	0.83 ± 0.06	UV-vis	110
	740 Da HCO ₂ -PEGSH	4.1 ± 0.8	1.33	pH	149
	3.4 kDa FITC-PEGSH	27.6 ± 2.1	5.56	TGA	76
	2 kDa PS-SH	4.4 ± 1.2	3.45	TGA	70
	7 kDa PNIPAM	5.2	0.83	TGA	73
	4.7 kDa cumyl-NIPAM	2.2 ± 0.8	2.2	TGA	72
	HS-DNA (10 bp)	20	0.69	ES-DMA	146
	HS-DNA (12 bp) ^ψ	15.7 ± 1.2	0.21 ± 0.01	PL	97
	HS-DNA (25 bp)	10	0.21 ± 0.04	PL	101
	HS-DNA (25 bp)	15	0.23	PL	100
	HS-DNA (32 bp) [†]	15.7 ± 1.6	0.17 ± 0.01	PL	102
	BSA	20	0.13 ± 0.01	PL	109
	BSA	30	0.03	ES-DMA	148
	tiopronin	3.9 ± 1.7	3.83	TGA	81
	MBI	13	3.44 ± 0.03	Raman	144
	MBI	13	3.80 ± 0.05	Raman	61
	1-pyrenebutanethioic acid S-butyl ester	12.5 ± 1.5	4.08 ± 0.17	PL	108
	MMC	5.3 ± 2.1	0.86	UV-vis	51
	calix[4]arene enantiomers	4.7 ± 1.3	1.10	UV-vis	112
	calix[6]arene derivatives	4.2 ± 0.9	0.42 ± 0.03	UV-vis	113
calix[8]arene phosphinoxides	4.3 ± 0.8	0.44	UV-vis	114	
CdS	thiophenol	2.4 ± 0.1	1.37 ± 0.34	NMR	126
CdSe	oleate	3.5 ± 0.1	4.6 ± 0.4	NMR	139
	oleate	4.2	4.1	NMR	22
	oleate/tetradecanoate	3.3 ± 0.2	2.9 ± 0.5	NMR	57
	oleate/tetradecanoate	3.5	4.2 ± 0.7	NMR	131
	1 kDa LA-PEG-CHO	6.2	1.66 ± 0.09	UV-vis	111
	TOPO/TOPSe	3.7 ± 0.4	3.72	NMR	143
	CH ₃ -TP	3.7	4.1 ± 2.7	NMR	24
Fe ₃ O ₄	350 Da SiPEG	30-40	0.79	TGA	87
	glycine	14	1.27	TGA	85

Particle Type	Ligand Identity	Reported NP Size ^a (nm)	Packing Density (Ligands/nm ²)	Quantification Technique	Source
InP	TOPO	4.7	3	NMR	138
PbS	oleate/tetradecanoate	3.1	4.3 ± 0.5	NMR	131
PbSe	oleate	3-7	4.2	NMR	123
	oleate	4.9	3.18	NMR	22
	oleate/tetradecanoate	3.7	3.1 ± 0.5	NMR	131
Pd	1-octyne	2.5 ± 0.3	7.69	TGA	29
	DDT	2.2 ± 0.7	3.49	TGA	91
	DDT	3.4 ± 1.0	4.57	TGA	28
	butylphenyl	2.2 ± 0.4	4.76	TGA	89
Pt	chlorophenyl	1.9 ± 0.3	12.50	TGA	94
	butylphenyl	2.9 ± 0.5	17.24	TGA	95
Ru	1-octynyl	2.6 ± 0.2	6.67	TGA	93
SiO ₂	2 kDa PNIPAM	54.3 ± 3.7	0.58	TGA	82
	alanine	7	2.02 ± 0.13	TGA	84
	lysine	7	2.3 ± 0.2	TGA	83
SiO ₂ @Au	<i>p</i> MA-PEG2000-FI	90 nm core, 17 nm shell	0.28 ± 0.13	Raman	145
ZnO	DDA	3.6 ± 0.4	1.2 ± 0.2	NMR	142

^a For all reported sizes where a standard deviation is not given in the table, a standard deviation was not reported in the original text. For NP size ranges, a size range (as opposed to a standard deviation) was reported in the original text.

^ψ In addition to a terminal thiol, this DNA sequence also includes a C₆ alkane spacer moiety before and after the ssDNA sequence.

^Γ In addition to a terminal thiol, this DNA sequence also includes a hexyloxy spacer moiety between the thiol group and the ssDNA sequence.

[‡]The size reported for this NP is an edge length of Au nanocages.

1.3 THERMOGRAVIMETIC ANALYSIS (TGA)

One of the earliest and most common methods used to assess NP ligand density is TGA.⁶³⁻⁷⁶ In a typical experiment, the sample is thoroughly dried and its dry mass recorded. Then, the sample is heated (rates range from 5-20 °C/minute), and its change in mass is recorded as a function of temperature. The temperature of mass loss is related to ligand identity. After heating, the percentage of mass loss within a ligand-specific temperature range can be correlated with the

number of ligands appended to the particle. The corresponding NP concentration is typically determined from the remaining mass after heating.

Early studies of TGA-based NP ligand quantification were reported by Murray and co-workers. The authors examined various thiolated ligands appended to small, pseudospherical AuNPs ($d = 1.5 - 5.2$ nm).⁷⁷⁻⁸⁰ Throughout these studies, the authors found that ligand density varied only slightly depending on particle size and ligand identity. For example, the studies found that dodecanethiol (DDT) ligand densities were approximately 4.6 ligands/nm² for both 2.8 nm and 5.2 nm diameter AuNPs.⁷⁷ Larger ligands such as α -methoxy- ω -mercaptopoly(ethylene glycol) (PEGSH, molecular weight (MW) = 5 kDa) on similarly sized NPs ($d = 2.8 \pm 1$ nm) produced lower ligand densities (2.88 ligands/nm²),⁷⁹ demonstrating that larger ligands may pack less densely on AuNP surfaces, even when the surface has a high radius of curvature.

The authors extended their studies to more diverse ligands, including the thiol-terminated, biologically relevant molecule tiopronin. Tiopronin (MW = 163 Da) is smaller than PEGSH but sterically bulkier than DDT and exhibits a ligand density of 2.68 ligands/nm² on 3.1 ± 1.2 nm diameter AuNPs. Interestingly, this tiopronin ligand density is markedly lower than for either the polymeric ligand or the alkanethiol. In this case, the decreased ligand density was attributed to the steric bulk directly surrounding the NP binding moiety.⁸¹ Taken together, these studies indicate that for a given particle binding moiety (and NP surface), the steric bulk directly at this molecular region is the limiting factor in determining ligand surface coverage, independent of both the size of the remainder of the molecule (e.g. the case of PEGSH) and the particle radius of curvature.

Thiol-terminated PEG ligands (range of MWs = 2.1 - 51.4 kDa) on AuNPs ($d = 15 - 170$ nm) were also studied using TGA by Holmes and co-workers.⁶³ The authors observed a decrease in surface ligand density as polymer MW increases, consistent with other studies of thiol-terminated polymeric ligands (Figure 2). Colvin and co-workers also investigated the ligand density of various thiolated PEG molecules using TGA, and importantly, compared those results with ligand density values obtained by two other methods: analytical ultracentrifugation (AU) and total organic carbon analysis (TOC). The authors found that ligand loading densities were similar for all three methods with values that deviated by less than 22% across a variety of PEGSH MWs (MW = 1 - 20 kDa) and particle diameters ($d = 5, 10, 15,$ or 20 nm).⁶⁴

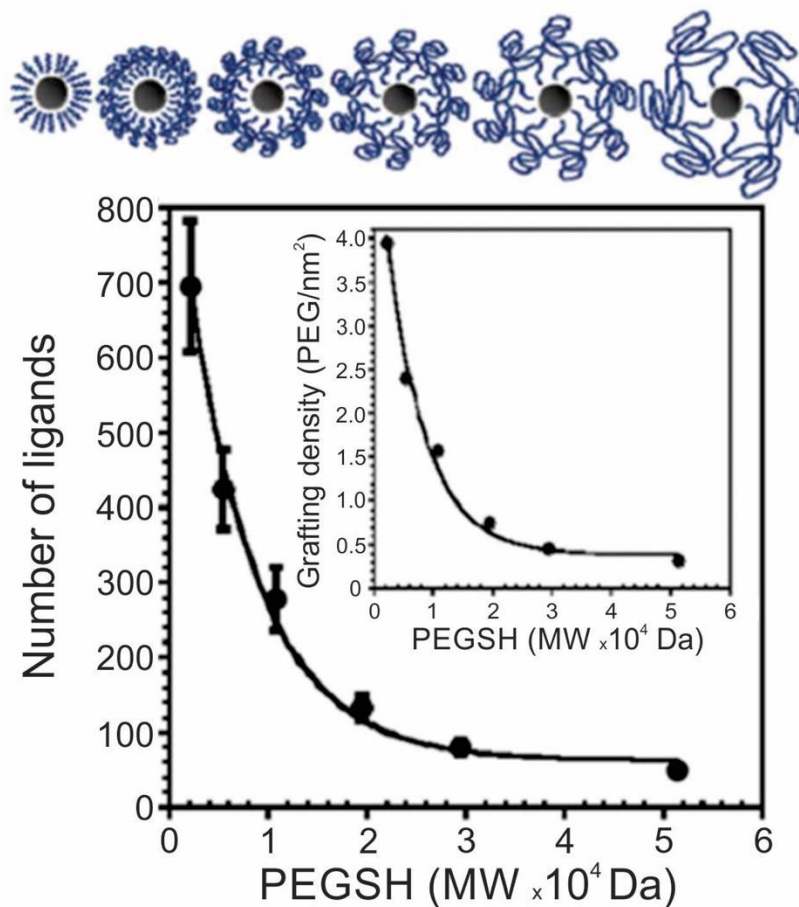


Figure 2. Number of PEGSH ligands on 15 nm AuNPs as a function of PEGSH molecular weight, showing that ligand density decreases as ligand chain length increases; inset plots “grafting” (i.e. ligand) density as a function of PEGSH molecular weight. Modified from ref. 63 with permission from The Royal Society of Chemistry.

While AuNP-ligand conjugates are the most thoroughly studied NPs using TGA, TGA has also been used to study ligand densities on other particle types, including silica,⁸²⁻⁸⁴ magnetite,⁸⁵⁻⁸⁷ Ag,⁸⁸ Pd,^{28, 29, 89-92} Ru,⁹³ and Pt.⁹⁴⁻⁹⁶ These studies have been conducted primarily in conjunction with catalysis or biomedical studies that draw connections between NP ligand density and particle performance in a given application. For example, Shon and co-workers investigated the correlation between ligand density and catalytic activity of PdNPs in the isomerization of allyl alcohols to their carbonyl analogues. Using a variety of alkanethiol and thiosulfate ligands, the authors found that NPs with lower ligand densities exhibited enhanced catalytic activity.^{28, 91, 92} Various other reports also correlate ligand densities on Pd and Pt NPs to catalytic figures of merit, including activity.^{29, 89, 94, 95}

For biological investigations, Davis and co-workers have found that lymph node uptake of magnetite NPs ($d = 40 - 50$ nm) was influenced by the ligand density of pendant PEG molecules (PEG terminally substituted by trimethoxysilane, SiPEG; MW = 350, 550, 750, or 1,000 Da).⁸⁶ By comparing different ligand densities with various MWs of SiPEG, the authors found that the biodistribution of these particles could be tuned for optimized lymph node uptake. The highest uptake was observed for magnetite particles capped with 750 Da SiPEG with a maximum loading of $0.8 \mu\text{mol}/\text{m}^2$ (0.48 ligands/ nm^2), although improved lymph node uptake was observed in nearly all cases with the addition of SiPEG compared to the un-PEGylated magnetite NPs.⁸⁶

The above studies demonstrate that TGA is an effective technique for ligand quantification for a wide range of both ligand and particle types. However, it is important to note that this method is limited in the characterization of multicomponent ligand shells (i.e. particle

ligand shells that contain more than one ligand type), since often it is not possible to distinguish between ligand removal temperatures, especially for ligands with similar masses.

1.4 OPTICAL SPECTROSCOPY

Ligand quantification using optical spectroscopy includes both absorption and photoluminescence (PL) measurements. These techniques frequently exploit optically active indicators, such as fluorescein, which are used to label ligands appended to the particle surface. Typically, these labelled ligands are released for measurement by digesting the particle. The optical signal from the labelled ligands is then compared to a calibration curve prepared from standards to determine unknown ligand concentrations. Colorimetric or fluorescence assays may also be used to quantify the concentration of free ligand before and after the introduction of particles, where the change in concentration after particle introduction is attributed to ligands attaching to the particle surface. For plasmonic particles, techniques have been developed to correlate changes in the LSPR to ligand densities. Additionally, if optically active ligands are used, techniques such as time-correlated single photon counting (TCSPC) or measurements of ligand excimer PL can be used to measure the amount of ligand present in a sample. Following quantification of ligand concentrations by the above methods, the corresponding NP concentration is typically determined using either atomic or absorption spectroscopy.

1.4.1 Photoluminescence (PL) Spectroscopy

A variety of PL techniques have been developed to quantify ligand density and functionality. These methods require ligands that are inherently fluorescent, ligands that are labelled with a fluorophore, or the addition of a fluorescent indicator. Both steady-state and time-resolved techniques have been used.

1.4.1.1 Fluorescently-labelled Ligands

In 2000, Mirkin and Letsinger used PL spectroscopy to quantify oligonucleotide loading on AuNPs ($d = 15.7 \pm 1.2$ nm) and established relationships between various ligand properties and the extent of DNA hybridization on the NP surface.⁹⁷ Specifically, the authors used fluorescein to label individual thiolated oligonucleotides (12 base pair (bp) single-stranded DNA (ssDNA) with a hexanethiol spacer before and after the DNA sequence) and then exploited the quenching properties of AuNPs as a signal mediator. AuNPs and other metals are known to quench the emission of nearby luminophores through decay pathways such as nanosurface energy transfer (NSET), in which conduction electrons in the metal interact with the luminophore dipole.^{98, 99} Therefore, in these experiments, no PL was observed from the fluorophore-labelled ligands when appended to the NPs. After incubating the AuNPs in 2-mercaptoethanol, the thiolated ssDNA was displaced, and after separation from remaining AuNPs via centrifugation, PL from the displaced oligonucleotides was measured at 520 nm. The concentration of released ssDNA was determined by comparing this PL signal to a standard calibration curve and used to calculate a ligand density of 0.21 ± 0.01 ligands/nm².⁹⁷ Using similar methods, the authors also showed that only 4% of particle-bound ssDNA hybridized with a complementary strand when the oligonucleotide sequences were directly appended to the AuNP via a terminal thiol linkage.

However, hybridization efficiency increased to 44% if a 20 base pair “spacer” sequence was added between the thiol and the DNA sequence of interest.⁹⁷

This general method of quantification via the release of fluorescently-labelled ligands has been slightly modified to study a variety of particle morphologies and ligand types.^{98, 100-105} Mirkin and co-workers expanded their initial studies to quantify ligand density on different sizes of AuNPs ($d = 10 - 250$ nm) and investigated how parameters such as salt concentration and post-conjugation treatments (e.g. sonication) impacted final DNA density on the NPs.¹⁰⁰⁻¹⁰² In these studies, dithiothreitol (DTT) was used to displace the fluorescein-labelled ligand shell (Figure 3). The ligand density decreased with AuNP size from 0.20 ± 0.04 ligands/nm² for 10 nm AuNPs to 0.06 ± 0.01 ligands/nm² for planar Au.¹⁰¹ The same group used these quantitative values to establish surface ligand-dependent particle properties. For example, the authors observed a positive correlation between AuNP cellular uptake and oligonucleotide loading density.¹⁰³ Liu and co-workers have also used fluorescence-based techniques to analyze DNA loading on AuNPs ($d = 50$ nm) in different salt concentrations and in a 2% PEG solution (MW = 20 kDa), where the PEG in solution does not adsorb to the particles but is thought to improve particle stability.¹⁰⁴

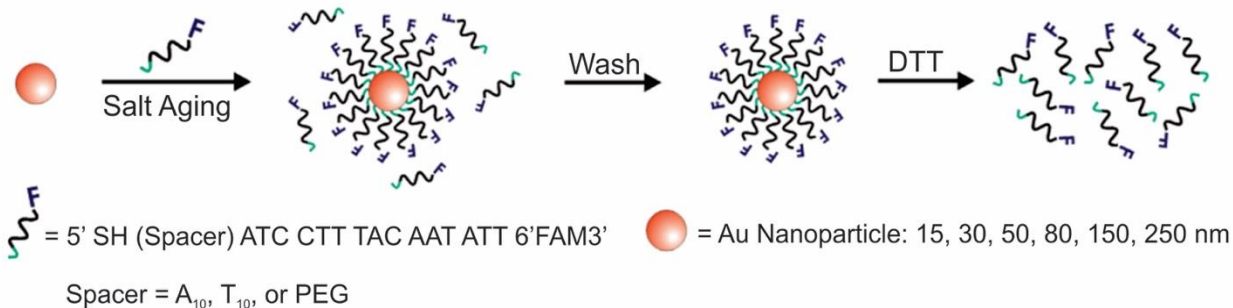


Figure 3. Scheme illustrating the quantitative analysis of oligonucleotide-functionalized AuNPs of various core diameters. Here, AuNPs are functionalized with fluorescein-labelled oligonucleotides in the presence of salt, purified, and then exposed to DTT, which removes the ligands from the NP surface. The released ligands are then quantified using photoluminescence spectroscopy. Adapted with permission from ref. 100. Copyright 2006 American Chemical Society.

In addition to total ligand density, fluorophore labelling has also been used to quantify the density of functional groups available for modification. For example, Fiammengo and co-workers quantified the number of “modifiable” amino groups on AuNPs ($d = 29 - 41$ nm) capped by different fractions of amine- and carboxylic acid-terminated PEGSH (MW = 600 Da or 3 kDa). The amine-functionalized ligands were post-synthetically labelled with 5(6)-carboxylfluorescein NHS ester, displaced using DTT, and then quantified using PL spectroscopy.¹⁰⁵ While this technique does not provide a full quantitative description of ligands on the AuNP surface, it instead reports on the number of amino groups that are available for functionalization, as not all of the amino groups were able to be fluorescently labelled.

1.4.1.2 “Turn on” Fluorescent Indicators

Another class of PL-based methods uses “turn on” fluorescent indicators to quantify ligand density and/or functionality. In these techniques, an indicator is used that only shows

luminescence in the presence of specific analytes. For example, Perry and Heinz used fluorescamine, which exhibits PL in the presence of primary amines, to investigate peptide loadings on silica particles as part of a wider study on silica NP surface chemistry.¹⁰⁶ The fluorescamine assay also has been used by Weller and co-workers, who quantified the number of accessible amino groups on 3-sulfanylpropyltrimethoxysilane-capped AuNPs ($d = 2.2 \pm 0.5$ nm) after the NPs underwent silane polycondensation with 3-aminopropyldimethylethoxysilane.¹⁰⁷

1.4.1.3 Optically Active Ligands

Similarly, certain ligands may exhibit unique PL properties that are dependent upon their chemical environment. For instance, Katz and co-workers investigated the ligand density of 1-pyrenebutanethioic acid *S*-butyl ester and thiocarbonic acid *O*-(4-pyren-1-ylbutyl) *S*-butyl ester ligands on AuNPs ($d = 12.5 \pm 1.5$ nm) and exploited the fact that, when appended to the NP surface, the hydrophobic pyrene moieties aggregate, which leads to an approximately 25 to 35-fold increase in the excimer emission band area.¹⁰⁸ In these experiments, known concentrations of citrate-stabilized AuNPs were titrated into a solution that contained a known concentration of either the thiocarbonate or thioester ligands. The fluorescence area between 360 and 600 nm was measured following each AuNP addition, and the titration continued until the fluorescence area reached a maximum, indicating saturation of the AuNP surface. This experiment was repeated at several different ligand concentrations, and a linear plot of the AuNP concentration at the saturation point versus the corresponding ligand concentration was obtained. The slope of the line corresponds to the number of ligands per saturated AuNP, and a ligand footprint of $24.5 \pm 1.0 \text{ \AA}^2$ (4.08 ± 0.17 ligands/nm²) was determined.¹⁰⁸

An additional method using optically active ligands exploits differences in the luminescent lifetime between the ligand luminophores when they are on or off a particle surface.

Franzen and co-workers used TCSPC to determine the number of $[\text{Ru}(\text{bipy})_2\text{bipy}-\text{C}_6\text{H}_{12}\text{S}]^{2+}$ (RCBS)-labelled bovine serum albumin (BSA) ligands on AuNPs ($d = 20 \text{ nm}$).¹⁰⁹ Emission from RCBS is partially quenched when appended to AuNPs, resulting in a shorter lifetime. The AuNPs were incubated in an excess of the RCBS-labelled BSA ligands (500:1 ligand:AuNP ratio), and a biexponential lifetime was observed. From these data, two distinct lifetimes could be extracted, consistent with RCBS on and off particle. The coefficients of the fit for each lifetime corresponded to the relative ratios of each species in solution, and, in combination with the measured quantum yields, the concentration of the RCBS on and off particle could be determined. This method was validated using a second PL technique, in which a known concentration of the AuNPs was incubated in rhodamine B isothiocyanate-labelled BSA and then the particle-ligand conjugates were removed via centrifugation. The fluorescence of the BSA was measured before and after AuNP introduction and compared to a standard curve; the decrease in fluorescence (and therefore ligand concentration) was attributed to the BSA appended to the NP.¹⁰⁹

1.4.2 Absorption Spectroscopy

Ligand quantification using absorption spectroscopy typically requires the use of indicators, labels, or particles that produce optical signals that quantitatively correlate with ligand loading values.

1.4.2.1 Ligands Tagged with Optically Active Labels

Absorption spectroscopy methods may monitor the absorbance of the ligand, the particle, or an external indicator to assess ligand density. Mattoussi and co-workers monitored the absorbance

of a ligand by synthesizing a modular molecule consisting of a thioctic acid anchoring unit, a PEG chain, and a maleimide terminal group (TA-PEG-Mal). This ligand was then appended to AuNPs ($d = 10$ or 15 nm).¹¹⁰ The particle-bound maleimide was coupled to a peptide and Cy5 dye in a two-step reaction. Following particle purification, the Cy5 concentration was measured at 649 nm; extinction from non-Cy5 coupled AuNPs was subtracted as a blank. Footprints of 1.20 ± 0.08 and 1.27 ± 0.10 nm² (0.83 ± 0.06 and 0.79 ± 0.06 ligands/nm²) were measured for the 10 and 15 nm AuNPs, respectively. However, the authors point out that these values underestimate ligand concentration because they are based on the assumption that both coupling steps were 100% efficient.¹¹⁰ The same group used an analogous technique to investigate the loading of aldehyde-terminated ligands (lactic acid-PEG-CHO) on CdSe@ZnS semiconductor NPs ($d = 6.2$ and 6.8 nm) by conjugating 2-hydrazinopyridine to the aldehyde, which forms a chromophore with distinct absorption at 350 nm. In these experiments, the authors found that the ligand density was relatively insensitive to core size but that the ligand density decreases with increased ligand density.¹¹¹

1.4.2.2 Plasmonic NPs

For plasmonic AuNPs, the LSPR can also be used to monitor ligand loading. Katz and co-workers have reported a number of such studies. In 2008, the authors found that titrating 5,11,17,23-tetrakis-mercaptomethyl-25,26,27,28-tetrapropoxycalix[4]arene (MMC) into a known concentration of tetraoctylammonium bromide (TOAB)-capped AuNPs ($d = 5.3 \pm 2.1$ nm) produced a linear red-shift in the LSPR.⁵¹ Upon saturation of the AuNP surface with MMC, the LSPR ceased to shift in response to additional ligand. The ligand concentration at the saturation point and the AuNP concentration are both known, providing a quantitative assessment of ligand footprint, which was 116 \AA^2 (0.86 ligands/nm²).⁵¹ The same group has also

used this technique to quantify calix[4]arene enantiomers ($1.10 \text{ ligands/nm}^2$),¹¹² calix[6]arenes ($0.42 \pm 0.03 \text{ ligands/nm}^2$),¹¹³ and calix[8]arenes ($0.44 \text{ ligands/nm}^2$).¹¹⁴ Similarly, Weinstock and co-workers observed a consistent blue shift in the LSPR as function of 11-mercaptoundecanoic acid (MUA) addition to a solution of AuNPs ($d = 13.8 \pm 0.9$) originally terminated by the inorganic cluster $\alpha\text{-AlW}_{11}\text{O}_{39}^{9-}$. Upon saturation of the AuNP surface with MUA, no further change in the LSPR wavelength was noted, and the concentration of ligand added at this saturation point was used to determine the ligand footprint (Figure 4).⁵²

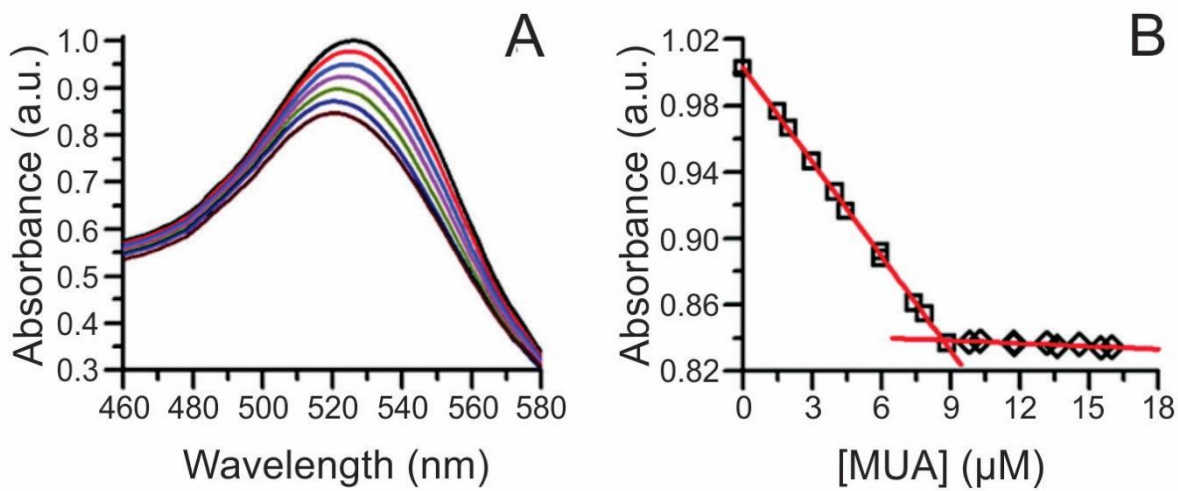


Figure 4. Ligand exchange of the $\alpha\text{-AlW}_{11}\text{O}_{39}^{9-}$ cluster-capped AuNPs with MUA. (A) Absorption spectra of the AuNP LSPR during the ligand exchange, and (B) plot of the change in LSPR absorbance at the initial λ_{max} of 526 nm as a function of added MUA concentration. Adapted with permission from ref. 52. Copyright 2012 American Chemical Society.

1.4.2.3 Optically Active Indicators

Finally, the absorbance of an external indicator can also be used to study ligand loading. Liang and co-workers quantified the conjugation of the therapeutic peptide p12 and a targeting peptide onto tiopronin-capped AuNPs ($d = 2 \text{ nm}$) using the colorimetric bicinchoninic acid assay and observed 65% and 90% conjugation efficiency for the therapeutic and targeting peptides, respectively.¹¹⁵ Similar techniques have been used to quantify peptide¹¹⁶ and ssDNA¹¹⁷ loadings on AuNPs. In these studies, the free ligand concentration was monitored by UV absorption before and after AuNP incubation, which demonstrates that dye-free, absorption-based ligand quantification is also possible.

Xia and Chen used a ninhydrin assay as part of their investigation of α -amino- ω -mercapto-poly(ethylene glycol) (NH_2PEGSH) density as a function of polymer molecular weight ($\text{MW} = 3, 5, \text{ or } 20 \text{ kDa}$) on various sizes of Au pseudospherical NPs, nanorods, and nanocages (Figure 5). Ninhydrin reacts with primary amines to produce a dark purple color with an absorbance peak at 565 nm.⁹⁸ A known concentration of the AuNPs was incubated in a known concentration of NH_2PEGSH . Aliquots of the free NH_2PEGSH were removed before and after this incubation step and were mixed with ninhydrin. The change in absorbance before and after particle incubation was measured at 565 nm and compared to a standard curve, which allowed the change in NH_2PEGSH concentration (i.e. the concentration of ligands on particle) to be quantified. This method indicated that the ligand densities ranged from 2.21 to 0.21 ligands/ nm^2 for 3 kDa and 20 kDa NH_2PEGSH , respectively, on 50 nm Au nanocages.⁹⁸ The authors compared this method to several other techniques, where the ninhydrin assay consistently indicated higher ligand loadings compared to other approaches including a fluorescamine assay (see Section 4.1.2; 2.21 ligands/ nm^2 versus 1.64 ligands/ nm^2 for 50 nm Au nanocages). While the

fluorescamine assay had a lower detection limit (~250 nM versus 500 nM), it was more sensitive to discrepancies in sample preparation (e.g. whether or not all AuNPs had sedimented prior to measurement). Consequently, the authors recommended the ninhydrin assay as a more robust technique for quantification.

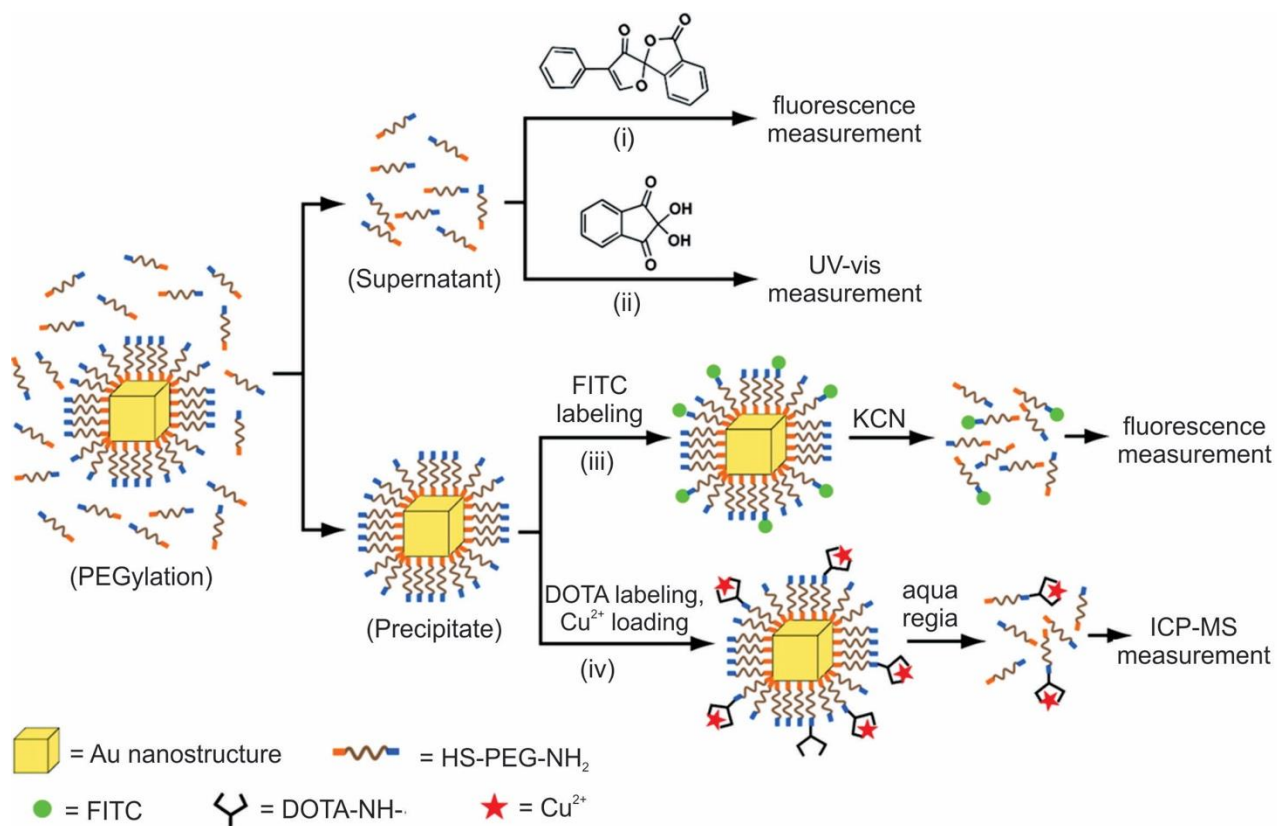


Figure 5. Scheme demonstrating 4 different techniques for the quantitative characterization of NH_2PEGSH on AuNPs: (i) a fluorescamine photoluminescence assay, (ii) a ninhydrin-based absorption spectroscopy method, (iii) fluorescein labelling of terminal amines on the appended ligand, and (iv) Cu^{2+} labelling of terminal amines, an ICP-MS method. Techniques (i) and (ii) quantify ligand density, whereas (iii) and (iv) quantify the amino groups available for functionalization. Adapted with permission from ref. 98. Copyright 2012 American Chemical Society.

Chan and co-workers have used an external indicator to investigate the impact of PEGSH grafting on both the serum protein absorption and subsequent macrophage uptake of AuNPs. Here, they incubated AuNPs ($d = 15, 30, 60, \text{ or } 90 \text{ nm}$) in various concentrations of PEGSH ($\text{MW} = 5 \text{ kDa}$) and assumed all pendant thiol groups were unavailable for further reaction. After incubation, the remaining thiol content was quantified using 5,5'-dithiobis(2-nitrobenzoic acid), which reacts with thiols in a stoichiometric fashion to produce an absorption band at 412 nm .¹¹⁸ The intensity of this band can then be monitored and compared to a standard curve in order to extract a quantitative value of unreacted thiol, which can be used to infer a quantity of thiols that had been adsorbed to NP surfaces.

Despite broad use, it is important to note that these optical spectroscopy methods can be limited because either the particle core or the ligands must be spectroscopically active or modified to be so post-synthetically. Such modifications can have undesired consequences for the ligand architecture. For example, changes can occur in ligand density due to an increase in ligand size as a result of fluorophore labelling. Further, when labelling is used, the efficiency of the labelling reaction is typically not 100%. Finally, absorption or luminescence from metal or semiconductor NPs may interfere with ligand-based PL or absorption measurements and therefore the ligand of interest must be extensively purified or spectroscopically distinct from the NP core optical features.

1.5 ATOMIC SPECTROSCOPY

ICP is an atomic spectroscopy method that uses high temperature plasma to decompose an analyte into its constituent atoms, and these atomized products can be subsequently analyzed by

either a MS or AES detector. ICP is most commonly used in the quantitative analysis of transition metals. However, it can also be used to detect lighter elements such as sulfur^{119, 120} or phosphorus^{121, 122} under certain conditions, which allows NP concentration and ligand concentration to be determined simultaneously in some cases.

For example, Lämmerhofer and co-workers used ICP-MS to quantify gold:sulfur ratios for AuNPs with various diameters between 13.2 ± 1.4 and 26.2 ± 4.4 nm.¹¹⁹ They demonstrated a linear relationship between ligand density and ligand chain length with various mercaptoalkanoic acids (MAAs) and examined NP ligand density with thiolated oligo EGs. The authors report average ligand densities of 4.96 ± 0.27 and 4.29 ± 0.45 ligands/nm² for shorter (MW = 282 Da) and longer oligo ethylene glycols (EGs, MW = 459 Da), respectively, and these values are consistent with other ligand densities reported for oligo EGs appended to AuNPs. While atmospheric interferences (e.g. oxygen or nitrogen with sulfur) can be a challenge for sulfur atom concentration quantification using ICP-MS, Lämmerhofer used an internal standard as well as spike recovery experiments to validate their sulfur detection approach. Here, spike recovery experiments involve adding a known amount of the compound of interest to standards that already contain this compound. The sample is then analyzed, and the standard concentration is subtracted from the total sulfur concentration in order to confirm that the added amount is retained.¹¹⁹ Further, since Au concentrations can be much higher than sulfur concentrations for large AuNPs, this method incorporates operating parameters that reduce the Au signal to as little as 0.1% to prevent it from overloading the detector. By reducing the amount of Au signal reaching the detector, this method can simultaneously measure both the sulfur signal from the thiolated ligands and the Au signal from the NPs.

ICP-AES has also been used to quantify ligand densities. Hackley and co-workers examined the gold:sulfur ratio for a variety of particle sizes, observing that packing density is largely independent of particle size ($d = 5 - 100$ nm). Working without an internal standard in this case, Hackley cautions that the particles and ligands must be sufficiently concentrated to ensure that the sulfur is present at a significant percentage of the total sample mass for accurate quantification.¹²⁰ Weiss and co-workers have applied similar techniques to study phosphorus-containing ligands on CdSe NPs.^{121, 122} Importantly, by observing the number of ligands post-purification in conjunction with NMR data, Weiss was able to establish particle binding equilibria for these ligands (*vide infra*).¹²¹

While not demonstrated yet, it is straightforward to envision expanding these atomic spectroscopy methods to examine mixed-moiety ligand shells, provided that each ligand contains spectroscopically distinct elements.

1.6 NUCLEAR MAGNETIC RESONANCE (NMR) SPECTROSCOPY

Given the distinct advantages of NMR spectroscopy for small molecule characterization, significant efforts have been devoted to developing NMR approaches for ligand density determination. A common method to study ligand densities using NMR involves the addition of an internal standard. With this method, a known concentration of a molecule that has NMR resonances distinct from the ligands of interest is added to the NP solution. The internal standard peak is then integrated along with the ligand peak of interest, and the concentration of the ligand can be determined by one of two methods. The first method uses comparison to a calibration curve, which is generated by plotting the ratio of the integrated ligand peak divided by the

integrated internal standard peak against the known ligand concentrations.⁵⁴ The alternative approach involves quantification based on the number of ^1H nuclei contributing to the internal standard peak and the ligand peak of interest and does not necessarily require a calibration curve. Here, a known concentration of internal standard is added to the unknown sample. The concentration of the unknown sample can be determined by comparing the integral of an internal standard peak to the integral value from the sample ligand peak of interest, both of which must correspond to a known number of protons.¹²³ In these experiments, NMR offers the advantage of being able to analyze multi-component ligand shells under various conditions. Further, unlike many of the other methods discussed, NMR has the additional capability to probe ligand dynamics and arrangement in addition to ligand quantities in real time. Here, we primarily focus on ligand densities but discuss additional findings from NMR, if reported.

The expanded capabilities of NMR come with several technical considerations that strongly influence spectral interpretation. The major consideration for analyzing the NMR spectra of molecules appended to a colloidal surface are related to how that surface and core material may change the observed NMR features of the appended ligands. Specifically, ligands bound to NP surfaces typically exhibit broader NMR linewidths and/or differences in chemical shift compared to the ligands free in solution. These changes in NMR signals can necessitate reassignment of the particle-bound spectra (e.g. using 2D NMR analysis such as homonuclear correlation spectroscopy (COSY) and/or heteronuclear single quantum correlation (HSQC) to determine the segment of the ligand that corresponds to the new NMR resonances upon NP binding) and often result in lower (in some cases, prohibitively low) signal to noise ratios. The physical underpinnings of this line broadening vary depending on the system, but they can generally be attributed to either inhomogeneous line broadening (e.g. chemical shift

distribution),^{124, 125} homogeneous line broadening (e.g. dipolar coupling due to ligand packing¹²⁶ or electron-nuclear coupling¹²⁷), or a combination of both.^{128, 129}

Unfortunately, this line broadening can obscure quantification in some cases. For example, when ligands bind to NPs with a high population of free carriers (e.g. metal NPs or doped semiconductor NPs), the NMR resonances from nuclei on the ligand that are in proximity to the carriers are attenuated by ligand-carrier spin interactions. The degree of attenuation is related to the distance between the nuclei and free carriers, and thus inaccurate quantification can occur if all nuclei corresponding to a particular resonance are not accounted for in a given peak integration. Regardless of whether the analysis is performed on or off particle, the NP concentration for these methods is typically determined by either absorption or atomic spectroscopy methods.

1.6.1 “Off particle” NMR Analysis

To avoid the adverse effects associated with line broadening and chemical shift changes, ligands can be removed from the NPs for routine, quantitative NMR analysis. In the case of metal NPs, which have a high concentration of conduction electrons, ligands *must* be removed from the particle surface to achieve accurate quantification. In other systems, quantification of unbound species may be employed as a matter of convenience to provide higher resolution spectra and avoid spectral reassignment. In addition, when monitoring dynamic processes, such as ligand exchange, the species of interest may be released from the particle surface during the reaction. Here, we will discuss literature examples from each of these scenarios in which off particle species were analyzed.

In our laboratory, we have shown that a combination of TEM for AuNP sizing, ICP-MS for Au quantification, and ^1H NMR for ligand quantification can reveal physical processes underpinning the formation and properties (e.g. final ligand density) of both single and mixed ligand shells on metal NPs. Here, we use acetonitrile (ACN) as an internal standard and use a calibration curve to perform quantitative analysis of ligand shells (Figure 6). The accuracy of this method was verified by synthesizing a molecule that was detectable by both our method using ^1H NMR as well as ICP-AES (using a Se tag). Both NMR and ICP-AES were in statistical agreement, indicating that the NMR quantification approach is reliable for metal NPs.⁵⁴ In this work, we found that PEGSH (MW = 1 kDa) is easily displaced by incoming MAAs and is amenable to post-synthetic modification. In contrast, more densely packed monolayers (e.g. if the original ligand shell is composed of MAAs) are not readily modified, exhibiting exchange efficiencies as low as 2% with other thiolated ligands, likely due to inter-ligand interactions (e.g. van der Waals forces) between neighboring alkyl chains. This NMR-based approach can be applied to a wide range of particle and ligand types, limited only by chemical resolution in the NMR spectrum.^{25, 130}

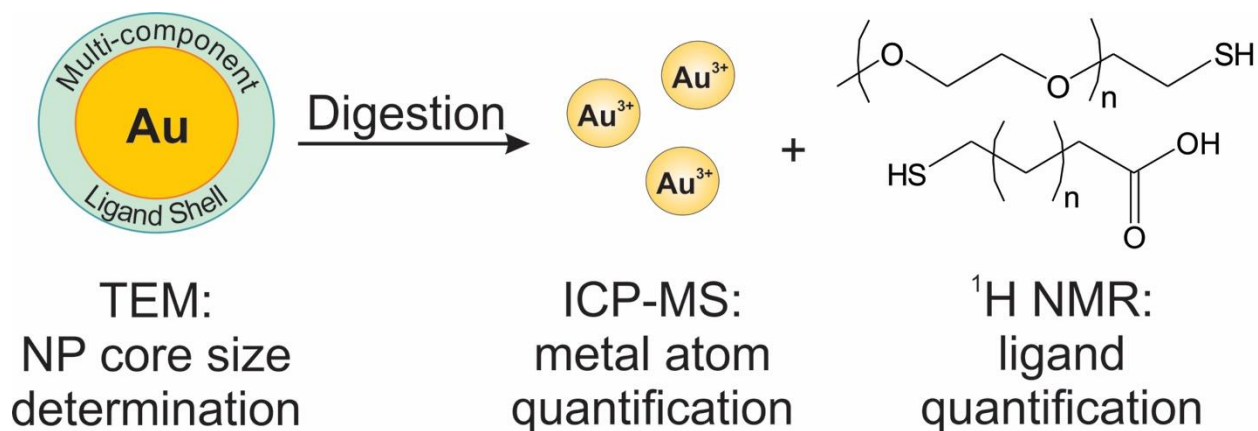


Figure 6. Scheme of a typical off particle NMR analysis. Here, NP conjugates are digested for quantification by ICP-MS, while the released ligands are quantified by ¹H NMR. Adapted with permission from ref. 54. Copyright 2015 American Chemical Society.

This work was preceded by studies of semiconductor NP systems. For example, Owen and co-workers have used a ferrocene internal standard to quantitatively study the displacement of cadmium carboxylate from CdSe NPs.¹³¹ In this study, the original particles remained intact, but the as-synthesized ligands (carboxylate complexes) were displaced using one of several different reagents (such as *N,N,N',N'*-tetramethylethylene-1,2-diamine (TMEDA)). Serial precipitation and centrifugation of the NPs (to which TMEDA had been added) were performed, followed by collection of the supernatant, which was then dried under vacuum. The concentration of free carboxylate ligands that had been displaced from the NPs by TMEDA was determined. Similar experiments quantified the species displaced during ligand exchange on CdS, PbSe, and PbS NPs. From the quantitative NMR analysis, the authors demonstrated that the composition changes due to metal-carboxylate displacement could be correlated to optoelectronic features of semiconductor NPs, including specific absorption transitions as well as PL quantum yield.¹³¹ Likewise, Weiss and co-workers have used ferrocene as the internal

standard for the quantification of 4-hexylphenyldithiocarbamate (C6-PTC) on CdS NPs.¹³² The NPs were originally functionalized with oleate and underwent a ligand exchange with C6-PTC. The number of C6-PTC ligands bound to the particles was obtained by quantifying bound and unbound oleate (based on the differences in peak shape and chemical shift) and also determining the stoichiometry of the ligand exchange, where one bound C6-PTC displaces at least two oleate ligands.¹³²

Even in semiconductor NP systems, line broadening upon particle attachment can be extreme, making on particle quantification approaches prohibitively time consuming. In order to overcome this barrier, Weiss and co-workers demonstrated that CdSe NP ligand densities could be quantified by ¹H NMR using an alternative external standard approach, in which only unbound species are observed.²⁴ To measure ligand densities of methylthiophenolate (CH₃-TP) on CdSe NPs, the authors compared NMR spectra from the NP sample and a sample of CH₃-TP that did not contain NPs. The NMR response of the sample was compared to the NMR signal obtained from mixing the CdSe NPs with the same amount of CH₃-TP as in the external standard. Here, an assumption is made that any ligands that attach to the NP surface will be shifted and dramatically dephased and thus too broad to distinguish from the spectral baseline. Therefore, since both the reference and the sample contain the same quantity of ligands, the signal from the ligand + NP sample comes only from the unbound ligands free in solution, and it was inferred that the remaining quantity has adsorbed to the particle surface. Using this approach, the measured difference in NMR signal between the NP-free sample and the NP-containing sample is proportional to the number of bound CH₃-TP ligands. From this study, typical ligand densities ranged from 1.4 - 7.6 ligands/nm² for CdSe NPs with a variety of diameters between 2.26 - 4.74 nm.²⁴

1.6.2 “On Particle” NMR Analysis

On particle ligand quantification is feasible in NP systems with low free charge carrier densities (e.g. intrinsic semiconductors), because line broadening is likely the result of factors such as ligand packing,¹²⁶ chemical shift distributions from faceting on the particle surface,¹³³ and slow tumbling^{134, 135} rather than a result of coupling to free carriers. Therefore, all species contributing to a specific resonance can be accounted for. However, on particle approaches, even where physically possible, can be significantly more expensive than their off particle analogues in terms of time and material due to lower signal to noise ratios and in some cases, the need for additional spectral assignment.^{136, 137} Despite these challenges, on particle NMR analyzes of ligand shells is attractive because of the potential to not only characterize ligand quantity but also to elucidate features such as ligand arrangement and binding affinity on the particle surface all within a single experiment.

Early work developing on particle NMR quantification was performed on intrinsic semiconductor NPs. Here, Pines and co-workers used the internal standard method without a calibration curve for the quantification of thiophenol on CdS NPs exhibiting different core sizes ($d = 1.18 \pm 0.1 - 1.92 \pm 0.1$ nm).¹²⁶ Using dichloromethane (DCM) as the internal standard, the authors found that as the size of the NPs increases, the number and percent coverage of thiophenol ligands decreases, indicating that larger NPs have less dense ligand shells. Interestingly, the authors noticed that as particle size was reduced, ¹H NMR lines were broadened, contrary to what is expected given the faster tumbling rate of the smaller NPs. Detailed models of selective spin-spin relaxation (T_2) measurements showed that the increase in linewidth was most likely the result of tightly bundled thiophenol islands on the surface of the CdS NPs, providing not only quantitative information on the NP ligand shell but also

information on the ligand arrangement as a function of NP size.¹²⁶ The insight provided by NMR allowed the authors to correlate ligand shell morphology in terms of packing arrangement with ligand density – parameters that influence the resulting NP physical behavior.

More recent work exploring on particle NMR ligand quantification was conducted by Hens and co-workers, analyzing both InP¹³⁸ and PbSe¹²³ NPs with dibromomethane as the internal standard. When PbSe NPs ($d = 3 - 7$ nm) are capped with oleate, an average ligand density of 4.2 oleate/nm² was determined.¹²³ The authors have also studied oleate densities using Quantas software that is derived from the pulse-length-based concentration determination (PULCON) method, where the software adds an artificial peak of standard intensity.^{22, 139} This simulated peak can then be integrated along with the ligand peaks to determine the ligand concentration. The authors analyzed the impact of washing with NP nonsolvents on oleate ligand densities on CdSe and PbSe NPs. They found that the ligand density decreases as a consequence of increased methanol washing steps, from an initial 4.1 oleate/nm² to 3.2 oleate/nm² and 3.18 oleate/nm² to 1.16 oleate/nm² for CdSe and PbSe NPs, respectively.²² The ligand density for PbSe NPs obtained with the Quantas approach is lower than that found using the internal standard approach (further interpretation likely requires additional information about the particle dispersity). Finally, Hens and co-workers also used the Quantas approach to determine the ligand density of oleate on the surface of the CdSe NPs ($d = 3.5 \pm 0.1$ nm) to be 4.6 ± 0.4 oleate/nm² in the absence of additional methanol washing steps.¹³⁹ The ligand densities for CdSe NPs without additional methanol washing steps are comparable, which is expected given the synthetic similarities between the studies.

In order to understand the relationship between optical properties and surface chemistry in semiconducting NPs, Owen and co-workers again used ferrocene as an internal standard to

determine ligand density on CdSe NPs before and after ligand exchange.⁵⁷ Here, ferrocene was used to provide distinct resolution between proton chemical shifts of the standard versus the ligands of interest, due to the deshielding effects noted for many metal-containing compounds.¹⁴⁰ In this report, the particle concentration was measured using the absorbance and molar extinction coefficient of the NPs. The authors found that the original carboxylate-terminated CdSe NPs undergo a quantitative (> 99%) ligand exchange with tri-*n*-butylphosphine (Bu₃P). After replacement of carboxylate with Bu₃P, the CdSe NPs are then replaced by various *n*-alkylamines, and an aliquot of *n*-alkylamine-capped NPs was placed into deuterated medium for analysis following washing to remove unbound ligands. The resulting ligand shells were more dense than the Bu₃P ligand shells,⁵⁷ leading the authors to conclude that *n*-alkylamine ligands provide higher surface coverage than Bu₃P. This increase in amine ligand density was then correlated to higher NP quantum yields.

Apart from metal chalcogenide particles, on particle NMR-based ligand quantification has also been used to analyze ligand shells on a variety of other NP cores, including silica¹⁴¹ and metal oxides.¹⁴² For example, Mayer and co-workers determined the density of dodecylamine (DDA) ligands on the surface of zinc oxide (ZnO) NPs using trimethoxybenzene as an internal standard, where NP concentration was determined with ICP-AES.¹⁴² The authors found that there were both “strongly” and “weakly” bound DDA populations present on the surface of the NPs and were able to quantify the contributions of each type of ligand to the overall ligand density. The average density of the strongly bound ligands was 1.0 ± 0.3 DDA/nm², while the average density of both the strongly and weakly bound ligands was higher at 1.9 ± 0.4 DDA/nm². Interestingly, these ligand densities are much lower than anticipated based on the estimated maximum surface coverage on an extended flat surface of ZnO (Figure 7). Particle surface

coverage could be increased by annealing the NPs to remove surface hydroxide ligands, which may block surface sites and make them unavailable for DDA binding. Indeed, after annealing, the average strongly bound ligand density increased to 3.5 ± 0.3 DDA/nm².¹⁴²

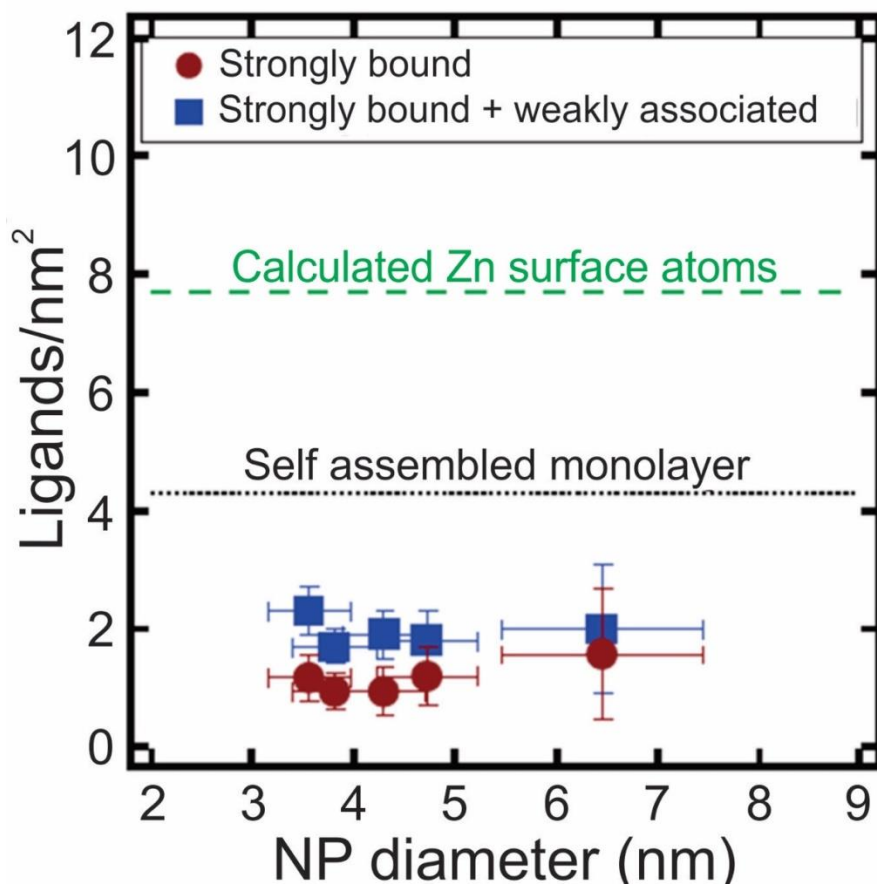


Figure 7. Ligands/nm² as a function of NP diameter for ZnO NPs. Particle ligand densities are lower than predicted for a self-assembled monolayer (SAM) of DDA ligands on a flat ZnO surface. Adapted with permission from ref. 142. Copyright 2014 American Chemical Society.

In addition to solution phase NMR techniques, solid state NMR has also been used to quantify NP ligand densities. For example, Griffin and co-workers measured the number of trioctylphosphine oxide (TOPO) and trioctylphosphine selenide (TOPSe) ligands on CdSe NPs ($d = 3.7 \pm 0.4$ nm) using a ^{31}P spin counting method by comparing to a known amount of gallium phosphide.¹⁴³ In this work, the authors used a combination of isotropic ^{31}P chemical shift and ^{31}P - ^{77}Se rotational echo double resonance (REDOR) techniques in magic-angle spinning experiments to distinguish between TOPO and TOPSe ligands, which are bound to Cd atoms on the surface of the NPs. Quantitative analysis assumed the CdSe NPs to be stoichiometric in the Cd and Se composition and found an average of 150-170 ligands/particle (3.72 ligands/nm²). From a combination of synthetic manipulation of growth conditions and computational modelling, the authors established that all the Cd sites on the particle surface are passivated, while no binding occurs at the Se sites. This observation was supported by spin echo measurements that were consistent with an average P-P distance of 8-10 Å, indicating capping of alternate sites on the particle surface.

In summary, NMR quantification overcomes many of the limitations imposed in the previously discussed methods, such as the ability to simultaneously identify multiple ligand types while avoiding the need for post-synthetic modification of the ligand itself, as is often the case for optical spectroscopy methods. Further, NMR techniques are amenable to a variety of experimental conditions (e.g. temperature or solvent), can assess ligand arrangement and dynamics, and have the potential to perform quantification studies *in situ*. However, there are drawbacks to the approach, including potential challenges of spectral peak assignment, and depending on sample concentration, long experiment times due to the inherently low sensitivity of NMR.

1.7 VIBRATIONAL SPECTROSCOPY

Another method that has been explored for NP ligand quantification is vibrational spectroscopy, which includes Raman and attenuated total reflectance-Fourier transform infrared (ATR-FTIR) spectroscopies. For both of these spectroscopies, ligand signal must be calibrated before concentrations can be determined. Analogous to the NMR methods discussed above, an internal standard can be added to samples in a surface-enhanced Raman spectroscopy (SERS) measurement to extract quantitative ligand values. In the work discussed here, NP concentrations are typically found by measuring the absorbance at a certain wavelength and then converting to concentration using the molar extinction coefficient.

1.7.1 Raman Spectroscopy

Zhang and co-workers used an isotope-encoded surface-enhanced Raman spectroscopy internal reference (IESIR) method to quantify mercaptobenzimidazole (MBI) on the surface of AuNPs.¹⁴⁴ In this method, the internal standard used was of identical structure but different isotopic substitution than the ligand of interest. Using this identical structure helps to eliminate quantification errors arising from matrix interferences or variations in SERS substrate activity. First, a calibration curve was prepared with varying ratios of MBI- d_0 and MBI- d_4 . Next, AuNP samples were incubated in a known amount of MBI- d_0 . The AuNP samples were centrifuged to remove the MBI-capped AuNPs, and MBI- d_4 was added to the supernatant, which was used to measure the SERS spectra. The data was fit to a Langmuir isotherm, which gave a maximum MBI packing density of 571 ± 4.6 pmol/cm² (3.44 ± 0.03 ligands/nm²).¹⁴⁴ Zhang and co-workers subsequently extended their analysis to various solution pH values, which changed the form of

the MBI ligand on the AuNPs (thione at low pH versus thiolate at higher pH).⁶¹ The change in the MBI form altered the binding constants and packing density, with a higher density at low pH and a lower density at high pH.

Halas and co-workers have used SERS to quantify *p*-mercaptoaniline-PEG-fluorescein (*p*MA-PEG-FI) on silica@Au nanoshells.¹⁴⁵ The authors first constructed a Langmuir isotherm to calibrate the SERS response of *p*MA molecules adsorbed on the Au nanoshells by taking SERS spectra at various *p*MA concentrations. A binding constant of $9.48 \times 10^3 \pm 884 \text{ M}^{-1}$ was found, representing the affinity of the *p*MA for the nanoshell surface. Then, the packing density of *p*MA-PEG-FI could be determined by referencing this calibration. The packing density of *p*MA-PEG2000-FI is $46.7 \pm 20.8 \text{ pmol/cm}^2$ ($0.28 \pm 0.13 \text{ ligands/nm}^2$), and the packing density of *p*MA-PEG5000-FI is $15.3 \pm 7.9 \text{ pmol/cm}^2$ ($0.09 \pm 0.05 \text{ ligands/nm}^2$).¹⁴⁵

1.7.2 Infrared Spectroscopy

ATR-FTIR spectroscopy has also been used to quantify NP ligand density. Hackley and co-workers used ATR-FTIR to quantify PEGSH and MPA on AuNPs and subsequently confirmed their method via comparison to ES-DMA measurements (*vide infra*).²³ The authors generated calibration curves by plotting the intensity of IR absorbance versus the concentration of free ligand to quantify the maximum surface density of PEGSH with different molecular weights (MW = 1, 5, or 20 kDa). The ligand density of PEGSH was found to be inversely proportional to the molecular weight. In addition, since IR allows multiple ligands to be distinguished, the authors studied the effects of the addition of a secondary ligand either simultaneously (co-loading) or sequentially (backfilling) on PEGSH surface density. When MPA was added at the same time as PEGSH, the amount of PEGSH that was adsorbed to the AuNPs was reduced.

When BSA was added to an already existing PEGSH monolayer, there was a decrease in the amount of PEGSH adsorbed if the molecular weight of the PEGSH was small (here, 5 kDa or less). However, if the molecular weight of the PEGSH was larger (20 kDa), the amount of PEGSH adsorbed remained the same.²³

Similar to the optical methods, vibrational spectroscopy methods require spectroscopically active molecules to be effective. However, like NMR (*vide supra*), as long as those molecules have spectroscopically distinct features, vibrational spectroscopy can simultaneously quantify multiple ligand types.

1.8 ELECTROSPRAY-DIFFERENTIAL MOBILITY ANALYSIS (ES-DMA)

Electrospray-differential mobility analysis (ES-DMA) aerosolizes and then separates NPs based on their electrical mobility. The electrical mobility of the particles is dependent on both particle charge and size and results from the particle acceleration that occurs in an electric field in the differential mobility analyzer, balanced by a drag force. Particles with larger or more ligands appended to them have a higher drag force than particles with smaller or fewer ligands on the surface. The applied voltage in the DMA is varied with time in order to scan the particle size distribution, which is then detected by a condensation particle counter. By comparing the particle sizes before and after the introduction of ligands, the ligand density can be determined. An advantage of this technique is that no specific labelling is needed, and the surface coating thickness can be determined relatively easily. However, a disadvantage is that in order to convert the surface coating thickness to ligand coverage, the conformation of the ligands must be known

a priori. In these measurements, NP size instead of concentration is used to determine ligand density as described above.

Zachariah and co-workers have used ES-DMA to find the ligand density of ssDNA on AuNPs ($d = 20$ nm).¹⁴⁶ The authors first measured the surface coating thickness and then converted to surface coverage based on the known random coil conformation of poly-T ssDNA ligands. Depending on the length of the ssDNA, the model for DNA packing, and the concentration of salt, the surface coverage ranges from 2.0×10^{12} to 6.9×10^{13} ligands/cm² (0.02 to 0.69 ligands/nm²), with the shorter strands having the higher surface coverage, consistent with the ligand densities found in other studies of ssDNA on AuNPs in the presence of salt.¹⁴⁶ Hackley and co-workers have also used ES-DMA to quantify the competitive adsorption of PEGSH (MW = 5 kDa) and mercaptopropionic acid (MPA) on AuNPs ($d = 30$ or 60 nm).^{23, 147} The authors found that as the amount of MPA added to the NPs increased, the surface density of PEGSH decreased.

In an attempt to avoid the need for *a priori* knowledge of ligand conformation mentioned above, Zachariah and co-workers modified their technique by coupling an aerosol particle mass analyzer (APM) to the ES-DMA system to study AuNPs ($d = 30$ nm) capped with BSA.¹⁴⁸ First, the size distribution of citrate-capped AuNPs was measured, and then NPs with a selected mobility were analyzed with the APM to determine their mass distribution. This analysis was repeated for the BSA-functionalized AuNPs. The mass difference between these two types of NPs was then used to calculate the ligand coverage. At the highest amount of BSA added to the AuNPs, the coverage was determined to be 3 mg/m² (0.03 ligands/nm²).¹⁴⁸ However, although this modified technique does not require knowledge of the ligand conformation to determine

ligand density, there is another limitation in that the mass of the ligand on the NP before functionalization (in this case citrate) is neglected, and the particles are assumed to be “bare.”

While a wide range of molecules can be analyzed without specialized modification, this technique remains limited by the approximation of ligand conformation unless APM is used. Further, neglecting initial ligand mass on the NP sample when using APM can lead to overestimations of the mass of the original NPs, which yields a ligand density that is lower than the true value.

1.9 PH TITRATIONS

Another approach for ligand quantification uses pH titration.^{149, 150} In this process, acid or base is titrated into a known amount of NPs. The pH change is monitored, and based on the equivalence point, the ligand concentration can be extracted. Of course, this technique requires that the particles are not sensitive to aggregation caused by changes in pH and that the ligand has some well-known pH response. For these studies, ICP-AES is used to determine the corresponding AuNP concentration.

Latham and Williams demonstrated this method on AuNPs by titrating a potassium hydroxide solution into a known amount of carboxylic acid-terminated PEGSH-capped AuNPs (MW = 700 Da, $d = 4.1 \pm 0.8$ nm).¹⁴⁹ In contrast to unbound ligand, where a sharp transition occurs, the transition for AuNP-bound ligands was longer and occurred at more basic pH values. With the known particle concentration, the equivalence point of the titration corresponded to the quantity of ligands on the particle. However, the authors cautioned that the particle mass was estimated without taking the mass of the ligands bound to the particle into account and therefore

the ligands/particle may actually be a 10-15% underestimation.¹⁴⁹ Parak and co-workers presented a similar method for quantifying MAAs and an amphiphilic polymer on AuNPs. The authors also observed a broadening of the pH curve and shift in the pKa of the bound MAA ligands relative to the free ligand. The authors emphasized that the pH data also provides information regarding colloidal stability of the NP solutions.¹⁵⁰

While using pH titrations to quantify particle ligand density is relatively simple, the main disadvantage is that it can only be used with ligands that have a pH-sensitive component.

1.10 X-RAY PHOTOELECTRON SPECTROSCOPY (XPS)

XPS measurements have long been commonplace for studying the elemental composition of flat surfaces and have been applied to NP films as well.^{151, 152} Therefore, it seems expected that the technique would also be explored for quantification of NP ligand shells. However, because XPS is a surface-sensitive technique, the use of XPS for NP ligand density determination is nuanced. In a recent report, Hamers and co-workers used XPS to quantify the density of ω -(1-mercaptoundec-11-yl)hexa(ethylene glycol) carboxylic acid (HS-(CH₂)₁₁(EG)₆-COOH) ligands on AuNPs (d = 1.3 – 6.3 nm). By dropcasting their samples onto silicon wafers, the authors find an average ligand density of 3.9 ± 0.2 ligands/nm². Further, they found that the radius of curvature of small (d < 2 nm) NPs must be taken into account for dropcast samples.¹⁵³ Several additional studies have also demonstrated the use of dropcast samples for an XPS quantification approach.¹⁵⁴⁻¹⁵⁶

Another method for XPS ligand quantification was demonstrated by Alivisatos and co-workers examining phosphorous-containing ligands on CdSe NPs.¹⁵⁷ By analyzing only a single

monolayer of NPs and accounting for the escape depths of the electrons for the different elements, they established NP size dependent (range, $d = 0.9 - 3.0$ nm) surface coverages of between 30-60% TOPO ligands on CdSe NPs, with higher coverages on smaller NPs.¹⁵⁷ However, the article implies several caveats to XPS for ligand quantification. First, the authors demonstrate that a monolayer of particles is needed to extract accurate ligand quantities. The authors also note that in order to form the monolayer, some portion of the original ligand may be displaced with substrate-binding moieties and therefore the method might systematically underestimate total ligand quantities.

Taking all factors together, XPS is a particularly complex approach for ligand quantification. In addition to particle curvature and substrate coverage densities, the technique, by definition, does not probe the core concentration directly (i.e. electron escape depth is much shorter than the particle diameter in many cases). It is also important to note that because of the surface bias, the signal to noise ratio for core and surface elements will be different, especially in the case where the ligand moieties facilitate adsorption of adventitious carbon.

1.11 SUMMARY AND OUTLOOK

Given the diversity of techniques used and systems studied, how does one select a method to quantify ligand density in their NP systems and evaluate the meaning the resulting values? For example, do different ligand quantification techniques agree with one another? If not, are there systematic deviations between methods? For example, compare results for a well-studied system such as PEGSH-terminated AuNPs (MW = 1-2 kDa, NP diameters above 6 nm). While TGA and NMR techniques agree that ligand densities are approximately 2.5 ligands/nm², other

quantification approaches such as absorption spectroscopy give much smaller values. Likewise, absorption spectroscopy also finds lower ligand densities when examining other systems such as DNA appended to AuNPs ($d = 15\text{-}20\text{ nm}$), indicating that absorption spectroscopy may systematically underestimate ligand densities. However, despite some discrepancies, careful sample preparation and measurements seem to facilitate general agreement in ligand densities between methods when the NP systems are comparable (Table 1). Therefore, method selection is primarily driven by particle properties. For example, one must evaluate experimental constraints such as whether the ligand and/or NP is optically active or whether the NMR chemical shifts of the ligand are spectroscopically discernible.

Collectively, these studies also make it clear that important barriers remain for the determination and accuracy of ligand quantification approaches both with respect to total ligand density and surface-specific ligand densities within a single given particle. The major obstacles include dispersity in NP size and shape as well as NP concentration determination. As these challenges are met, methods that can not only quantify NP ligands but also determine their arrangement and ultimately their dynamics will be needed. Motivation to address these challenges is clear: even for the information already in hand, strong correlations between surface chemistry and particle behavior are observed. We expect that the studies summarized here will be both a foundation and springboard to selectively, reproducibly, and effectively use surface chemistry to control the formation and properties of colloidal NPs.

2.0 QUANTITATIVE ANALYSIS OF THIOLATED LIGAND EXCHANGE ON GOLD NANOPARTICLES MONITORED BY ^1H NMR SPECTROSCOPY

(Portions of this work were published previously and are reprinted with permission from Smith, A. M.; Marbella, L. E.; Johnston, K. A.; Hartmann, M. J.; Crawford, S. E.; Kozycz, L. M.; Seferos, D. S.; Millstone, J. E., *Anal. Chem.* **2015**, *87*, 2771-2778. Copyright 2015, American Chemical Society.)

2.1 INTRODUCTION

The surface chemistry of nanoparticles (NPs) can impact nearly every aspect of their behavior including growth,¹⁵⁸⁻¹⁶⁰ optoelectronic properties,^{161, 162} and toxicity.^{163, 164} Gold (Au) NPs exhibit particularly versatile surface chemistry including straightforward functionalization with thiol-,²¹ selenol-,¹⁶⁵ phosphine-,¹⁶⁶ and carbene-terminated¹⁶⁷ ligands. A key aspect of understanding and tailoring this surface chemistry is developing analytical strategies to measure basic features of surface molecular architectures such as ligand identity, quantity, and arrangement.

Several methods have been developed in an effort to describe AuNP surface chemistry, as described above. For example, inductively coupled plasma mass spectrometry and optical emission spectroscopy (ICP-MS and ICP-OES, respectively) have been used to monitor S to Au

ratios in samples of thiol-functionalized AuNPs.^{168, 169} Thermogravimetric analysis (TGA) has also been applied to measure the number of ligands appended to AuNPs.^{63, 79, 81} While each of these methods is useful in determining the total number of ligands, they are limited in distinguishing between ligand types. Spectroscopic techniques, such as fluorescence-based methods and Raman, have been used to provide quantitative descriptions of ligand shells and can also yield information about molecular identity via molecular labeling. These spectroscopic methods provide the added benefit of ligand identification in addition to quantification, however, they require either the alteration of the original ligand through fluorescent labeling or are limited to SERS-active substrates.^{19, 108, 145, 170-173} Of the commonly used and widely available analytical methods to analyze surface chemistry, nuclear magnetic resonance (NMR) spectroscopy has become a particularly attractive technique. For example, NMR has been used to study patterns in molecular arrangement on metal NPs^{50, 56, 174-176} and to monitor ligand chemistry and dynamics on semiconductor NPs.^{57, 139, 177}

Here, we use NMR methods to quantify the extent of ligand exchange between different types of thiolated molecules on the surface of AuNPs. Specifically, we determine ligand density values for single-moiety ligand shells and then evaluate how these ligand loadings change based on temperature and salt concentration. We identify trends in AuNP functionalization efficiency with respect to ligand type, concentration, and reaction time. While well-studied in thin films,^{20, 178, 179} many of these trends are still to be elucidated in basic metal NP systems. The reported findings have important implications for how AuNP surface chemistry can be modified and used in a wide variety of applications.

2.2 EXPERIMENTAL

2.2.1 Materials and Methods

Hydrogen tetrachloroaurate (III) trihydrate ($\text{HAuCl}_4 \cdot 3\text{H}_2\text{O}$, 99.999%), 16-mercaptohexadecanoic acid (MHDA, 99%), 12-mercaptododecanoic acid (MDA, 96%), 8-mercaptooctanoic acid (MOA, > 95%), 6-mercaptohexanoic acid (MHA, >90%), 4-mercaptobutyric acid (MBuA, technical grade), *O*-(2-mercaptoethyl)-*O'*-methylhexa(ethylene glycol) ($\geq 95\%$), poly(ethylene glycol) methyl ether tosylate (PEG-tosylate, average $M_n = 900$ Da), potassium selenocyanate (KSeCN), and sodium citrate tribasic dihydrate (citrate, $\geq 99\%$) were obtained from Sigma-Aldrich (St. Louis, MO). Poly(ethylene glycol) methyl ether thiol (PEGSH, average $M_n = 1,000$ Da, 2,100 Da, or 4,800 Da), was obtained from Laysan Bio, Inc. (Arab, AL). 11-Mercaptoundecanoic acid (MUA, 98%) was obtained from Santa Cruz Biotechnology (Dallas, TX). Sodium chloride (NaCl, certified ACS), potassium chloride (KCl, certified ACS), magnesium chloride hexahydrate (MgCl_2 , certified ACS), sodium fluoride (NaF, certified ACS), sodium bromide (NaBr, certified ACS), sodium iodide (NaI, certified), potassium bromide (KBr, certified ACS), potassium iodide (KI, certified ACS), acetonitrile (ACN, 99.8%), dimethyl sulfoxide (DMSO, ACS grade), and chloroform (certified ACS) were obtained from Fisher Scientific (Waltham, MA). Deuterium oxide (D_2O , 99.9%), chloroform-d (99.8%), and dimethyl sulfoxide- d_6 (d-DMSO, 99.9%) were obtained from Cambridge Isotope Laboratories, Inc. (Tewksbury, MA). All reagents were used as received unless otherwise indicated. NANOpure™ (Thermo Scientific, > 18.2 $\text{M}\Omega \cdot \text{cm}$) water was used in the preparation of all solutions, and all reagent solutions are aqueous unless otherwise noted. Before use, all glassware and Teflon®-coated stir bars were washed with aqua regia (3:1 ratio of concentrated HCl and

HNO₃ by volume) and rinsed thoroughly with water. *Caution: Aqua regia is highly toxic and corrosive and requires proper personal protective equipment. Aqua regia should be handled in a fume hood only.*

2.2.2 AuNP Synthesis

AuNPs were synthesized using a modified Frens procedure.^{180, 181} In a 1 L, 3-neck round bottom flask containing a stir bar, 500 mL of aqueous HAuCl₄ (1 mM) solution were prepared. The solution was heated to vigorous reflux while stirring until a rapid drip rate was achieved (drip rate ~1 per second). Meanwhile, a 50 mL aqueous solution of citrate was prepared (concentrations used to generate various sizes of AuNPs are listed below in Table 2). This citrate solution was rapidly added to the refluxing HAuCl₄ solution. After addition, the reaction mixture changed from yellow, to colorless, to black, to purple-red within 1 minute. The resulting AuNP solution was allowed to reflux for 5 minutes before it was removed from heat. This mixture was cooled to room temperature and transferred to a clean glass media bottle for refrigerated storage (~4 °C).

Table 2. Conditions for synthesis of AuNPs with different diameters.

Molar Ratio (Au:Citrate)	Amount HAuCl ₄ · 3H ₂ O (g)	Amount Trisodium Citrate (g)	Particle Size by TEM* (nm)
1:3.31	0.1970	0.4857	13.01 ± 0.84
1:2.02	0.1971	0.2990	30.94 ± 1.13

*N ≥ 200 for all particle sizes, with average ± standard deviation.

2.2.3 UV-vis-NIR Analysis of AuNPs

Particles were characterized by ultraviolet-visible-near infrared (UV-vis-NIR) absorption spectroscopy using a Cary 5000 spectrophotometer (Agilent, Inc.). Spectra were baseline corrected with respect to the spectrum of water. In order to obtain each spectrum, the AuNP solution was diluted by 1/3 with NANOpure water.

2.2.4 TEM Analysis of AuNPs for Size Determination

An aliquot from each final AuNP solution was diluted 1/5 with NANOpure water prior to drop casting onto a Formvar-coated copper transmission electron microscopy (TEM) grid (Ted Pella, Inc.). Samples were allowed to air dry and then dried under vacuum before characterization using an FEI Morgagni TEM at 80 kV. The size distributions of the AuNPs were determined from TEM images of at least 200 AuNPs from various areas of the grid. ImageJ 1.47d (National Institutes of Health, USA) was used to measure and count all particles.

2.2.5 Synthesis of PEGSeCN

KSeCN (60 mg, 0.416 mmol) was dissolved in anhydrous ethanol (0.22 mL) and heated to 80°C in a 3-neck round bottom flask with a reflux condenser under an argon atmosphere. PEG-tosylate (333 mg) was added dropwise and an additional 0.2 mL of anhydrous ethanol was used to rinse the storage vessel. The mixture was stirred for 3 hours under reflux with an additional 1.2 mL of ethanol being added periodically over the course of the reaction to maintain constant volume and ensure dissolution of the salts. The mixture was then cooled to room temperature, and the solvent

removed by rotary evaporation. The crude product was then dissolved in ether (5 mL) and washed with 0.1 M NaOH (3 x 5 mL) and brine (3 x 5 mL). The aqueous fraction was concentrated, and the resultant solid stirred with ether (50 mL) for 20 minutes and filtered. This was repeated 3 times, and the combined ether washes were concentrated to give the product as a pale yellow semi-solid (124 mg). $^1\text{H NMR}$ (400 MHz, D_2O) δ 3.62 (s, 6H), 3.30 (s, 3H), 3.09 (t, 3H).

2.2.6 Ligand Exchange of Citrate-capped AuNPs

Prior to use, AuNPs were filtered using a polyvinylidene fluoride (PVDF) filter membrane with a pore size of 0.45 μm (25 mm GD/XP disposable filters, Whatman, Inc). Immediately after filtration, the AuNPs were concentrated by separating 1 mL aliquots into 1.5 mL centrifuge tubes and centrifuging the solution at 20,000 rcf for 5 minutes (Eppendorf 5424 centrifuge). The supernatant was removed, and another 1 mL aliquot of filtered particles was added. The pellet was resuspended, and the process was repeated until 3 mL of filtered particles were concentrated to 1 mL in centrifuge tubes. The particles were centrifuged once more, and the supernatant was removed. The resulting pellet was resuspended in 50 μL of PEGSH (various concentrations and molecular weights) and 950 μL of water. This mixture was then placed on a temperature controlled mixer (Eppendorf R Thermomixer) for 4 hours at 1,000 rpm and 25 $^\circ\text{C}$. After 4 hours, the particles were washed twice. Here, washing indicates centrifuging the sample and removing all supernatant followed by resuspension in water. After the second washing cycle, the particles were resuspended in a mixture of 990 μL of water and 10 μL of phosphate buffer (100 mM, pH 10) and placed on a temperature controlled mixer overnight at 1,000 rpm and 25 $^\circ\text{C}$. After this time, the particles were washed with phosphate buffer twice, followed by two washes in water

and two washes in D₂O. After the last wash cycle, the supernatant was removed to yield a concentrated pellet of PEGSH-capped AuNPs (Figure 8).

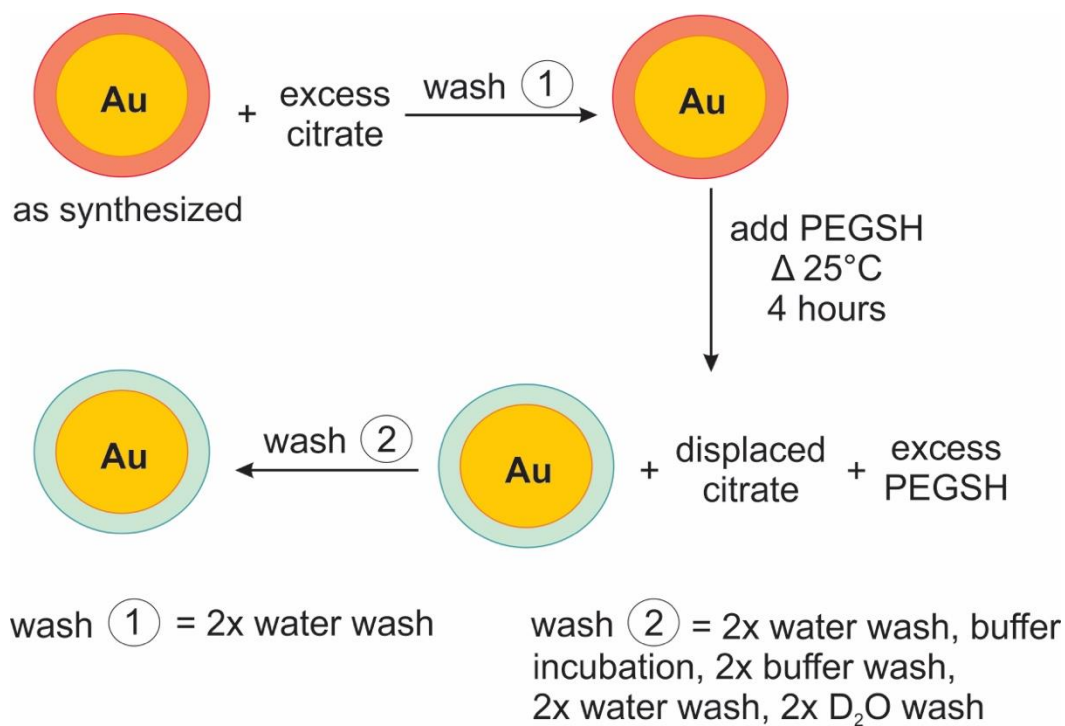


Figure 8. Scheme for ligand exchange of citrate-capped AuNPs.

An identical procedure was followed for ligand exchanges with MUA, MOA, MHA, or MBuA using 250 μL of the mercaptoalkanoic acid solution (various concentrations) and 750 μL of water. Together, this process replaces the capping ligand on the AuNPs from citrate molecules to a thiolated molecule.

N. B. Buffer washes and overnight incubation in buffer are used to disrupt hydrogen bonds between carboxylic acid-terminated ligands, which may lead to multi-layer formation. While this step is only necessary for the mercaptoalkanoic acids, we chose to use the same

conditions for all ligands in order to facilitate comparison between particle samples. We conducted controls to assess the impact of these washes in two ways. First, we compared the measured ligand loading of PEGSH under the conditions described above to the PEGSH loading on AuNPs where the overnight buffer incubation had been eliminated, and all 4 aqueous washes were conducted with pure water. In this control, no significant loading difference was observed (Figure 9). The second control was to determine the amount of ligand that desorbs from the particle during overnight incubation in buffer, and this is also negligible (< 2% of the total ligand shell) compared to an overnight incubation in water (Figure 9).

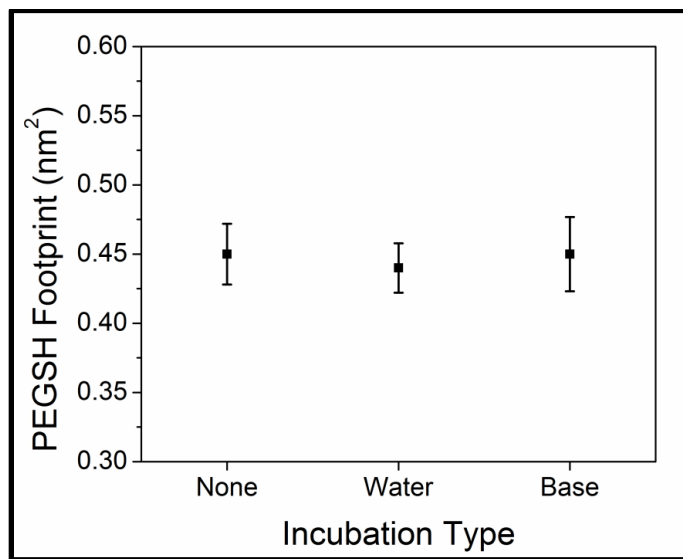


Figure 9. Comparison of PEGSH footprint measured from particles analyzed immediately after purification, analyzed after purification and subsequent incubation overnight in base (phosphate buffer, 10 mM, pH = 10), and analyzed after purification and subsequent incubation overnight in pure water, where error bars represent standard error of at least 5 trials. No significant difference is observed between the sets of AuNPs.

2.2.7 Ligand Exchange of Citrate-capped AuNPs in Organic Solvents

Prior to use, AuNPs were filtered using a PVDF filter membrane with a pore size of 0.45 μm (25 mm GD/XP disposable filters, Whatman, Inc). Immediately after filtration, the AuNPs were concentrated by separating 1 mL aliquots into 1.5 mL centrifuge tubes and centrifuging the solution at 20,000 rcf for 5 minutes. The supernatant was removed, and another 1 mL aliquot of filtered particles was added. The pellet was resuspended, and the process was repeated until 3 mL of filtered particles were concentrated to 1 mL in centrifuge tubes. The particles were centrifuged once more, and the supernatant was removed. The resulting pellet was resuspended in 50 μL of MUA, MDA, or MHDA (1 mM) and 950 μL of DMSO. This mixture was then placed on a temperature controlled mixer for 4 hours at 1,000 rpm and 25 $^{\circ}\text{C}$. After 4 hours, the particles were washed twice with DMSO and twice with d-DMSO. After the last wash cycle, the supernatant was removed to yield a concentrated pellet of mercaptoalkanoic-capped AuNPs in DMSO. Working in organic solvent precludes the formation of hydrogen bonds between the terminal carboxylic acids, eliminating the need for base washes. An identical procedure can be followed for AuNPs in chloroform.

2.2.8 Ligand Exchange of Citrate-capped AuNPs in Salt Solutions

Prior to use, AuNPs were filtered using a PVDF filter membrane with a pore size of 0.45 μm (25 mm GD/XP disposable filters, Whatman, Inc). Immediately after filtration, the AuNPs were concentrated as outlined above until 3 mL of filtered particles were concentrated to 1 mL in centrifuge tubes. The particles were centrifuged once more, and the supernatant was removed. The resulting pellet was resuspended in 50 μL of PEGSH (various concentrations and molecular

weights) and 950 μL of 158 mM aqueous salt solution. This mixture was then placed on a temperature controlled mixer under the conditions outlined above. After the base incubation, the particles were washed with phosphate buffer twice, followed by two washes in water and two washes in D_2O . After the last wash cycle, the supernatant was removed to yield a concentrated pellet of PEGSH-capped AuNPs.

2.2.9 Ligand Exchange of Citrate-capped AuNPs at Various Temperatures

The AuNPs were prepared as discussed above. After the pellet was resuspended in the desired ligand, the mixture was placed on either a temperature controlled mixture for the elevated temperature samples or in a 4 $^\circ\text{C}$ refrigerator for the decreased temperature samples.

2.2.10 ICP-MS Analysis

Inductively coupled plasma mass spectrometry (ICP-MS) analysis was performed using an argon flow with a NexION spectrometer (PerkinElmer, Inc.). An aqua regia solution was prepared with a 3:1 ratio of hydrochloric acid (Sigma-Aldrich, > 99.999% trace metal basis): nitric acid (Sigma-Aldrich, > 99.999% trace metal basis) and diluted with water for a 5% (by volume) aqua regia matrix. AuNP samples were taken from the concentrated pellet after ligand exchange and digested overnight in ~ 5 μL of fresh and concentrated aqua regia solution. From the digested solution, 1 μL was further diluted to 15 mL using 5% aqua regia matrix, and the remainder of the digest was reserved for $^1\text{H-NMR}$ analysis (*vide infra*).

Unknown Au concentrations were determined by comparison to a 5-point standard curve with a range of 1 - 30 ppb (1, 5, 10, 20, and 30 ppb prepared by volume) from a gold standard for

ICP (Fluka, TraceCERT $1,001 \pm 2$ mg/L Au in HCl) diluted in the 5% aqua regia matrix. All standards were measured 5 times and averaged, while all unknown samples were measured in triplicate and averaged. A 5 minute flush time with 5% aqua regia matrix was used between all runs, and a blank was analyzed before each unknown sample to confirm removal of all residual metals from the instrument.

2.2.11 ICP-OES Analysis of PEGSeCN

ICP-OES analysis was performed using an argon flow with an Optima spectrometer (Perkin Elmer, Inc.). An aqua regia solution was prepared with a 3:1 ratio of hydrochloric acid (Sigma Aldrich, > 99.999% trace metal basis): nitric acid (Sigma Aldrich, > 99.999% trace metal basis) and diluted with water for a 5% v/v aqua regia matrix. AuNP samples capped with the PEGSeCN ligand were taken from the concentrated pellet after ligand exchange as described above and digested overnight in ~ 5 μL of fresh and concentrated aqua regia solution. The digested solution was diluted to a volume of 500 μL in D_2O for ^1H NMR analysis. After analysis by NMR, 400 μL was further diluted to 2.5 mL using the 5% aqua regia matrix. Unknown Se concentrations were determined by comparison to a 5-point standard curve with a range of 0.10 - 10 ppm (0.10, 0.50, 1.0, 5.0, and 10 ppm prepared by volume), from a selenium standard for ICP (Fluka, TraceCERT 1000 ± 2 mg/L Se in HNO_3) diluted in 5% aqua regia matrix. All standards were measured 5 times and averaged, while all unknown samples were measured in triplicate and averaged. A 7 minute flush time with 5% aqua regia matrix was used between all runs, and a blank was analyzed before each unknown sample to confirm removal of all residual metals from the instrument.

2.2.12 ^1H NMR Analysis

All NMR measurements were performed on a Bruker 400 Ultrashield™ magnet with an AVANCE III 400 Console or a Bruker 600 Ultrashield™ magnet with an AVANCE III 600 Console (Bruker Biospin, Billerica, MA) at 298 K. For all experiments, a minimum recycle delay of 5 seconds was used, which was sufficiently greater than T_1 . NMR samples were prepared as described above by concentrating the AuNPs, followed by digestion with 1 drop (~5 μL) of concentrated aqua regia. These samples were allowed to digest overnight before dilution with D_2O to a total volume of 600 μL . An ACN reference was used for the determination of unknown ligand concentrations. To each sample, 5 μL of dilute ACN (0.24 % v/v; 15 μL of ACN in 6 mL of D_2O) was added. The unknown ligand concentrations were determined by comparison to a 5-point standard curve with a range of 1.00 – 0.01 mM ligand (1.00, 0.50, 0.10, 0.05, and 0.01 mM, prepared in D_2O). For each standard, the integral of a specific ligand peak was divided by the integral of the ACN peak and plotted against the known concentration of ligand (Figure 12). For all quantitative analyzes, a minimum signal-to-noise ratio of 360 was used. Following an internal standard approach for the unknown concentrations of ligand on the AuNP,¹⁸² the ligand peak was integrated and similarly divided by the known integrated ACN peak to yield the concentration upon comparison with the calibration curve. See Appendix A for representative NMR spectra with labelled peaks for ligand quantification.

2.2.13 Minimum Ligand Footprint and Ligand Excess Determination

In order to form a full monolayer of surface-adsorbed species, the concentration of ligand must be in some excess of available surface sites. Here, we estimate excess with respect to total

available surface area of the AuNPs and the minimum theoretical footprint area of the incoming ligand on a flat gold surface. The total available surface area of the AuNPs is calculated from the concentration of AuNPs (determined by ICP-MS) and the average core diameter (determined by TEM) (Figure 11). The minimum theoretical footprint of the incoming ligand was determined using a model system generated by the Avogadro molecular editor,¹⁸³ which was also used to aid in the measurement of atomic distances (Figure 10). Specifically, the geometry of an alkane thiol on a flat gold slab was geometrically optimized by relaxation with the universal force field (UFF) to an average force of 10^{-4} kJ/mol/atom before bond lengths and angles were obtained.

The length of carbon-hydrogen bonds were measured to be 1.112 Å and 1.111 Å for each carbon-hydrogen bond, with the slight (0.001 Å) variation observed depending on the presence of adjacent molecules (Figure 10). This measurement is from one atom center to the other. Therefore, the van der Waals sphere must also be considered, where the van der Waals radius for hydrogen was estimated to be 1.09 Å.¹⁸⁴ The linear distance between carbon atoms in the alkane chain was calculated to be 0.509 Å by considering the triangular geometry indicated below. By summing the bond lengths (Figure 10B), we obtain an overall molecular diameter estimate of 0.491 nm and corresponding minimum footprint of 0.189 nm²/ligand. From this footprint, a maximum of 2,813 ligands could be added to the surface of a 13 nm AuNP. This minimum footprint value is used only to estimate percent excess incoming ligand with respect to AuNP surface area.

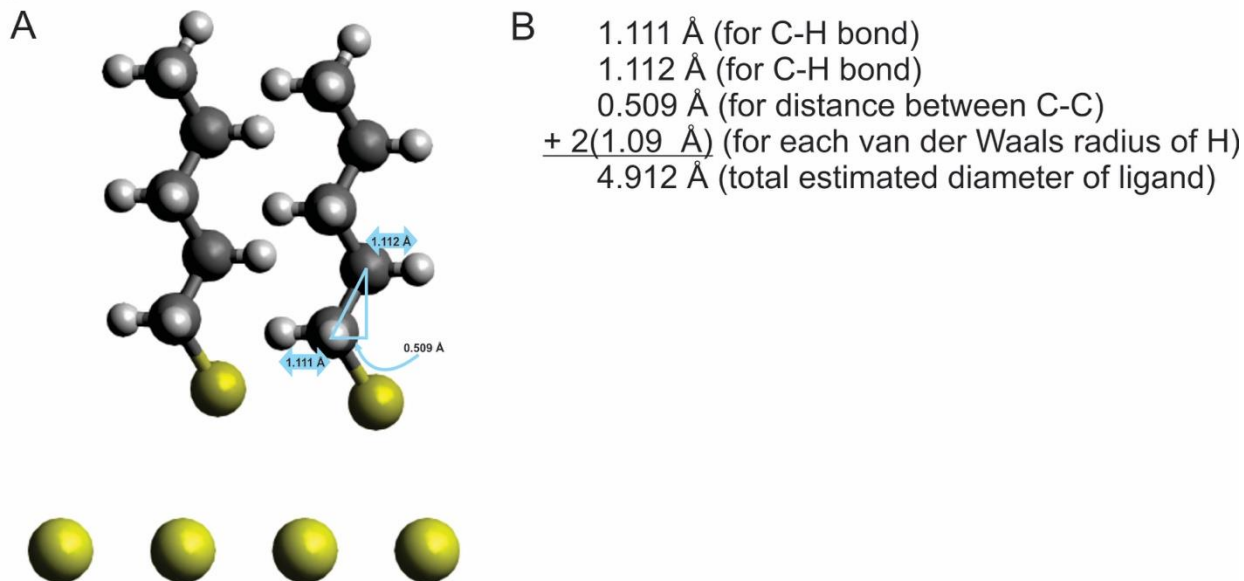


Figure 10. Representative molecule for minimum ligand occupation area of alkane thiol ligands on a flat gold surface (A) and corresponding calculation for ligand “diameter” based on the estimated geometry (B).

2.3 RESULTS AND DISCUSSION

2.3.1 Ligand Quantification Method

For a given ligand and NP surface, there are two primary factors that will influence the extent of incoming ligand adsorption during mass-action ligand exchange: incoming ligand concentration and reaction time in excess incoming ligand (i.e. incubation time). Here, we define excess ligand with respect to total NP surface area and a modeled minimum “footprint” of the incoming ligand (Figure 10).

To determine reaction times and ligand concentrations that produce constant ligand loading values with respect to a given parameter, we evaluate the NP ligand loading as function of both ligand concentration at a fixed incubation time, as well as at various incubation times at a fixed ligand concentration. For all ligand quantification experiments, the number of ligands on the AuNP surface was quantified using ^1H NMR. Specifically, the integrated peak intensity associated with a given resonance is compared to a standard curve of known ligand concentrations and an internal standard, as described above. In order to facilitate comparison of findings reported here with ligand quantification in other systems including metal clusters,^{72, 79} metal NPs,^{63, 168, 171} and quantum dots,^{131, 185, 186} we use three figures of merit to describe the ligand shell: (i) the total number of ligands obtained per particle, (ii) ligand footprint (nm^2), and (iii) ligand density ($\text{ligands} \cdot \text{nm}^{-2}$).

For all ligand exchange experiments, we considered two commonly used AuNP sizes with average diameters of 13 and 30 nm. Both NP sizes were synthesized using a modified Frens method and characterized by TEM and UV-vis-NIR spectroscopy.^{180, 187} Particles exhibited characteristic extinction maxima for both 13 ± 1 nm and 31 ± 1 nm AuNPs (Figure 11).

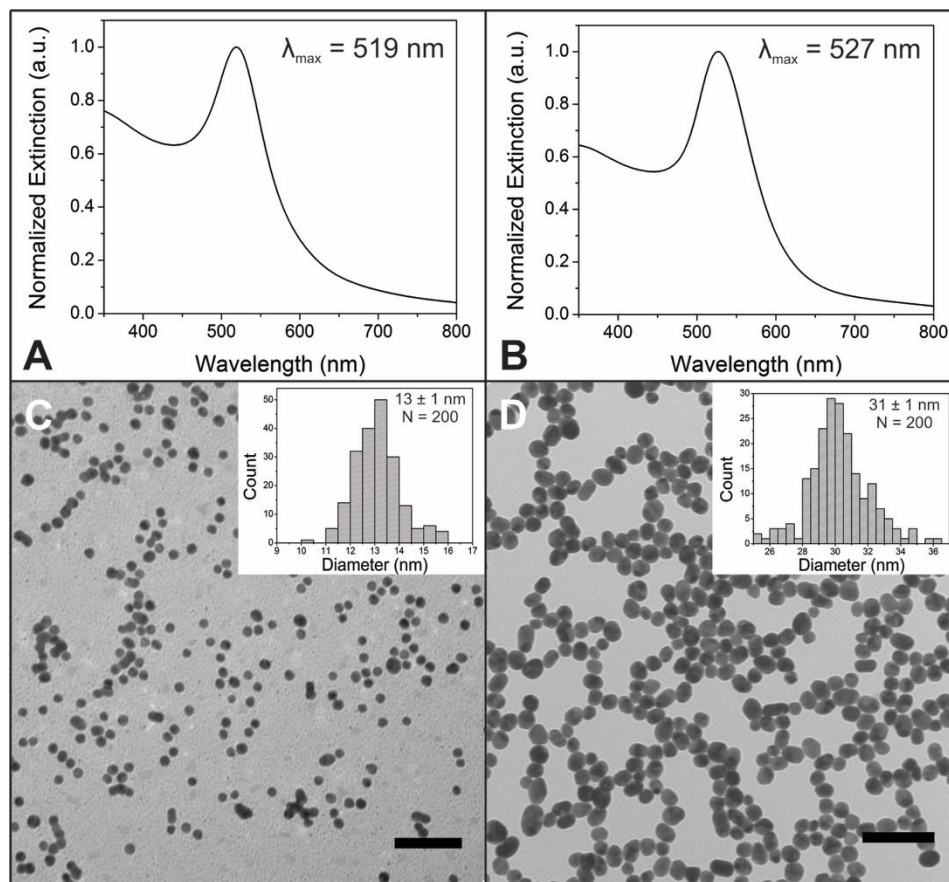


Figure 11. Representative UV-vis-NIR spectra for 13 nm (A) and 30 nm (B) NPs and corresponding TEM images, (C) and (D). Insets are histograms for 13 nm and 30 nm NPs generated from measurements of at least 200 NPs. Scale bars are 100 nm.

After basic AuNP characterization, ligand exchange of the citrate-stabilized AuNPs was performed and evaluated by ^1H NMR. To construct the calibration curve, proton peaks from both PEGSH and ACN are integrated. For PEGSH, the peak corresponding to the methylene protons of the ethylene glycol repeat unit (excluding the terminal methyl group of the PEGSH and those adjacent to the thiol) is used. For ACN, only a single peak is observed, which corresponds to three methyl protons. The PEGSH integration value is divided by the ACN integration value, and this ratio (y) is plotted against the known ligand concentration (x), with the intercept forced through zero. Using this procedure, linear agreement is achieved, with an average R^2 value of 0.9999 (over at least 15 independent trials in all cases reported here). Ligand concentration of the unknown samples was determined using the linear regression equation obtained from these curves (Figure 12).

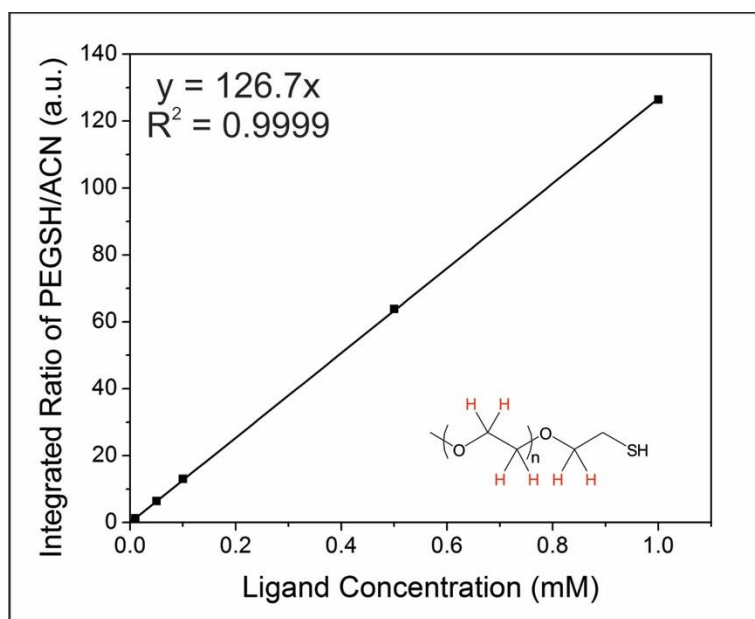


Figure 12. Sample calibration curve obtained for PEGSH by plotting integrated ratios of PEGSH/ACN against the concentration of PEGSH. PEGSH protons used for this analysis are highlighted in red.

It is well-known that ^1H NMR signals from ligands bound to NPs typically display broad linewidths (Figure 13). All particle-bound ligand ^1H resonances experience slower molecular tumbling and correlation times in solution as a result of attachment to a structure with a hydrodynamic radius that is much larger than the free ligand. These factors can decrease transverse relaxation time (T_2), which leads to line broadening according to the following equation:¹³⁷

$$\nu_{fwhm} = \frac{1}{\pi T_2} \quad \text{Equation 1}$$

where ν_{fwhm} is the full width at half maximum of the NMR peak.⁷⁷ Additionally, ligand segments close to the particle surface exhibit line broadening associated with the chemical shift distribution that arises from adsorption to different crystallographic sites on the AuNP¹⁸⁸ and the coupling of ^1H resonances to conduction electrons from the metallic AuNP. The paramagnetic contribution to dipolar transverse relaxation depends on the average electron-nuclear distance, R , and can be described by the proportional relation:^{189, 190}

$$\frac{1}{T_2} \propto \frac{1}{R^6} \quad \text{Equation 2}$$

In this case, R represents the average distance between the ^1H nuclei on the ligand and the electrons on the AuNP surface. This T_2 decrease leads to additional line broadening according to equation 1.

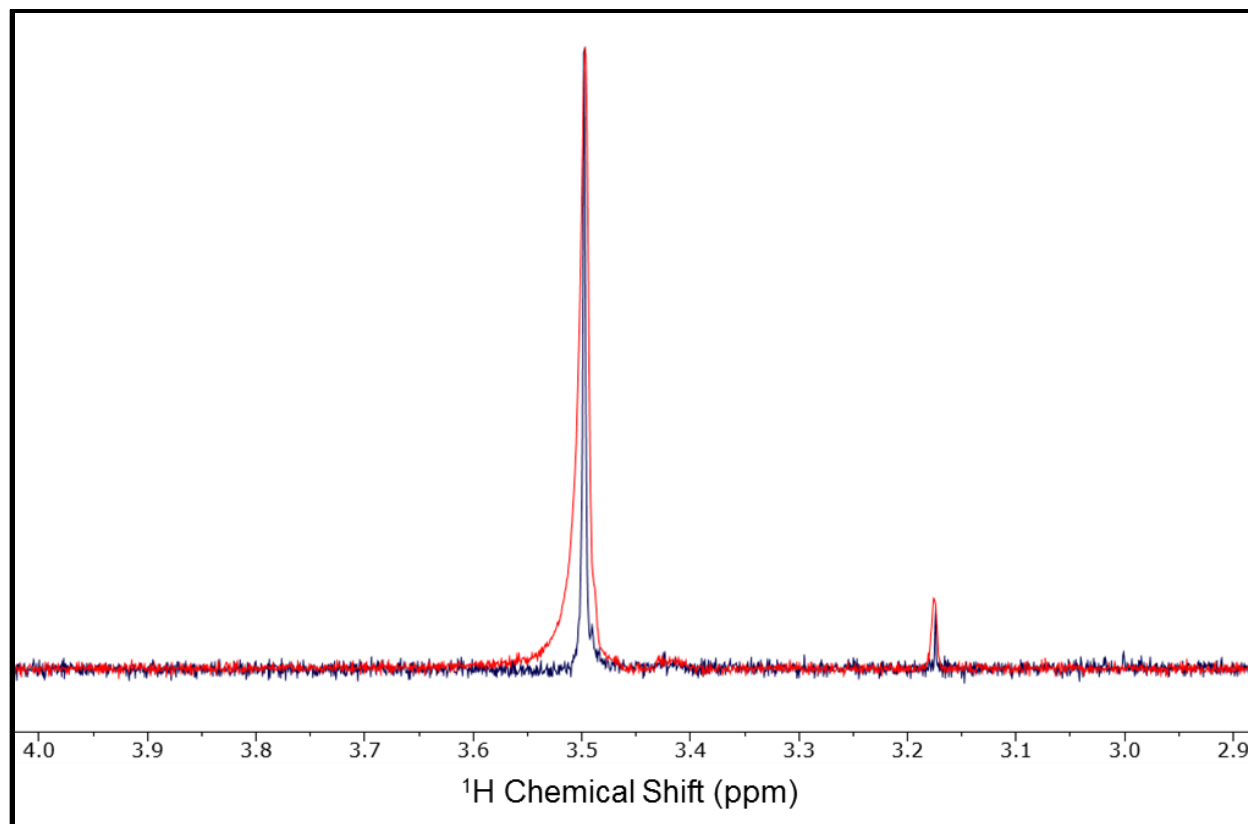


Figure 13. Representative ^1H NMR spectra of PEGSH on-particle (red line) and off-particle (blue line) in D_2O for 13 nm AuNPs. Line broadening observed with the on-particle spectrum can obscure accurate quantification.

Together, these ^1H NMR line broadening mechanisms obscure accurate ligand quantification via signal integration for ligands appended to a solid metal surface.^{188, 191-193} To eliminate the effects of NP-induced line broadening, all AuNP samples analyzed in this study were digested after purification in order to release NP-bound ligands into solution. The resulting mixture was then analyzed by both NMR and ICP-MS. It is important to note that analyzing the *same* solution ensures that there is direct correlation between the measurements of AuNP concentration (ICP-MS) and the measurements of ligand concentration (NMR).

To test the validity of this approach, we developed a specialized molecule containing a selenocyanate binding moiety in place of the thiol. This selenium-containing ligand could be quantified by both NMR using our method, and ICP (via Se detection) in order to obtain a secondary confirmation of ligand counts. Here, we used an analogue of PEGSH, poly(ethylene) glycol selenocyanate (PEGSeCN). The PEGSeCN ligand exhibits a peak at 3.62 ppm in the ^1H -NMR spectrum, which corresponds to the methylene protons in the polymer backbone and is used for ligand quantification (Appendix A, Figure 55). The PEGSeCN also contains a selenium atom that can be analyzed using ICP-OES, which allows the same molecule to be quantified using two different analytical approaches. (*N. B.* Se could not be detected using ICP-MS due to argon interferences).

When comparing ligand density values obtained by ^1H NMR versus ICP-OES, a ligand footprint of $0.32 \pm 0.01 \text{ nm}^2$ is obtained via NMR, while a footprint of $0.34 \pm 0.01 \text{ nm}^2$ is obtained via ICP-OES. The differences in the results from the two methods are not statistically significant at a 95% confidence interval.¹⁹⁴

2.3.2 Ligand Concentration and Incubation Time

With a reliable quantification method in hand, we determined the minimum incoming ligand excess and minimum incubation time necessary to establish ligand loading values that do not increase with increased ligand excess or with increased incubation times. First, at a high ligand excess (50× with respect to total NP surface area), we determine the amount of time required for each ligand exchange to proceed until no further changes were observed in the ligand footprint. For both 13 and 30 nm AuNPs, replacement of the as-synthesized citrate capping ligand with PEGSH occurs on the timescale of minutes. This exchange is indicated by the negligible change in ligand footprint observed across even the initial time points (Figure 14), where an average ligand footprint of $0.44 \pm 0.01 \text{ nm}^2/\text{PEGSH}$ ($1,200 \pm 40$ ligands/NP) for 13 nm AuNPs and $0.45 \pm 0.01 \text{ nm}^2/\text{PEGSH}$ ($6,800 \pm 200$ ligands/NP) for 30 nm AuNPs is established within the first 30 minutes.

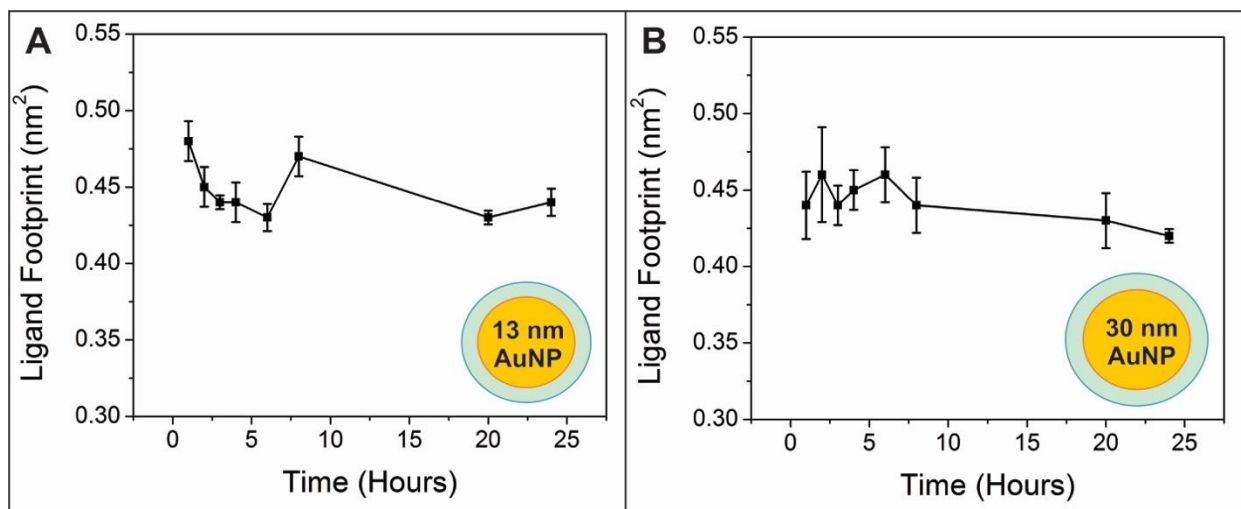


Figure 14. Plots of PEGSH footprint on the AuNP surface as a function of time in excess PEGSH (50 \times) for 13 nm (A) and 30 nm (B) AuNPs. Results indicate that ligand loading reaches a steady state (with standard errors of < 10% for at least 5 trials) on the timescale of minutes under the conditions tested.

Similar experiments were conducted for both MUA and MOA, using an excess of ligand (50 \times) to evaluate the necessary time of exchange for these thiolated small molecules. With MUA (Figure 15) and MOA (Figure 16), a consistent ligand footprint was reached within 2 hours with little fluctuation observed after this point for both AuNP sizes (standard errors of < 10%). While the exact time is dependent upon ligand identity, ligand exchange of citrate with a thiol-functionalized ligand is on the timescale of minutes to hours, which is consistent with self-assembled monolayer (SAM) formation observed on 2D Au surfaces.^{195, 196} In general, for all three thiol-functionalized ligands, 4 hours is sufficient for the ligand footprints to reach a consistent value with standard errors of < 10%.

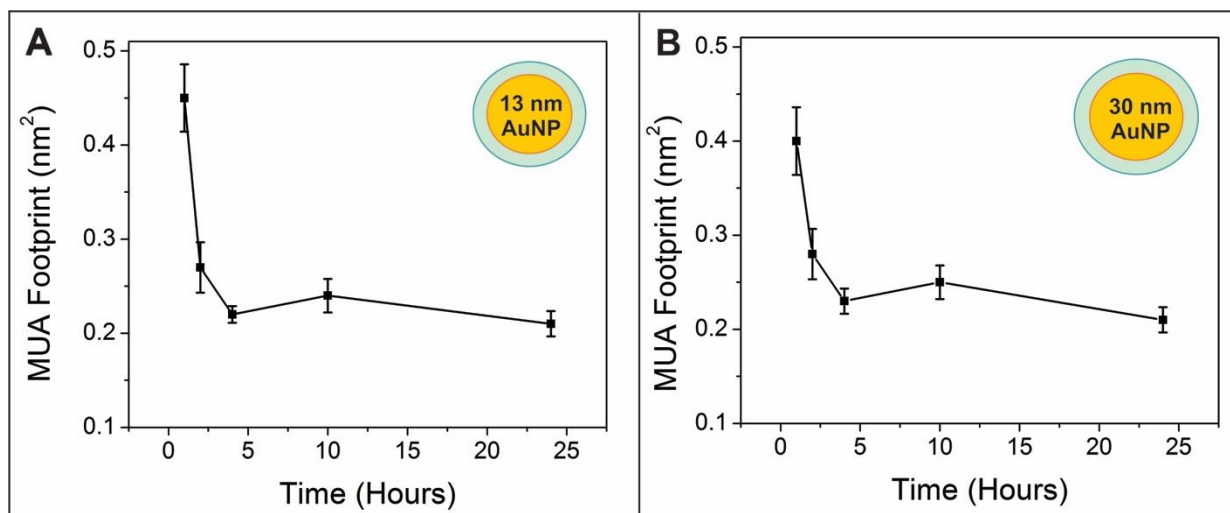


Figure 15. Plots of MUA footprint on the NP surface as a function of AuNP time in excess MUA (50x) for 13 nm (A) and 30 nm (B) AuNPs, where error bars represent the standard error of at least 5 trials. Results indicate that ligand loading reaches a plateau on the timescale of 2-3 hours under the conditions tested.

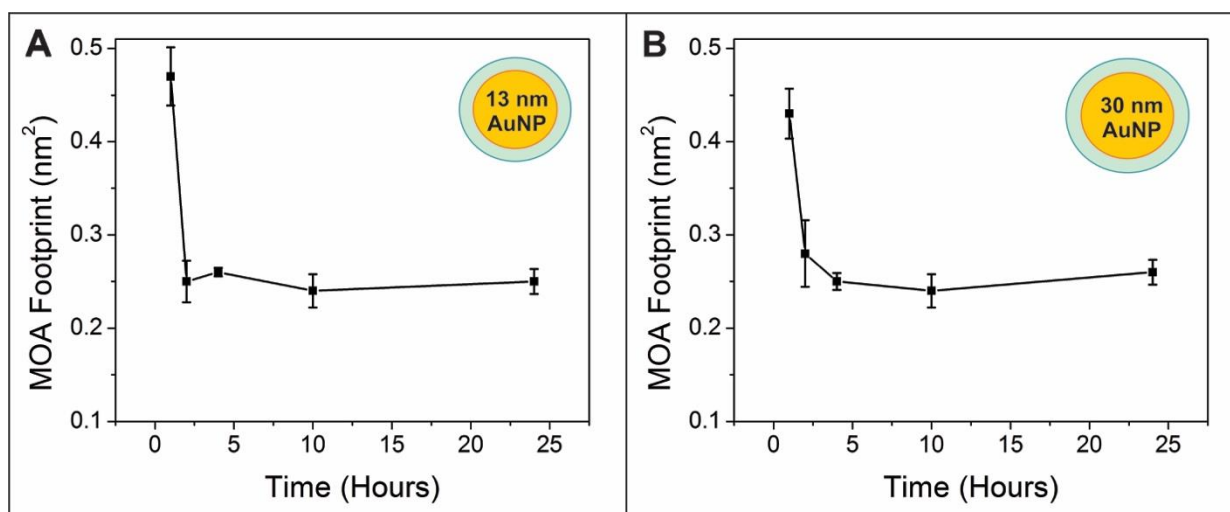


Figure 16. Plots of MOA footprint on the NP surface as a function of AuNP time in excess MOA (50x) for 13 nm (A) and 30 nm (B) AuNPs, where error bars represent the standard error of at least 5 trials. Results indicate that ligand loading reaches a plateau on the timescale of 2-3 hours under the conditions tested.

With a time frame for functionalization defined, we then determined the ligand loading values as a function of ligand concentration. Various concentrations of PEGSH were tested with both 13 and 30 nm AuNPs for a 4 hour exchange period. After reaching 20× excess (with respect to total particle surface area, *vide supra*), little change in the ligand footprint is observed (standard errors of < 10%) with an average footprint of $0.45 \pm 0.01 \text{ nm}^2/\text{PEGSH}$ and $0.47 \pm 0.02 \text{ nm}^2/\text{PEGSH}$ for the 13 and 30 nm AuNPs, respectively (Figure 17). Similarly, for MUA (Figure 18) and MOA (Figure 19), the ligand footprint reaches a plateau at ligand excesses above 20×. Overall, for both AuNP sizes and all three thiolated ligand types, a consistent ligand footprint was reached at $\geq 20\times$ excess ligand with respect to the total NP surface area. From these experiments, we conclude an excess of 50× is sufficient to ensure that incoming ligand concentration will not be a limiting factor in achieving maximum ligand loading on the AuNPs studied.

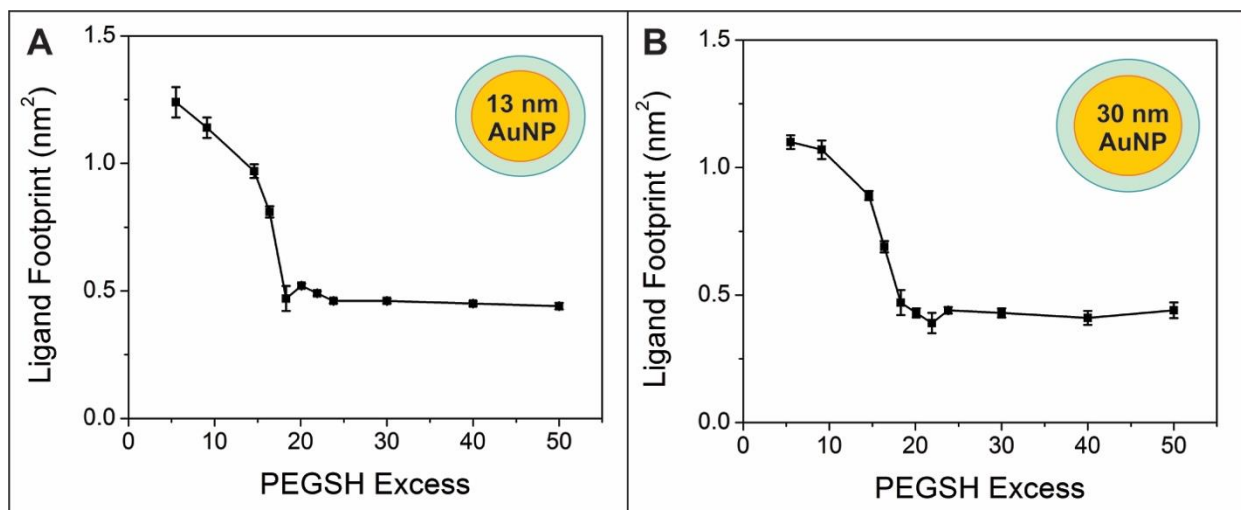


Figure 17. Graphs displaying PEGSH footprint as a function of PEGSH excess with respect to NP surface area after 4 hours for 13 nm (A) and 30 nm (B) AuNPs. Results indicate that maximum loading under the conditions evaluated reaches a steady state at an excess above 20× (with standard errors of < 10% for at least 5 independent trials).

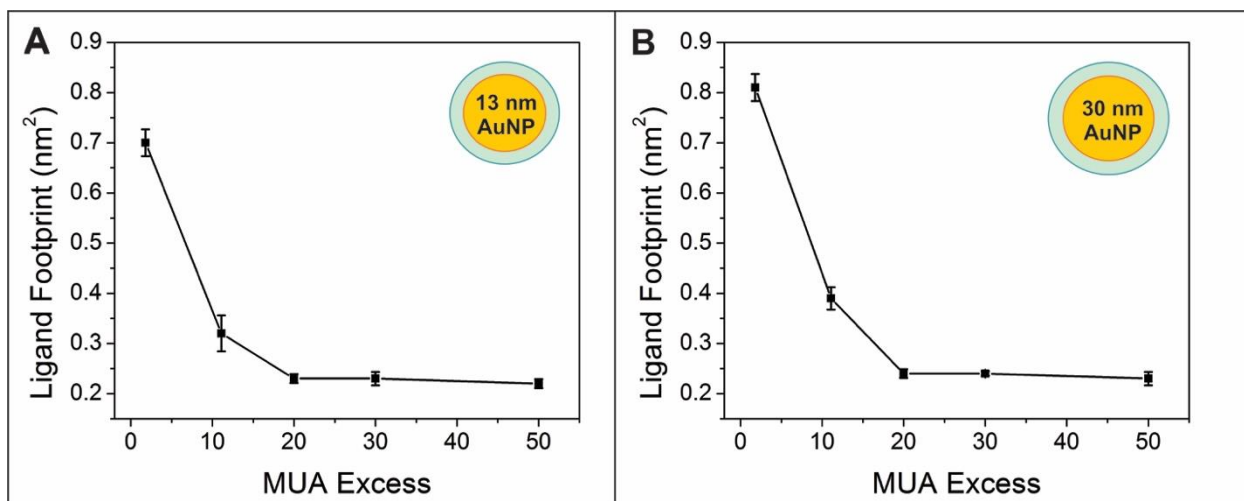


Figure 18. Graphs displaying MUA ligand footprint as a function of MUA excess with respect to surface area after 4 hours for 13 nm (A) and 30 nm (B) AuNPs, where error bars represent the standard error of at least 5 trials. Results indicate that loading reaches a consistent value at a ligand excess above 20x.

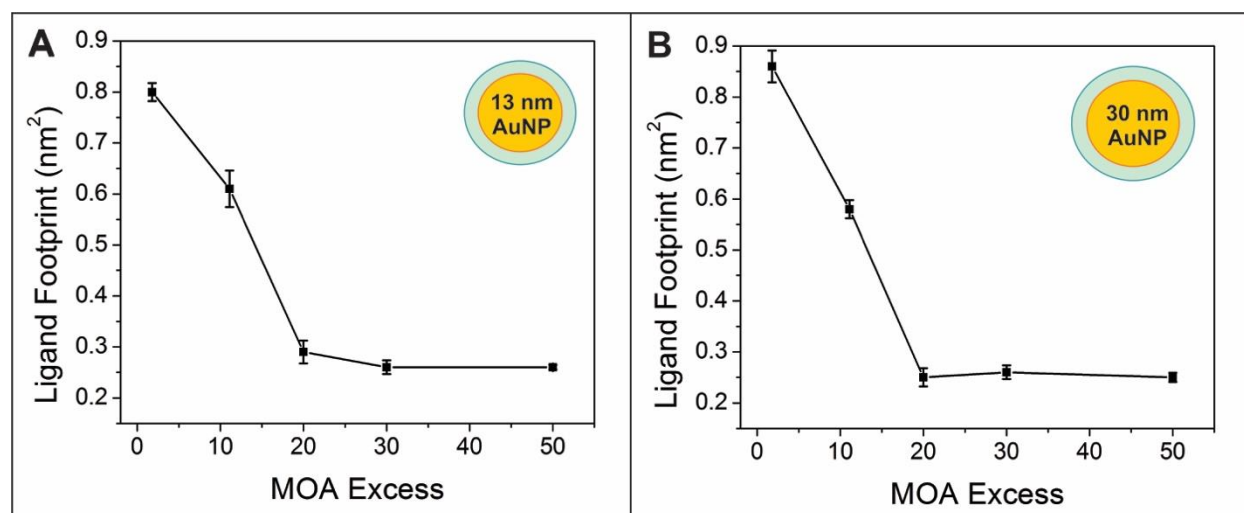
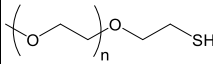
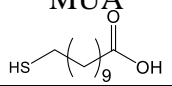
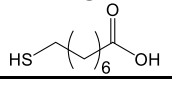


Figure 19. Graphs displaying MOA ligand footprint as a function of MOA excess with respect to surface area after 4 hours for 13 nm (A) and 30 nm (B) AuNPs, where error bars represent the standard error of at least 5 trials. Results indicate that loading reaches a consistent value at an excess above 20x.

2.3.3 Ligand Densities in Single-Moiety Ligand Shells

The ligand excess and reaction time conditions determined in the experiments above (50× and 4 hours, respectively), were used to perform all subsequent ligand exchanges (Table 3). Under these conditions PEGSH yields a ligand footprint that is similar for both the 13 and 30 nm AuNPs ($0.47 \pm 0.02 \text{ nm}^2/\text{PEGSH}$ and $0.44 \pm 0.02 \text{ nm}^2/\text{PEGSH}$, respectively). MUA yields the smallest ligand footprint ($0.22 \pm 0.01 \text{ nm}^2/\text{MUA}$ and $0.23 \pm 0.01 \text{ nm}^2/\text{MUA}$ for the 13 and 30 nm AuNPs, respectively). In all cases, the NP radius of curvature seems to play a negligible role in determining ligand density. This observation is consistent with geometric calculations (Figure 20). Plotting curvature as a function of particle diameter, one can identify a particle diameter “threshold” ($\sim 10 \text{ nm}$), above which little change in curvature is observed as function of particle size with respect to ligand size. In other words, we compare the radius of curvature to the size of the ligand considered, and just like a human does not perceive the curvature of the earth due to the scale discrepancy between the two, so does a certain size of nanoparticle arise such that the ligand no longer “perceives” surface curvature. Our experiments and calculations suggest that this diameter is 10 nm. Murray et al describes a similar transition where the ligand no longer behaves as if it is on a 3D surface, but instead packs as if experiencing a 2D surface.⁷⁷ Therefore, it may be expected that ligand loading values on pseudo-spherical NPs with diameters $> 10 \text{ nm}$ do not exhibit marked size dependence.

Table 3. Ligand densities for 13 and 30 nm AuNPs (average size \pm standard deviation) functionalized with PEGSH, MUA, or MOA, where the errors represent standard error for at least 20 trials.

Particle Size (nm)	Ligand Type	Ligands/Particle	Ligand footprint (nm ²)	Ligands/nm ²
13 \pm 1	PEGSH	1,200 \pm 30	0.47 \pm 0.01	2.1 \pm 0.1
31 \pm 1		6,900 \pm 200	0.44 \pm 0.02	2.3 \pm 0.1
13 \pm 1	MUA	2,500 \pm 60	0.22 \pm 0.01	4.5 \pm 0.1
32 \pm 1		13,000 \pm 500	0.23 \pm 0.01	4.4 \pm 0.2
14 \pm 1	MOA	2,100 \pm 20	0.26 \pm 0.01	3.9 \pm 0.1
31 \pm 1		12,000 \pm 300	0.25 \pm 0.01	4.0 \pm 0.1

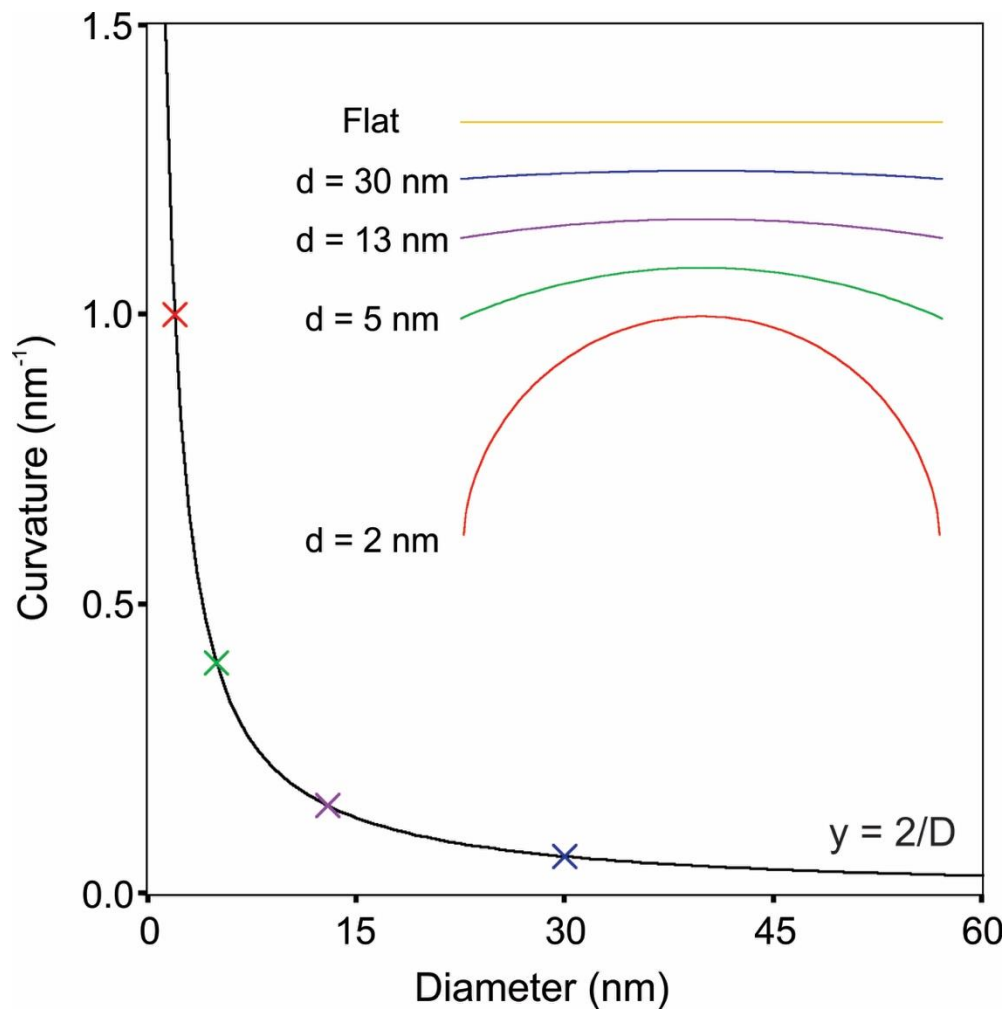


Figure 20. Surface curvature as a function of particle diameter. The figure illustrates that for particles with diameters larger than 10 nm, change in curvature as a function of particle diameter decreases dramatically.

PEGSH likely exhibits a larger footprint than the two carboxy-terminated alkane thiol ligands because the polymer chains may interact with the Au surface via van der Waals interactions as well as exhibit both intra- and intermolecular hydrogen bonding, leading to a random coil morphology that is sterically cumbersome.^{26, 197, 198} Therefore, while the thiol-functionality is most likely anchored to the surface, it is unlikely that the chains will remain extended in a conformation that could maximize on-particle loading.^{26, 198}

For comparison, MUA and MOA form more dense monolayers on the AuNPs (consistent for both AuNP sizes). MUA has the smallest ligand footprint, indicating that it forms the most densely packed monolayer. Van der Waals interactions between adjacent methylene units in the alkane chains may provide a driving force for ordered assembly of both MUA and MOA on the NP surface. However, the shorter chain length of MOA decreases the total number of inter-ligand interactions and may limit the ordering of (or increase defects in) the SAM of NP ligands. Such observations are consistent with formation of alkanethiol SAMs on Au thin films.^{15, 17, 199}

2.3.4 Influence of Ligand Chain Length on Ligand Loading

Given that we have observed that the longer polymeric PEGSH ligands pack less densely than the smaller thiolated MUA or MOA ligands, it is desirable to understand the ligand loading trends with respect to ligands that are identical except for chain length. In order to probe this type of system, various MWs of PEGSH (350, 1000, 2000, or 5000 Da) or mercaptoalkanoic acids can be used. Given that no significant differences in ligand loading were observed between 13 nm and 30 nm AuNPs, trends will be examined on 13 nm AuNPs.

Consider first the PEGSH system, where the ligand shell reaches a steady state within 4 hours and at a 50x excess (Figure 21) for all molecular weights. From the trends observed above

with the mercaptoalkanoic acids and the 1 kDa PEGSH, it is expected that the shortest PEGSH (here, 350 Da) will load with the highest number of ligands, while the longest PEGSH (5 kDa) will have fewer ligands per particle. As predicted, the shorter chain length of the PEGSH packs with the highest number of ligands, with a footprint of $0.21 \pm 0.05 \text{ nm}^2$, while the 5 kDa PEGSH has the largest footprint of $2.31 \pm 0.12 \text{ nm}^2$, and the intermediate 1 kDa and 2 kDa chain lengths fall in between with footprints of $0.47 \pm 0.01 \text{ nm}^2$ and $1.14 \pm 0.09 \text{ nm}^2$, respectively (Figure 22). Given the range of ligand footprints that are accessible for PEGSH ligands that can be tuned based solely upon chain length, a wide library of NPs with various ligand footprints can be prepared with this system.

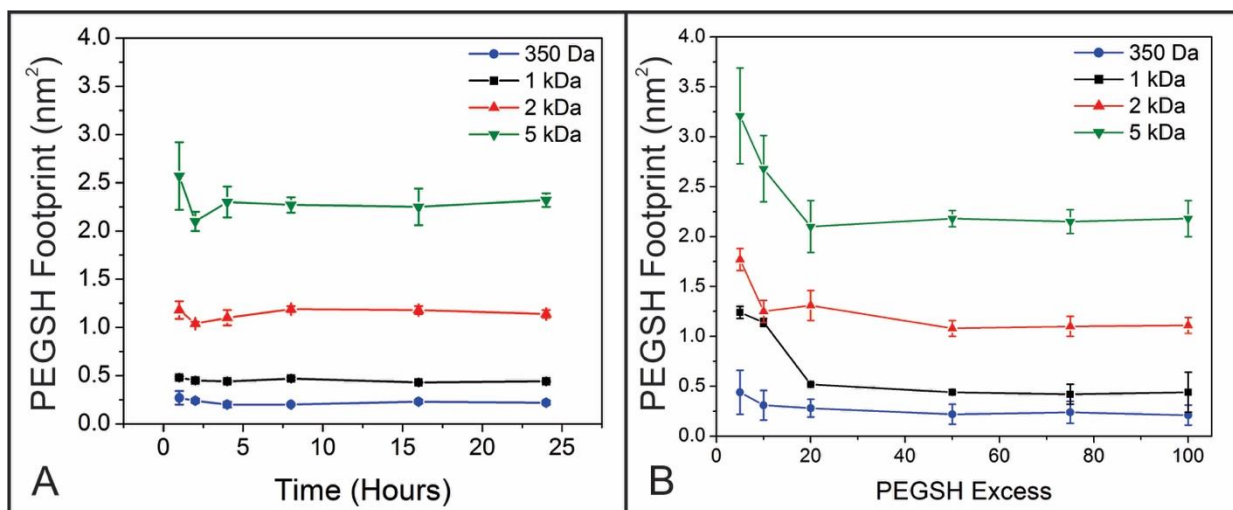


Figure 21. Plots of PEGSH footprint on 13 nm AuNPs as a function of time in excess PEGSH (50 \times) (A) and PEGSH excess with respect to surface area after 4 hours (B) for different MWs of PEGSH, where error bars represent the standard error of at least 5 trials. Results indicate that loading reaches a consistent value at a ligand excess above 20 \times and above 4 hours under the conditions tested.

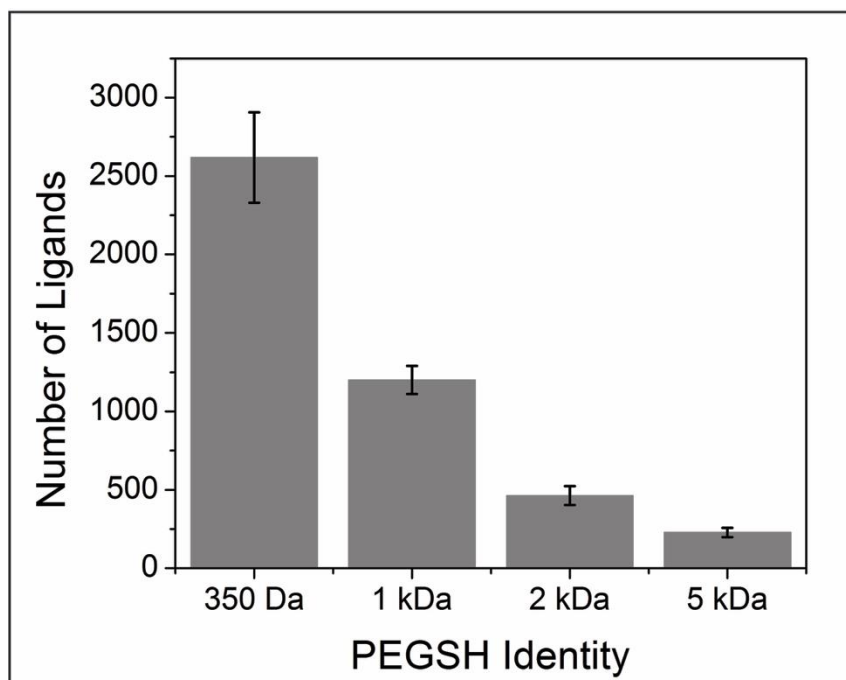


Figure 22. Graph of number of PEGSH ligands per particle as a function of PEGSH chain length, where error bars represent the standard error of at least 5 trials. Shorter polymer chains have fewer ligands per particle than longer chains.

While the polymeric PEGSH ligands follow the expected trend, significant deviations are observed with the mercaptoalkanoic acid system, which includes MBuA (4 carbons), MHA (6 carbons), MOA (8 carbons), and MUA (11 carbons) (Figure 23). While the shortest MBuA ligand loads with the highest number of ligands, as expected, the 8 and 11 carbon chains display a trend opposite to what would be expected, indicating that chain length is not the only factor that dictates ligand loading. Here, we hypothesize that the longer ligands have stronger inter-ligand interactions that facilitate higher ligand loading. Preliminary 2D NMR experiments (see Appendix A, Figure 61) indicate that MUA may form “islands” on the particle surface, supporting the cooperative mechanism hypothesis. Such cooperative behavior has also been observed in other NP systems,⁵⁰ as well as for alkane thiol SAMs on gold films.²⁰⁰

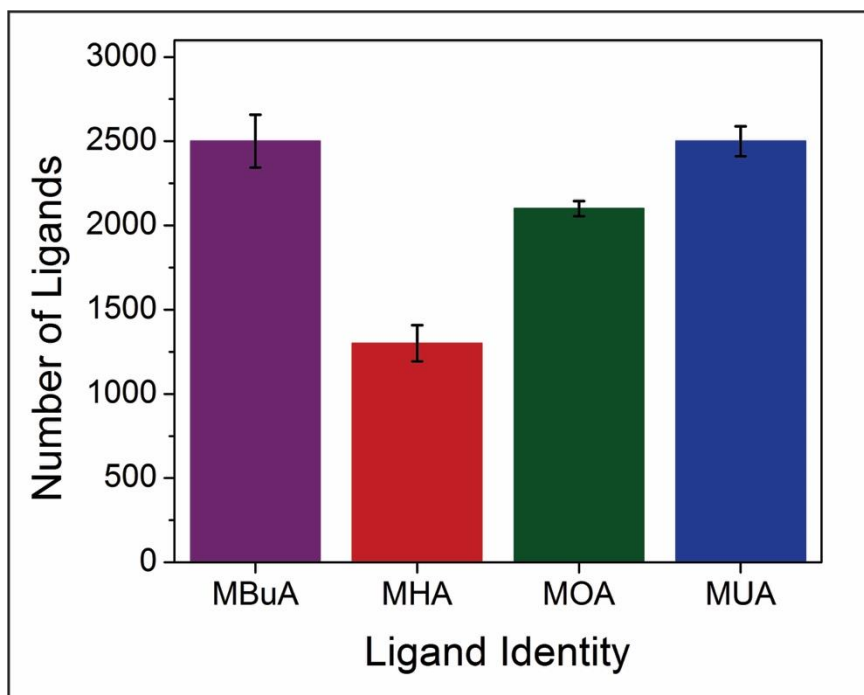


Figure 23. Graph of number of mercaptoalkanoic ligands per particle as a function of chain length, where error bars represent the standard error of at least 5 trials.

Given the deviations from the expected behavior with the 4, 6, 8, and 11 carbon chain mercaptoalkanoic acids, studying longer chain lengths could also yield important insights into AuNP ligand exchange behavior. In order to facilitate this study, a solvent other than water is necessary due to solubility concerns with chain lengths longer than 11 carbons. Controls were conducted with MUA in water, DMSO, and chloroform to ensure that performing the ligand exchange in organic solvent did not affect the final MUA ligand density. No evidence of altered ligand loading was observed in either DMSO or chloroform (Figure 24).

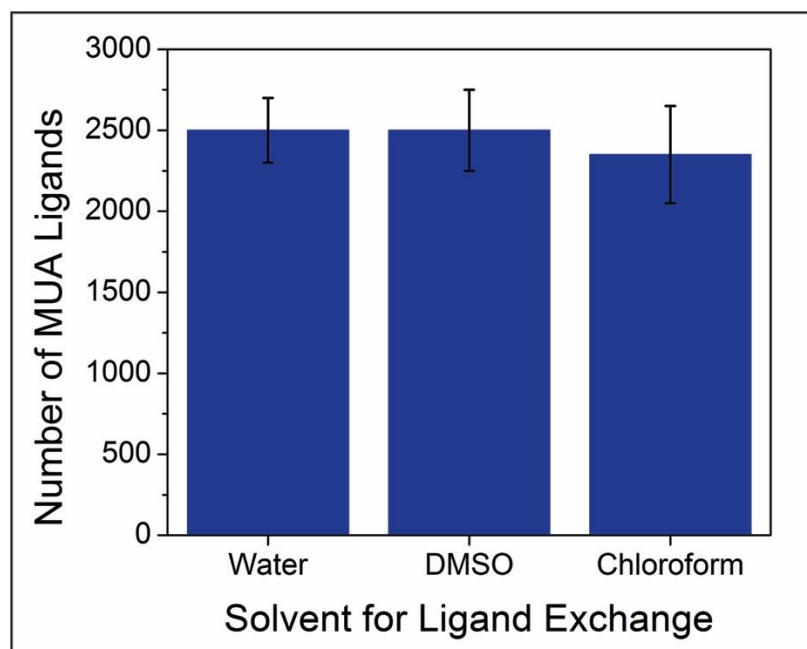


Figure 24. Graph of number of MUA ligands per particle in various solvents, where error bars represent the standard error of at least 3 trials. No significant difference is observed in ligand loading in organic solvents.

Working in DMSO for ligand solubility, the effect of ligand chain length on a longer series of mercaptoalkanoic acids was examined using MUA (11 carbons), MUDA (12 carbons), and MHDA (16 carbons). With this group of mercaptoalkanoic acids, the expected trend is observed, where the shorter ligand (here, MUA with 11 carbons) has a higher number of ligands than the MUDA or MHDA (Figure 25). This return to the expected trend with the mercaptoalkanoic acids indicates that for ligand chains longer than 11 carbons, the inter-ligand interactions are no longer enough to ensure cooperative behavior. The longer chain lengths begin to behave more similarly to the polymeric PEGSH ligands, where the chains are not fully extended to allow for maximum ligand loading.

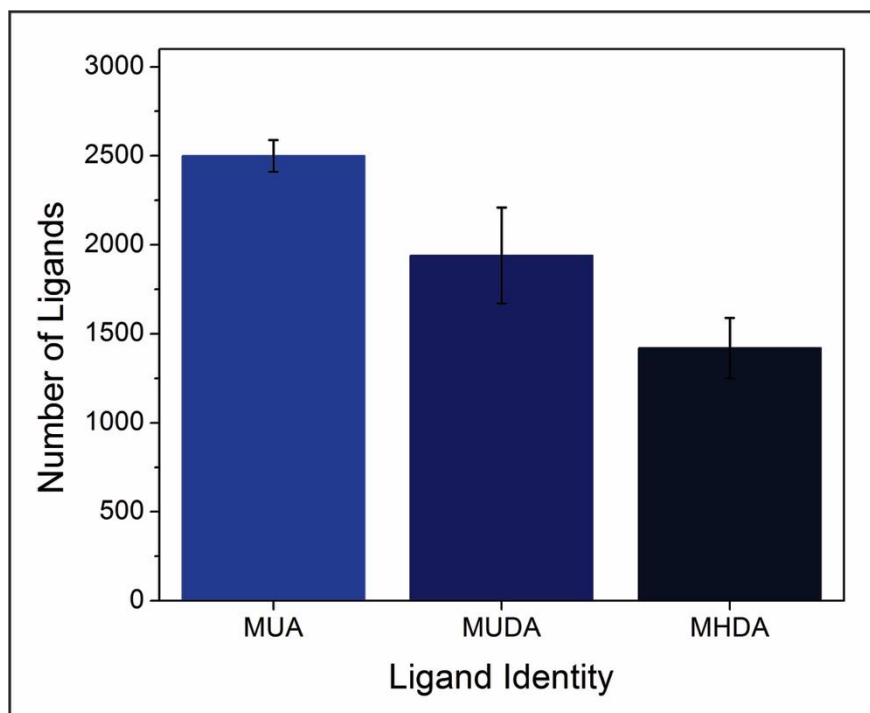


Figure 25. Graph of number of mercaptoalkanoic ligands per particle as a function of chain length, where error bars represent the standard error of at least 5 trials. The shorter ligands have a higher ligand density.

2.3.5 Influence of Salt and Temperature on Ligand Loading Density

When considering homogeneous ligand shells, it may be of interest to maximize ligand loading for the densest possible ligand shell, either to improve stability or enhance functionality. Both incubation in salt and higher temperatures have been shown to increase DNA loading on AuNPs.¹⁰⁰ In order to evaluate the impact of salt during ligand exchange, PEGSH ligand exchanges were completed in the presence of 150 mM of various salts (Figure 26). The identity of the salt influenced the PEGSH loading, where the anion identity has a more pronounced effect than the cation, which did not have a significant impact on loading. Interestingly, the anion with the largest ionic radius (I⁻) yields NP ligand shells with a decreased number of ligands, while the

anion with the second largest ionic radius (Br^-) produced no change when compared to unsalted solution. The anions with smaller ionic radii (Cl^- and F^-), however, yielded particles with a higher number of ligands. This increased loading results from the smaller anions' ability to screen the inter-ligand interactions between the PEGSH ligands on the particle surface, reducing their charge repulsion for a more dense ligand shell.²⁰¹

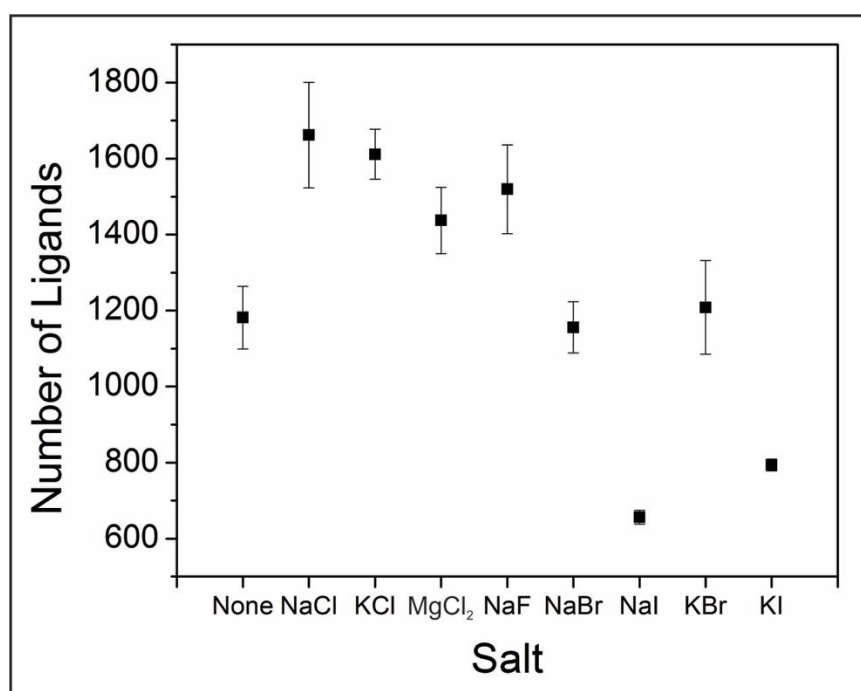


Figure 26. Plot of the number of PEGSH ligands per particle as a function of salt identity. The identity of the salt impacted the PEGSH loading on the basis of ionic radius.

Given the increase in the 1 kDa PEGSH loading observed with NaCl above, the impact of NaCl on the higher MWs of PEGSH was evaluated (Figure 27). While an increase of only 23% in ligand loading was observed for the 1 kDa PEGSH ligand, increases of 24 and 43% in 150 mM NaCl were observed in the 2 kDa and 5 kDa PEGSH cases, respectively, when compared to

a 0 mM NaCl solution. The enhanced impact of the salt on the higher MWs of PEGSH can likely be attributed to the salts screening the nonspecific interactions between the longer polymeric chains. Ligand exchanges in salt were also conducted for the MUA and MOA ligands, but no significant change in the number of ligands was observed for either. Finally, ligand exchanges conducted at temperatures other than room temperature were also evaluated with PEGSH (Figure 28). Working at both an elevated (37 °C) and a decreased (4 °C) temperature, the PEGSH excess experiments were completed in the same way as outlined above. However, no significant change in ligand loading was observed at either temperature at the highest ligand excess. Thus, performing the ligand exchanges in salt results in PEGSH ligand shells with a higher number of ligands.

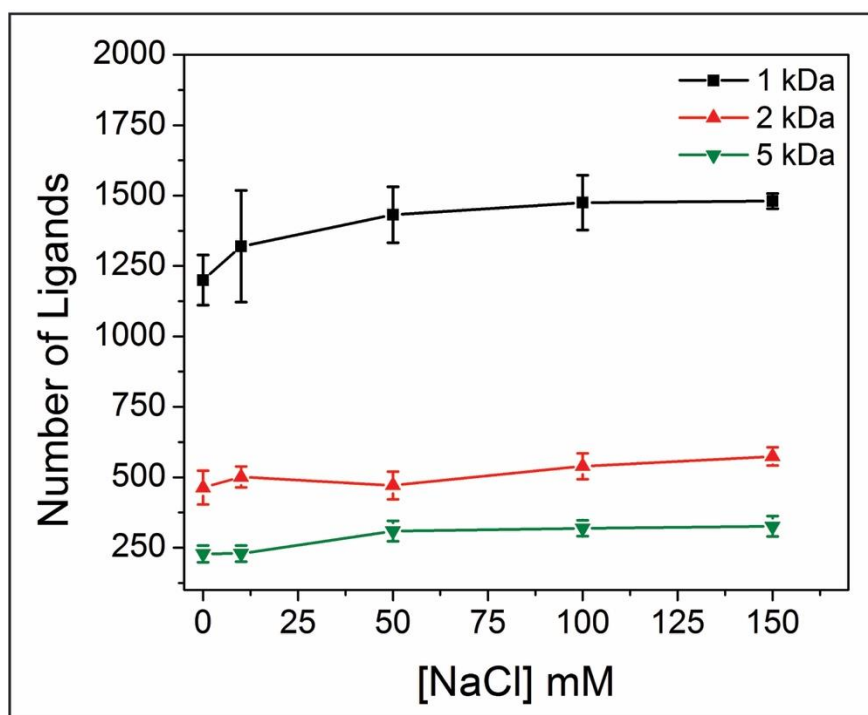


Figure 27. Plot of the number of PEGSH ligands as a function of NaCl concentration. Increased loading is only observed for the 1 kDa PEGSH, likely due to the longer chain lengths with the 2 kDa and 5 kDa PEGSH.

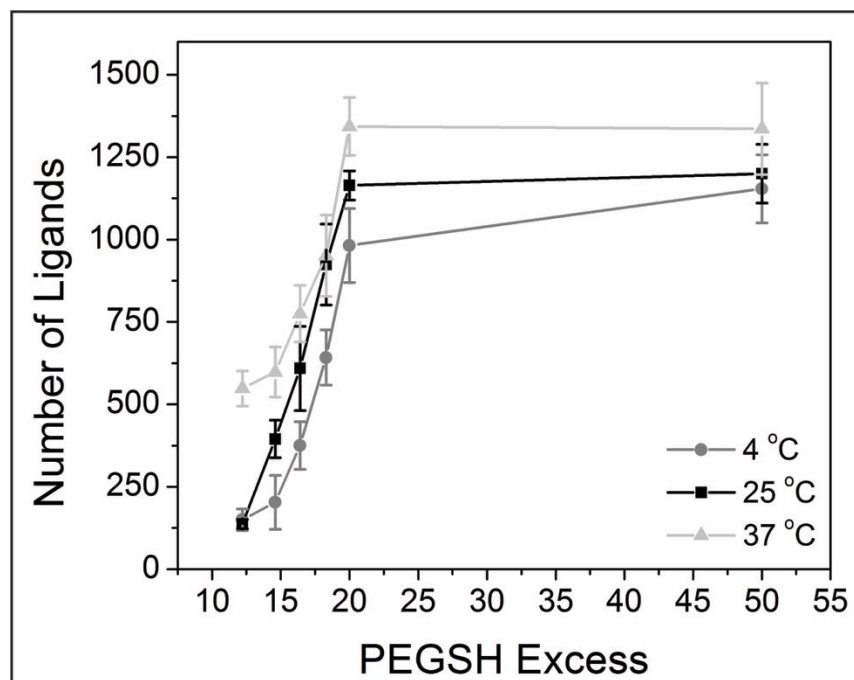


Figure 28. Plot of the number of PEGSH ligands as a function of PEGSH excess at various temperatures. No significant change in ligand loading is observed at elevated or decreased temperatures.

2.4 CONCLUSION

Taken together, these experiments suggest that ligand addition mechanisms are strongly influenced not only by the ligand functionalities directly interacting with the NP surface (here, a thiol moiety) but also by intermolecular interactions within the ligand shell itself. Specifically, the current results indicate that PEGSH SAMs on AuNPs can present a wide range in the number of ligands in a ligand shell, modifiable through a variety of means including ligand chain length and salt incubation during ligand exchange. Mercaptoalkanoic acid ligands generally form ligand shells with a higher number of ligands on AuNPs, dictated by both chain length and inter-ligand interactions. We expect these findings will have important implications for routine surface

characterization of AuNPs as well as using surface chemistry to enhance or expand AuNP use in a wide variety of biomedical and electronic applications.

3.0 QUANTITATIVE EVALUATION OF LIGAND BACKFILLING AND CO-LOADING ON GOLD NANOPARTICLE FUNCTIONALIZATION

(Portions of this work were published previously and are reprinted with permission from Smith, A. M.; Marbella, L. E.; Johnston, K. A.; Hartmann, M. J.; Crawford, S. E.; Kozycz, L. M.; Seferos, D. S.; Millstone, J. E., *Anal. Chem.* **2015**, *87*, 2771-2778. Copyright 2015, American Chemical Society. Other portions of this work are being prepared for submission as Smith, A. M.; Johnston, K. A.; Marbella, L. E.; Millstone, J. E. **2017**, in preparation)

3.1 INTRODUCTION

Gold nanoparticles (AuNPs) are versatile materials,²⁰²⁻²⁰⁵ but the performance of these particles strongly depends on their ligand shell.^{25, 103, 115, 206} Among the parameters one can tune within ligand shell architectures, ligand shell identity and composition are foundational. In terms of composition, ligand shells can either be composed on one ligand type (homogenous) or two or more ligand types. For a NP with a homogeneous ligand shell, there are currently two primary methods to then create a multicomponent ligand shell: “backfilling” by sequentially adding the desired ligands to the NP surface or “co-loading” by simultaneously adding multiple ligands to the NP surface. In order to truly understand the factors that will allow for control of the final ligand shell architecture, ligand properties and loading method must be systematically probed.

The efficiency of these mass-action ligand exchange techniques depends upon several aspects of the system including properties of both the NP (e.g. size, shape, and composition) and the ligands (both those coming off and going onto the NP) as well as temperature, reaction time, and solvent. A common way to vary the composition of a mixed ligand shell is by altering the initial molar ratio of ligands added to the NP system. However, the concentration of ligands attaching to the NP from these ligand mixtures varies significantly from system to system, and the final ratio of ligands does not always match with the ratio of ligands that was added.^{51, 131} Because of this discrepancy, it is important to use a method of characterization that can distinguish and quantify multiple ligands. In this work, we investigate the influence of loading method and ligand properties on final NP ligand shell compositions to begin to establish design rules that will allow for enhanced tailorability of ligand shells for ultimate use in various downstream applications.

3.2 EXPERIMENTAL

3.2.1 Materials and Methods

Hydrogen tetrachloroaurate (III) trihydrate ($\text{HAuCl}_4 \cdot 3\text{H}_2\text{O}$, 99.999%), 11-mercaptoundecylphosphoric acid (MUPA, 95%), 8-mercaptooctanoic acid (MOA, > 95%), 6-mercaptohexanoic acid (MHA, 90%), 11-aminoundecanoic acid (AUA, 97%), 8-aminooctanoic acid (AOA, 99%), 6-aminohexanoic acid (AHA, $\geq 98.5\%$), 3-mercaptopropionic acid (MPA, $\geq 99\%$), hydrochloric acid (HCl, > 99.999% trace metal basis), nitric acid (HNO_3 , > 99.999% trace metal basis), and sodium citrate tribasic dihydrate (citrate, $\geq 99\%$) were obtained from Sigma-

Aldrich (St. Louis, MO). Poly(ethylene glycol) methyl ether thiol (PEGSH, average MW = 1,000 Da), was obtained from Laysan Bio, Inc. (Arab, AL). Biotin-terminated poly(ethylene glycol) methyl ether thiol (biotinPEGSH, > 95%, average MW = 1,000 Da) and methoxypoly(ethylene glycol) amine (PEGNH₂, > 95%, average MW = 1,000 Da) were obtained from NanoCS (Boston, MA). 11-Mercaptoundecanoic acid (MUA, 98%) was obtained from Santa Cruz Biotechnology (Dallas, TX). 11-Amino-1-undecanethiol hydrochloride (AUT, ≥ 90%) was obtained from Dojindo Molecular Technologies, Inc. (Rockville, MD). Acetonitrile (ACN, 99.8%), and sodium hydroxide (NaOH, ≥ 97%) were obtained from Fisher Scientific (Waltham, MA). Deuterium oxide (D₂O, 99.9%) was obtained from Cambridge Isotope Laboratories, Inc. (Tewksbury, MA). All reagents were used as received unless otherwise indicated. NANOpure™ (Thermo Scientific, > 18.2 MΩ · cm) water was used in the preparation of all solutions, and all reagent solutions are aqueous unless otherwise noted. Before use, all glassware and Teflon®-coated stir bars were washed with aqua regia (3:1 ratio of concentrated HCl and HNO₃ by volume) and rinsed thoroughly with water. *Caution: Aqua regia is highly toxic and corrosive and requires proper personal protective equipment. Aqua regia should be handled in a fume hood only.*

3.2.2 AuNP Synthesis

AuNPs were synthesized using a modified Frens procedure.^{180, 181} In a 1 L, 3-neck round bottom flask containing a stir bar, 500 mL of aqueous HAuCl₄ (1 mM) solution were prepared. The solution was heated to vigorous reflux while stirring until a rapid drip rate was achieved (drip rate ~1 per second). Meanwhile, a 50 mL aqueous solution of citrate was prepared (concentrations used to generate various sizes of AuNPs are listed above in Table 2). This citrate

solution was rapidly added to the refluxing HAuCl_4 solution. After addition, the reaction mixture changed from yellow, to colorless, to black, to purple-red within 1 minute. The resulting AuNP solution was allowed to reflux for 5 minutes before it was removed from heat. This mixture was cooled to room temperature and transferred to a clean glass media bottle for refrigerated storage ($\sim 4^\circ\text{C}$).

3.2.3 UV-vis-NIR Analysis of AuNPs

Particles were characterized by ultraviolet-visible-near infrared (UV-vis-NIR) absorption spectroscopy using a Cary 5000 spectrophotometer (Agilent, Inc.). Spectra were baseline corrected with respect to the spectrum of water. In order to obtain each spectrum, the AuNP solution was diluted by 1/3 with pure water.

3.2.4 TEM Analysis of AuNPs for Size Determination

An aliquot from the final AuNP solution was diluted 1/5 with water prior to drop casting onto a Formvar-coated copper transmission electron microscopy (TEM) grid (Ted Pella, Inc.). Samples were allowed to air dry and then dried under vacuum before characterization using an FEI Morgagni TEM at 80 kV. The size distributions of the AuNPs were determined from TEM images of at least 200 AuNPs from various areas of the grid. ImageJ 1.47d (National Institutes of Health, USA) was used to measure and count all particles.

3.2.5 Initial Ligand Exchange of Citrate-capped AuNPs

Prior to use, as-synthesized AuNPs were filtered using a polyvinylidene fluoride (PVDF) filter membrane with a pore size of 0.45 μm (25 mm GD/XP disposable filters, Whatman, Inc). Immediately after filtration, the AuNPs were concentrated by separating 1 mL aliquots into 1.5 mL centrifuge tubes and centrifuging the reaction mixture at 20,000 rcf for 5 minutes (Eppendorf 5424 centrifuge). The supernatant was removed, and another 1 mL aliquot of filtered particles was added. The pellet was resuspended, and the process was repeated until 3 mL of filtered particles were concentrated to a pellet in centrifuge tubes. For thiolated PEG ligands, the resulting pellet was resuspended in 50 μL of 5 mM PEGSH (or biotinPEGSH) and 950 μL of water. This mixture was then placed on a temperature-controlled mixer (Eppendorf R Thermomixer) for 4 hours at 1,000 rpm and 25 $^{\circ}\text{C}$. After 4 hours, the particles were washed twice. Here, washing indicates centrifuging the sample and removing all supernatant followed by resuspension in water. After the second washing cycle, the particles were resuspended in a mixture of 990 μL of water and 10 μL of phosphate buffer (100 mM, pH 10) and placed on a temperature-controlled mixer overnight at 1,000 rpm and 25 $^{\circ}\text{C}$. After this time, the particles were washed with phosphate buffer twice, followed by two washes in water and two washes in D_2O . After the last wash cycle, the supernatant was removed to yield a concentrated pellet of PEGSH- or biotinPEGSH-capped AuNPs. An identical procedure was followed for ligand exchanges with MHA, MOA, MUA, or MUPA using 250 μL of the desired thiolated ligand solution (1 mM) and 750 μL of water.

To introduce aminated ligands to citrate-terminated NPs, the citrate-capped, concentrated pellet was resuspended in 50 μL of 5 mM PEGNH₂, 50 μL of 0.1 M NaOH, and 900 μL of water. This mixture was then placed on a temperature-controlled mixer for 4 hours at 1,000 rpm and 25

°C. After this time, the particles were washed with the NaOH solution twice, followed by a wash in water and in D₂O. After the last wash cycle, the supernatant was removed to yield a concentrated pellet of PEGNH₂-capped AuNPs. An identical procedure was followed for ligand exchanges with AHA, AOA, or AUA using 250 µL of the desired ligand solution (1 mM), 50 µL of NaOH (0.1 M), and 700 µL of water. *N.B.* 0.1 M NaOH is used with all aminated ligands instead of phosphate buffer (which is used for the thiolated ligands) in order to maintain a deprotonated amine. The pH of the NP solution with NaOH upon aminated ligand addition is 12.

3.2.6 Backfilling of PEGSH-capped AuNPs with a Second Thiolated Ligand

A freshly washed, concentrated pellet of PEGSH-capped particles (whose synthesis is outlined above) was resuspended in 250 µL of the new thiolated ligand (1 mM of either MUA, MOA, MHA, or AUT) and 750 µL of water. The resulting mixture was placed on a temperature-controlled mixer for 4 hours at 1,000 rpm and 25 °C. Immediately after 4 hours, the particles were washed twice with water. After the second wash cycle, the particles were resuspended in a mixture of 990 µL of water and 10 µL of phosphate buffer (100 mM, pH 10). This mixture was placed on a temperature-controlled mixer overnight at 1,000 rpm and 25 °C. After this time, the particle conjugates were washed with phosphate buffer twice, followed by two washes in water and two washes in D₂O. After the final wash cycle, the supernatant was removed to yield the concentrated pellet. An identical procedure was followed for backfilling with biotinPEGSH, resuspending the PEGSH-capped particles in 50 µL of 5 mM biotinPEGSH and 950 µL of water.

3.2.7 Backfilling of PEGNH₂-capped AuNPs with a Second Aminated Ligand

Starting from the freshly washed, concentrated pellet of PEGNH₂-capped particles, whose synthesis is outlined above, the pellet was resuspended in 250 μ L of the new aminated ligand (1 mM of either AUA, AOA, or AHA), 50 μ L of 0.1 M NaOH, and 700 μ L of water. The resulting mixture was placed on a temperature-controlled mixer for 4 hours at 1,000 rpm and 25 °C. After this time, the particles were washed with phosphate buffer twice, followed by a wash in water and a wash in D₂O. After the final wash cycle, the supernatant was removed to yield the concentrated pellet.

3.2.8 Backfilling of Mercaptoalkanoic Acid-capped Particles with PEGSH

Starting from the freshly washed, concentrated pellet of MUA-, MOA-, or MHA-capped particles, whose synthesis is outlined above, the pellet was resuspended in 50 μ L of 5 mM PEGSH and 950 μ L of water. The resulting mixture was placed on a temperature-controlled mixer for 4 hours at 1,000 rpm and 25 °C. Immediately after these 4 hours, the particles were washed twice with water. After the second washing cycle, the particles were resuspended in a mixture of 990 μ L of water and 10 μ L of phosphate buffer (100 mM, pH 10). This mixture was placed on a temperature-controlled mixer overnight at 1,000 rpm and 25 °C. After this time, the particles were washed with the phosphate buffer twice, followed by two washes in water and two washes in D₂O. After the final wash cycle, the supernatant was removed to yield the concentrated pellet.

3.2.9 Backfilling of Aminoalkanoic Acid-capped Particles with PEGNH₂

Starting from a freshly washed, concentrated pellet of AUA-, AOA-, or AHA-capped particles, whose synthesis is outlined above, the pellet was resuspended in 50 μL of 5 mM PEGNH₂, 50 μL of 0.1 M NaOH, and 900 μL of water. The resulting mixture was placed on a temperature-controlled mixer for 4 hours at 1,000 rpm and 25 °C. After this time, the particles were washed with the 0.1 M NaOH solution twice, followed by a wash in water and a wash in D₂O. After the final wash cycle, the supernatant was removed to yield the concentrated pellet.

3.2.10 Backfilling of MUA-capped Particles with MUPA and MUPA-capped Particles with MUA

Starting from the freshly washed, concentrated pellet of MUA-capped particles, whose synthesis is outlined above, the MUA-capped pellet was resuspended in 250 μL MUPA and 750 μL of water. The resulting mixture was placed on a temperature-controlled mixer for 4 hours at 1,000 rpm and 25 °C. Immediately after these 4 hours, the particles were washed twice with water. After the second washing cycle, the particles were resuspended in a mixture of 990 μL of water and 10 μL of phosphate buffer (100 mM, pH 10). This mixture was placed on a temperature-controlled mixer overnight at 1,000 rpm and 25 °C. After this time, the particles were washed with the phosphate buffer twice, followed by two washes in water and two washes in D₂O. After the final wash cycle, the supernatant was removed to yield the concentrated pellet. An identical procedure was followed for MUPA-capped particles backfilled with MUA.

3.2.11 Co-loading of Ligands on AuNPs

The resulting citrate-capped concentrated pellet described above was resuspended in either thiolated or aminated ligand mixtures. For thiol-capped particles, the resulting pellet was resuspended in 750 μL of water. To this solution, a mixture of 2 ligands was added: either 125 μL each of any combination of MUPA, MUA, MOA, or MHA or 25 μL of PEGSH and 125 μL any one of the previously listed five ligands. This mixture was then placed on a temperature-controlled mixer for 4 hours at 1,000 rpm and 25 $^{\circ}\text{C}$. After 4 hours, the particles were washed twice. After the second washing cycle, the particles were resuspended in a mixture of 990 μL of water and 10 μL of phosphate buffer (100 mM, pH 10) and placed on a temperature-controlled mixer overnight at 1,000 rpm and 25 $^{\circ}\text{C}$. After this time, the particles were washed with phosphate buffer twice, followed by two washes in water and two washes in D_2O . After the last wash cycle, the supernatant was removed to yield a concentrated pellet of co-loaded AuNPs.

For amine-capped particles, the resulting pellet was resuspended in 700 μL of water and 50 μL of 0.1 M NaOH. To this solution, a mixture of 2 ligands was added: either 125 μL each of any combination of AUA, AOA, and AHA or 25 μL of PEGNH₂ and 125 μL of either AUA or AOA. This mixture was then placed on a temperature-controlled mixer for 4 hours at 1,000 rpm and 25 $^{\circ}\text{C}$. After this time, the particles were washed with 0.1 M NaOH twice, followed by a wash in water and a wash in D_2O . After the last wash cycle, the supernatant was removed to yield a concentrated pellet of co-loaded AuNPs.

3.2.12 ICP-MS Analysis

Inductively coupled plasma mass spectrometry (ICP-MS) analysis was performed using an argon flow with a NexION spectrometer (PerkinElmer, Inc.). An aqua regia solution was prepared with a 3:1 ratio of hydrochloric acid (Sigma-Aldrich, > 99.999% trace metal basis): nitric acid (Sigma-Aldrich, > 99.999% trace metal basis) and diluted with water for a 5% (by volume) aqua regia matrix. AuNP samples were taken from the concentrated pellet after ligand exchange as described above and digested overnight in ~5 μL of fresh and concentrated aqua regia solution. From the digested solution, 1 μL was further diluted to 15 mL using 5% aqua regia matrix, and the remainder of the digest was reserved for ^1H -NMR analysis (*vide infra*). Unknown Au concentrations were determined by comparison to a 5-point standard curve with a range of 1 - 30 ppb (1, 5, 10, 20, and 30 ppb prepared by volume) from a gold standard for ICP (Fluka, TraceCERT 1,001 \pm 2 mg/L Au in HCl) diluted in the 5% aqua regia matrix. All standards were measured 5 times and averaged, while all unknown samples were measured in triplicate and averaged. A 5 minute flush time with 5% aqua regia matrix was used between all runs, and a blank was analyzed before each unknown sample to confirm removal of all residual metals from the instrument.

3.2.13 ^1H NMR Analysis

All NMR measurements were performed on a Bruker 400 Ultrashield™ magnet with an AVANCE III 400 Console or a Bruker 600 Ultrashield™ magnet with an AVANCE III 600 Console (Bruker Biospin, Billerica, MA) at 298 K. For all experiments, a minimum recycle delay of 5 seconds was used, which was sufficiently greater than T_1 . NMR samples were prepared as

described above by concentrating the AuNPs, followed by digestion with 1 drop (~5 μ L) of concentrated aqua regia. These samples were allowed to digest overnight before dilution with D₂O to a total volume of 600 μ L. An ACN reference was used for the determination of unknown ligand concentrations. To each sample, 5 μ L of 0.24% ACN (15 μ L of ACN in 6 mL of D₂O) was added. The unknown ligand concentrations were determined by comparison to a 5-point standard curve with a range of 1.00 – 0.10 mM ligand (1.00, 0.75, 0.50, 0.25, and 0.10 mM, prepared in D₂O). For each standard, the integral of the ligand peak was divided by the integral of the ACN peak and plotted against the known concentration of ligand. Following an internal standard approach for the unknown concentrations of ligand on the AuNP,¹⁸² the ligand peak was integrated and similarly divided by the known integrated ACN peak to yield the concentration upon comparison with the calibration curve.

3.3 RESULTS AND DISCUSSION

For a given AuNP, we hypothesize that the method of ligand loading and the initial molar ratios of the added ligands will impact the final composition of the ligand shell. We expect that the ligand loading trends will also be influenced by the ligand binding moiety and ligand intermolecular regions. When co-loading or backfilling two ligands of similar affinity for the Au surface, such as two thiolated ligands or two aminated ligands, it remains unclear what factors (i.e. ligand moiety binding strength to the AuNP, initial molar ratios of the ligands, etc.) determine whether or not stoichiometric loading is observed in the final ligand shell architecture.

In order to probe how variations in ligand identity (i.e. intermolecular region, binding moiety, and terminal functional group) influence the composition of the ligand shell, we examine

both ligand loading methods (co-loading and backfilling) to produce mixed ligand shells on 13 nm AuNPs (Figure 29). In both cases, the weakly bound citrate ligand is fully displaced by the incoming ligands, regardless of binding moiety (e.g. thiol or amine). However, upon addition of a second thiolated or aminated ligand with relatively equal affinity for the AuNP surface (based on the ligand's binding functionality), both ligands will be present to some extent in the ligand shell. With the backfilling method, ligand exchange proceeds sequentially in two steps, where the first thiolated or aminated ligand is added to the citrate-capped AuNPs and allowed to exchange. After 4 hours, the second thiolated or aminated ligand is added to the particles that are capped with the first ligand, and this mixture is allowed to react for 4 hours to form the final AuNP ligand shell that is subsequently purified. Meanwhile with the co-loading method, the mixed ligand shell is formed by adding the two pre-mixed thiolated or aminated ligands to the citrate-capped AuNPs concurrently. This mixture is allowed to sit for 4 hours before purification. (*N.B.* As we demonstrated above,⁵⁴ 4 hours is sufficient time for the thiolated ligand shell to reach a steady state, where no significant change is observed in the number of ligands. Amine time studies confirm 4 hours is sufficient for these ligands as well (Figure 30).) For comparison, ligand exchanges were also performed with mixtures of thiolated and aminated ligands, which do not have relatively equal affinities for the AuNP surface; in all cases the thiolated ligand dominated the ligand shell population across all loading methods (Figure 31). Representative ¹H NMR spectra and further particle characterization after ligand exchange are shown in Appendix B.

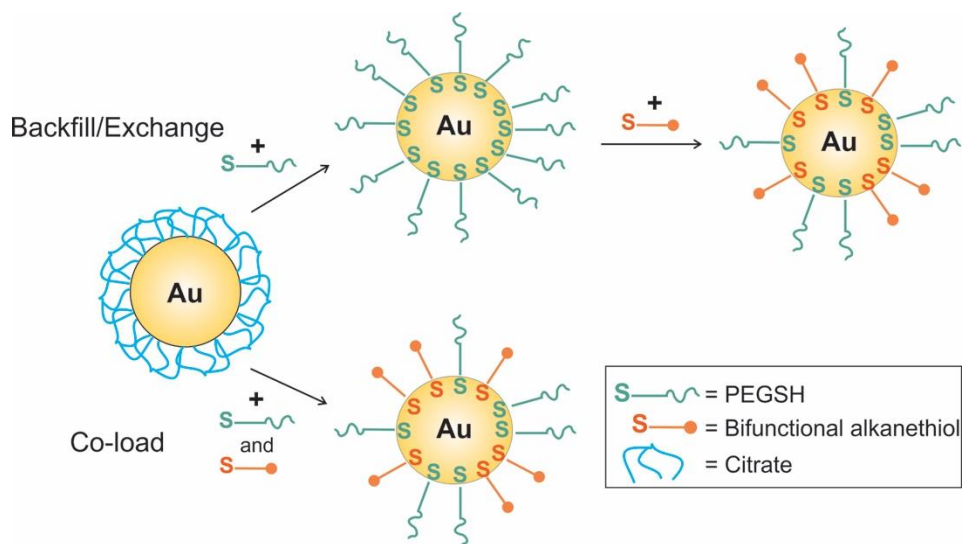


Figure 29. Scheme depicting the two types of ligand addition used in this study to form mixed thiolated ligand shells on AuNPs. An analogous process is used to form aminated mixed ligand shells.

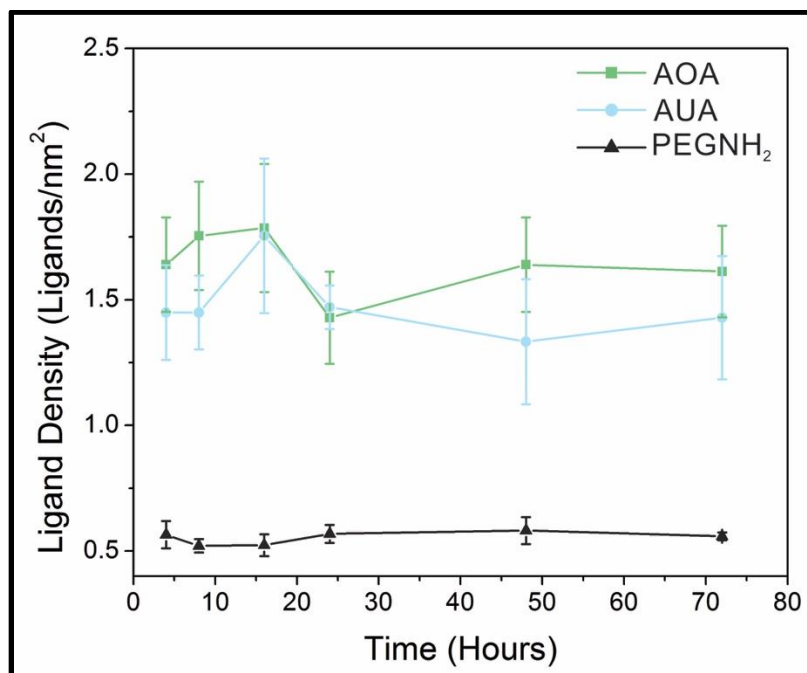


Figure 30. Plot of PEGNH₂ (gray triangles), AUA (blue circles), and AOA (green squares) densities on the NP surface as a function of AuNP incubation time in presence of the aminated ligand for 13 nm AuNPs where the error bars represent standard error of at least 5 trials. Results indicate that ligand loading is consistent for all the time points studied after 4 hours.

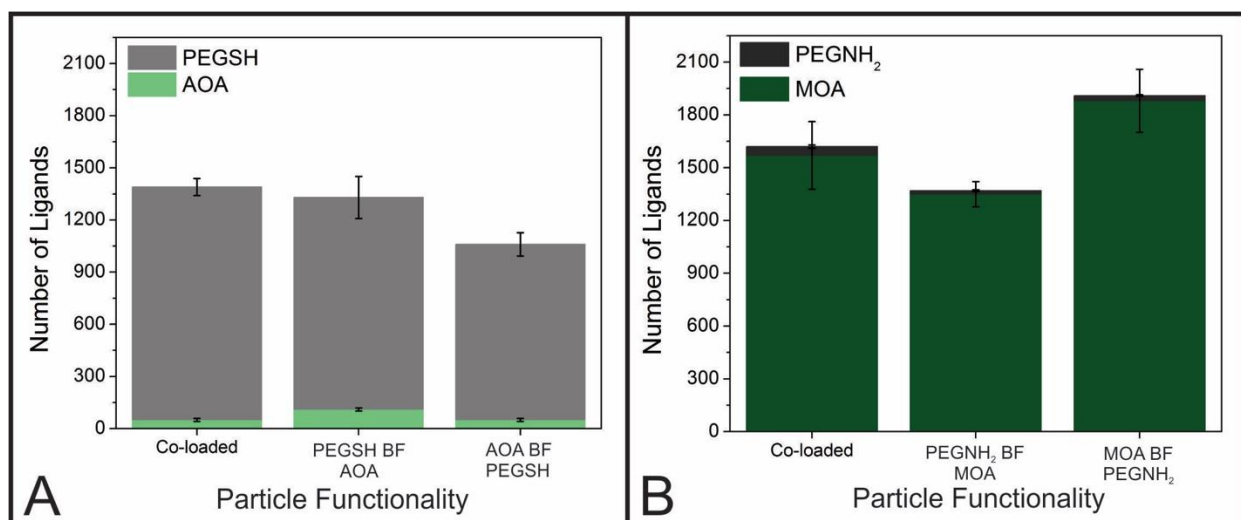


Figure 31. Comparison of the ligand loading values for PEGSH with AOA (A) and PEGNH₂ with MOA (B) for 13 nm AuNPs. In both cases of combining a short chain amine with a longer thiol and combining a short chain thiol with a longer amine, the thiol dominates the ligand shell in all three systems of backfilling and co-loading.

3.3.1 Quantification of Thiolated Mixed Ligand Shells

For a ligand shell comprised of a single ligand (*vide supra*), it is of interest to understand the extent of exchange when a second ligand with the same NP binding moiety is added to the system. Here, we investigated the result of this addition using PEGSH-, MUA-, and MOA-functionalized AuNPs. See Appendix B for additional AuNP characterization after ligand exchange.

First, PEGSH-functionalized AuNPs were incubated with AUT, MUA, MOA, or MPA. Trials were conducted to confirm that the incubation time of the AuNPs in the secondary ligand was sufficient to obtain consistent ligand shell compositions (Appendix B). These secondary thiolated ligands were used to investigate the effect of intermolecular region as well as terminal functional group on exchange with the existing AuNP ligand shell. Interestingly, for all of the small molecule ligands tested (AUT, MUA, MOA, and MPA) significant but not complete

displacement of the existing PEGSH shell is observed for AuNPs of both 13 and 30 nm (Figure 32), and the total number of ligands appended to the AuNP increases. This pattern of displacement suggests that since the existing PEGSH monolayer is has a low number of ligands it can be significantly altered by the addition of a small molecule ligand which can take advantage of this loosely packed monolayer.^{56, 207}

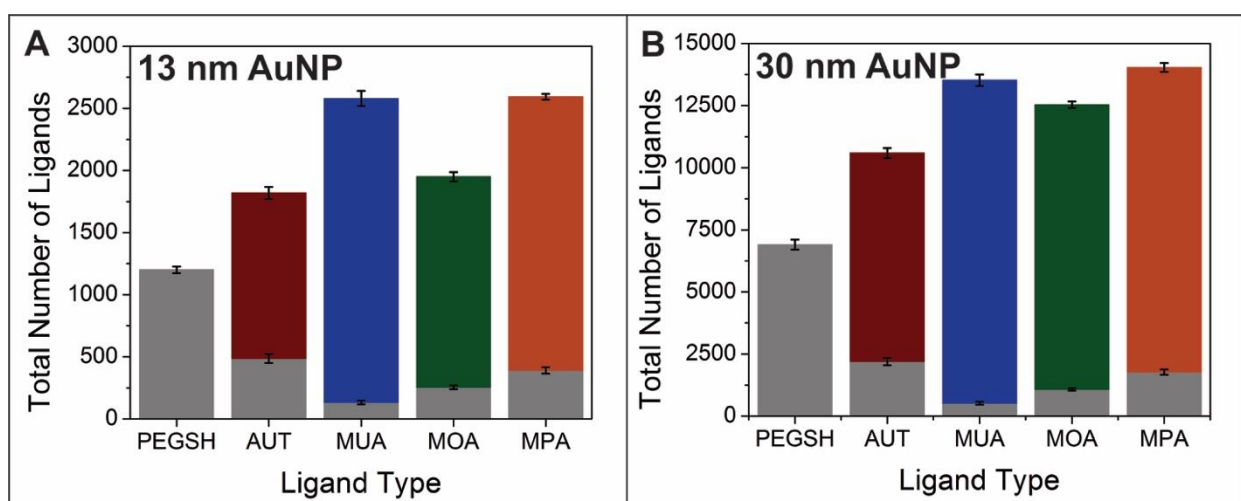


Figure 32. Comparison of the amount of PEGSH displaced upon secondary ligand exchange with a smaller thiolated ligand of various chain lengths and terminal functional groups, where error bars represent standard error for at least 20 trials. Gray = PEGSH, burgundy = AUT, blue = MUA, green = MOA, and peach = MPA.

Smaller incoming ligands may be expected to more easily take advantage of defects or unpassivated sites in the existing monolayer and add more extensively. However, MUA, with the longest carbon chain tested, yields the highest number of additional ligands and exhibits the highest exchange efficiencies of the 4 ligands tested (92% and 95% for the 13 and 30 nm AuNPs, respectively). These high exchange efficiencies are consistent with a cooperative binding mechanism, where the interligand interactions play a large role in determining the composition

of the ligand shell. The terminal functional group of the ligand may also influence exchange with the PEGSH layer, as the 11 carbon chain, carboxylic acid-terminated MUA adds in significantly higher numbers than the 11 carbon chain, amine-terminated AUT (> 90% exchange efficiency for MUA vs. ~70% exchange efficiency for AUT), which also has an 11 carbon chain but contains a terminal amine.

3.3.2 Influence of Existing Thiolated Ligand Shell on Ligand Exchange Efficiency

We compared exchange mechanisms observed for the loosely packed PEGSH-functionalized AuNPs with those observed for densely packed monolayers with MUA- and MOA-functionalized AuNPs (Figure 33). In the case of MUA- and MOA-functionalized AuNPs, exposure to PEGSH produced little to no modification in the total number of ligands present on the particle surface, and very few PEGSH ligands are added (less than 2% exchange efficiency for both AuNP sizes functionalized by either MUA or MOA). These results indicate that almost none of the original small molecule ligand is displaced. This low displacement is consistent with a limited backfill mechanism in which the PEGSH adds only to unpassivated or monolayer defect sites in the existing MUA or MOA shell and further that there is not rapid exchange of the existing ligand shell with the surrounding medium.

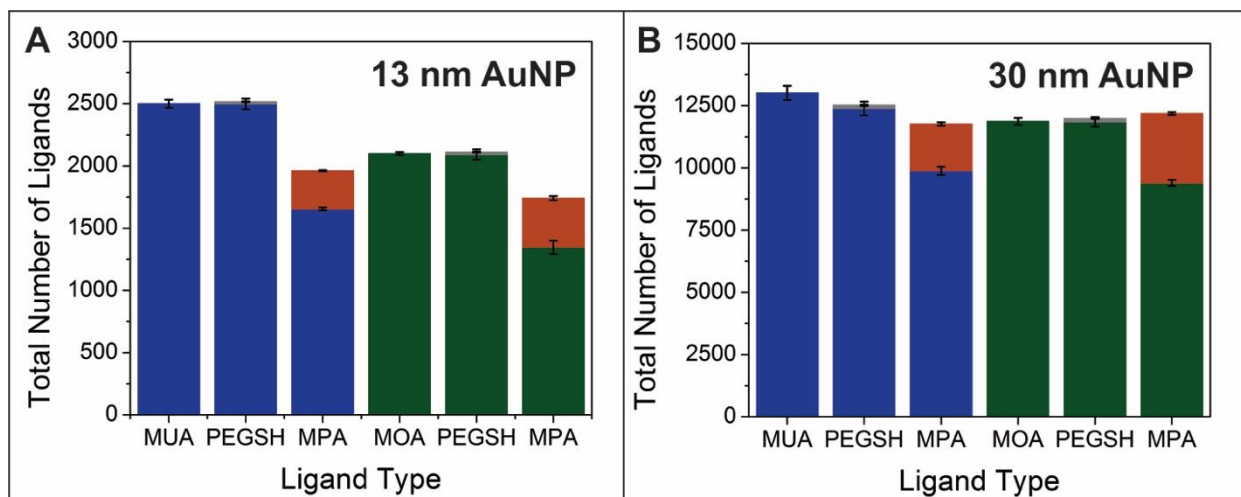


Figure 33. Comparison of the amount of MUA or MOA displaced upon secondary ligand addition with either PEGSH or MPA, where error bars represent standard error for at least 15 trials. The first bar in each series represents the homogeneous ligand shell of MUA (blue bar) or MOA (green bar). Blue = MUA, green = MOA, peach = MPA, and gray = PEGSH (same color scheme as in Figure 32).

The lack of PEGSH addition is likely a combination of a dense initial ligand shell with the mercaptoalkanoic acid (MAA) SAMs and the significantly longer chain length of the incoming ligand. For example, the PEGSH may be too large to take advantage of some smaller monolayer defect sites, even when they occur.²⁰ Meanwhile, the 3 carbon chain MPA is more likely to have steric accessibility to these AuNP surface sites, and in addition, does displace some of the existing ligand from the NP surface (16% with the MUA shell and 23% with the MOA shell for both particle sizes). However, in both cases the total particle ligand loading decreases and suggests that although MPA is able to either exchange with the mercaptoalkanoic acid SAMs or bind in SAM defect sites (to a moderate degree), a resulting MPA-containing layer is less dense than the other MAAs studied.

These studies indicate that the two primary routes of ligand addition to an existing ligand monolayer, ligand shell exchange or ligand shell “backfilling” (Figure 34), are strongly dependent on the identity of the existing ligand shell. Importantly, this identity includes not only the ligand binding moiety (i.e. the thiol group) but also the intermolecular interactions between the ligands themselves. It is also important to note that the two addition pathways are not mutually exclusive and may occur to differing extents within the same system (e.g. addition of MPA to MUA- and MOA-capped AuNPs). With this information, we can begin to build design parameters. For instance, with a loosely-packed PEGSH ligand shell, an exchange mechanism is predominantly observed, with the number of PEGSH ligands significantly decreasing as the new thiolated ligands add to the AuNP surface. On the other hand, denser SAMs of MAAs exhibit little exchange with either larger or smaller molecules.

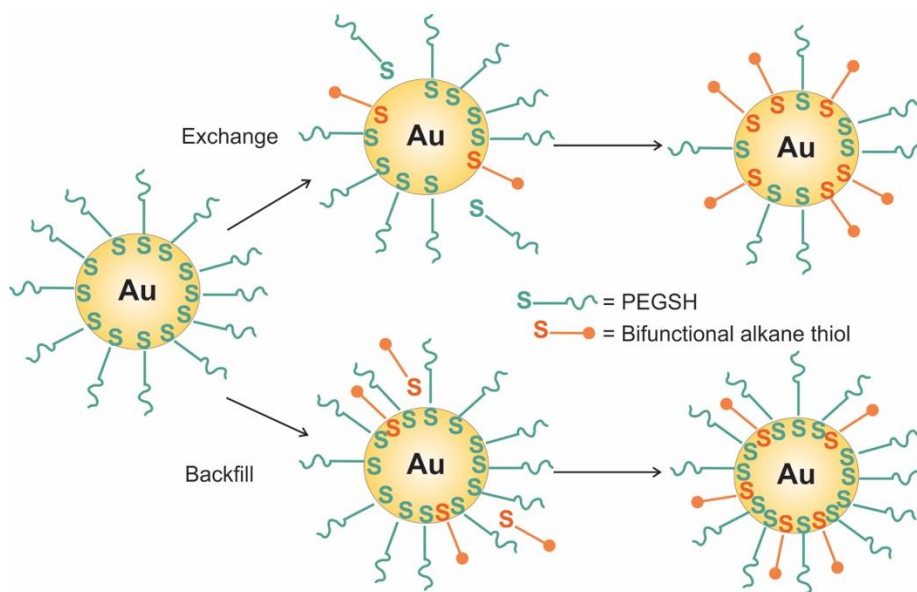


Figure 34. Scheme depicting two possible pathways of secondary ligand addition.

3.3.3 Co-loading of Thiolated and Aminated Ligands on AuNPs

To further elucidate correlations between ligand loading method and ligand chemical properties, thiolated mixed ligand shells were also formed by co-loading with a variety of MAAs and PEGSH on 13 nm AuNPs (Figure 35). Here, the ligand binding moiety and terminal functionality are held constant while only varying the intermolecular region. At all of the studied MUA:PEGSH, MOA:PEGSH, and MHA:PEGSH ratios, the MAA tends to dominate the ligand shell, adding in numbers higher than those that would reflect the initial ratios. The smallest deviations from 1:1 incorporation are observed at the highest (i.e. 90:10) and lowest ratios (i.e. 10:90) of MAA addition, with the larger deviations occurring in the middle regions (i.e. 50:50). In this system, all of the thiol ligands have a high and relatively comparable affinity for the AuNP surface. Due to this similar affinity for the AuNP surface, the intermolecular interactions between the ligands are likely playing a dominant role in the final ligand shell stoichiometry.

As stated above, at all of the ratios where the ligands have a strong affinity for the AuNP surface, significant deviations from 1:1 loading are observed, and interligand interactions appear to play a key role in these deviations. To probe the role of these interligand forces in the formation of the co-loaded ligand shell, we moved to a ligand system with weaker affinity for the AuNP surface, varying the binding moiety but working within the same family of ligands. Aminated ligands are ideal for this situation, as they adsorb to the AuNP to form stable particles but are bound more weakly than the thiolated ligands.^{208, 209} Using a similar approach to the thiolated system, aminated mixed ligand shells were formed by co-loading with a variety of aminoalkanoic acids (AAA) and PEGNH₂ on 13 nm AuNPs (Figure 36).

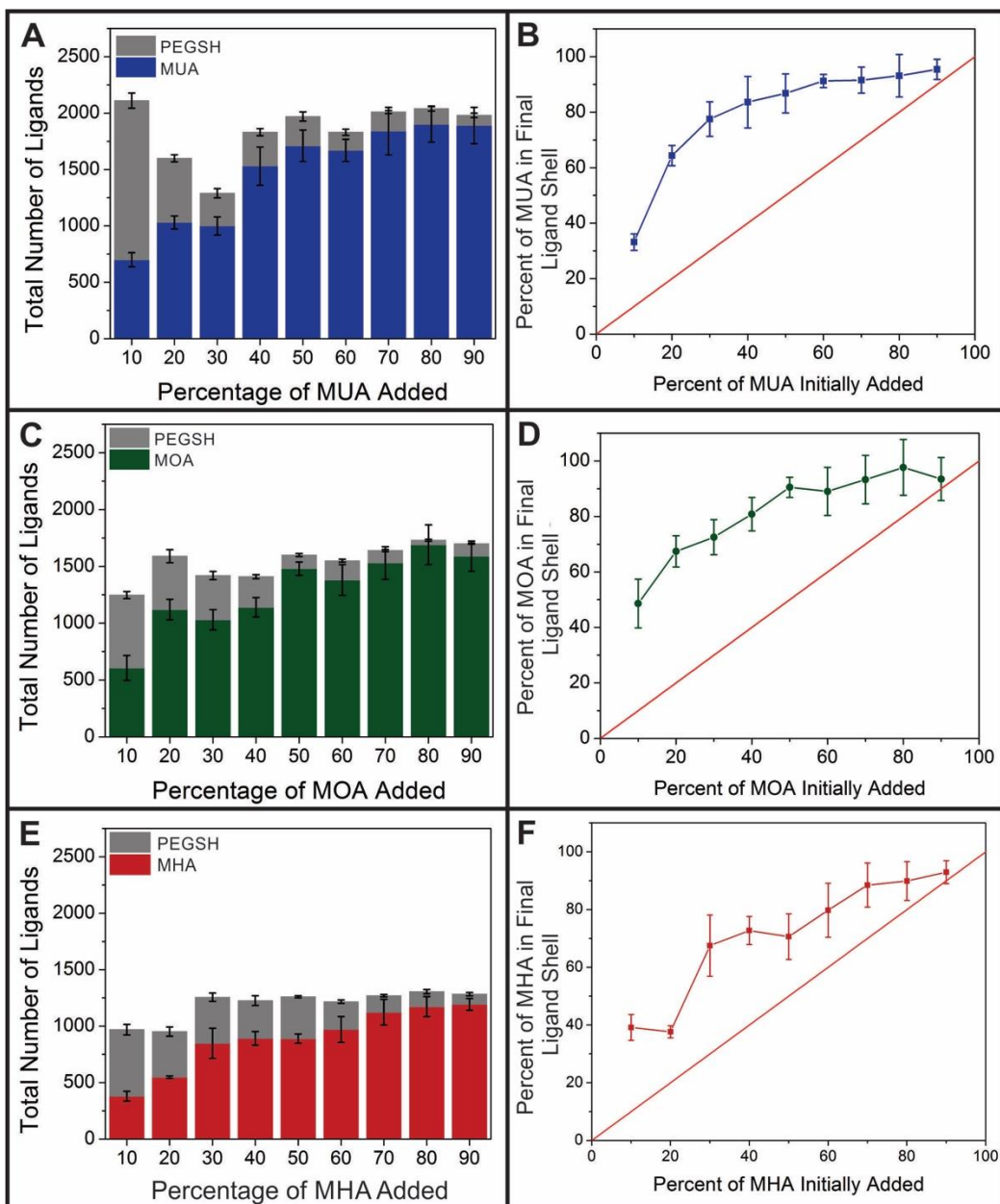


Figure 35. Comparison of the percent loadings of MUA (A, B), MOA (C, D), or MHA (E, F) in the final ligand shell when co-loaded with PEGSH, where error bars represent the standard error of at least 5 trials.

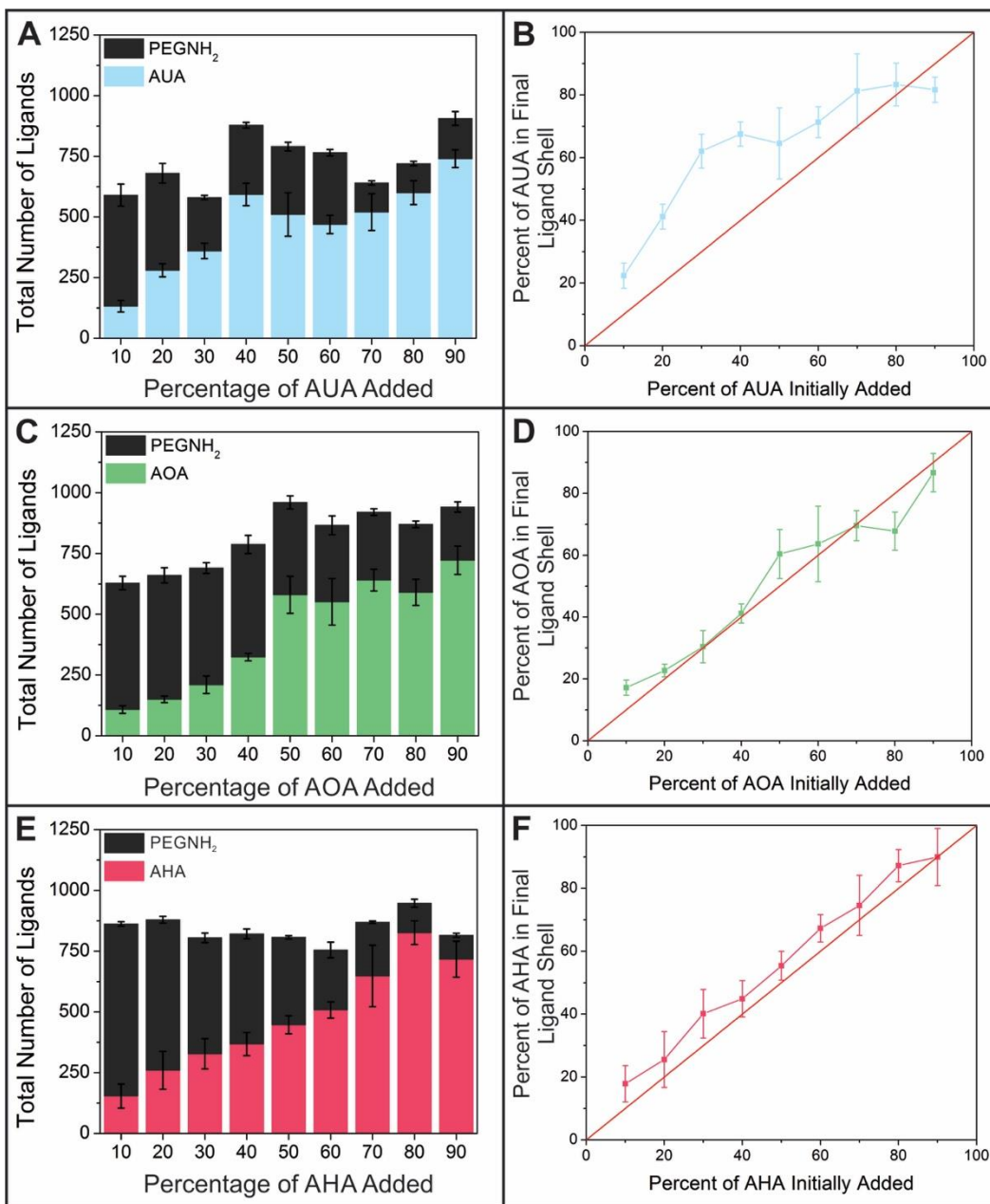


Figure 36. Comparison of the percent loadings of AUA (A, B), AOA (C, D), or AHA (E, F) in the final ligand shell when co-loaded with PEGNH₂, where error bars represent the standard error of at least 5 trials.

Unlike in the case of MAAs, where significant deviations from the initial ratio were observed, the aminated ligands load in quantities that closely reflect the initial molar ratio. These results suggest that a key factor in obtaining ligand shell compositions that reflect the initial stoichiometry of ligands added is the magnitude of the ligand affinity for the particle surface. Specifically, our observations indicate that stoichiometric loading can be achieved in co-loaded ligand shells when the ligands have a relatively weak affinity (i.e. aminated ligands) to the AuNP surface compared with thiolated compounds. On the other hand, non-stoichiometric loading that does not agree with the initially added ratio will be observed when the ligands exhibit a strong affinity for the particle surface, and especially when they also have strong intermolecular interactions, as in the case of the thiolated ligands studied here. However, it is important to note that as ligand chain lengths are increased (i.e. as is the case for AUA), deviation from a 1:1 incorporation behavior is observed compared to shorter chain ligands, indicating that after a certain chain length ($C \geq 11$) the additive effect of inter-ligand interactions begins to play a role in amine addition to AuNP surfaces. Even for shorter ligands, such as the MHA with less availability for intermolecular interactions (~ 1.6 kJ/mol per methylene-methylene interaction),²¹⁰ the strongly binding thiol group prevents stoichiometric loading and allows the MAA to dominate the ligand shell.

3.3.4 Backfilling of Thiolated and Aminated Ligands on AuNPs

As we have demonstrated in previous work,⁵⁴ for single ligand loading, both MUA and MOA form dense shells on the surface of AuNPs possibly via cooperative binding mechanisms. In contrast, PEGSH and MHA load onto the particle in much smaller final numbers. For comparison with the 50:50 co-loading method, two different variations were observed with the

three MAAs backfilled with PEGSH as well as PEGSH backfilled with each MAA. Consistently, the mixed-moiety ligand shells present different final compositions based on ligand loading method (Figure 37). For MAA ligands under back-filling conditions, as the ligand chain length decreases, the amount of PEGSH added to the mixed ligand shell on the AuNP increases. MUA shows the highest loading across all trials, followed by the MOA. In all backfilling cases, like with all co-loading compositions, the MAA dominates the ligand shell, with very little PEGSH found in the final ligand shell composition.

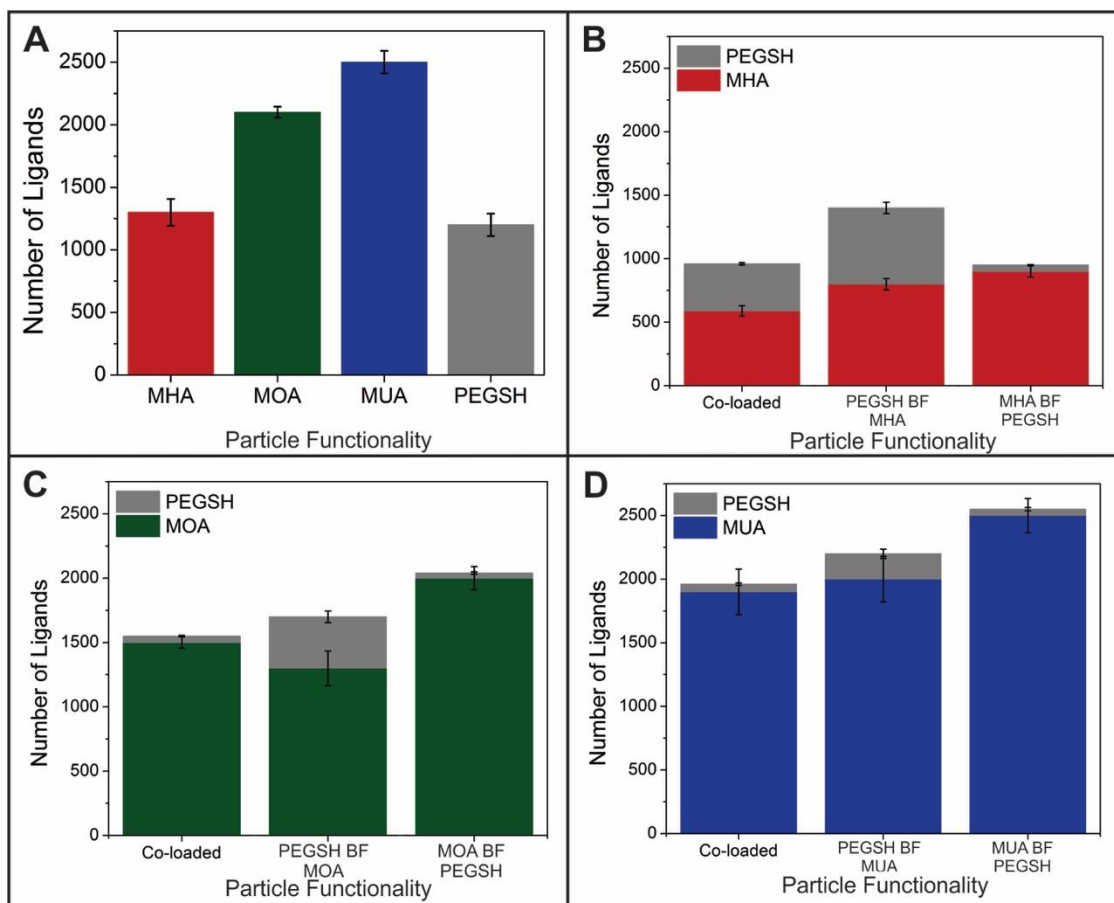


Figure 37. Comparison of single ligand loading of PEGSH and various MAAs (A) and of ligand loading when co-loading at a 50:50 ratio of PEGSH with a MAA, MAAs backfilled with PEGSH, and PEGSH backfilled with each MAA (B-D), where error bars represent standard error of at least five trials.

Conversely, when aminated analogues of the MAAs are used (i.e. AAAs) (Figure 38), we find that AAAs load in statistically similar numbers to each other. Likewise, similar to PEGSH, PEGNH₂ adds with the lowest overall amount of ligands. Despite this similar overall trend where AAAs load with higher numbers than the PEGNH₂, the amine ligands tend to add in much smaller numbers than their thiolated analogues (i.e. $\sim 2,500 \pm 100$ vs. $\sim 780 \pm 50$ for the C = 11 ligands). Similar to the co-loading trends, this discrepancy can likely be attributed to differences in binding affinity of thiols vs. amines to the Au surface.^{209, 211}

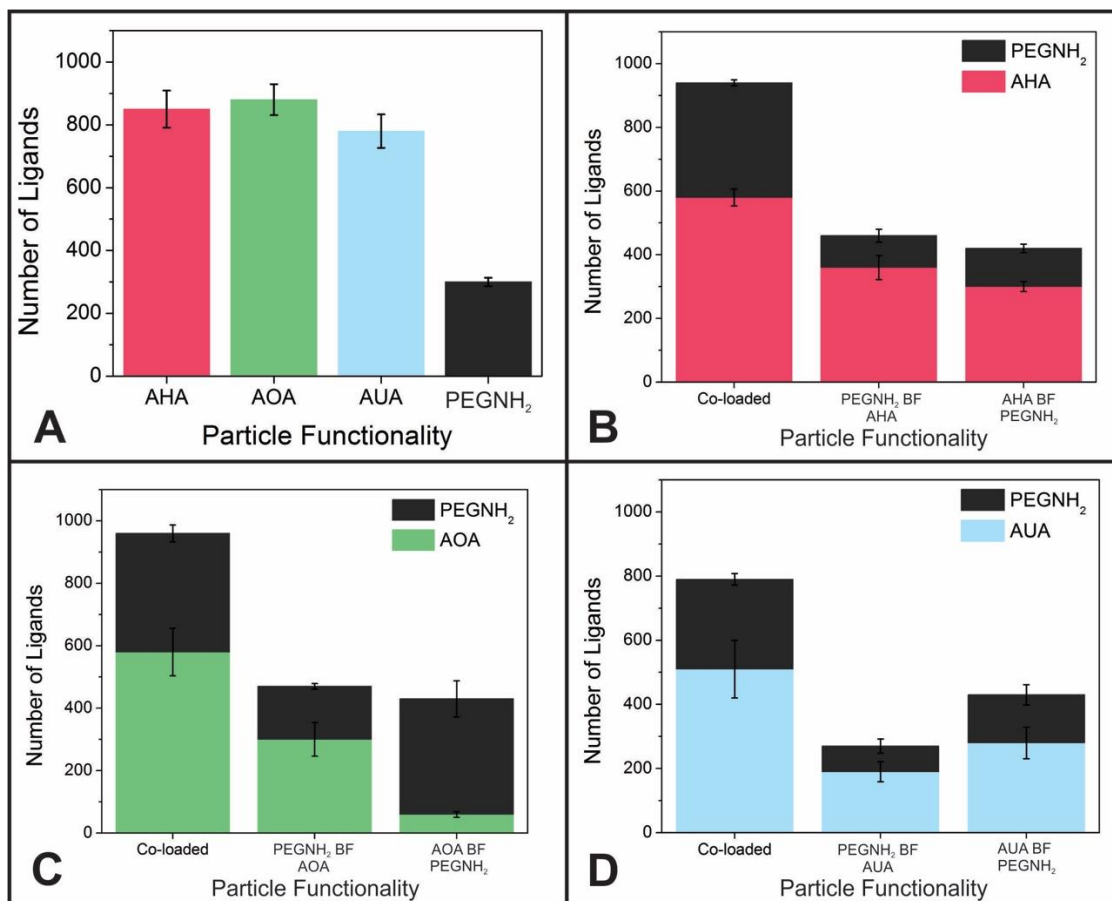


Figure 38. Comparison of single ligand loading of PEGNH₂ and the AAAs (A), and of ligand loading when co-loading at a 50:50 ratio of PEGNH₂ with each AAA, AAAs backfilled with PEGNH₂, and PEGNH₂ backfilled with each AAA (B-D), where error bars represent standard error of at least five trials.

For comparison purposes, the aminated backfilling cases are again presented alongside the 50:50 co-loading results. In the backfilling cases, two variations in the loading method were studied: AAA backfilled with PEGNH₂ and PEGNH₂ backfilled with AAA (Figure 38B-D). Again, the mixed-moiety ligand shells exhibit different final compositions based on the ligand loading method in all cases. In the samples with PEGNH₂ backfilled with the AAAs, similar results to the MAAs are observed, where the AAA dominates the ligands shell. However, for the AAAs backfilled with PEGNH₂, additional incorporation of the incoming PEGNH₂ ligand is observed, indicating that the AAA layers on the AuNP surface are less dense or more easily displaced compared to the monolayers formed with the analogous MAAs. For the aminated ligands, where the binding moieties have a lower affinity for the Au surfaces than thiols, the larger equilibrium disassociation constant likely facilitates ligand loading composition to be closer to the initially added ligand molar ratios. Only when using molecules with longer chain lengths (AUA, C = 11) do intermolecular interactions begin to play a role in ligand loading, manifesting as an AAA-rich ligand shell composition. In terms of design rules, the final ligand loading that closely reflects the initially added ligand ratios suggests that ligands with a weaker affinity for the AuNP yield final ligand shells may be able to overcome limitations imposed by strong intermolecular interactions (although not completely) and more closely reflect the initial molar ratio introduced.

3.3.5 Examining the Factors that Dictate Final Ligand Shell Composition

Ultimately, these studies are an important foundation for understanding and predicting which intrinsic and extrinsic factors will influence the final composition of a NP ligand shell. For example, we consider the relative influence of incoming ligand structure versus the chemical

structure of the ligand initially present on the AuNP surface. In order to probe that question, ligand exchanges were performed with two sets of similar thiolated ligands which share both a binding moiety and the same intermolecular region. The ligands compared in these experiments differ only in their terminal functionality (Figure 39). The first set included MUA and its phosphoric acid analogue (MUPA), where both ligands exhibited a thiol binding moiety and a chain length of 11 carbons. The second set was composed of methyl-terminated PEGSH (PEGSH) and biotin-terminated PEGSH (biotinPEGSH) with the same molecular weight and thiol binding moiety. By comparing ligands with similar intermolecular regions and binding groups (but that have at least one distinct ^1H NMR peak), we can distinguish if the original ligand shell or the incoming ligand more greatly influence the final ligand shell composition.

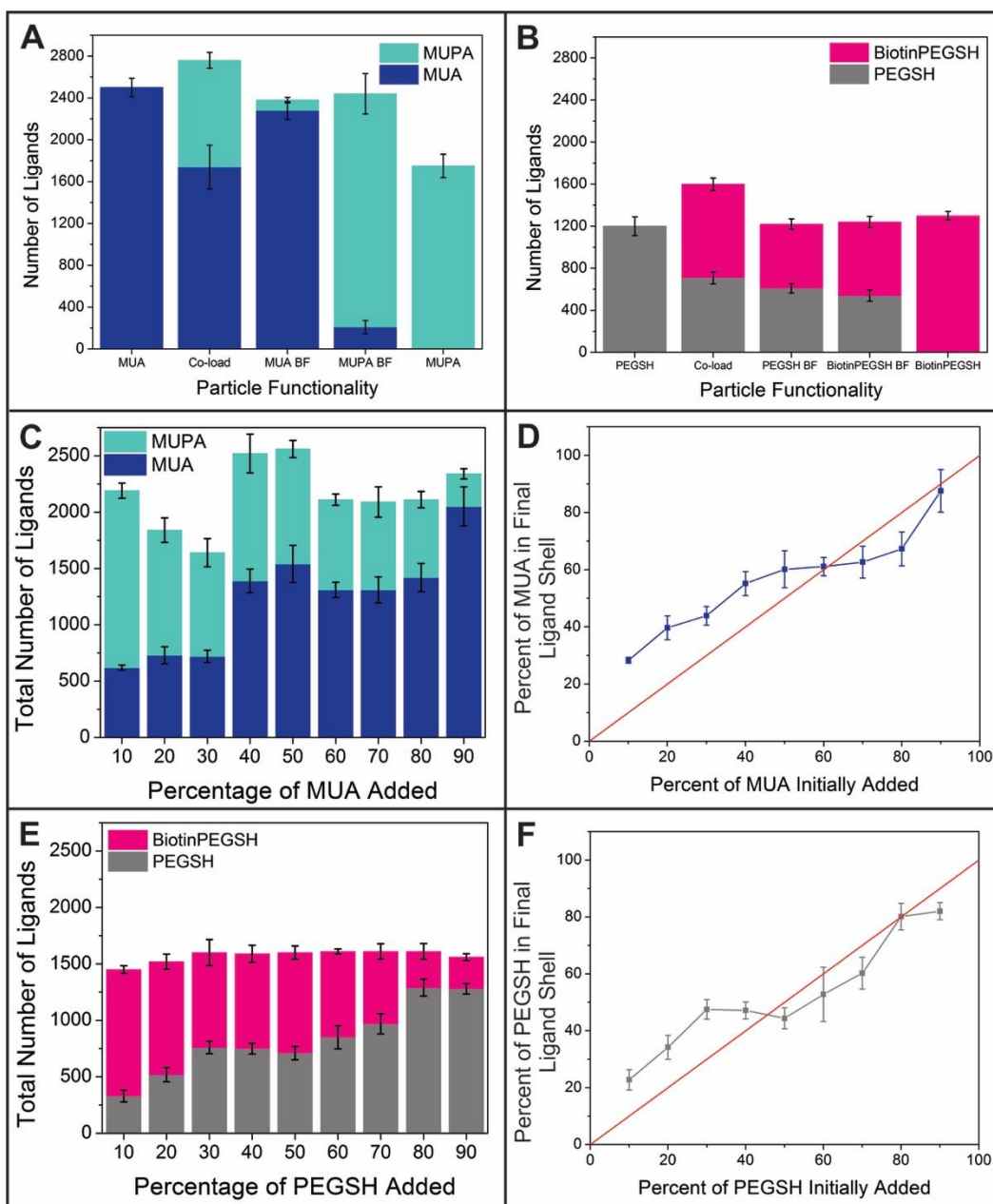


Figure 39. Comparison of similar ligand loading between two 11-carbon MAA analogues with backfilling and 50:50 co-loading (A), as well as various co-loading ratios (C, D) and two PEGSH analogues with backfilling and 50:50 co-loading (B), as well as various co-loading ratios (E, F), where the error bars represent standard error of at least five trials.

In the first set of ligands which vary only in terminal functionality, both MUA and MUPA load in high, yet statistically different, numbers when they are the only ligand on the AuNP (Figure 39A). Further, both ligands add in roughly similar numbers when co-loaded at a 50:50 ratio of MUA:MUPA. In the cases of other co-loaded ratios, the final ligand shell architecture roughly follows a 1:1 incorporation (Figure 39C-D). However, when combined with their respective counterpart, differing only in terminal functionality, the ligand added first dominates the ligand shell, and the ligand added second is present only in very small quantities. We hypothesize that this discrepancy in loading is due to the conformation of the ligand shell before the addition of the second ligand. For instance, if MUPA is added to a AuNP capped with MUA, the initial MUA shell is quite dense (4.5 ± 0.1 MUA/nm²). Therefore, few incoming MUPA ligands succeed in penetrating the existing MUA shell or finding space on the NP surface to form a bond on the particle surface. A dense MUA shell allowing only very little ligand exchange is consistent with the previous observations, where the PEGSH addition to the MUA-capped AuNPs was extremely limited.⁵⁴

Conversely, for the PEGSH ligand set (Figure 39B) the single-ligand loading is statistically the same at a 95% confidence interval for the two PEG ligands, with statistically similar loading in the co-loading case with a 50:50 ratio of PEGSH:biotinPEGSH. Examination of other co-loaded ratios reveals that the final ligand shell architecture again roughly follows a 1:1 incorporation, with a trend similar to the MUA:MUPA system (Figure 39E-F). Therefore, we conclude that when both ligands have roughly equal affinity for the AuNP and similar intermolecular regions, incorporation close to 1:1 will be achieved, even when the terminal functional group is markedly different. For the backfilled particles, both with PEGSH added to an existing biotinPEGSH ligand shell or biotin PEGSH added to an existing PEGSH ligand shell,

statistically similar (within a 95% confidence interval) loading of the two ligands is again observed in both backfilling situations. Likewise, this loading behavior can again be attributed to the conformation of the existing ligand shell on the AuNP, similar to the MUA/MUPA system. Both the PEGSH and its biotin analogue form less dense ligand shells than the MUA, allowing the incoming ligand access to the NP surface.

3.4 CONCLUSION

In conclusion, we report ligand shell compositions obtained using two common ligand loading methods (backfilling and co-loading). Using each method, we compare final ligand compositions obtained using both thiolated and aminated ligands and specifically consider the impact of ligand intermolecular region, binding moiety, and terminal functionality. Taken together, these findings suggest certain design rules for obtaining AuNP ligand shells with specific stoichiometries using these specific ligand types. For instance, in cases of backfilling for thiolated ligands, polymeric ligands that yield less densely packed ligand shells are amenable to displacement, but MAA ligands shells are not (< 2% exchange efficiency), due to the dense initial ligand packing. We observed that in all cases, co-loading or shorter ligands produce the most dense ligand shells. Additionally, the strength of the ligand head group interaction with the AuNP surface governs the stoichiometries obtained when using the co-loading functionalization method, where for thiolated ligands, which interact strongly with the AuNP surface, significant deviations from 1:1 incorporation are observed. However, when co-loading aminated ligands, stoichiometric addition is more straightforward to achieve. We expect these studies, and the emerging design rules they provide, will have important implications for using surface chemistry to enhance or expand

AuNP use in a wide variety of biomedical and electronic applications, by facilitating the synthesis of specifically tailored ligand shells for these applications.

4.0 EXPANDING LIGAND SHELL DESIGN RULES TO PHOSPHINES AND TERNARY THIOL SYSTEMS

4.1 INTRODUCTION

Gold nanoparticles (AuNPs) are popular materials due to their potential to advance a variety of fields ranging from biomedicine^{202, 212} and drug delivery^{205, 213} to catalysis.^{203, 214, 215} We have previously described a method for ligand quantification and presented detailed studies of both thiolated and aminated ligand shell formation. From these studies, we extracted a set of design rules for the synthesis of binary ligand shells from a selected set of molecular ligands.^{54, 216} The next step in advancing these design parameters with the ultimate goal of exact synthetic control over ligand shell formation for multiple applications is to characterize a greater variety of functionalities within the ligand shell (where, in the ideal case, both ligand quantity and arrangement are known. Here, we consider only ligand quantities that arise as a result of synthetic route). A NP ligand shell is composed of three distinct regions (the particle-binding moiety, the intermolecular region, and terminal functionality) that each contribute to the tunability and activity of the final NP ligand shell functionality (Figure 1). In previous chapters, we have shown that terminal functionality has little impact on the final stoichiometries of binary NP ligand shells. Further, there is significant variation in terminal functional groups used throughout the literature because these species are typically designed for functions such as cell

targeting or sensing, and are therefore highly application specific.^{65, 217} Therefore, in expanding our understanding of multi-component ligand shell formation, this chapter focuses on preliminary studies of new particle binding moieties as well as ligand shells that contain three or more ligands (where binding moiety is constant and intermolecular regions are distinct).

4.2 EXPERIMENTAL

4.2.1 Materials and Methods

Hydrogen tetrachloroaurate (III) trihydrate ($\text{HAuCl}_4 \cdot 3\text{H}_2\text{O}$, 99.999%), 8-mercaptooctanoic acid (MOA, > 95%), 3-mercaptopropionic acid (MPA, $\geq 99\%$), 8-aminooctanoic acid (AOA, 99%), bis(p-sulfonatophenyl)phenylphosphine dihydrate dipotassium salt (BSPP, 97%), 4-(diphenylphosphino)benzoic acid (4-DPPBA, 97%), and sodium citrate tribasic dihydrate (citrate, $\geq 99\%$) were obtained from Sigma-Aldrich (St. Louis, MO). Poly(ethylene glycol) methyl ether thiol (PEGSH, average $M_n = 1,000$ Da), was obtained from Laysan Bio, Inc. (Arab, AL). Methoxyl poly(ethylene glycol) amine (PEGNH₂, > 95%, average $M_n = 1,000$ Da) was obtained from NanoCS (Boston, MA). Acetonitrile (ACN, 99.8%) and sodium hydroxide (NaOH, certified ACS) were obtained from Fisher Scientific (Waltham, MA). Deuterium oxide (D₂O, 99.9%) was obtained from Cambridge Isotope Laboratories, Inc. (Tewksbury, MA). All reagents were used as received unless otherwise indicated. NANOpure™ (Thermo Scientific, > 18.2 MΩ · cm) water was used in the preparation of all solutions, and all reagent solutions are aqueous unless otherwise noted. Before use, all glassware and Teflon®-coated stir bars were washed with aqua regia (3:1 ratio of concentrated HCl and HNO₃ by volume) and rinsed

thoroughly with water. *Caution: Aqua regia is highly toxic and corrosive and requires proper personal protective equipment. Aqua regia should be handled in a fume hood only.*

4.2.2 AuNP Synthesis

13 nm AuNPs were synthesized using a modified Frens procedure.^{54, 180} Briefly, in a 1 L, 3-neck round bottom flask containing a stir bar, 500 mL of aqueous HAuCl₄ (1 mM) solution were prepared. The solution was heated to vigorous reflux while stirring until a rapid drip rate was achieved (drip rate ~1 per second). Meanwhile, a 50 mL solution of citrate (33 mM) was prepared. This citrate solution was rapidly added to the refluxing HAuCl₄ solution. After addition, the reaction mixture changed from yellow, to colorless, to black, to purple-red within 1 minute. The resulting AuNP solution was allowed to reflux for 5 minutes before it was removed from heat. This mixture was cooled to room temperature and transferred to a clean glass media bottle for refrigerated storage (~4 °C).

4.2.3 Absorption Spectroscopy

Particles were characterized by ultraviolet-visible-near infrared (UV-vis-NIR) absorption spectroscopy using a Cary 5000 spectrophotometer (Agilent, Inc.). Spectra were baseline corrected with respect to the spectrum of water. In order to obtain each spectrum, the AuNP solution was diluted by 1/3 with pure water.

4.2.4 Transmission Electron Microscopy (TEM)

An aliquot from the final AuNP solution was diluted 1/5 with water prior to drop casting onto a Formvar-coated copper transmission electron microscopy (TEM) grid (Ted Pella, Inc.). Samples were allowed to air dry and then dried under vacuum before characterization using an FEI Morgagni TEM at 80 kV. The size distributions of the AuNPs were determined from TEM images of at least 200 AuNPs from various areas of the grid. ImageJ 1.47d (National Institutes of Health, USA) was used to measure and count all particles.

4.2.5 Initial Ligand Exchange of Citrate-capped AuNPs

Prior to use, as-synthesized AuNPs were filtered using a polyvinylidene fluoride (PVDF) filter membrane with a pore size of 0.45 μm (25 mm GD/XP disposable filters, Whatman, Inc). Immediately after filtration, the AuNPs were concentrated by separating 1 mL aliquots into 1.5 mL centrifuge tubes and centrifuging the reaction mixture at 20,000 rcf for 5 minutes (Eppendorf 5424 centrifuge). The supernatant was removed, and another 1 mL aliquot of filtered particles was added. The pellet was resuspended, and the process was repeated until 3 mL of filtered particles were concentrated to a pellet in centrifuge tubes. The resulting pellet was resuspended in 250 μL of 1 mM of the desired ligand (for MOA, AOA, 4-DPPBA, or BSPP) or 50 μL of the PEG ligand (PEGSH or PEGNH₂), 50 μL of 100 mM NaOH, and 700 μL of water or 900 μL of water for the PEG ligands. This mixture was then placed on a temperature-controlled mixer (Eppendorf R Thermomixer) for 4 hours (for the thiolated or aminated ligands) or 8 hours (for the phosphine-containing ligands) at 1,000 rpm and 25 °C. After this time, the particles were

washed with 10 mM NaOH twice, followed by two washes in water and two washes in D₂O. After the last wash cycle, the supernatant was removed to yield a concentrated pellet of AuNPs.

4.2.6 Backfilling of BSPP-capped AuNPs with a Thiolated or Aminated Ligand

A freshly washed, concentrated pellet of BSPP-capped particles (whose synthesis is outlined above) was resuspended in 250 μ L of the -OA ligand (1 mM of either MOA or AOA), 50 μ L of 100 mM NaOH, and 700 μ L of water. The resulting mixture was placed on a temperature-controlled mixer for 4 hours at 1,000 rpm and 25 °C. After this time, the particles were washed with 10 mM NaOH twice, followed by two washes in water and two washes in D₂O. After the final wash cycle, the supernatant was removed to yield the concentrated pellet. An identical procedure was followed for backfilling with PEG (either PEGSH or PEGNH₂), resuspending the BSPP-capped particles in 50 μ L of 5 mM PEG, 50 μ L of 100 mM NaOH and 900 μ L of water.

4.2.7 Sequential Addition of Three Ligands

A freshly washed, concentrated pellet of PEGSH-capped particles (whose synthesis is outlined above) was resuspended in 250 μ L of 1mM MOA, 50 μ L of 100 mM NaOH, and 700 μ L of water. The resulting mixture was placed on a temperature-controlled mixer for 4 hours at 1,000 rpm and 25 °C. After this time, the particles were washed with 10 mM NaOH twice, followed by two washes in water and two washes in D₂O. After the final wash cycle, the supernatant was removed to yield the concentrated pellet. The concentrated pellet of PEGSH and MOA-capped particles was then resuspended in 250 μ L of 1mM MPA, 50 μ L of 100 mM NaOH, and 700 μ L of water. The resulting mixture was placed on a temperature-controlled mixer for 8 hours at

1,000 rpm and 25 °C. After this time, the particles were washed with 10 mM NaOH twice, followed by two washes in water and two washes in D₂O. After the final wash cycle, the supernatant was removed to yield the concentrated pellet with a three component ligand shell.

4.2.8 Inductively Coupled Plasma Mass Spectrometry (ICP-MS)

Inductively coupled plasma mass spectrometry (ICP-MS) analysis was performed using an argon flow with a NexION spectrometer (PerkinElmer, Inc.). An aqua regia solution was prepared with a 3:1 ratio of hydrochloric acid (Sigma-Aldrich, > 99.999% trace metal basis): nitric acid (Sigma-Aldrich, > 99.999% trace metal basis) and diluted with water for a 5% (by volume) aqua regia matrix. AuNP samples were taken from the concentrated pellet after ligand exchange and digested overnight in ~5 µL of fresh and concentrated aqua regia solution. From the digested solution, 1 µL was further diluted to 15 mL using 5% aqua regia matrix, and the remainder of the digest was reserved for ¹H-NMR analysis.

Unknown Au concentrations were determined by comparison to a 5-point standard curve with a range of 1 - 30 ppb (1, 5, 10, 20, and 30 ppb prepared by volume) from a gold standard for ICP (Fluka, TraceCERT 1,002 ± 2 mg/L Au in HCl) diluted in the 5% aqua regia matrix. All standards were measured 5 times and averaged, while all unknown samples were measured in triplicate and averaged. A 5 minute flush time with 5% aqua regia matrix was used between all runs, and a blank was analyzed before each unknown sample to confirm removal of all residual metals from the instrument.

4.2.9 ^1H NMR Spectroscopy

All NMR measurements were performed on a Bruker 400 Ultrashield™ magnet with an AVANCE III 400 Console or a Bruker 600 Ultrashield™ magnet with an AVANCE III 600 Console (Bruker Biospin, Billerica, MA) at 298 K. For all experiments, a minimum recycle delay of 5 seconds was used, which was sufficiently greater than T_1 . NMR samples were prepared as described above by concentrating the AuNPs, followed by digestion with 1 drop (~5 μL) of concentrated aqua regia. These samples were allowed to digest overnight before dilution with D_2O to a total volume of 500 μL . An ACN reference was used for the determination of unknown ligand concentrations. To each sample, 5 μL of 0.24% ACN (15 μL of ACN in 6 mL of D_2O) was added. The unknown ligand concentrations were determined by comparison to a 5-point standard curve with a range of 1.00 – 0.01 mM ligand (1.00, 0.50, 0.10, 0.05, and 0.01 mM, prepared in D_2O). For each standard, the integral of the ligand peak was divided by the integral of the ACN peak and plotted against the known concentration of ligand. Following an internal standard approach for the unknown concentrations of ligand on the AuNP,¹⁸² the ligand peak was integrated and similarly divided by the known integrated ACN peak to yield the concentration upon comparison with the calibration curve. Relevant representative ^1H NMR spectra can be found in Appendix C.

4.3 PHOSPHINE LIGANDS

4.3.1 Introduction

Both in our work, and in the broader literature, sulfur-containing molecules are the most well-studied ligands,²¹ enabling the production of NPs that are both stable and easily functionalized for specific applications.²¹⁸ Although amines do not interact as strongly with the Au surface as thiols, amines shown promise as capping ligands in both AuNP synthesis^{219, 220} and for bioconjugation applications.²²¹ A third interesting class of AuNP binding moieties are phosphines, which have also long been studied and used to synthesize AuNPs that are amenable to post-synthetic modification.^{25, 65} However, despite their widespread utility, the ligand loading behavior of this phosphine class has yet to be described in detail. Herein, we quantify the ligand loading behavior of single-moiety phosphine ligand shells and then probe the interaction of this common, water soluble phosphine ligand with well-studied straight chain thiol and amine ligands to describe the final ligand shell compositions under conditions of co-loading and sequential ligand addition (backfilling).

4.3.2 Phosphine Ligand Densities

Bulky phosphine ligands on AuNPs are prevalent in the literature, both as the as-synthesized ligand²²² and as a result of successful ligand exchange.^{223, 224} Given this precedence, ligand exchanges were attempted with two common phosphines, 4-DPPBA and BSPP ligands in acidic (pH = 1.5), neutral (pH = 7), and basic (pH = 11.5) solutions. (*N. B.* 4-DPPBA is sparingly soluble in water. The addition of 20 mM NaOH was necessary to ensure solubility.) While the

exchanges conducted in acidic solution did not yield stable particles, both the neutral and basic exchanges were successful. Moving forward, all phosphine ligand exchanges with both 4-DPPBA and BSPP were performed in basic conditions for consistency with previous thiol and amine studies.^{54, 216}

Since both BSPP and 4-DPPBA yield stable AuNPs after undergoing ligand exchange from citrate to the phosphine ligand, the subsequent ligand densities of the resulting phosphine-capped AuNPs can be quantified after allowing the ligand exchange to proceed for 24 hours at a 50x ligand excess with respect to NP surface area (Table 4). BSPP ligand shells are approximately twice as dense as those formed from 4-DPPBA. Moving forward, while both phosphine ligands yield stable NP systems, BSPP will be evaluated with the thiol and amines ligands due to its superior water solubility over 4-DPPBA.

Table 4. Comparison of the number of ligands and the ligand densities for BSPP- and 4-DPPBA-capped AuNPs after 24 hours at a 50x ligand excess with respect to NP surface area.

Ligand Identity	Number of Ligands/Particle	Ligand Density (Ligands/nm ²)
BSPP	870 ± 140	1.61 ± 0.23
4-DPPBA	410 ± 70	0.75 ± 0.12

Because, the particle binding moiety of a ligand can influence both the necessary ligand concentration and incubation time for the ligand shell to reach a steady state (i.e. a ligand shell where the ligand composition and quantity do not change with increased ligand incubation times or concentration), we must first establish parameters for a robust ligand exchange with BSPP. For both aminated and thiolated ligands, a steady state is reached after 4 hours and at a ligand

excess of 25x. Interestingly, the BSPP ligand requires both a longer time (~8 hours) and a higher ligand excess (~30x) for the ligand shell to reach a steady state when undergoing ligand exchange from citrate to BSPP (Figure 40). In subsequent experiments, all ligand exchanges with BSPP were allowed to incubate for 16 hours at a 50x ligand excess to ensure that neither time nor excess would limit the ligand shell density.

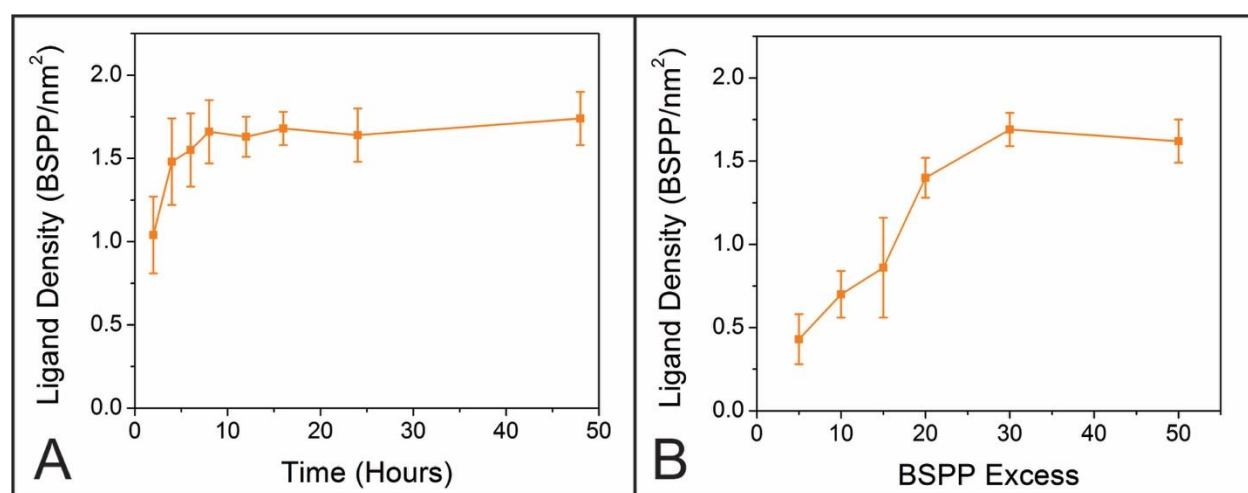


Figure 40. Plots of the BSPP ligand density as a function of time at a 50x ligand excess (A) and incubation in various ligand excesses for 16 hours (B). Results indicate that ligand loading reaches a steady state after approximately 8 hours and at a ligand excess of 30x.

BSPP is a sterically bulky ligand, subsequently it is anticipated that fewer BSPP ligands should be able to pack on the AuNP surface when compared with straight chain ligands. Indeed, a BSPP ligand density of only $1.65 \pm 0.08 \text{ BSPP}/\text{nm}^2$ ($870 \pm 90 \text{ BSPP}/\text{particle}$) is obtained. For comparison, 1 kDa PEGSH, a long polymeric thiolated ligand, yields a ligand density of $0.47 \pm 0.01 \text{ PEGSH}/\text{nm}^2$ ($1,200 \pm 30 \text{ PEGSH}/\text{particle}$), while MUA, a short chain thiolated ligand, gives a ligand density of $0.22 \pm 0.01 \text{ MUA}/\text{nm}^2$ ($2,500 \pm 60 \text{ MUA}/\text{particle}$) and AUA, a short chain

aminated ligand, loads with a ligand density of 1.33 ± 0.04 AUA/nm² (730 ± 90 AUA/particle).⁵⁴ With such a low density of BSPP ligands on the AuNP surface, this loosely packed ligand provides an interesting NP ligand shell from which to further study ligand packing. Previous studies have indicated that loosely packed ligands on AuNPs are more amenable to post synthetic modification,⁵⁴ so BSPP presents a phosphine-based ligand platform to probe the interaction of straight chain thiols and amines with this bulky phosphine. Moving forward, we will study the ligand loading of BSPP in conjunction with two thiolated ligands (MOA and PEGSH) and two aminated ligands (AOA and PEGNH₂) to learn how these well-understood ligand types both co-load and add sequentially into final ligand shells with BSPP.

4.3.3 Ligand Shell Quantification of BSPP-containing Mixed Ligand Shells

With the following series of experiments, while the structure of the phosphine ligand is markedly different from either the thiolated or aminated ligands, we can gain insight into the behavior of this bulky molecule in the presence of these well-studied straight chain ligands. In all cases when the BSPP is co-loaded with thiolated or aminated ligands (either short alkanolic acids or longer polymeric ligands), the number of BSPP ligands is reduced (Figure 41). Marked differences, however, are observed in the total number of ligand loadings between the BSPP/thiol and the BSPP/amine cases. When the BSPP is co-loaded with either short straight chain or longer polymeric thiolated ligands, the overall number of ligands nearly doubles with respect to only BSPP-capped AuNPs, while the number of BSPP ligands is reduced to nearly 1/6 of their original numbers. Consistent with previous studies (*vide supra*), the shorter MOA adds in higher numbers than the longer polymeric PEGSH ligand. When the amines are co-loaded with the BSPP, however, the overall number of ligands remains unchanged. Interestingly, while the

number of BSPP ligands is still reduced compared to BSPP-only ligand shells, the decrease is much less dramatic than in the thiol co-loading cases. For example, in the thiol co-loaded ligand shells, the number of BSPP ligands decreases by ~80%, while in the amine co-loaded ligand shells, the number of BSPP ligands shows only a ~20% decrease.

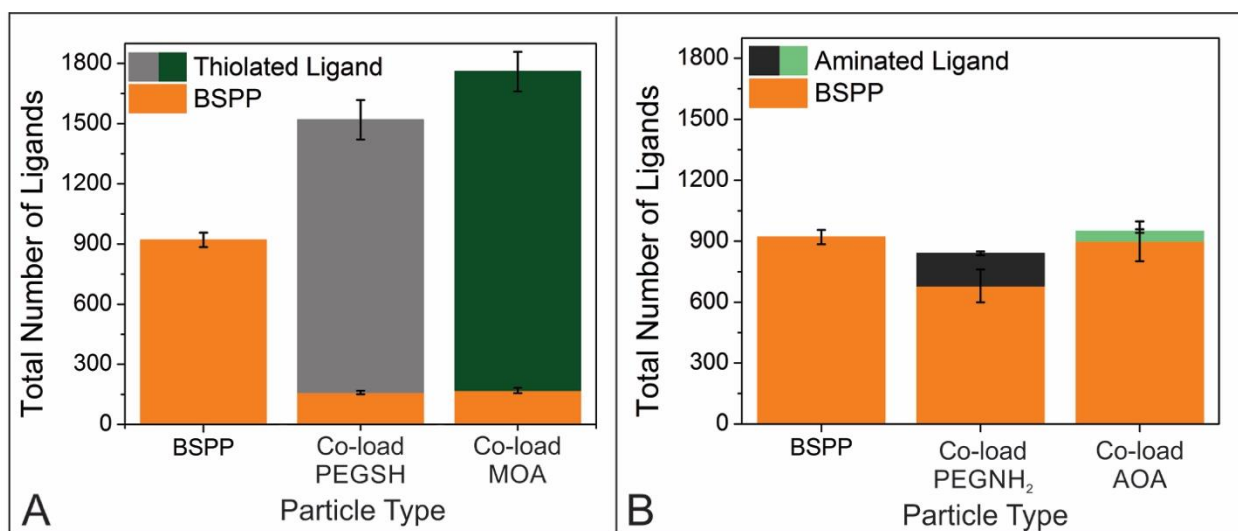


Figure 41. Plots of the total number of ligands for BSPP particles as well as when they are co-loaded with thiolated ligands (A) or aminated ligands (B). Markedly different ligand shells are obtained by changing the identity of the co-loaded ligand.

Ligand shells initially composed of BSPP can also be backfilled with either thiolated or aminated ligands (Figure 42). Consistent with previous observations, thiolated ligands load in higher numbers than amines due to the thiol's higher affinity for the AuNP surface. A significant difference in total number of ligands is also observed between BSPP backfilled with the thiols and the BSPP backfilled with the amines. These cases can be compared to their inverse situations, where the BSPP is backfilled into originally thiolated or aminated ligand shells

(Figure 43). In all of these cases, the number of BSPP ligands is significantly reduced from homogeneous BSPP ligand shells. With the exception of the MOA backfilled with the BSPP ligand shell, all final shells have decreased number of ligands compared to most other loading methods.

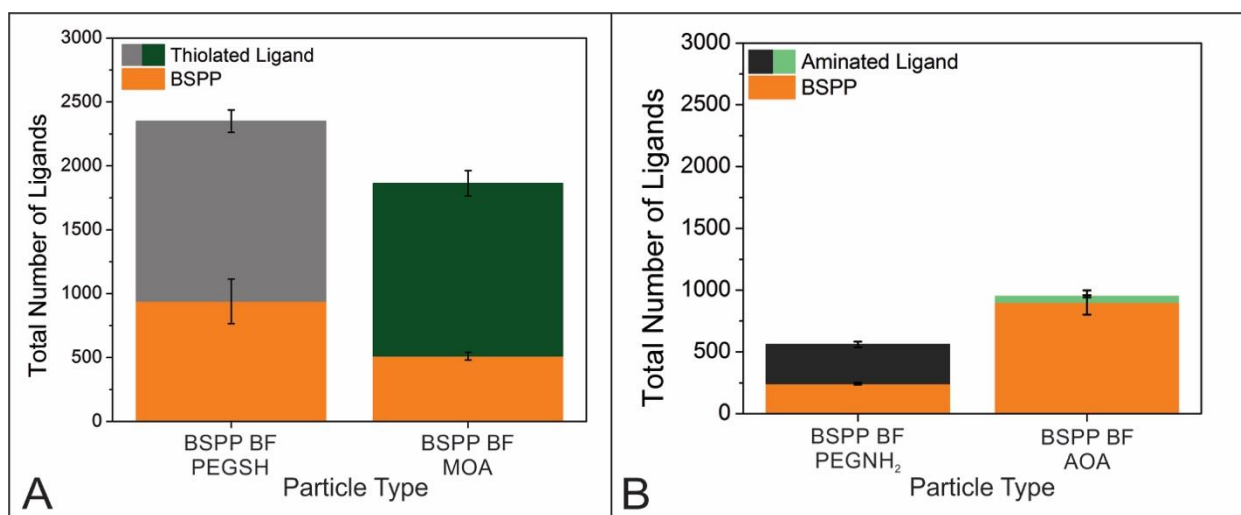


Figure 42. Plots of the total number of ligands for BSPP particles when they are backfilled with either thiolated (A) or aminated ligands (B).

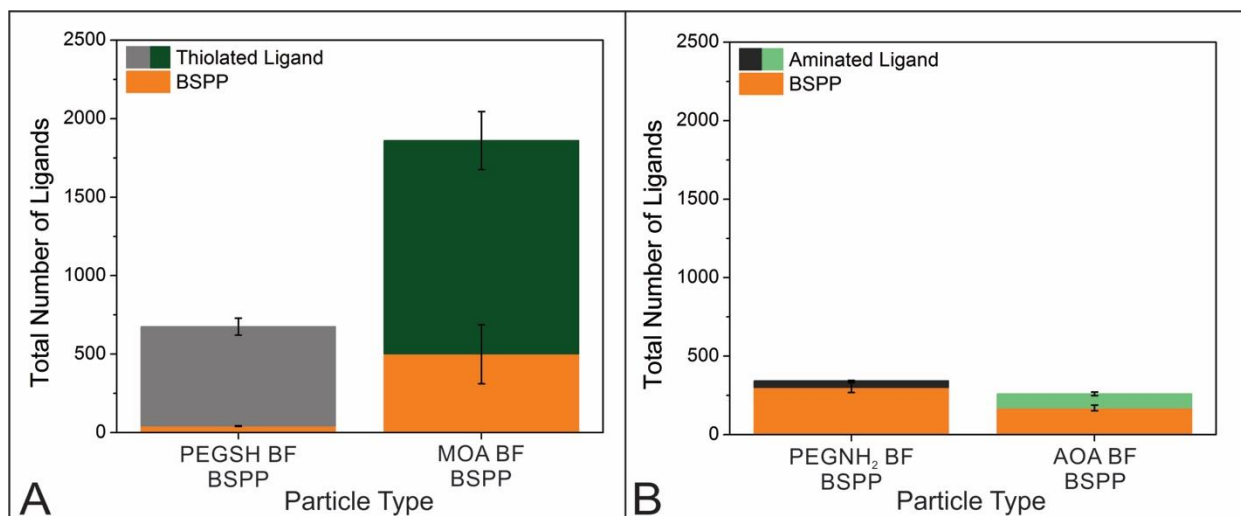


Figure 43. Plots of the total number of ligands for AuNPs when thiolated (A) or aminated (B) ligand shells are backfilled with BSPP.

4.3.4 Ongoing and Future Work

Given that the BSPP ligand used in the above studies is structurally dissimilar from the classes of thiol and amine ligands, it is desirable to probe if the ligand behavior, such as lower ligand density compared to thiolated ligands, results from the binding moiety or whether it results from the bulky ligand structure compared to the straight chain ligands used.

In our first series of ongoing experiments, we aim to distinguish between the effects of ligand structure and binding moiety. Conditions for ligand exchange with a structurally similar phosphine, ideally a ligand such as PH_2R (where R is an alkane straight chain) will be established. Here, we have selected 4-aminobutylphosphine, with a phosphine particle binding moiety and an amine terminal group, as our phosphine ligand. This ligand can be made via reduction of a butyl azide by lithium aluminum hydride under nitrogen.²²⁵ With the ligand in hand, we will then examine its ligand shell formation behavior alone, and in combination with

various thiolated and aminated straight chain ligands as well as BSPP for a bulky phosphine comparison, under both backfilling and co-loading scenarios.

While still in progress, already completed experiments suggest that the bulky phosphine ligand studied, BSPP, can form mixed ligand shells with both the thiols and amines.

4.4 TERNARY LIGAND SHELLS

4.4.1 Introduction

Beyond altering the particle binding moiety, ternary and higher order ligand shells have emerged as desirable targets due to their potential to enhance the role of NPs in downstream applications. For instance, two-moiety ligand shells, here composed of 3-mercaptopropylsulfonic acid and octanethiol, showed enhanced catalytic activity compared to traditional zeolite-based materials.²²⁶ However, NP functionality can be expanded even further through the incorporation of three distinct ligands into a single ligand shell. Siriwardana and coworkers started to illustrate this point when they demonstrated that the final ligand shell composition of adenine, glutathione, and PEGSH on AuNPs critically depends on both the sequence of ligand addition and ligand concentration.²²⁷ Ligand shells consisting of three or more ligand varieties are the frontier in NP functionalization that needs to be more thoroughly understood, both in terms of preparation and on-particle architectures. Here we discuss expanding our emerging AuNP ligand shell design rules to ternary systems through sequential ligand addition of three thiolated ligands.

4.4.2 Selection of Three Ligands

Given that our NMR method can quantify any number of ligands as long as they have at least one distinct ^1H NMR signal, it is crucial to select ligands for the test system that will present well-separated, distinct NMR chemical shifts. PEGSH is a well-studied ligand that yields stable AuNPs while loading in modest numbers for a loosely packed monolayer. Given that the PEGSH is thiolated, the other two ligands must also be thiolated in order to allow them to load onto the NP without being out-competed by the strongly binding sulfur moiety. MOA would make an ideal choice for the second ligand. We have previously demonstrated the MOA will load in high numbers into an existing PEGSH ligand shell, yielding a particle with both ligands on the surface. The selection of the third ligand is more challenging; it must have peaks on the NMR distinct from the PEGSH and MOA and have the ability to bind to the NP through the already dense ligand shell. MPA, a thiolated ligand that is too short to stabilize 13 nm AuNPs alone, presents a good option since it will give the necessary discrete NMR peaks while being small to allow it to take advantage of low existing number of ligands (see Appendix C for relevant spectra).

4.4.3 Sequential Addition of Three Thiolated Ligands

With the selection for the three model ligands in hand, the AuNPs were sequentially loaded with the ligands. Citrate-capped NPs underwent ligand exchange to yield a PEGSH ligand shell. These PEGSH-capped particles were backfilled with MOA for a ligand shell composed of both components. Finally, dual ligand-capped particles were backfilled again with MPA for ligand shells with three components (Figure 44). As expected, the primary component of the ligand

shell was MOA, comprising 62% (Figure 45A). MPA and PEGSH composed the rest of the ligand shell with 35% and 3%, respectively. Consistent with previously observations, the MOA displaced the existing PEGSH ligand shell. Interestingly, however, MPA was able to bind to the particle in greater numbers than the remaining PEGSH, likely due to the PEGSH interrupting a well-formed MOA monolayer.

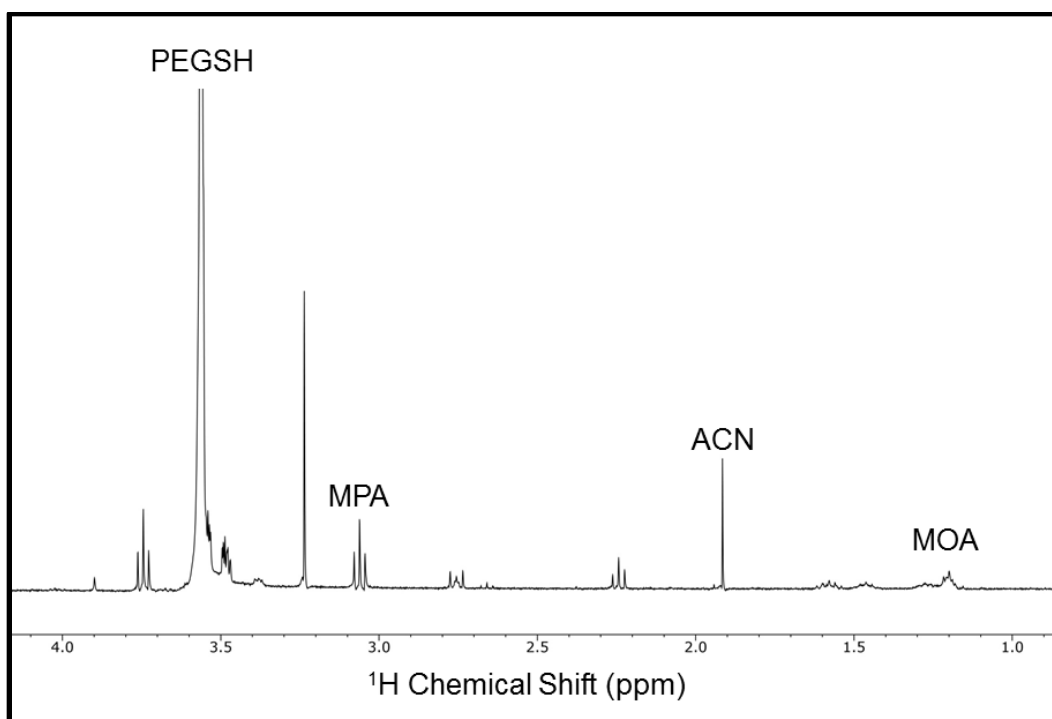


Figure 44. Representative ^1H NMR spectrum of three component ligand shells in D_2O after AuNP digestion. Labelled peaks correspond to peaks used for ligand quantification compared to the integrated intensity of the ACN peak.

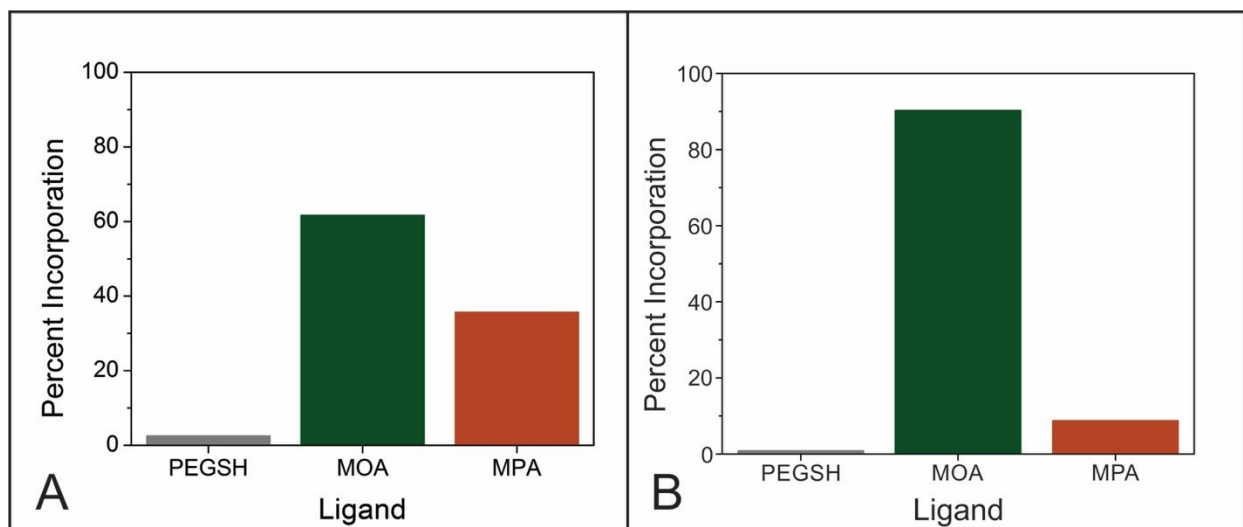


Figure 45. Graphs depicting the ligand incorporation for two different backfilling sequences: PEGSH backfilled with MOA backfilled with MPA (A) and MOA backfilled with MPA backfilled with PEGSH (B).

The observed loading raises the question as to if the final three component ligand shell composition can be changed by altering the ligand loading sequence. In order to test the final composition, the backfilling sequence began with MOA-capped particles. These particles were backfilled first with MPA and subsequently with PEGSH. After this loading sequence, MOA remained the majority component of the ligand shell, with 90% (Figure 45B). The MPA, however, was reduced to only 9% with the PEGSH at only 1%. This composition supports the hypothesis that the MPA in the first case was able to take advantage of the low number of ligands in the existing ligand shell to load in higher numbers. Here, the high number of MOA ligands ($2,470 \pm 310$ ligands) prevents significant amounts of either MPA (240 ± 70 ligands) or PEGSH (25 ± 10 ligands) from adding to the AuNP. Sequential loading with three ligands contributes to the evolving set of rational NP ligand shell design rules. For example, if a maximally dense ligand shell is desired, three thiolated ligands can be sequentially loaded, yielding a relatively dense final ligand shell.

4.4.4 Ongoing and Future Work

Overall, ternary ligand systems are promising for expanding NP functionality beyond what is accessible through only two-component systems. Sequentially loading three distinct thiolated ligands yields new compositions and denser final ligand shells compared to binary ligand shells, and which could be appealing in terms of both particle stability and enhanced functionality. However, ongoing experiments focus on further clarifying factors that influence the formation and final compositions of these ternary systems, including studies of both ligand identities and loading methods. It is hypothesized that final ligand shells with varying thiol compositions can be accessed through co-loading. Additionally, thus far only thiol-based ternary systems have been examined. However, we have observed previously that significant differences in final ligand shell composition are observed by altering only the particle binding moiety. Thus, working with ligands that have a weaker affinity for the AuNP are expected to yield final ligand shells that have a more evenly distributed composition of the three components.

4.5 CONCLUSION

Considered together, these experiments expand our understanding of the broad range of methods available to access and characterize a diversity of ligand shell compositions that will be necessary for NP use in downstream applications.

5.0 ESTABLISHING METHOD GENERALITY: APPLYING LIGAND QUANTIFICATION TO VARIOUS NP SIZES, SHAPES, AND COMPOSITIONS

(Portions of this work were published previously and are reprinted with permission from Crawford, S. E.; Smith, A. M.; Andolina, C. M.; Marbella, L. E.; Johnston, K. A.; Straney, P. J.; Hartmann, M. J.; Millstone, J. E., *J. Am. Chem. Soc.* **2015**, *137*, 14423-14429 and Johnston, K. A.; Smith, A. M.; Marbella, L. E.; Millstone, J. E., *Langmuir* **2016**, *32*, 3820-3826. Copyright 2015 and 2016, American Chemical Society.)

5.1 INTRODUCTION

Nanoparticles (NPs) have shown to be effective in a wide variety of fields, from sensing²²⁸⁻²³⁰ to biomedical applications.²³¹⁻²³³ While pseudospherical gold (Au) NPs are among the most highly cited particle types in the literature,^{203, 234, 235} other core types, such as silver (Ag)^{236, 237} or palladium (Pd),^{238, 239} as well as other shapes, including rods,^{240, 241} prisms,^{242, 243} and stars,²⁴⁴ are emerging with new and exciting properties to enhance and expand NP applicability.²⁴⁵⁻²⁴⁷ In all NP systems, regardless of size, shape, or composition, the NP behavior depends strongly upon the composition of its ligand shell. Therefore, a robust, widely applicable method to analyze the ligand shell, both in terms of composition and ligand quantity, is imperative for the implementation of these materials in all fields of interest.

Here we demonstrate the versatility of our previously reported ligand quantification method beyond the quantification of thiolated⁵⁴ and aminated²¹⁶ ligands on 13 nm AuNPs and test the validity of the proposed rational design rules on other particle sizes, compositions, and shapes. We highlight system-specific modifications and demonstrate the applicability of a combination of TEM, ¹H NMR, and ICP-MS on various sizes, shapes, and core compositions, including small AuNPs, AgNPs, and Au nanoprisms. Method alterations such as washing procedures for pure samples, matrix and digestion considerations, and atom per particle calculations are detailed so that our method may be accurately applied to other NP systems, both those outlined and others through extrapolation. We believe this demonstration of method expansion will allow for more wide-spread ligand quantification approach to broaden the utility of NPs in a range of applications.

5.2 EXPERIMENTAL

5.2.1 Materials and Methods

4-(diphenylphosphino)benzoic acid (4-DPPBA, 97%), hydrogen tetrachloroaurate(III) trihydrate (HAuCl₄, ≥ 99.9%), sodium borohydride (NaBH₄, ≥ 99.9%), 3-mercaptopropionic acid (MPA, ≥ 99%), 4-mercaptopbutyric acid (MBuA), 6-mercaptophexanoic acid (MHA, 90%), 8-mercaptopoctanoic acid (MOA, 95%), thioglycolic acid (TGA, ≥ 98%), bis(p-sulfonatophenyl)phenyl phosphine dipotassium dihydrate salt (BSPP, 97%), nitric acid (HNO₃, > 99.999% trace metal basis), hydrochloric acid (HCl, > 99.999% trace metal basis), silver nitrate (AgNO₃, 99.9999%), poly(vinylpyrrolidone) (PVP, average MW = 10,000 Da), L-ascorbic acid

(reagent grade), tannic acid (puriss. grade), hexadecyltrimethylammonium bromide (CTAB, 99%), L-ascorbic acid (99%), sodium iodide (NaI, 99.999%), and sodium citrate tribasic dihydrate (citrate, $\geq 99\%$) were purchased from Sigma-Aldrich (St. Louis, MO). Deuterium oxide (D_2O , 99.9%) was obtained from Cambridge Isotope Laboratories (Andover, MA). Poly(ethylene glycol) methyl ether thiol (PEGSH, average MW = 1,000 Da) was obtained from Laysan Bio, Inc. (Arab, AL). 11-amino-1-undecanethiol hydrochloride (AUT, 99.2%) was purchased from Dojindo (Rockville, MD). 11-Mercaptoundecanoic acid (MUA, 98%) and 3-mercapto-2-methylpropanoic acid (MMPA, 97%) were acquired from Santa Cruz Biotechnology, Inc. (Dallas, TX). Acetonitrile (ACN, $\geq 99.9\%$ Certified ACS), isopropanol (IPA, certified ACS plus), and sodium hydroxide (NaOH, $\geq 97\%$ Certified ACS) were purchased from Fisher Scientific (Waltham, MA). All reagents were used as received. All aqueous solutions were prepared using NANOpure water (Thermo Scientific, $> 18.2 M\Omega \cdot cm$), and all solutions were aqueous unless otherwise noted. Prior to use, all glassware and Teflon-coated stir bars were rinsed with aqua regia (3:1 ratio of concentrated HCl to HNO_3) and rinsed copiously with water prior to drying in an oven. *Caution: aqua regia is extremely toxic and corrosive, and should be handled in a fume hood only, using proper personal protection equipment.*

5.2.2 Synthesis of 4-DPPBA-Terminated AuNPs

To a clean 250 mL round-bottom flask, 81.25 mL of water, 6.75 mL of a 10.0 mM 4-DPPBA solution (prepared in 20 mM NaOH), and 2.00 mL of a 20.0 mM $HAuCl_4$ solution were added, while stirring at 1150 rpm using a benchtop stir plate, under ambient conditions. After 20 seconds, 10.00 mL of a 20.0 mM $NaBH_4$ solution were added, producing a red-orange colloid. The solution was stirred for 1 additional minute, and the particles were allowed to rest for 1 hour.

Afterward, the particles were centrifuged through 30 kDa molecular weight cutoff (MWCO) filters (Amicon Ultra-4, Millipore, Inc.) for 10 minutes at 4,000 rcf (Eppendorf centrifuge 5804R with swing bucket rotor A-4-44). The particles were then rinsed four additional times in a 3.30 mM NaOH solution (~4 mL) to ensure that the carboxylic acid groups remained deprotonated, thereby mitigating hydrogen bond formation and/or ligand multilayer formation.^{54, 248} These conditions were used during all exchanges to maintain consistency between samples. Following purification, the particles were diluted with water to 1.00 mL, and 6 aliquots of 166 μ L of the particles were added to separate 1.5 mL Eppendorf centrifuge tubes. To each tube, 50.0 μ L of 1.00 M NaOH, 684 μ L of water, and 100.0 μ L of 10.0 mM thiolated ligand solution were added. The particles were then placed on a temperature controlled mixer (Eppendorf R Thermomixer), where they were mixed at 1,000 rpm and 25 °C for ~16 hours. After mixing, particles were again centrifuged through 30 kDa MWCO filters for 10 minutes at 4,000 rcf. The particles were rinsed an additional four times with 3.30 mM NaOH.

5.2.3 Synthesis of Citrate-Capped AgNPs

AgNPs capped with citrate were prepared using a previously reported procedure.²⁴⁹ To synthesize ~25 nm AgNPs, a 100 mL aqueous reaction mixture containing citrate (5.00 mM) and tannic acid (0.40 mM) was prepared in a 3-neck round-bottom flask equipped with a reflux condenser. The molar ratio of tannic acid to citrate was 0.08:1. The reaction mixture was heated to reflux while stirring until a rapid drip rate was achieved (drip rate ~1/s). Then, 1.00 mL of AgNO₃ (25.00 mM) was injected. After addition, the reaction mixture quickly changed from a slight yellow color (due to the tannic acid) to a dark yellow within 1 min. This mixture was

cooled to room temperature and transferred to a clean glass media bottle for refrigerated storage (~4 °C).

5.2.4 Synthesis of Citrate-capped AuNPs

13 nm AuNPs were synthesized using a modified Frens procedure.^{54, 180} Briefly, in a 1 L, 3-neck round bottom flask containing a stir bar, 500 mL of aqueous HAuCl₄ (1 mM) solution were prepared. The solution was heated to vigorous reflux while stirring until a rapid drip rate was achieved (drip rate ~1 per second). Meanwhile, a 50 mL solution of citrate (24 mM) was prepared. This citrate solution was rapidly added to the refluxing HAuCl₄ solution. After addition, the reaction mixture changed from yellow, to colorless, to black, to purple-red within 1 minute. The resulting AuNP solution was allowed to reflux for 5 minutes before it was removed from heat. This mixture was cooled to room temperature and transferred to a clean glass media bottle for refrigerated storage (~4 °C).

5.2.5 Synthesis of PVP-capped AgNPs

AgNPs capped with PVP were synthesized using a modified literature procedure.²⁵⁰ To make the AgNPs, first, seeds were prepared by quickly injecting 0.60 mL of NaBH₄ (0.10 M) into a solution containing 5.00 mL of PVP (5 mM with respect to the number of PVP chains), 10 µL of HAuCl₄ (0.25 M), and 5.00 mL of H₂O. The seeds were then aged for 2 hours. Next, to synthesize AgNPs that were ~25 nm in diameter, 2.00 mL of PVP, 2.00 mL of ACN, 200 µL of ascorbic acid (0.10 M), and 2.00 mL of H₂O were mixed. The reaction mixture was placed in a cold water bath at 10 °C. Then, 150 µL of AgNO₃ (0.10 M) was added. Finally, 10 µL of the

seed solution was quickly injected while stirring. After addition, the reaction mixture slowly changed from clear, to yellow, to dark yellow, to dark yellowish-brown within 15 minutes.

5.2.6 Au Nanoprism Synthesis

Au nanoprisms were synthesized according to a modified literature protocol.²⁵¹ Briefly, Au seeds were prepared by adding 0.25 mL of 0.1 M NaBH₄ to a rapidly stirring solution containing 9.0 mL of H₂O, 0.25 mL of 0.01 M HAuCl₄, and 0.25 mL of 0.01 M trisodium citrate. The solution was stirred for 30 seconds, and then allowed to rest undisturbed at room temperature for two hours to allow degradation of remaining NaBH₄. After the aging period, three growth solutions were prepared (referred to as **A**, **B**, and **C**). Here, **A** was prepared by adding 2.5 mL of 0.01 M HAuCl₄, 0.5 mL of 0.1 M NaOH, and 0.5 mL of 0.1 M ascorbic acid to 90.0 mL of 0.05 M CTAB solution that was also 50 μM in NaI. The solution was mixed by hand after the addition of each reagent and was optically transparent after all reagents were added. Solutions **B** and **C** were prepared in an identical manner, except that the volume of all reagents was decreased ten-fold (for example, the volume of 0.05 M CTAB/0.05 mM NaI solution was decreased from 90.0 mL to 9.0 mL). Au nanoprisms were synthesized using an iterative seed addition protocol, where growth was initiated by adding 1.0 mL of the seed solution to **C**. Immediately after seed addition, **C** was mixed by hand for two seconds (as measured by standard lab timer) and a 1.0 mL aliquot was quickly removed and added to **B**. After mixing **B** for two seconds, the entire contents of **B** was added to **A**, which was then mixed by hand for 10 seconds and allowed to react for ~ 2 hours until nanoprism growth was complete.

5.2.7 Purification of Au Nanoprisms

Two hours after addition of the seed solution to the growth solution, the reaction mixture was heated in a water bath to 37 °C for one minute to dissolve any CTAB that may have recrystallized during the growth period which can interfere with purification by centrifugation. In order to purify the prisms from pseudospherical impurities and excess reagents, 90 mL of the reaction mixture was divided into 15 mL conical tubes and centrifuged at a gentle 820 rcf (Eppendorf centrifuge 5804 with swing bucket rotor A-4-44). After centrifugation, the nanoprisms deposit as a thin film on the walls of the conical tube, so both the supernatant and pellet were removed. The nanoprism film was resuspended in 1.0 mL of water, and this solution was then vortexed to yield a slightly green, translucent colloid. The mixture was subsequently transferred to a 1.5 mL centrifuge tube and purified one additional time by centrifugation (5 minutes at 2200 rcf using a Spectrum mini-centrifuge (SC1006-R)). After removal of the supernatant, the nanoprism pellets were resuspended in 1.0 mL of water and recombined in a 15 mL centrifuge tube.

5.2.8 Ligand Exchange of Citrate-Capped AgNPs

The citrate-capped AgNPs were concentrated by centrifuging a 1.50 mL aliquot at 20,000 rcf for 6 minutes. The supernatant was removed, and the particles were resuspended in another 1.50 mL aliquot of AgNPs and centrifuged again. The supernatant was removed, and the particles were resuspended in 1.00 mL of water. The particles were then washed by centrifuging once more. The supernatant was again removed, and the particles were resuspended in 1.00 mL of water. Then, the PEGSH was added in two separate addition steps. In the first addition, 15 μ L of

PEGSH (12.90 mM) was added to each tube. This mixture was then placed on a temperature-controlled mixer for 15 minutes at 800 rpm and 25 °C. After 15 minutes, the second addition of PEGSH was completed by adding PEGSH (12.90 mM) to each tube. The mixture was then replaced on the temperature-controlled mixer. Immediately after the desired mixing time, the particles were washed twice with H₂O and twice with D₂O to remove excess PEGSH. After the last wash cycle, the supernatant was removed to yield the concentrated pellet of AgNPs used in subsequent ligand analyzes.

5.2.9 Ligand Exchange of Citrate-Capped AuNPs

Prior to use, AuNPs were filtered using a polyvinylidene fluoride (PVDF) filter membrane with a pore size of 0.45 μm (25 mm GD/XP disposable filters, Whatman, Inc). Immediately after filtration, the AuNPs were concentrated by separating 1 mL aliquots into 1.5 mL centrifuge tubes and centrifuging the solution at 20,000 rcf for 5 minutes. The supernatant was removed, and another 1 mL aliquot of filtered particles was added. The pellet was resuspended, and the process was repeated until 3 mL of filtered particles were concentrated to 1 mL in centrifuge tubes. The particles were centrifuged once more, and the supernatant was removed. The resulting pellet was resuspended in 5 mM PEGSH, 50 μL of 10 mM NaOH, and 945 μL water. The amount of PEGSH added to each tube was determined by calculating a PEGSH excess with respect to the total surface area of the AuNPs and the calculated minimum area that one PEGSH molecule would occupy on a Au(111) surface (0.189 nm²). This mixture was then placed on a temperature controlled mixer for 4 hours at 1,000 rpm and 25 °C. After 4 hours, the particles were washed with 1 mM NaOH twice, followed by two washes in water and two washes in D₂O. After the last

wash cycle, the supernatant was removed to yield a concentrated pellet of PEGSH-capped AuNPs.

For PVP-capped AuNPs, the NPs were filtered as described above. Immediately after filtration, the particles were separated into 45 mL aliquots in 10 Falcon tubes and centrifuged for 40 minutes at 10,000 rcf (Eppendorf 5804 R centrifuge). The supernatant was removed, and the pellet in each tube of NPs was resuspended in 40 mL of water. All 10 tubes were combined in a glass media bottle containing a stir bar. While stirring, 11.2 mL of PVP (5 mM) was added to the solution, and the solution was allowed to stir overnight. The PVP-capped AuNPs were then separated into 1.5 mL aliquots in 1.5 mL Eppendorf tubes and spun down at 14,500 rpm for 5 minutes. The supernatant was removed, and another 1.5 mL aliquot of particles was added. This process was repeated until 6 mL of particles were concentrated into each tube. The pellet was then resuspended in 1 mL of water. The desired amount of PEGSH was added in one step (1.5 μ L to 41.5 μ L PEGSH (13 mM)). The mixture was then placed on a thermomixer for the desired amount of time (1 to 24 hours). Immediately after this mixing time, the particles were washed twice with water and twice with D₂O. After the last wash cycle, the supernatant was removed to yield the concentrated pellet of NPs.

5.2.10 Ligand Exchange of PVP-Capped AgNPs

Prior to use, 1.50 mL aliquots of as-synthesized PVP-capped AgNPs were centrifuged at 6,000 rcf for 2 minutes in 1.50 mL centrifuge tubes to remove any large aggregates (Eppendorf 5424 centrifuge). The supernatant was removed, transferred to a new centrifuge tube, and used for the subsequent steps. The AgNPs were then concentrated by centrifuging the 1.50 mL aliquot at 20,000 rcf for 6 minutes. The supernatant was removed, and the particles were resuspended in

1.00 mL of water. The particles were then washed by centrifuging once more. The supernatant was again removed, and the particles were resuspended in 1.00 mL of water. Then, the PEGSH was added in two separate addition steps. In the first addition, 15 μ L of PEGSH (12.90 mM) was added to each tube. This mixture was vortexed and then placed on a temperature-controlled mixer for 15 minutes at 800 rpm and 25 °C. After 15 minutes, the second addition of PEGSH was completed by adding PEGSH (12.90 mM) to each tube. The amount of PEGSH added to each tube was determined by calculating a PEGSH excess with respect to the total surface area of the AgNPs and the calculated minimum area that one PEGSH molecule would occupy on a Ag(111) surface (0.189 nm²). PEGSH excesses ranging from 1 to 40 times were used in the reported experiments. The mixture of AgNPs and PEGSH was vortexed and then replaced on the temperature-controlled mixer for 24 hours. Immediately after this mixing, the particles were centrifuged and washed twice with H₂O and twice with D₂O to remove excess PEGSH. After the last wash cycle, the supernatant was removed to yield the concentrated pellet of AgNPs used in subsequent ligand analyzes.

5.2.11 Ligand Exchange of Au Nanoprisms

To functionalize the CTAB-coated Au nanoprisms with a thiolated ligand (AUT, MUA, or MMPA), 2.0 μ L of 2 mM ligand solution was added to 1.0 mL of the purified Au nanoprism stock solution (O.D. = 1.0 a.u. at λ_{max} (approx. 1260 nm)) in a 1.5 mL centrifuge tube and mixed at 800 RPM for 12 hours at room temperature. After functionalization with the thiolated ligand, the Au nanoprisms were purified three times by centrifugation (5 minutes at 2200 rcf) and resuspended in 1.0 mL of H₂O.

5.2.12 ICP-MS of AuNPs

Inductively coupled plasma-mass spectrometry (ICP-MS) analysis was performed using an argon flow with a NexION spectrometer (PerkinElmer, Inc.). An aqua regia solution was prepared with a 3:1 ratio of hydrochloric acid:nitric acid and diluted with water to produce a 5% v/v aqua regia matrix. AuNP samples were taken from the concentrated pellet after ligand exchange and purification and digested overnight in ~5 μL of fresh and concentrated aqua regia solution. From the digested solution, 1 μL was further diluted to 5 mL using a 5% aqua regia matrix for ICP-MS analysis, while the remainder of the digest was reserved for ^1H NMR analysis (vide infra). Unknown Au concentrations were determined via comparison to a 5-point standard curve with a range of 1–30 ppb (1, 5, 10, 20, and 30 ppb prepared by volume) from a Au standard for ICP (Fluka, TraceCERT 999 mg \pm 2 mg/L Au in HCl) diluted in the 5% aqua regia matrix. All standards were measured 5 times and averaged, while all unknown samples were measured in triplicate and averaged. A 5 minute flush time with 5% aqua regia matrix was used between all runs, and a matrix blank was analyzed before each unknown sample to confirm removal of all residual metals.

5.2.13 ICP-MS of AgNPs

ICP-MS analysis was performed using an argon flow with a NexION spectrometer (PerkinElmer, Inc.). A nitric acid (Sigma-Aldrich, > 99.999% trace metal basis) solution was diluted with water for a 5 % volume nitric acid matrix. AgNP samples were taken from the digested and diluted NMR samples as described below. From this solution, 1 μL was further diluted to 15 mL using 5% nitric acid matrix. Unknown Ag concentrations were determined by comparison to a 5-point

standard curve with a range of 1–30 ppb (1, 5, 10, 20, and 30 ppb prepared by volume) from a Ag standard for ICP (Fluka, TraceCERT 1000 ± 2 mg/L Ag in HNO₃) diluted in the 5% nitric acid matrix. All standards were measured 5 times and averaged, while all unknown samples were measured in triplicate and averaged. A 5 minute flush time with 5% nitric acid matrix was used between all runs, and a blank was analyzed before each unknown sample to confirm removal of all residual metals from the instrument.

5.2.14 Ligand Quantification/Ligand Density Determination by ¹H NMR

Ligand density measurements were conducted using our previously reported method.⁵⁴ Briefly, following ICP-MS analysis, the remainder of the digested particles was diluted to a final volume of 500 μL using D₂O, and analyzed via ¹H NMR. Acetonitrile (ACN, 5 μL of 0.24% v/v) was added to AuNPs samples as an internal standard, while isopropanol (IPA, 5 μL of 0.24% v/v) was added to AgNPs samples. Specific proton peaks, typically those corresponding to the carbon backbone of the ligand, were integrated with respect to the standard, and a five-point calibration curve ranging from 0.1 to 1 mM was prepared for each ligand considered. The signal from each sample was used in conjunction with the equation of the calibration curve to determine ligand concentrations. Ligand densities were calculated by dividing the ligand concentrations by the concentration of particles, providing the number of ligands per particle (note that the ICP-MS and ¹H NMR values were always obtained from the same sample solution). Representative ¹H NMR spectra are included in Appendix D.

5.3 RESULTS AND DISCUSSION

5.3.1 NP Size Effects

In a previous study,⁵⁴ we demonstrated that NP size seems to play a negligible role in determining ligand loading above 10 nm. This observation is consistent with geometric calculations, where little change in curvature is experienced by the ligand at these ratios of ligand dimensions with respect to particle curvature (Figure 20). Therefore, while it is expected that ligand loading values on pseudospherical NPs with diameters greater than 10 nm do not exhibit marked size dependence, particles under this threshold should have ligand densities that depend on their size. We can probe the ligand loading on small AuNPs with a well-defined size and various thiolated ligands. AuNPs capped with various thiolated ligands will allow for direct parallels to the previously studied 13 nm particles.

Working with smaller NPs, however, presents an interesting challenge for purification. Washing through serial centrifugation and resuspension is ineffective, as the NPs are too small to centrifuge out of solution. Therefore, we used molecular weight cut-off (MWCO) filters, which allow for the NPs to be caught by the filters and the excess ligand can pass through for purification. All the particle samples were washed at least five times to ensure that all excess ligand is removed from solution. 1.8 ± 0.3 nm AuNPs were initially synthesized with 4-DPPBA, a phosphine terminated ligand.²⁵ With a ligand density of 4.52 ± 0.59 ligands/nm² (46 ± 6 ligands/particle), the phosphine ligand shell is significantly denser than a phosphine ligand shell on the larger AuNPs (1.65 ± 0.08 ligands/nm² measured with BSPP ligands on 13 nm AuNPs). While not a direct comparison between the same ligand type, 4-DPPBA and BSPP are both bulky phosphines where each ligand's phosphorous is surrounded by three phenyl rings. The

denser ligand shell on the smaller AuNPs is likely a direct result of the higher radius of curvature, which allows for the bulky ligands to pack with less steric interference from surrounding ligands.

Ligand density on the small AuNPs can also be studied under conditions of ligand exchange. The initially 4-DPPBA-capped AuNPs were backfilled with various mercaptoalkanoic acids ranging from 3 to 11 carbon atoms in length (Figure 46). In all cases, these ligand exchanges yielded particles with a mixed ligand shell since the incoming thiolated ligand did not fully displace the existing 4-DPPBA ligand shell. Interestingly, similar to the larger AuNPs where MUA and MOA backfilled into existing PEGSH ligand shells load in statistically similar numbers, we observe no statistical differences in either the number of thiolated ligands or the total number of ligands between any of the small AuNP ligand conjugates considered, with the exception of the MBuA-capped AuNPs. These particles have the same total number of ligands as all other samples tested, but MBuA–AuNPs exhibited a slightly lower number of thiol ligands. However, these statistical similarities are a marked difference from the addition of thiolated ligands to existing phosphine ligand shells for the larger AuNPs, where there is observed to be a significant increase in overall ligand loading, unlike with these smaller AuNPs.

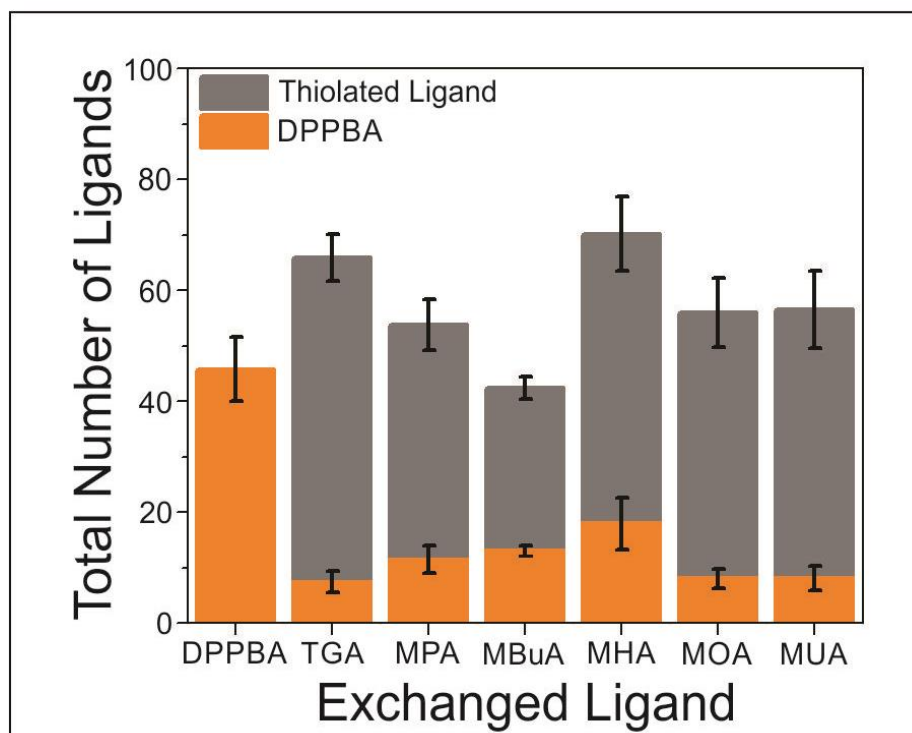


Figure 46. Total number of ligands per particle before and after the AuNPs underwent ligand exchange with thiolated ligands. Error bars represent the standard error of at least three measurements.

The mixed ligand shell on the small AuNPs introduces new properties, the most notable of which is photoluminescence, which can be tuned by the ligand chain length.²⁵ Although some similarities can be drawn between the ligand loadings on the small versus the large AuNPs, significant differences are also observed. Many of these differences can be attributed to the high radius of curvature for a small particle, whereas the larger particles have curvatures that approximate flat surfaces. The various densities and properties between small and large AuNPs work to enhance NP applicability and expand uses. However, we do note that the design parameters for sequential ligand exchange on these small AuNPs deviate from those observed in their larger counterparts.

5.3.2 NP Composition

As we demonstrated above and previously,^{25, 54, 216} NP size plays a significant role in ligand packing density due largely to the radii of curvature of the NPs. Composition of the NPs would also impact ligand packing density due to the different exposed facets from the constituent elements. AgNPs are an interesting parallel to our study of AuNPs and are used in a wide range of applications, including antimicrobial coatings,²⁵²⁻²⁵⁴ photocatalysis,^{255, 256} and sensing.^{257, 258} However, AgNPs will require alterations to both the ICP-MS and NMR portions of our ligand quantification method. Due to the formation of AgCl precipitate, AgNPs cannot be digested with aqua regia (due to the presence of HCl), so a new digestion component as well as a different ICP-MS matrix will be necessary. Nitric acid presents an alternative that can be used both to digest the AgNPs for NMR and ICP-MS, and it can be diluted to serve as the ICP-MS matrix. Further, due to the role of ACN in the AgNP synthesis, an alternative internal standard must be employed to avoid incorrect integration values due to ACN already being present in the samples. Here, we use IPA as the alternative internal standard for all AgNP samples.

25 nm AgNPs and 25 nm AuNPs were synthesized as described above with citrate as the initial capping ligand. These particles subsequently underwent ligand exchange with PEGSH to investigate if differences between the two particle core types are observed in the time and ligand excess necessary for ligand exchange to reach a steady state (Figure 47). In both the time and the ligand excess studies, the ligand density for AuNPs and AgNPs plateaus at significantly different values, 2.22 ± 0.22 PEGSH/nm² and 1.53 ± 0.14 PEGSH/nm², respectively. Interestingly, however, these steady states are reached at nearly identical points: at four hours for the time and at an excess of around 20x. Thus, although the ligand densities for the two cores are markedly different, they reach their maximum densities on roughly the same time and excess scale.

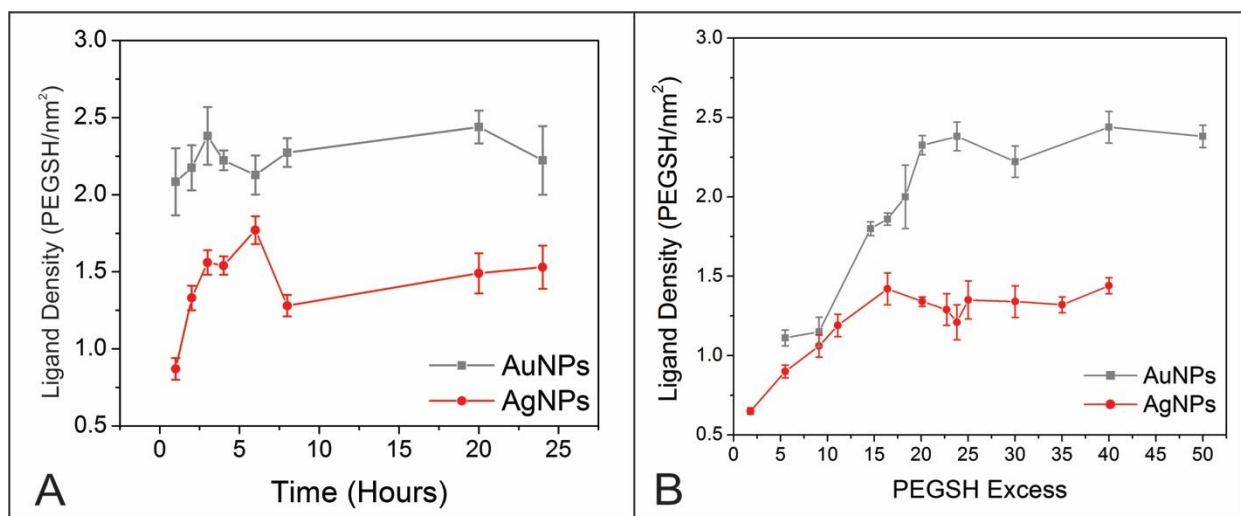


Figure 47. PEGSH ligand density plotted against time (A) and ligand density versus PEGSH excess with respect to surface area (B) for AuNPs (gray squares) and AgNPs (red circles) originally functionalized with citrate after ligand exchange with PEGSH. Error bars represent the standard error of at least five independent trials.

In order to gain a deeper understanding of ligand exchange on this particle core, AgNPs can be synthesized with different initial capping ligands and undergo ligand exchange with PEGSH to elucidate the role of the initial ligand in the final ligand density. Citrate as well as various MWs of PVP produce monodisperse AgNPs of approximately 25 nm.¹³⁰ AgNPs that were initially capped with citrate, 10 kDa PVP, or 40 kDa PVP underwent ligand exchange with PEGSH (Figure 48). For citrate-AgNPs, the PEGSH density is low at short incubation times. Conversely, for PVP-AgNPs a ligand density plateau is reached almost immediately. Similarly, when a low excess of PEGSH is added to the citrate-AgNPs at constant, long incubation times (24 hour), the PEGSH density is low, but for the PVP-AgNPs, a ligand density plateau is reached almost immediately. Both experiments support the conclusion that PVP is easier to remove from the AgNP surface than citrate.

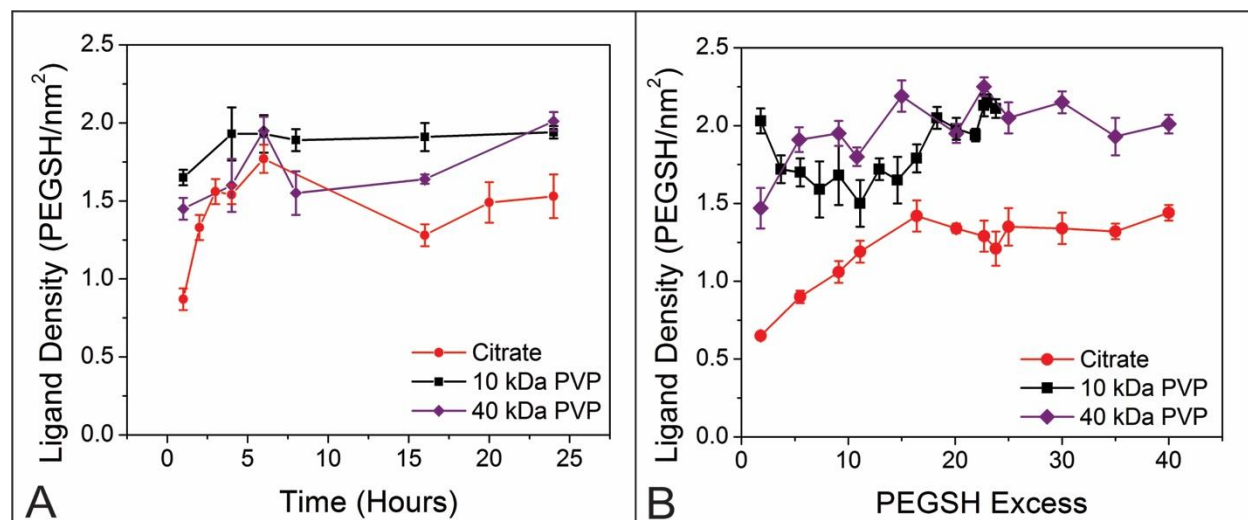


Figure 48. PEGSH ligand density plotted against time (A) and ligand density versus PEGSH excess with respect to surface area (B) for AgNPs originally functionalized with citrate (red), 5 mM 10 kDa PVP (black), and 5 mM 40 kDa PVP (purple) after ligand exchange with PEGSH. Error bars represent the standard error of at least five independent trials.

It is desirable to compare to the ease of removal of PVP and citrate on AuNPs as well as AgNPs. Since no synthesis currently exists to produce monodisperse 25nm AuNPs with PVP as the initial capping ligand, the AuNPs underwent ligand exchange with 10 kDa PVP. The ¹H NMR spectrum indicates complete displacement of the citrate by the incoming PVP. The now PVP-capped AuNPs were then ligand exchanged with PEGSH to investigate the necessary time and excess for ligand exchange to reach a steady state (Figure 49). With an initial PVP ligand shell, we find that the ligand density for both AgNPs and AuNPs plateau around 1.93 ± 0.22 ligands/nm², significantly lower than the packing density of 2.32 ± 0.13 ligands/nm² for initially citrate-capped AuNPs. Another marked difference is the time required for the ligand exchange for the PVP-capped AuNPs to reach a steady state. In all of the initially citrate-capped AuNP ligand exchanges, 4 hours is sufficient; however, in this case, 12 hours is required. While the

necessary ligand excess remains consistent regardless of initial capping ligand, the time data supports the conclusion that citrate is easier to remove than PVP from an AuNP, which is the opposite of the trend observed for AgNPs.

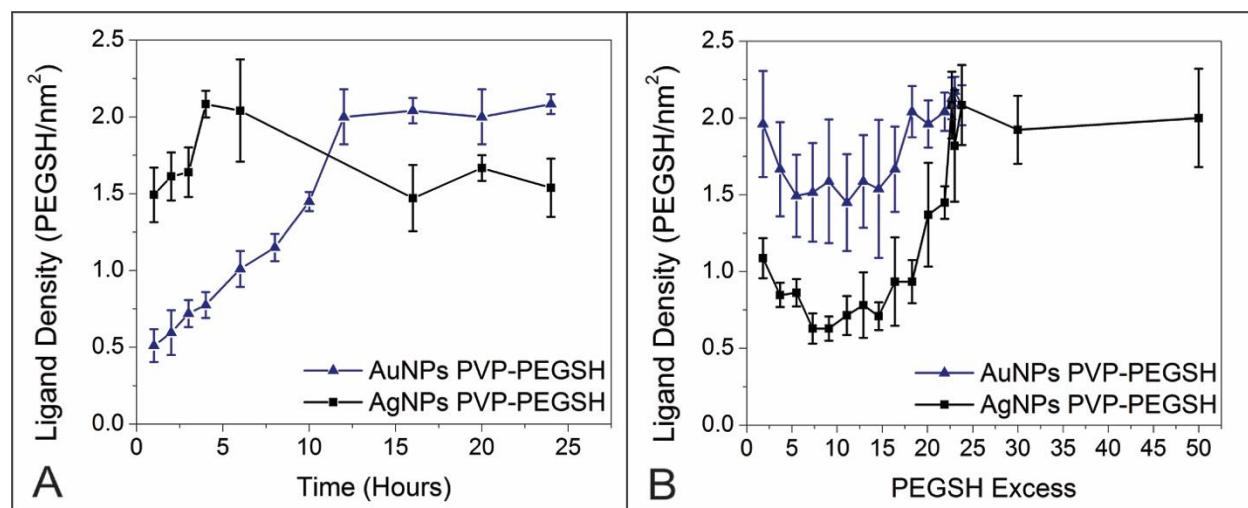


Figure 49. PEGSH ligand density plotted against time (A) and ligand density versus PEGSH excess with respect to surface area (B) for AuNPs (blue triangles) and AgNPs (black squares) functionalized with PVP followed by ligand exchange with PEGSH. Error bars represent the standard error of at least three independent trials.

5.3.3 NP Shape

A third aspect of the NPs that can impact their ligand loading density is the NP shape. A wide variety of Au shapes have been synthesized, ranging from rods²⁴⁰ and prisms^{259, 260} to more complex nanostars.²⁶¹ These anisotropic AuNPs have shown promise in applications ranging from gene delivery^{262, 263} to photovoltaics.²⁶⁴ However, despite these impactful uses, little is known about ligand packing on these particle shapes. Our method can be used to gain more insight into the ligand behavior and evaluating if our design parameters are shape-general, using

Au nanoprisms as a model case. However, one particular modification is necessary in calculating the number of atoms per particle. In all previous cases, the volume of the pseudospherical NPs was approximated with the volume of a sphere. Here, given that we know the edge lengths as well as the prism height, we can calculate the prism volume as that of a triangular prism. With this value, the number of ligands per prism can be calculated in the same manner as pseudospherical NPs.

Au nanoprisms were synthesized according to literature protocols to yield particles initially capped with CTAB.^{251, 265} Due to CTAB's low affinity for the Au surface and its high exchange rate with the surrounding media, CTAB cannot be reliably quantified, as no ligand steady state can be achieved. However, the prisms can undergo ligand exchange with various strongly binding molecules to probe their ligand density on the nanoprisms. The nanoprisms underwent ligand exchange with AUT (an eleven carbon thiol with an amine end functionality), MUA (analogous to AUT, except with a carboxylic acid terminus), and MMPA (a short thiol). On the nanoprisms, MUA loads with the highest ligand density (2.7 ligands/nm^2), followed by AUT (1.8 ligands/nm^2) and MMPA (1.0 ligands/nm^2). While MUA only differs from AUT in the terminal functionality, the increased MUA ligand loading is consistent with our previous results on pseudospherical AuNPs.⁵⁴ We attribute this higher loading to cooperative behavior of the MUA ligand that is not observed with the AUT, consistent with observations on pseudospherical AuNPs. Interestingly, these ligand loading trends can be used to control secondary metal deposition on the Au nanoprism surface due to the degree of their surface passivation on edges, faces, and vertices.²⁶⁶

5.4 CONCLUSION

In summary, our ligand quantification method can be applied to a wide range of NP systems, with various NP sizes, core compositions, and NP shapes with only a few specific modifications. For instance, with NP size, the washing procedure must be altered to ensure that all ligands that are not particle-bound are removed before analysis. Further, for core compositions, both the ICP-MS and digestion matrix can be changed to ensure complete metal solubility. The internal standard is amenable to modification based on the specific system, to avoid synthetic reagents as well as ligand peak overlap. Overall, by demonstrating the applicability of our ligand quantification method to a wide range of systems, we expect this method will have far reaching implications for routine surface characterization of NPs to expand NP use in a wide variety of applications.

APPENDIX A

SAMPLE CALCUATIONS FOR NANOPARTICLE LIGAND DENSITY, REPRESENATIVE ^1H NMR SPECTRA, AND GOLD NANOPARTICLE CHARACTERIZATION AFTER LIGAND EXCHANGE

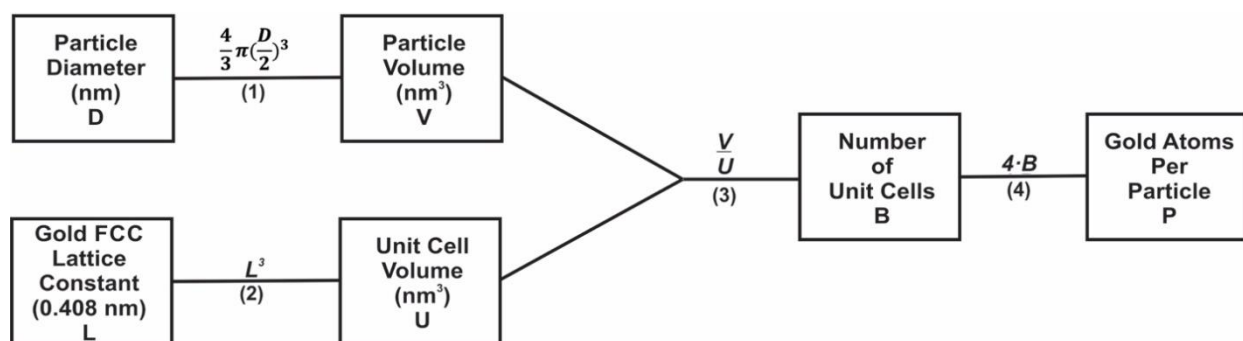


Figure 50. Flowchart depicting the process for calculating the number of gold atoms per particle for ligand density determination for pseudospherical particles.

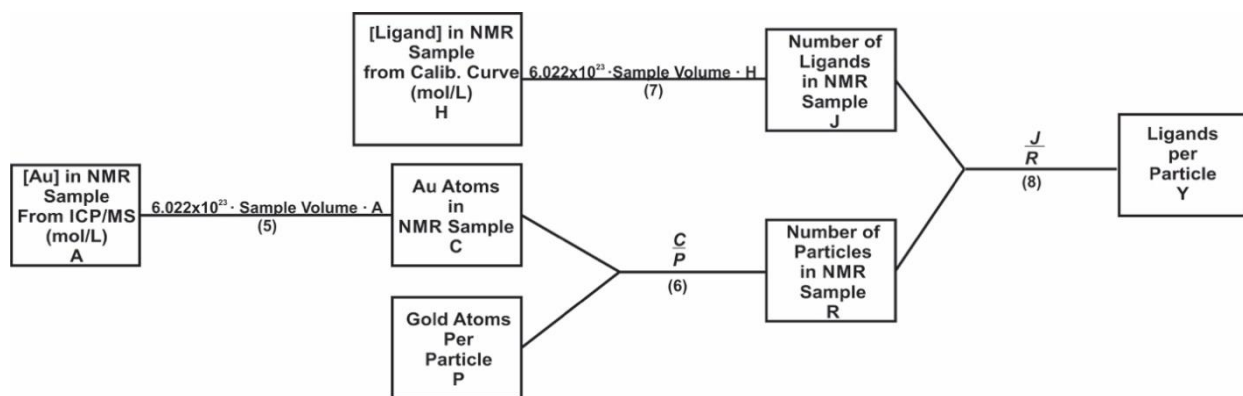


Figure 51. Flowchart depicting the process for calculating the number of ligands per particle for ligand density determination for pseudospherical particles.

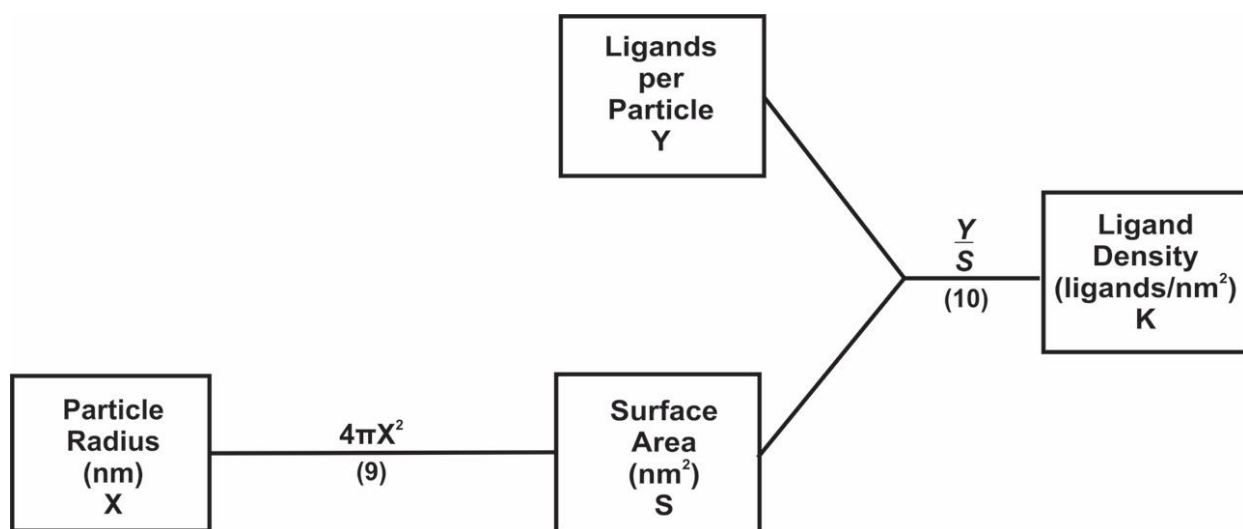


Figure 52. Flowchart depicting the process for ligand density determination for pseudospherical particles.

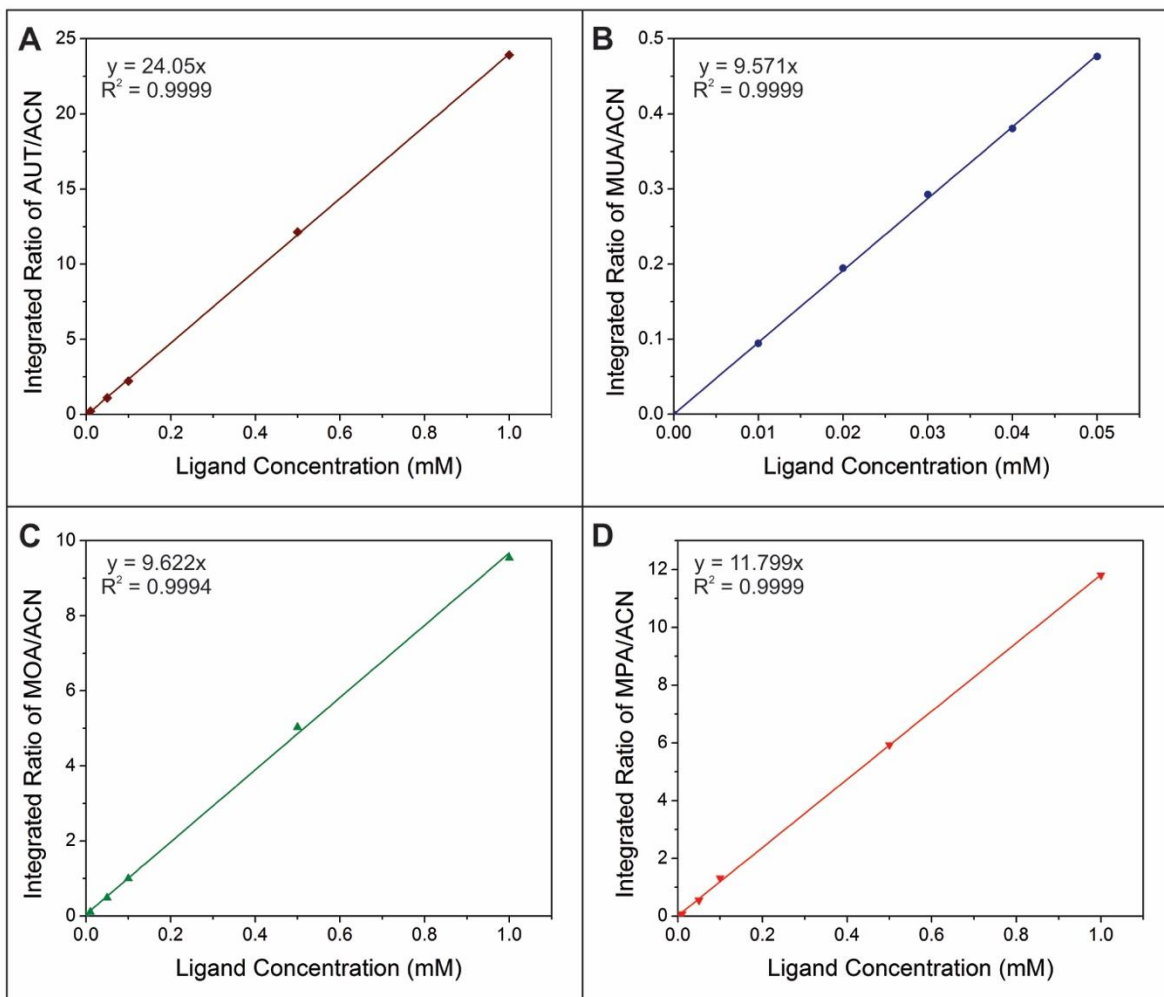


Figure 53. Representative calibration curves obtained for AUT (A), MUA (B), MOA (C), and MPA (D) by plotting integrated ratios of specific protons from each respective ligand/ACN against the concentration of that ligand to yield the equation for the line that will generate the unknown concentrations for each ligand.

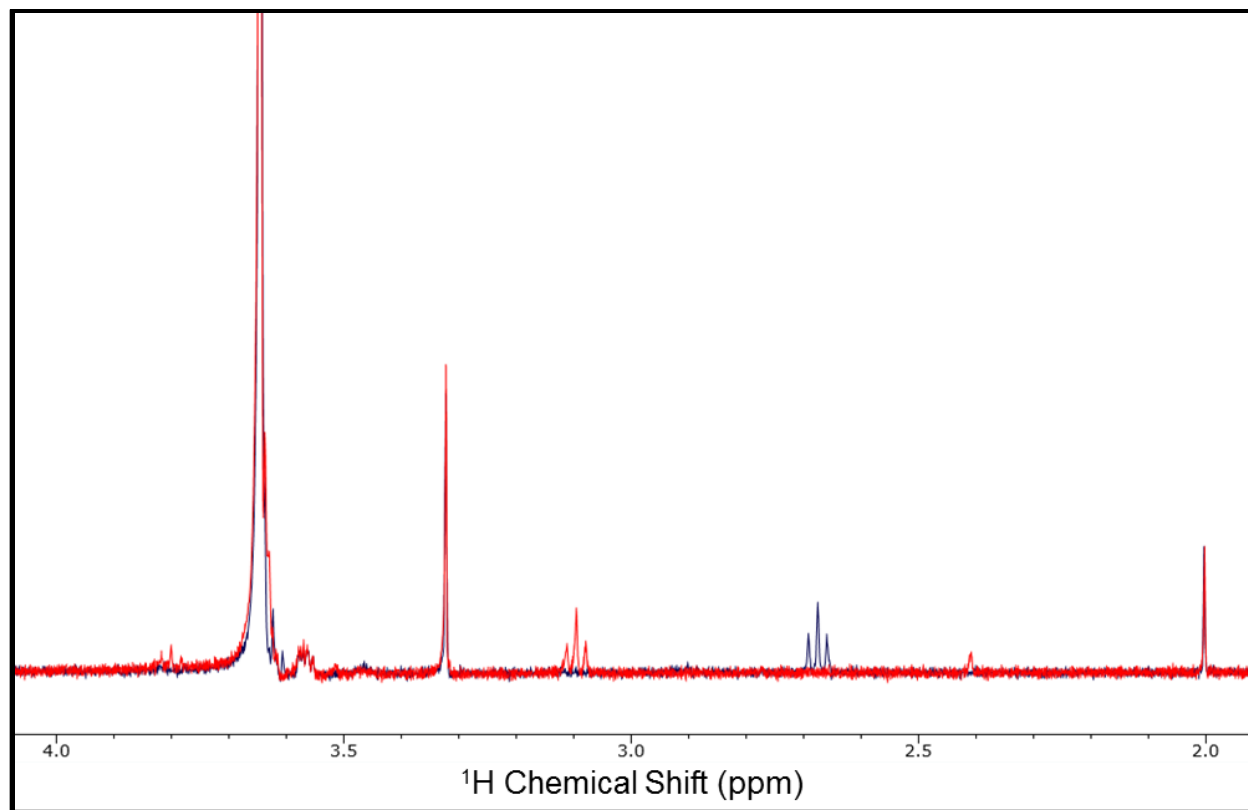


Figure 54. Representative ¹H NMR spectra of PEGSeCN (red) and PEGSH (blue). The discrepancy in the peak at 3.1 ppm (for the PEGSH) and 2.68 ppm (for the PEGSeCN) is due to the location of the protons on the carbon adjacent to either the sulfur (in PEGSH) or the selenium (in PEGSeCN).

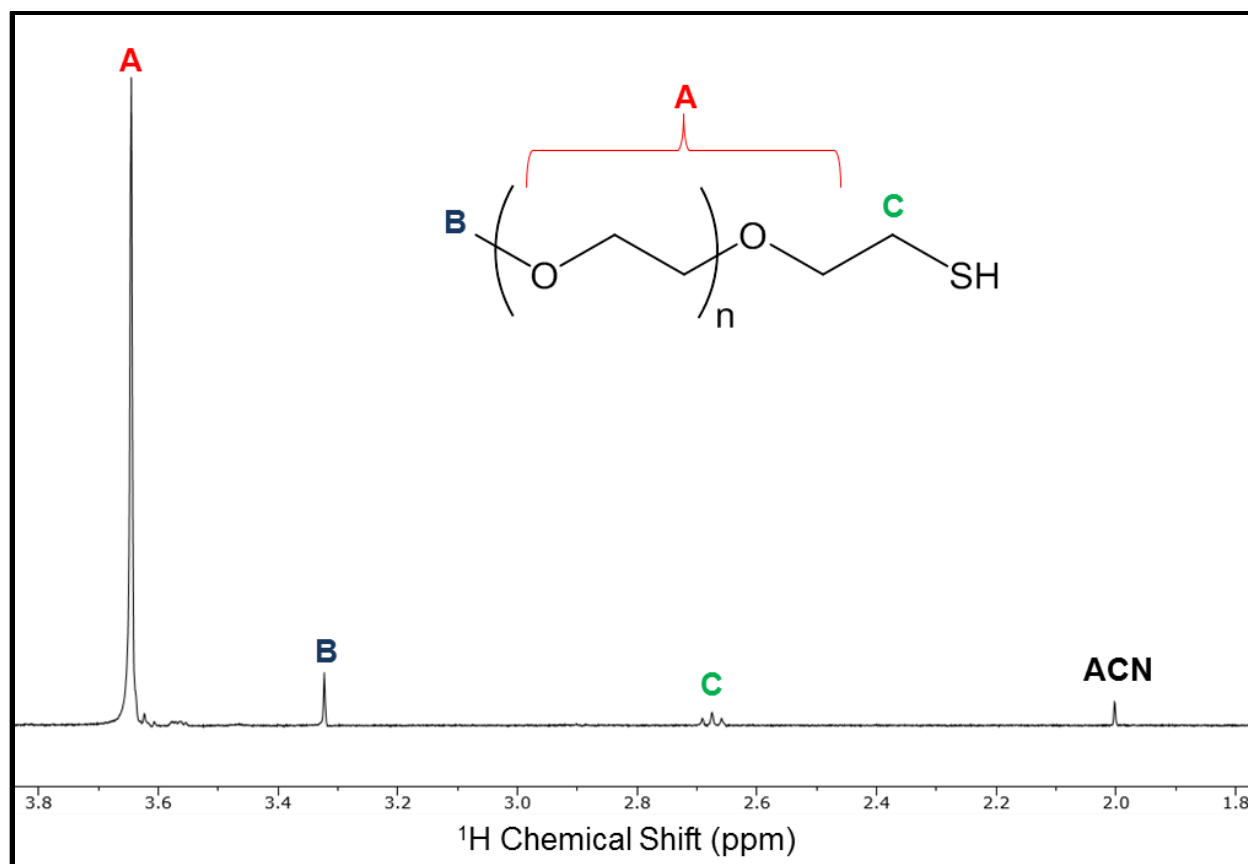


Figure 55. Representative ^1H NMR spectrum of PEGSH in D_2O with its labeled structure corresponding to plotted ^1H NMR peak locations. For calculation of PEGSH concentration, Peak A is integrated and compared to the integrated intensity of the ACN peak.

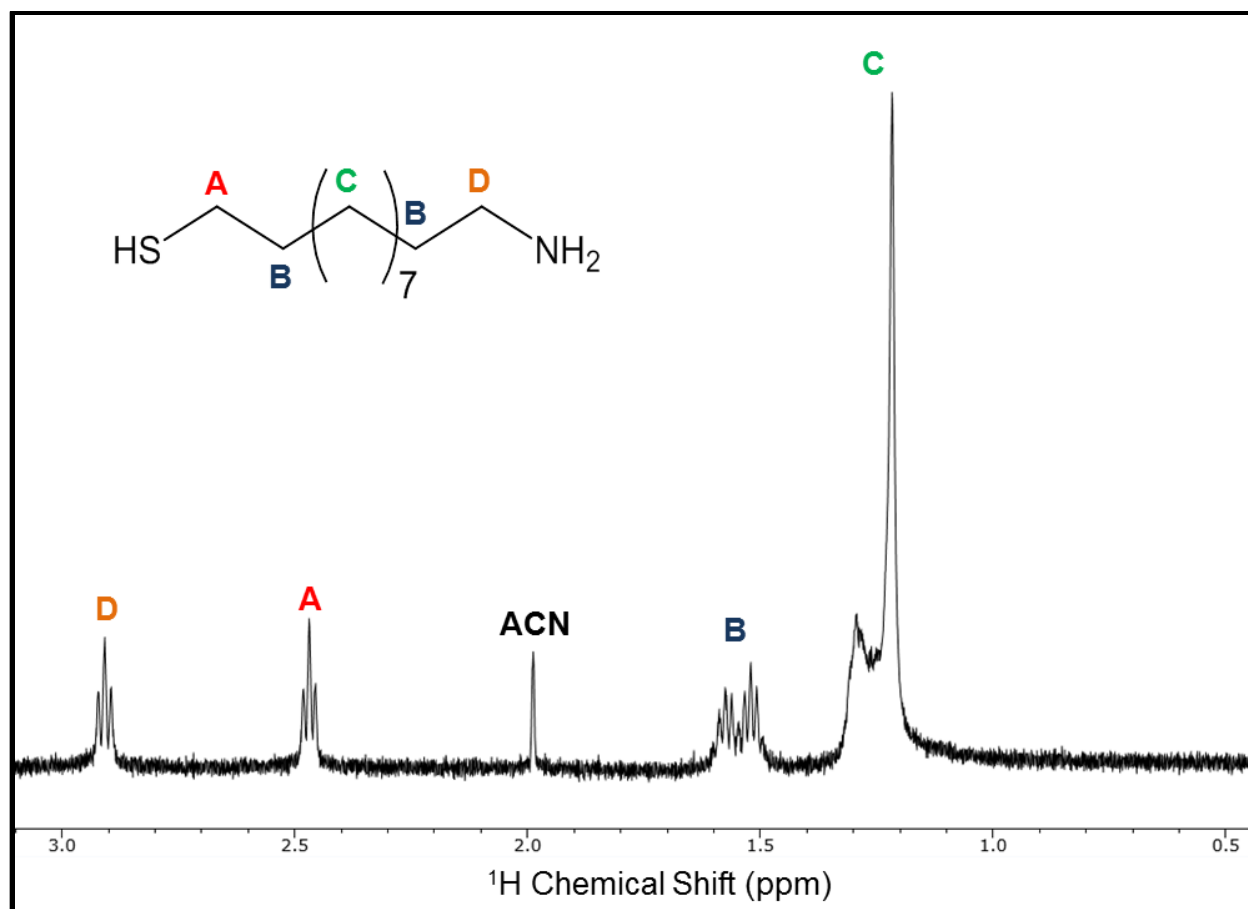


Figure 56. Representative ^1H NMR spectrum of AUT in D_2O with its labeled structure corresponding to plotted ^1H NMR peak locations. For calculation of AUT concentration, Peak C is integrated and compared to the integrated intensity of the ACN peak. Peaks from both the thiol and amine protons are not observed, as they exchange with the surrounding deuterated medium.

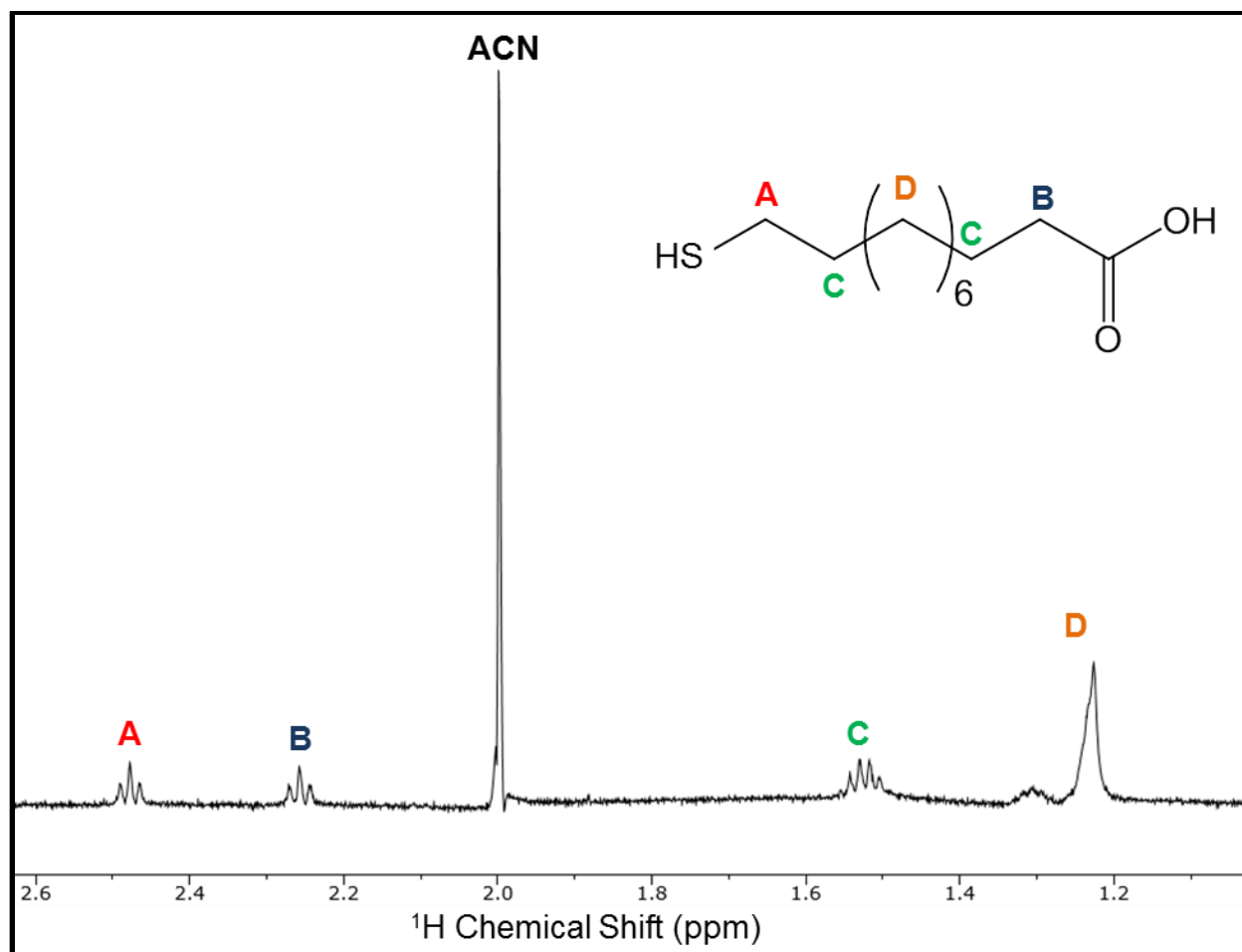


Figure 57. Representative ¹H NMR spectrum of MUA in D₂O with its labeled structure corresponding to plotted ¹H NMR peak locations. For calculation of MUA concentration, Peak D is integrated and compared to the integrated intensity of the ACN peak.

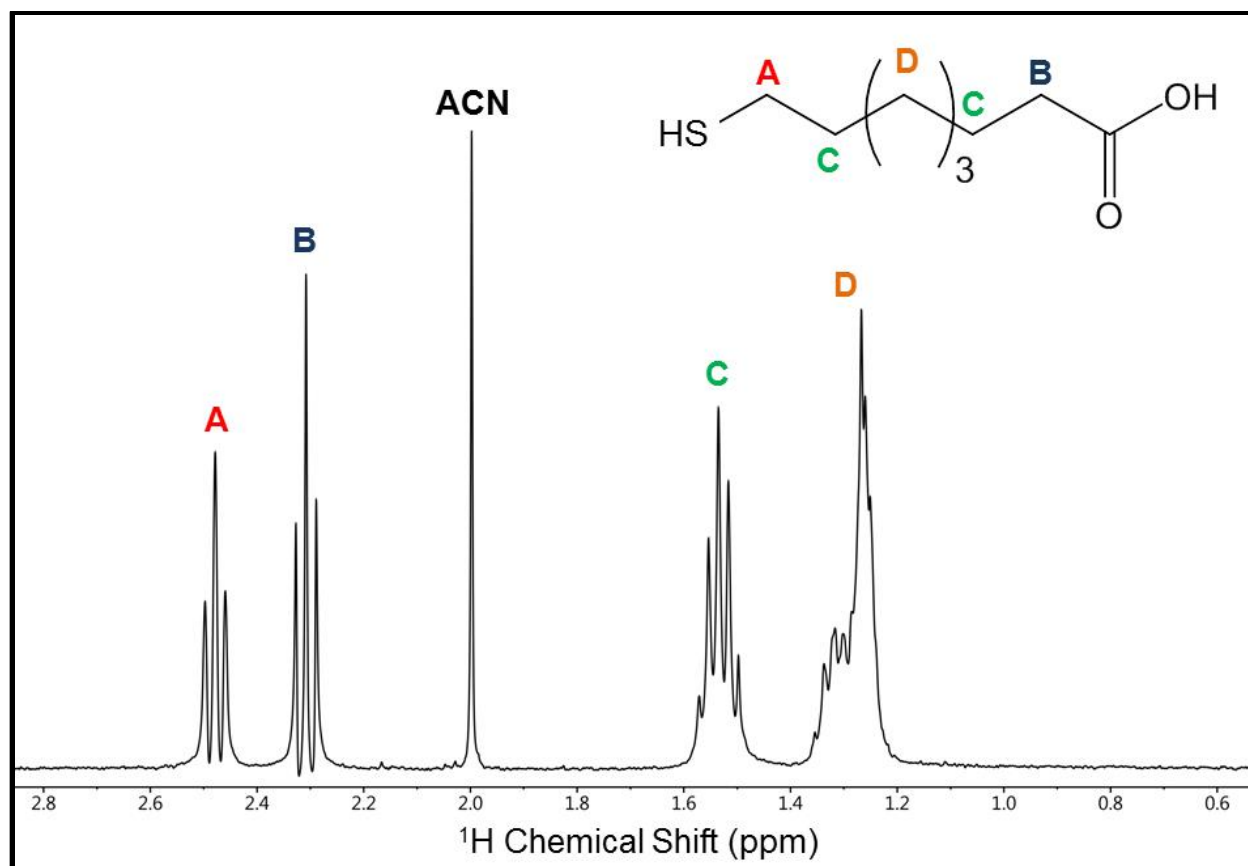


Figure 58. Representative ¹H NMR spectrum of MOA in D₂O with its labeled structure corresponding to plotted ¹H NMR peak locations. For calculation of MOA concentration, Peak D is integrated and compared to the integrated intensity of the ACN peak.

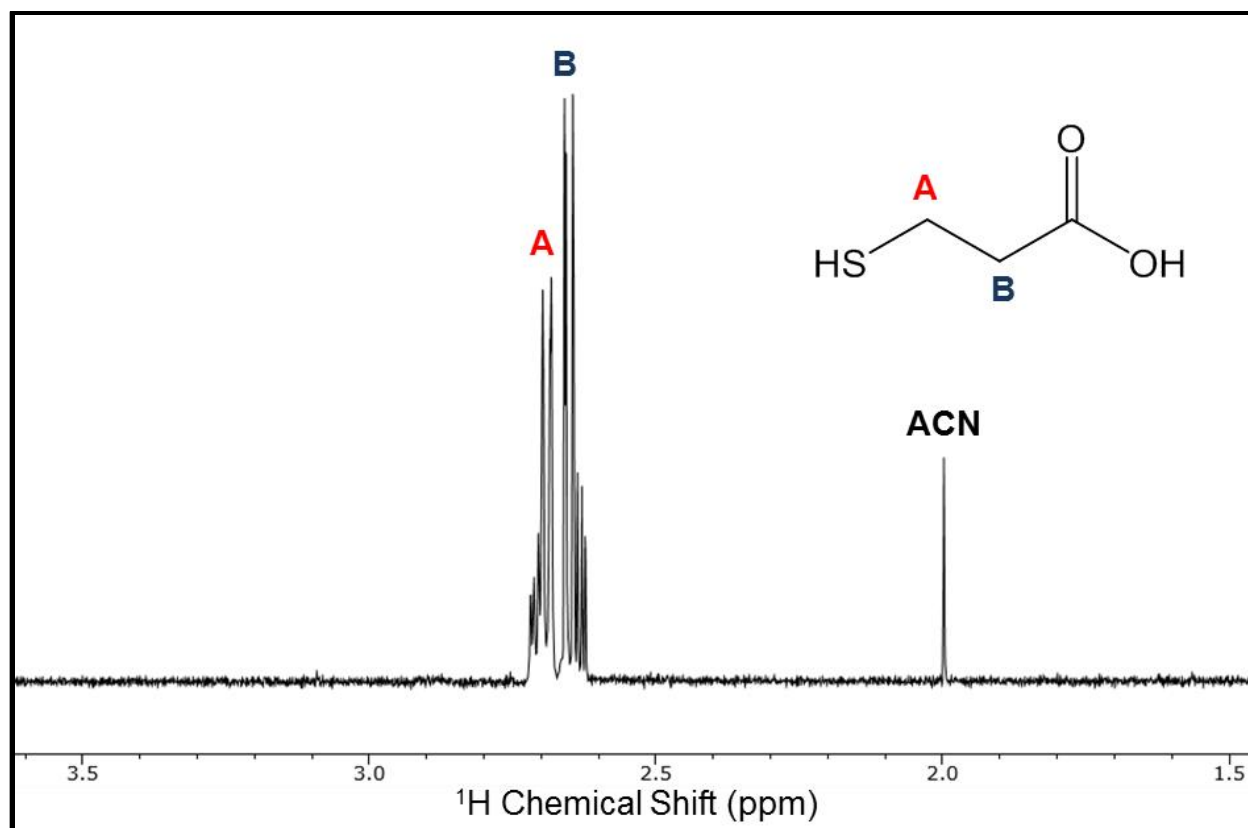


Figure 59. Representative ^1H NMR spectrum of MPA in D_2O with its labeled structure corresponding to plotted ^1H NMR peak locations. For calculation of MPA concentration, Peaks A and B (due to peak overlap) are integrated and compared to the integrated intensity of the ACN peak.

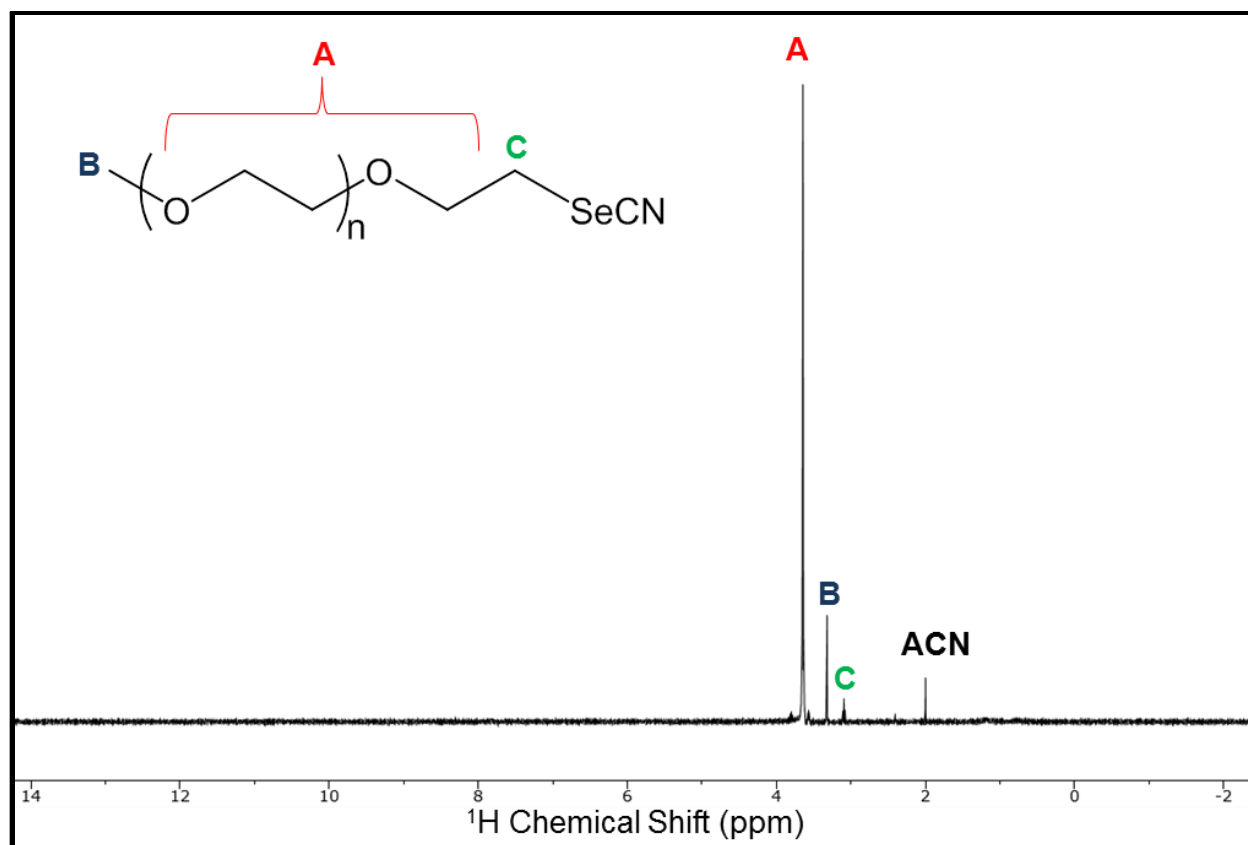


Figure 60. Representative ^1H NMR spectrum of PEGSeCN acquired in D_2O .

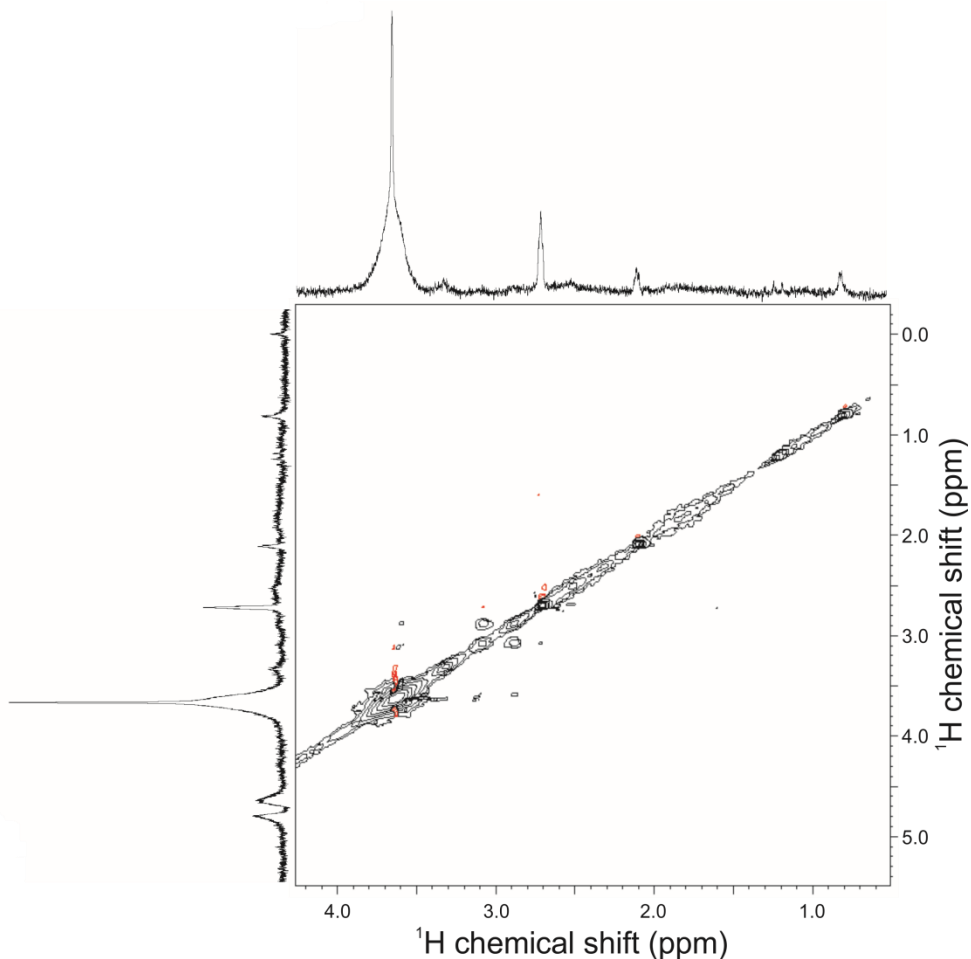


Figure 61. ^1H - ^1H Nuclear Overhauser Effect Spectroscopy (NOESY) of 13 nm AuNPs capped with PEGSH and ligand exchanged with MUA acquired with a 400 ms mixing time. MUA does not show any cross peaks with the PEGSH ligand, consistent with a segregated ligand shell architecture consisting of MUA and PEGSH domains. The formation of thiolated, small-molecule islands that are segregated from the original PEGSH shell are consistent with a cooperative binding mechanism for ligand exchange. The peaks at 4.7 ppm in the indirect dimension result from incomplete water suppression. The positive artifacts (red) on the PEGSH diagonal are residual T_1 noise that could not be completely removed.

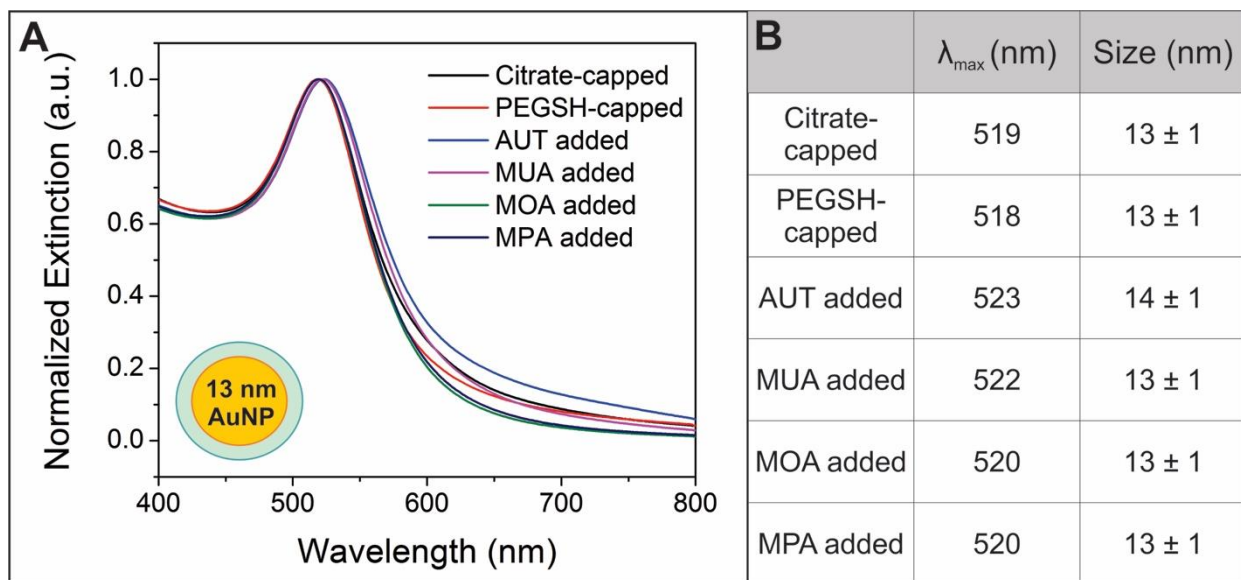


Figure 62. UV-vis spectra for all 13 nm PEGSH-functionalized AuNPs before and after secondary ligand addition (A). No significant change in particle size is observed (average ± standard deviation) (B).

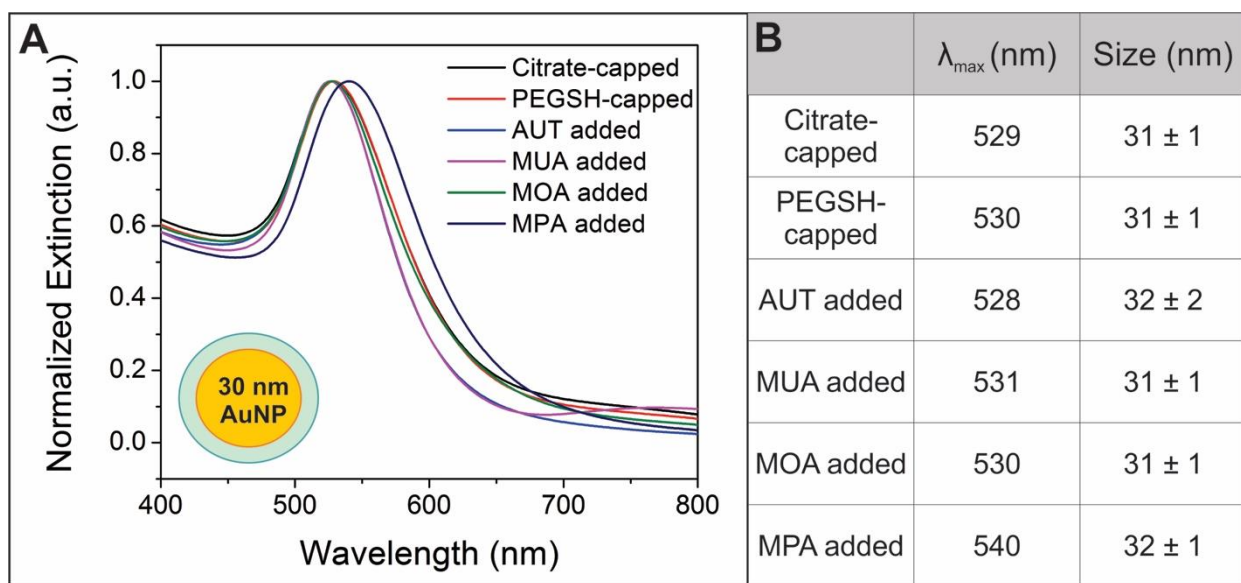


Figure 63. UV-vis spectra for all 30 nm PEGSH-functionalized AuNPs before and after secondary ligand addition (A). No significant change in particle size is observed (average ± standard deviation) (B).

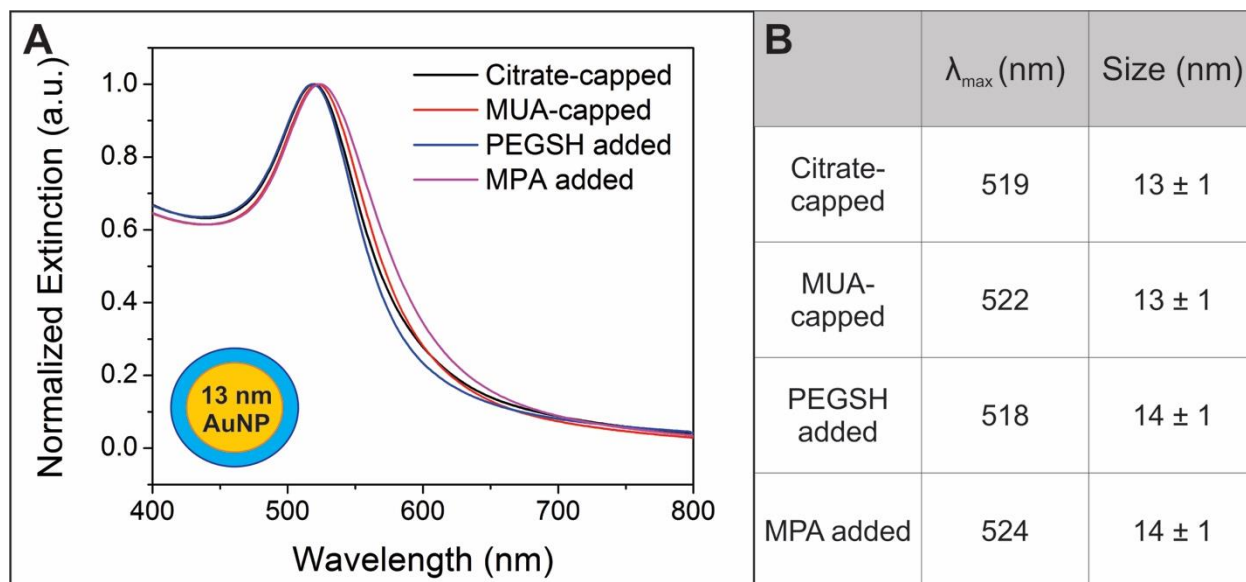


Figure 64. UV-vis spectra for all 13 nm MUA-functionalized AuNPs before and after secondary ligand addition (A). No significant change in particle size is observed (average \pm standard deviation) (B).

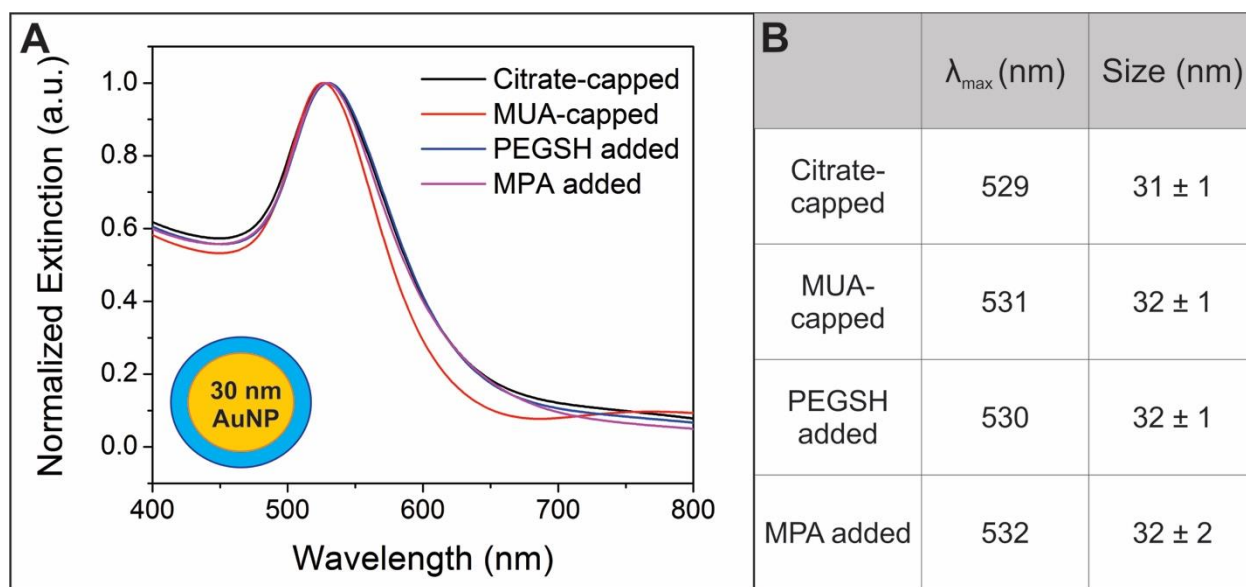


Figure 65. UV-vis spectra for all 30 nm MUA-functionalized AuNPs before and after secondary ligand addition (A). No significant change in particle size is observed (average \pm standard deviation) (B).

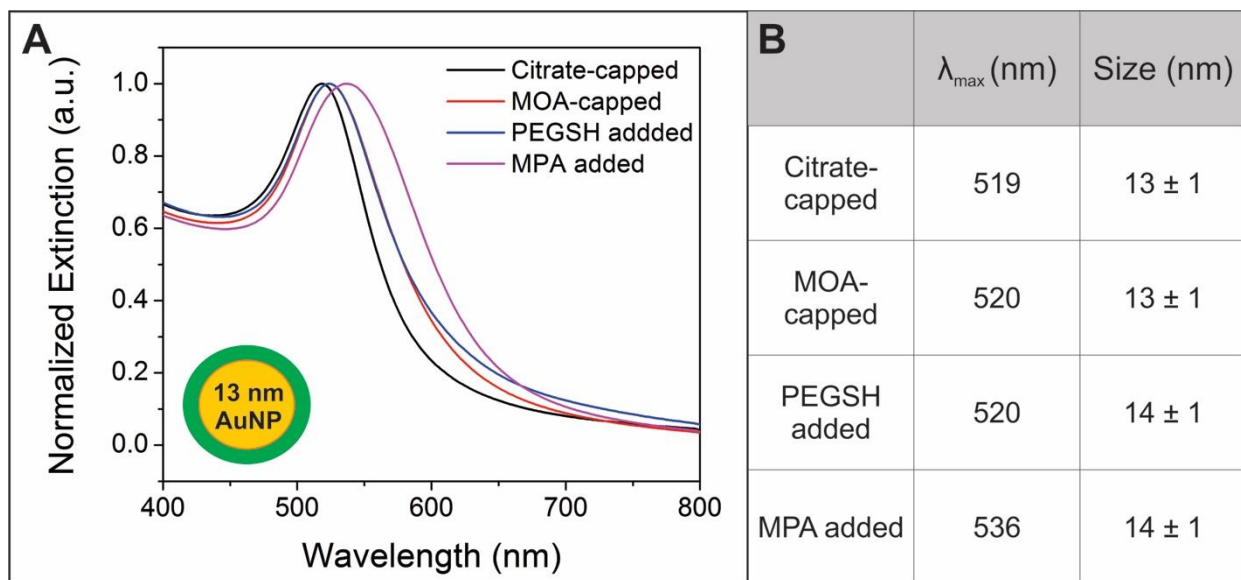


Figure 66. UV-vis spectra for all 13 nm MOA-functionalized AuNPs before and after secondary ligand addition (A). No significant change in particle size is observed (average \pm standard deviation) (B).

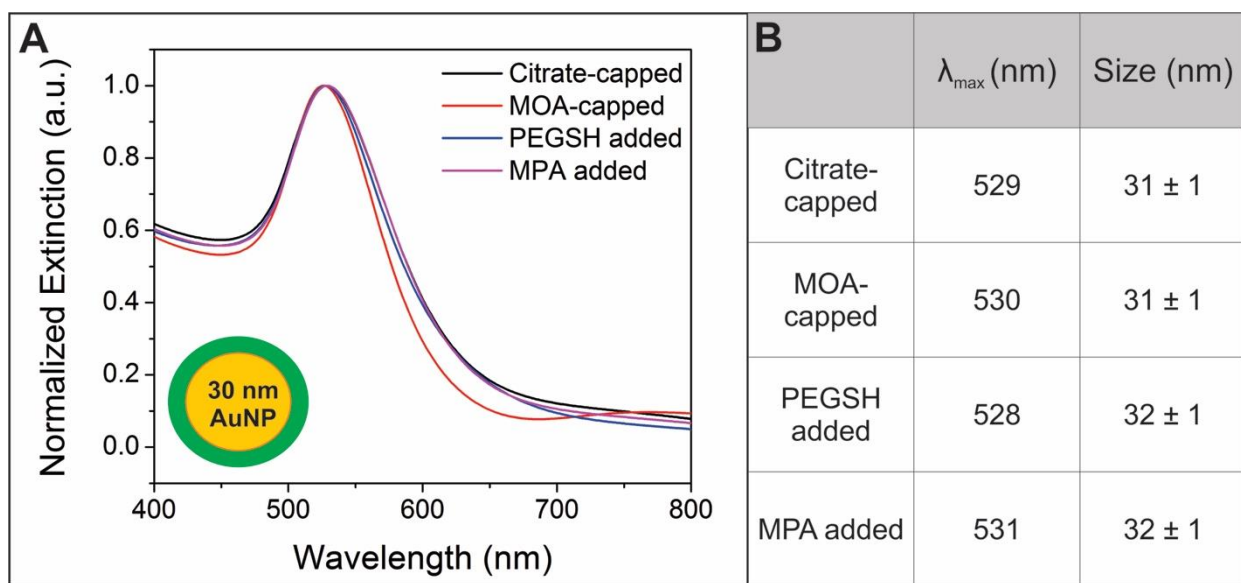


Figure 67. UV-vis spectra for all 30 nm MOA-functionalized AuNPs before and after secondary ligand addition (A). No significant change in particle size is observed (average \pm standard deviation) (B).

APPENDIX B

REPRESENTATIVE ^1H NMR SPECTRA AND GOLD NANOPARTICLE CHARACTERIZATION AFTER LIGAND EXCHANGE

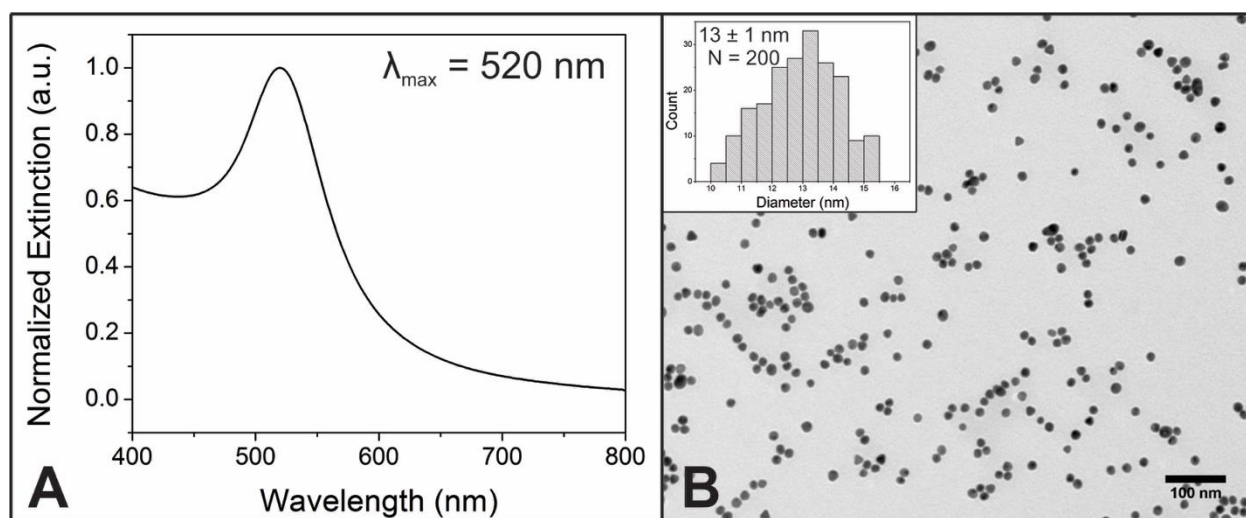


Figure 68. Representative UV-vis-NIR spectrum for 13 nm NPs (A) and corresponding TEM image (B). Inset is a histogram for 13 nm NPs generated from measurements of at least 200 NPs.

Below are representative ^1H NMR spectra of the ligands after AuNP digestion. Spectra are taken in D_2O and at 298 K. In all cases, the indicated ligand peaks are compared to an ACN internal standard. Peaks from both the thiol and alcohol protons are not observed because they exchange with the deuterated medium.

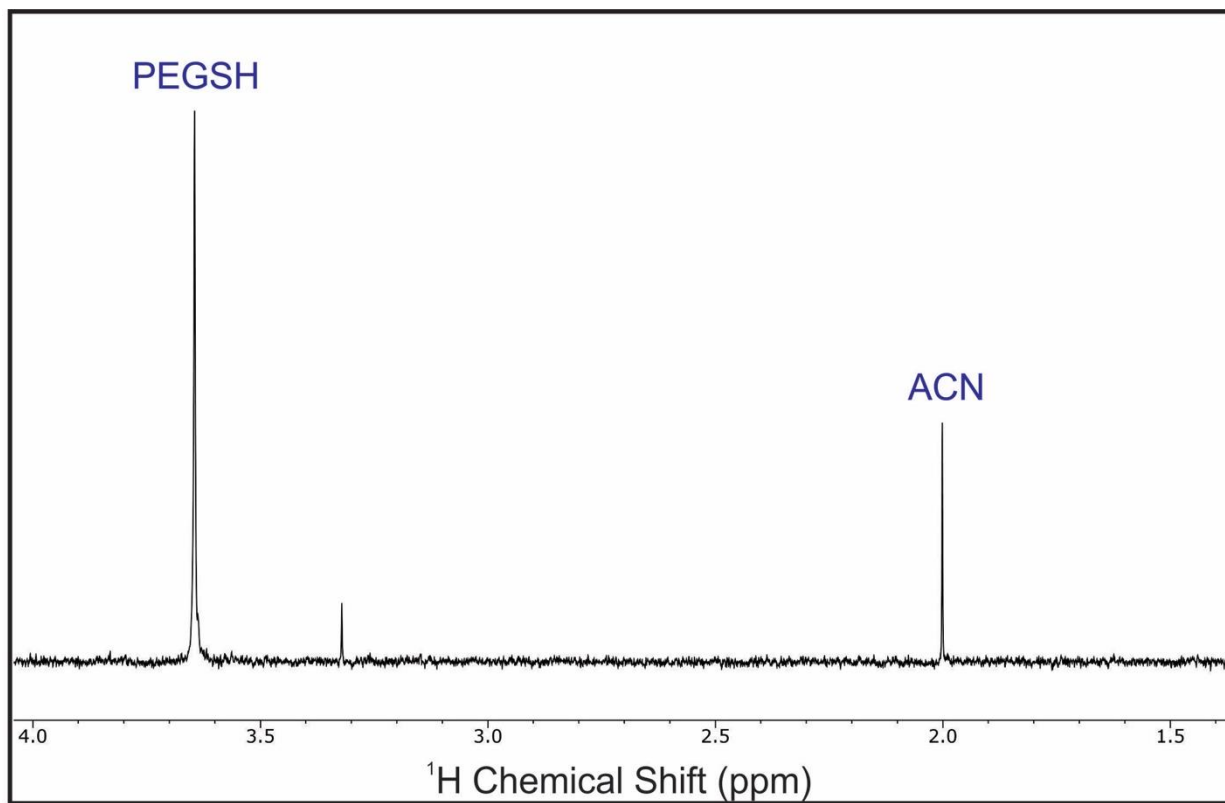


Figure 69. Representative ^1H NMR spectrum of PEGSH after AuNP digestion. For calculation of PEGSH concentration, the labeled peak is integrated and compared to the integrated intensity of the ACN peak.

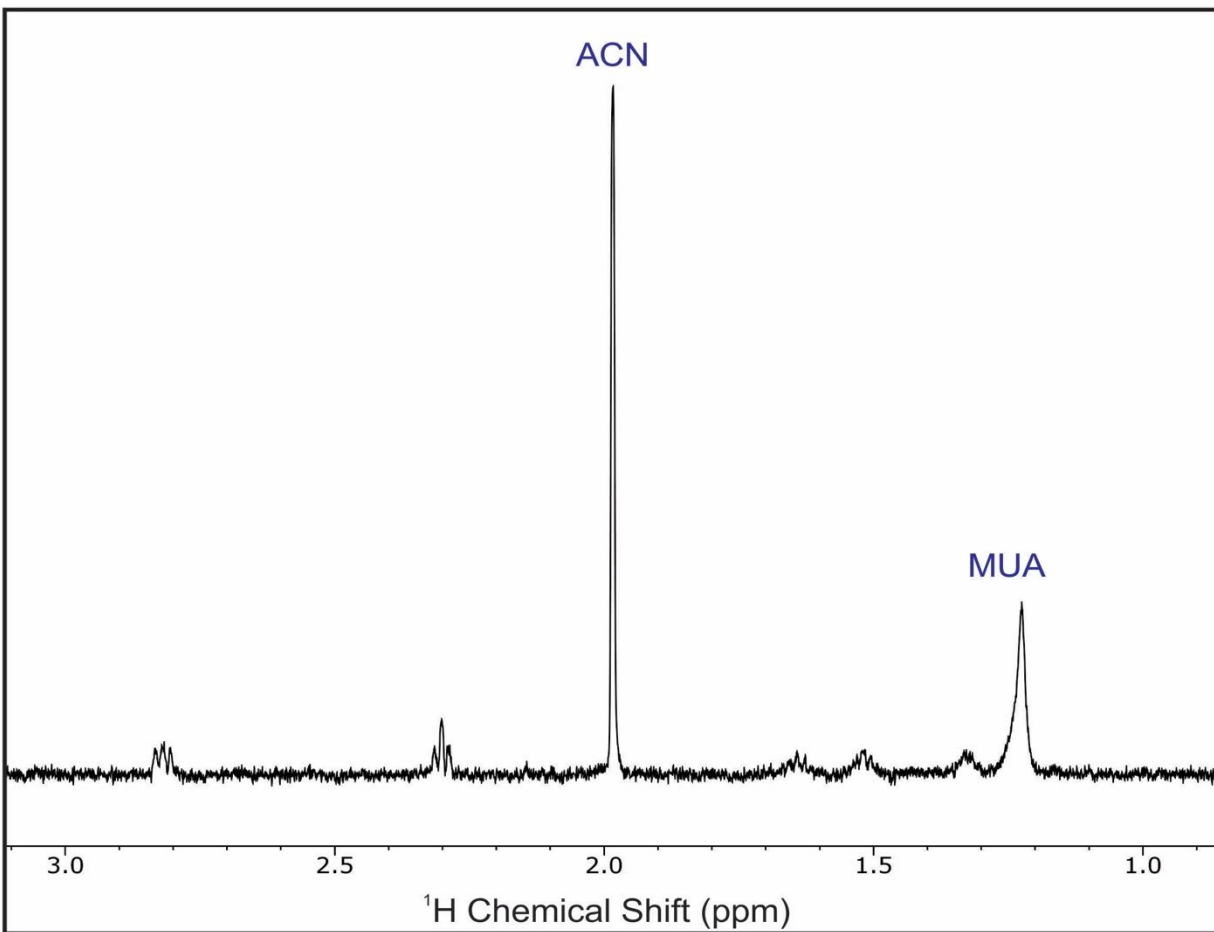


Figure 70. Representative ^1H NMR spectrum of MUA after AuNP digestion. For calculation of PEGSH concentration, the labeled peak is integrated and compared to the integrated intensity of the ACN peak.

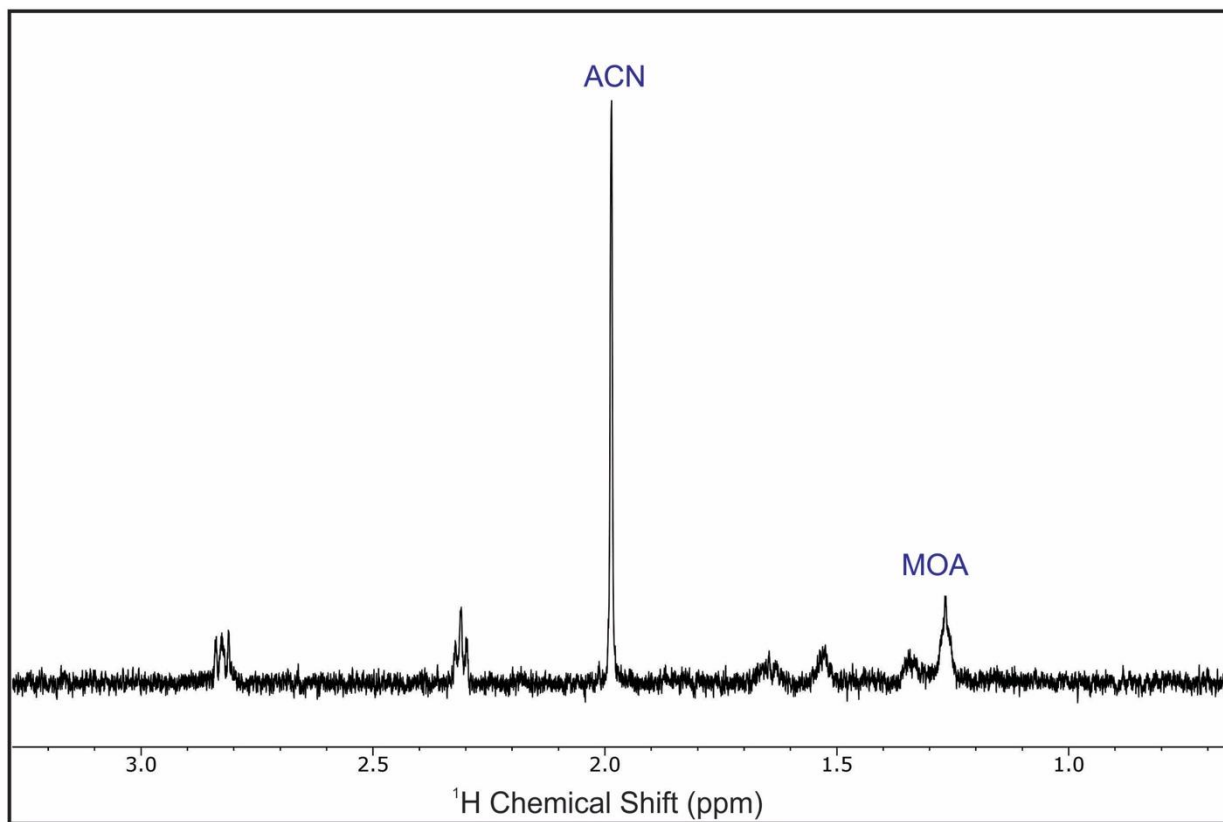


Figure 71. Representative ^1H NMR spectrum of MOA after AuNP digestion. For calculation of PEGSH concentration, the labeled peak is integrated and compared to the integrated intensity of the ACN peak.

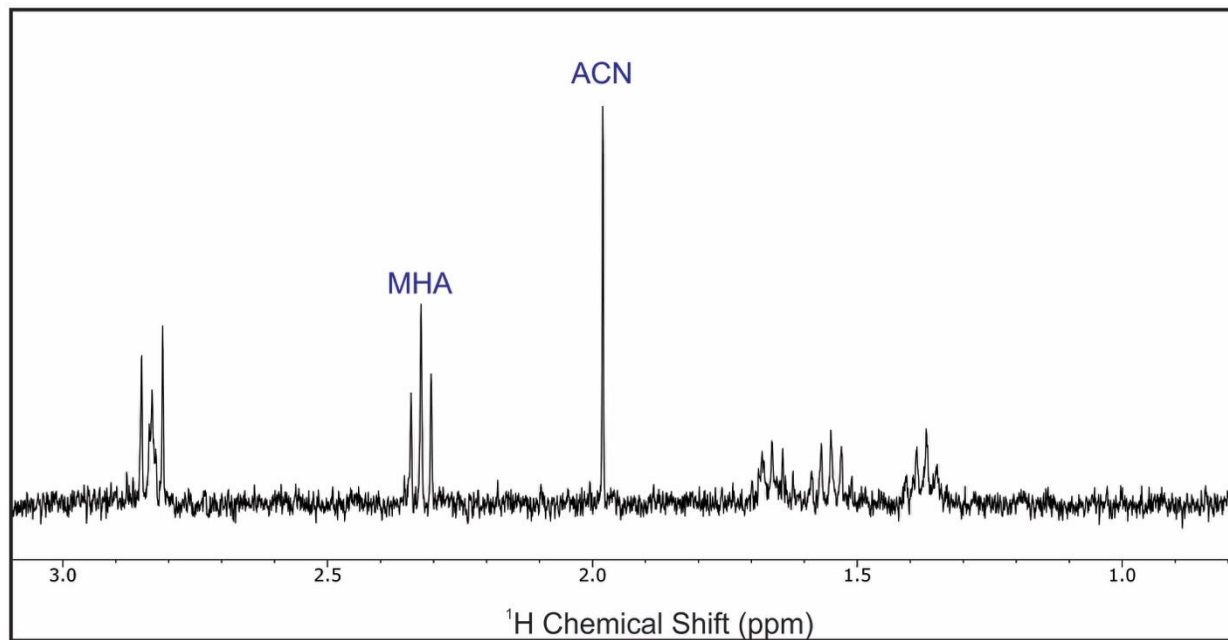


Figure 72. Representative ^1H NMR spectrum of MHA after AuNP digestion. For calculation of PEGSH concentration, the labeled peak is integrated and compared to the integrated intensity of the ACN peak.

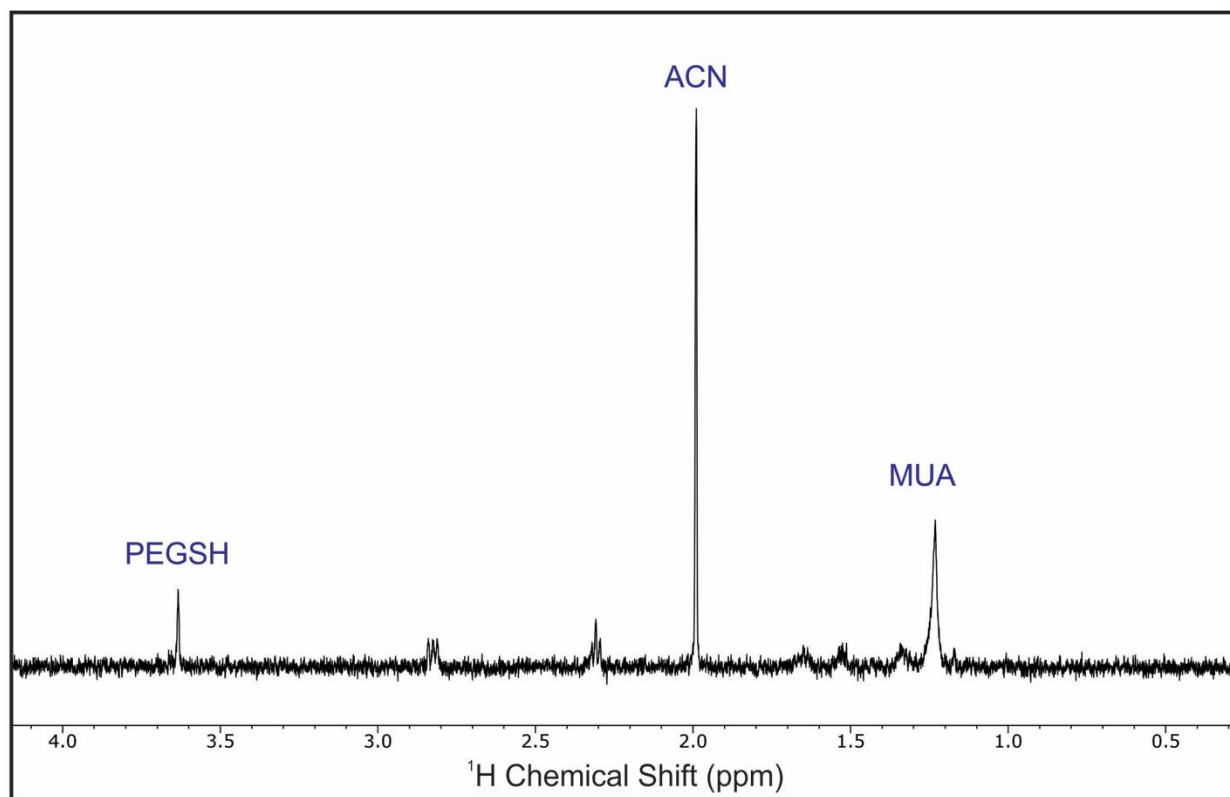


Figure 73. Representative ^1H NMR spectrum after digestion of co-loaded AuNPs with PEGSH and MUA. For calculation of ligand concentrations, the peaks labeled PEGSH and MUA are integrated and compared to the integrated intensity of the ACN peak.

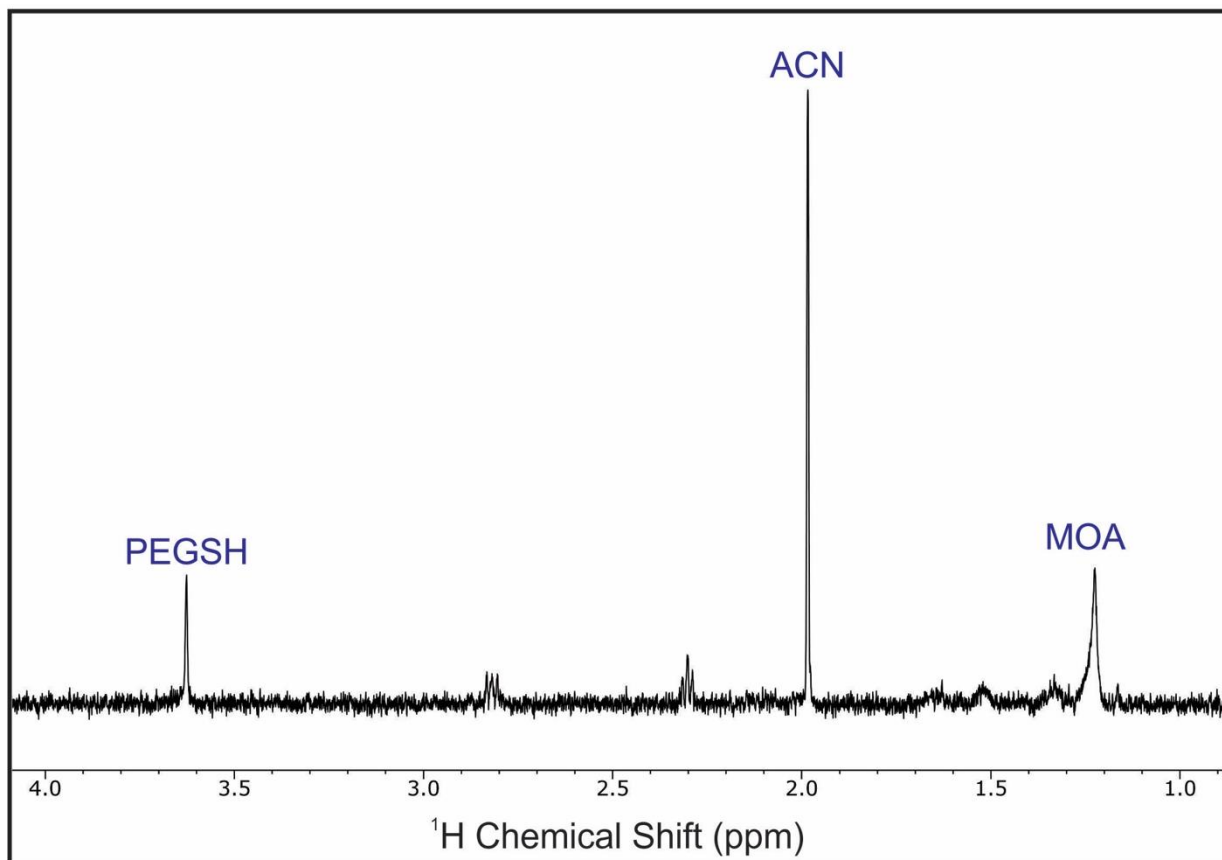


Figure 74. Representative ^1H NMR spectrum after digestion of backfilled AuNPs with MOA backfilled with PEGSH. For calculation of ligand concentrations, the peaks labeled PEGSH and MOA are integrated and compared to the integrated intensity of the ACN peak.

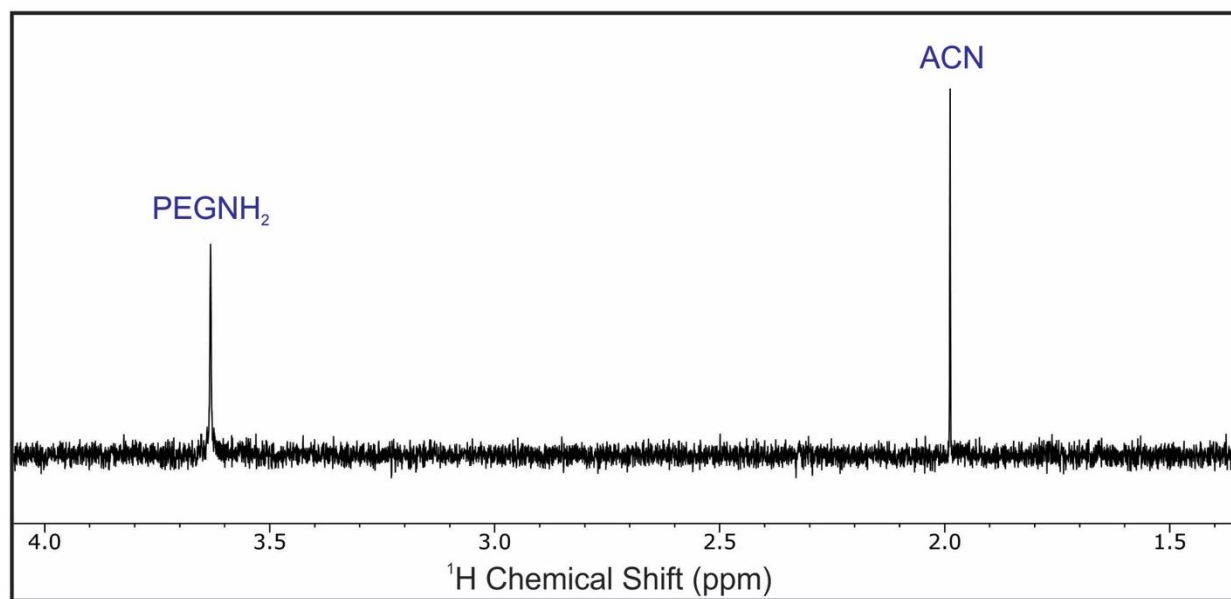


Figure 75. Representative ^1H NMR spectrum of PEGNH₂ after AuNP digestion. For calculation of PEGNH₂ concentration, the labeled peak is integrated and compared to the integrated intensity of the ACN peak.

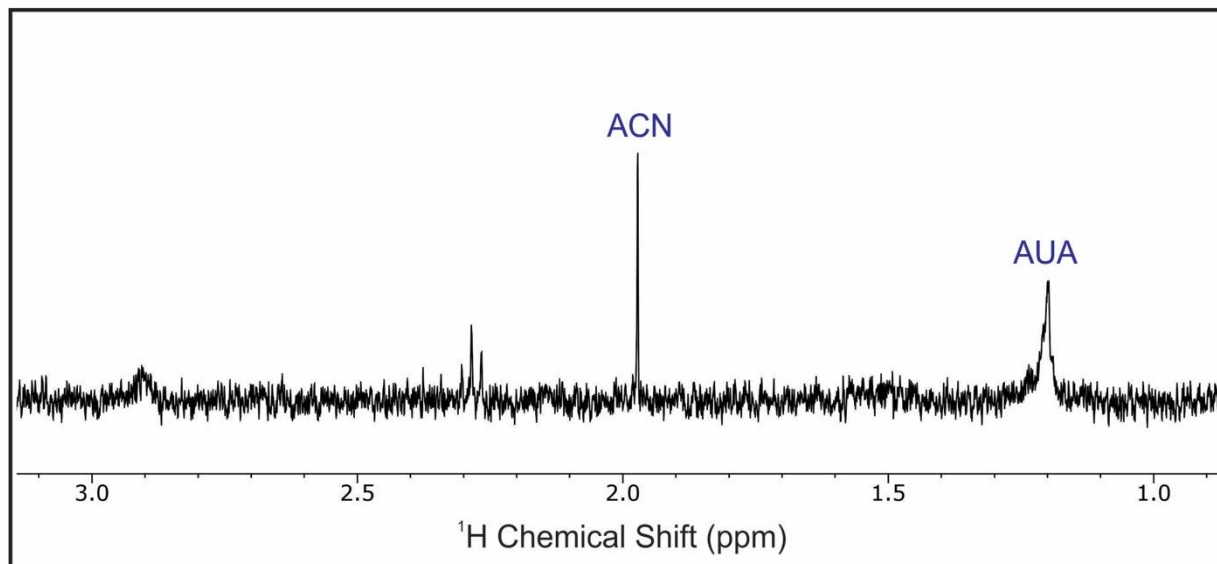


Figure 76. Representative ^1H NMR spectrum of AUA after AuNP digestion. For calculation of AUA concentration, the labeled peak is integrated and compared to the integrated intensity of the ACN peak.

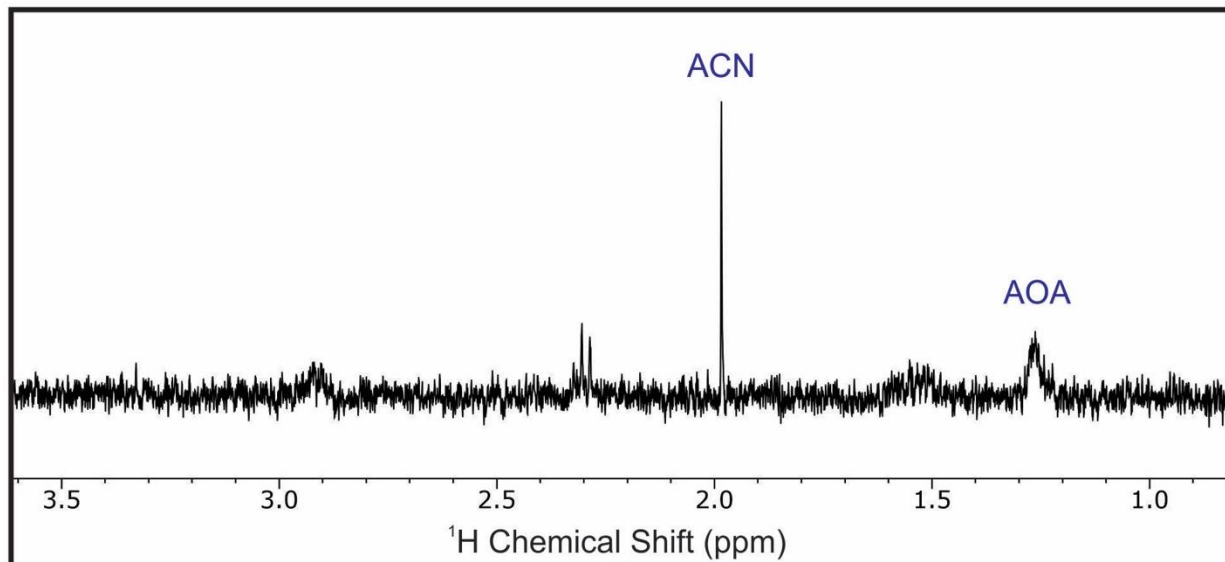


Figure 77. Representative ^1H NMR spectrum of AOA after AuNP digestion. For calculation of AOA concentration, the labeled peak is integrated and compared to the integrated intensity of the ACN peak.

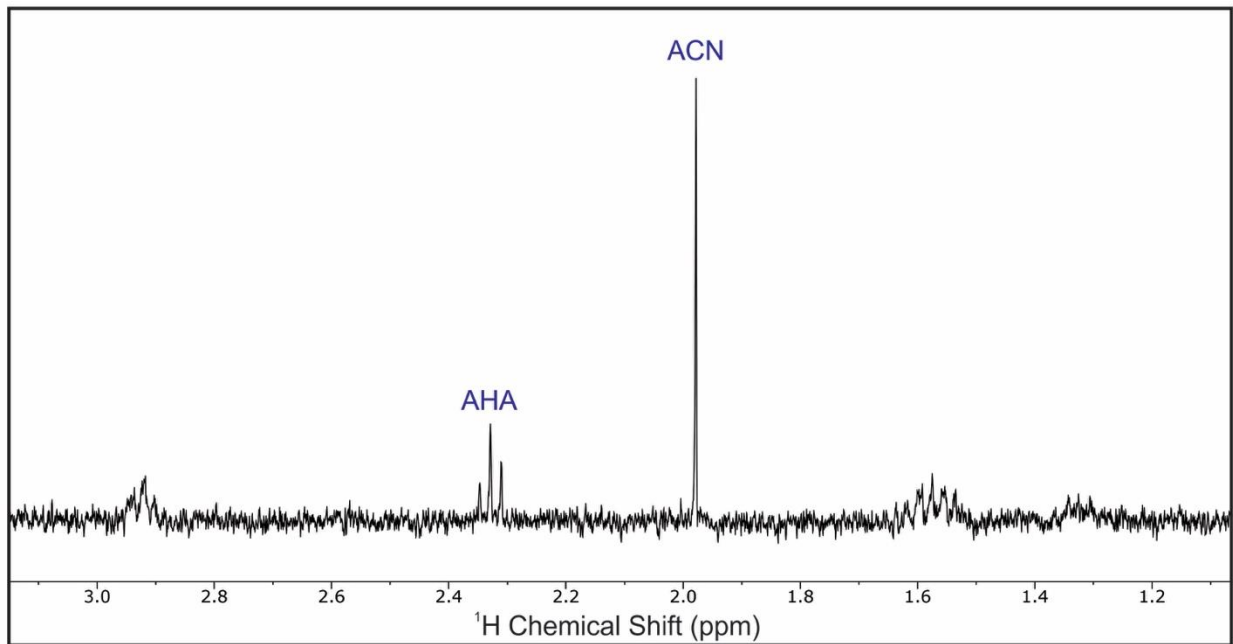


Figure 78. Representative ¹H NMR spectrum of AHA after AuNP digestion. For calculation of AHA concentration, the labeled peak is integrated and compared to the integrated intensity of the ACN peak.

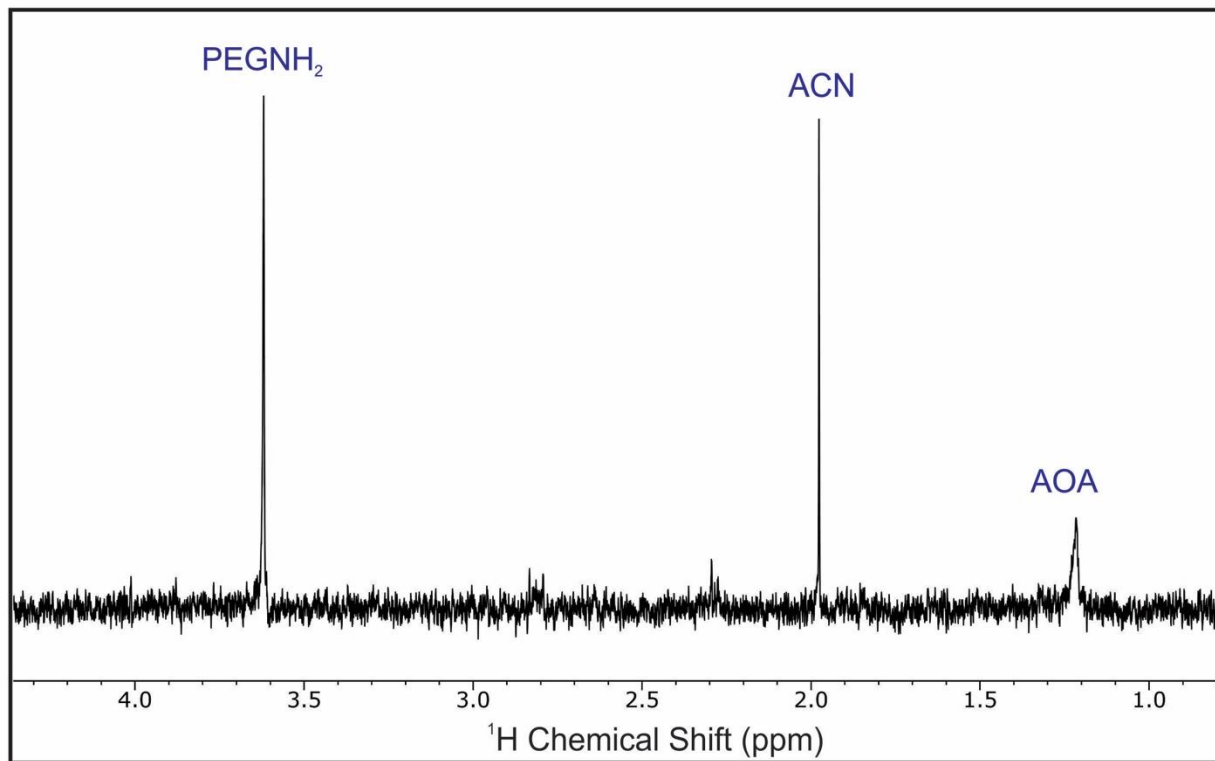


Figure 79. Representative ^1H NMR spectrum after digestion of co-loaded AuNPs with PEGNH₂ and AOA. For calculation of ligand concentrations, the peaks labeled PEGNH₂ and AOA are integrated and compared to the integrated intensity of the ACN peak.

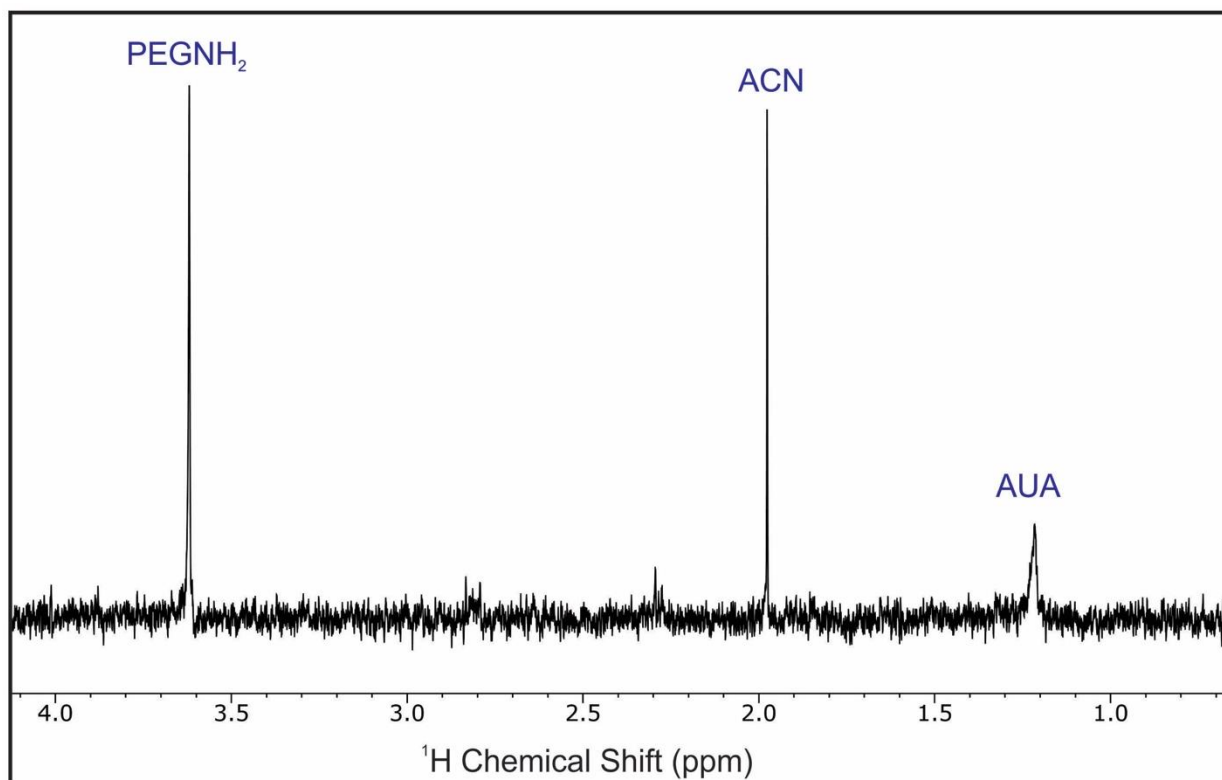


Figure 80. Representative ^1H NMR spectrum after digestion of backfilled AuNPs with AUA backfilled with PEGNH₂. For calculation of ligand concentrations, the peaks labeled PEGNH₂ and AUA are integrated and compared to the integrated intensity of the ACN peak.

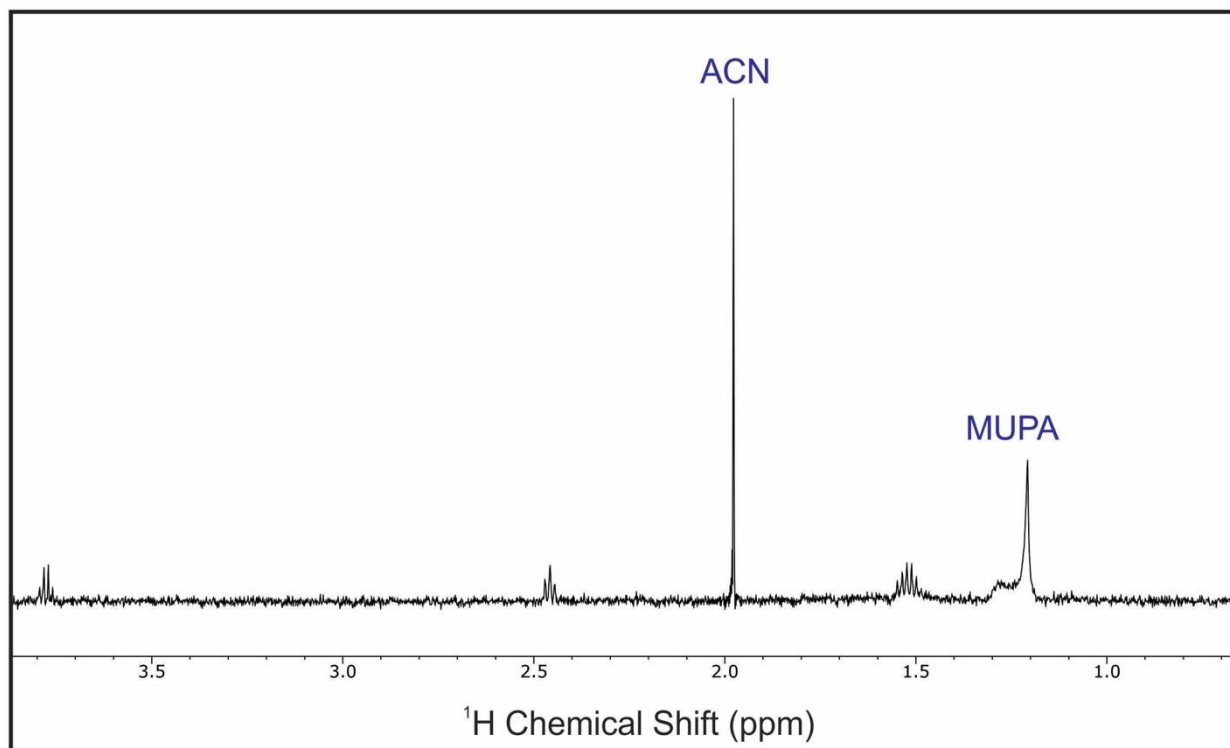


Figure 81. Representative ^1H NMR spectrum of MUPA after AuNP digestion. For calculation of MUPA concentration, the labeled peak is integrated and compared to the integrated intensity of the ACN peak.

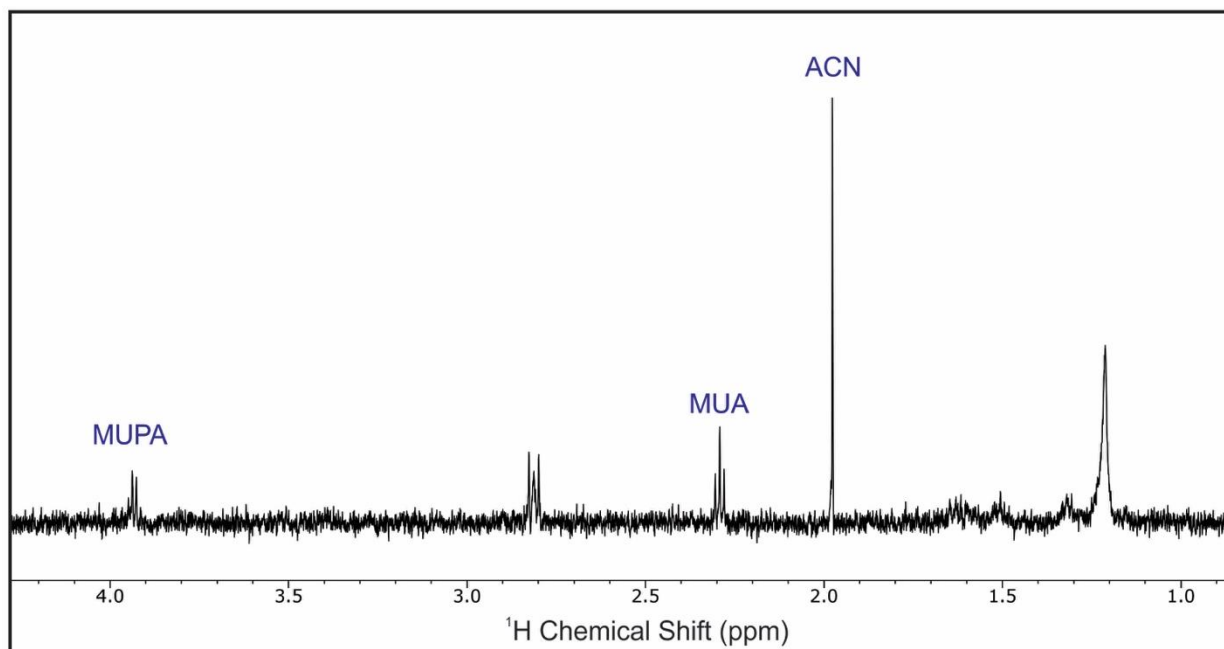


Figure 82. Representative ^1H NMR spectrum after digestion of MUPA and MUA co-loaded AuNPs. For calculation of ligand concentrations, the peaks labeled MUA and MUPA are integrated and compared to the integrated intensity of the ACN peak.

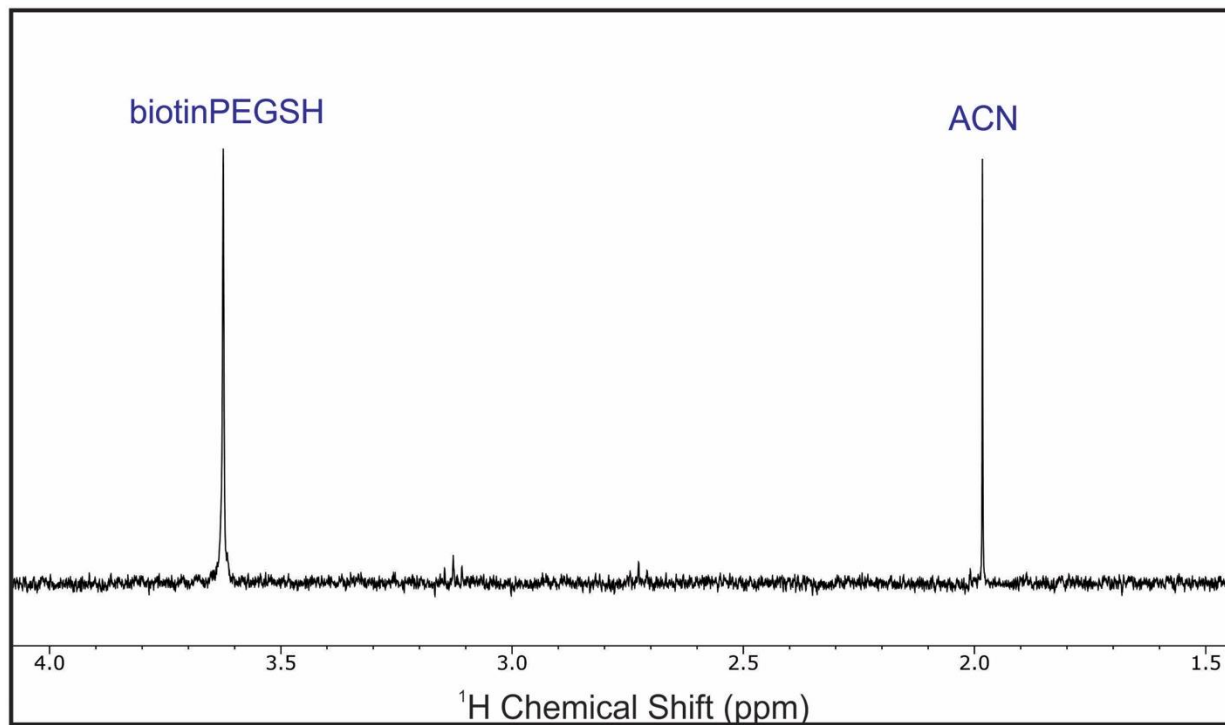


Figure 83. Representative ^1H NMR spectrum of biotinPEGSH after AuNP digestion. For calculation of biotinPEGSH concentration, the labeled peak is integrated and compared to the integrated intensity of the ACN peak.

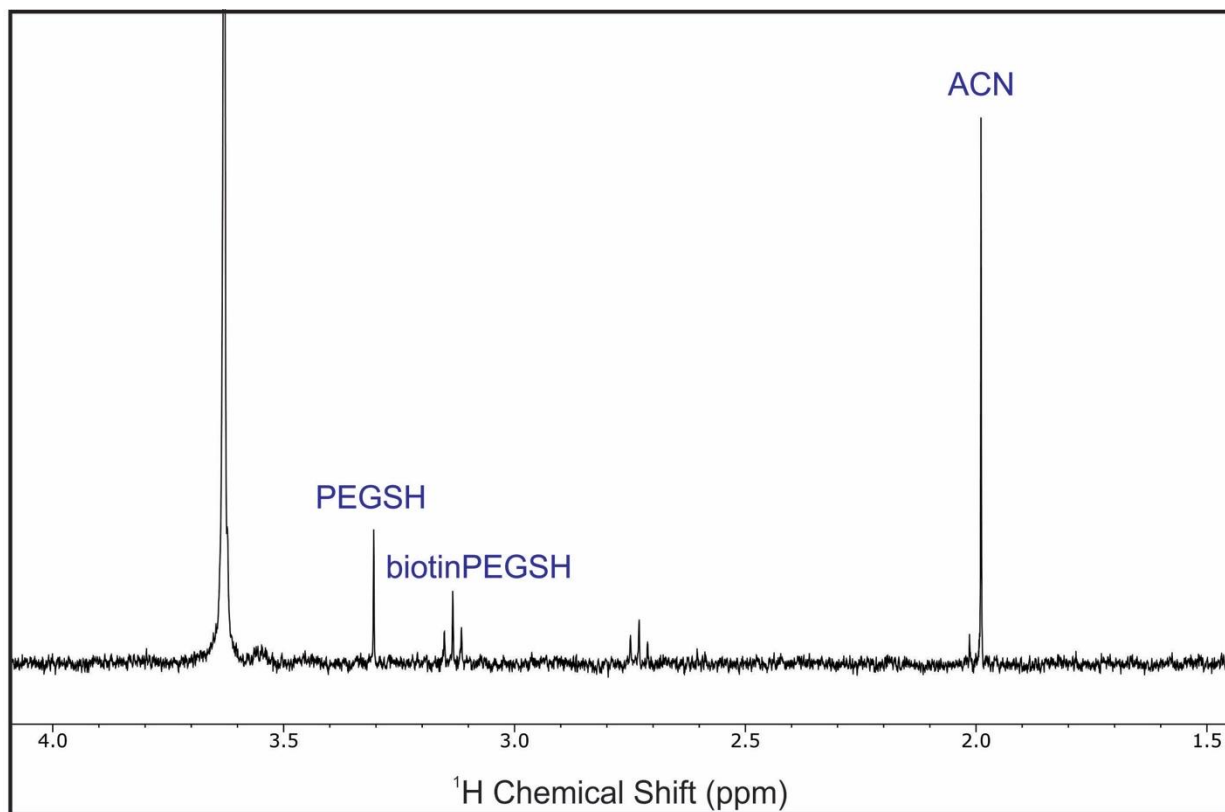


Figure 84. Representative ^1H NMR spectrum after digestion of biotinPEGSH and PEGSH co-loaded AuNPs. For calculation of ligand concentrations, the peaks labeled biotinPEGSH and PEGSH are integrated and compared to the integrated intensity of the ACN peak.

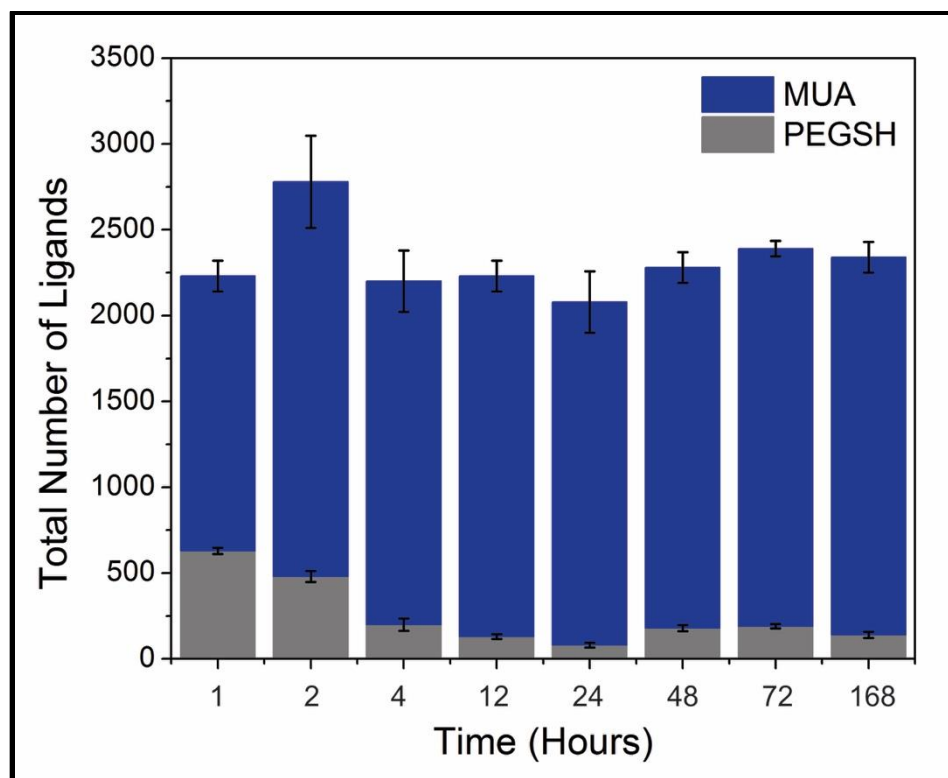


Figure 85. Graph of the total number of ligands on PEGSH AuNPs backfilled with MUA as a function of time for 13 nm AuNPs, where the error bars represent the standard error of at least 5 trials. Results indicate that ligand loading reaches consistent values on the timescale of 2-3 hours under the conditions tested.

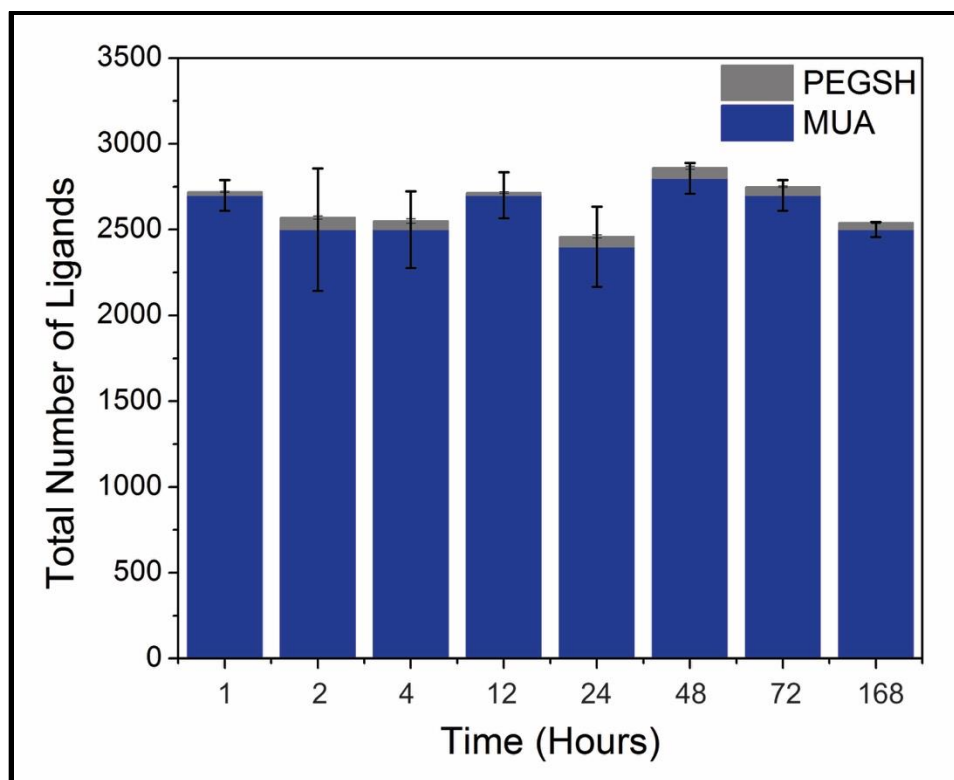


Figure 86. Graph of the total number of ligands on MUA AuNPs backfilled with PEGSH as a function of time for 13 nm AuNPs, where the error bars represent the standard error of at least 5 trials. Results indicate that ligand loading reaches consistent values on the timescale of 2-3 hours under the conditions tested.

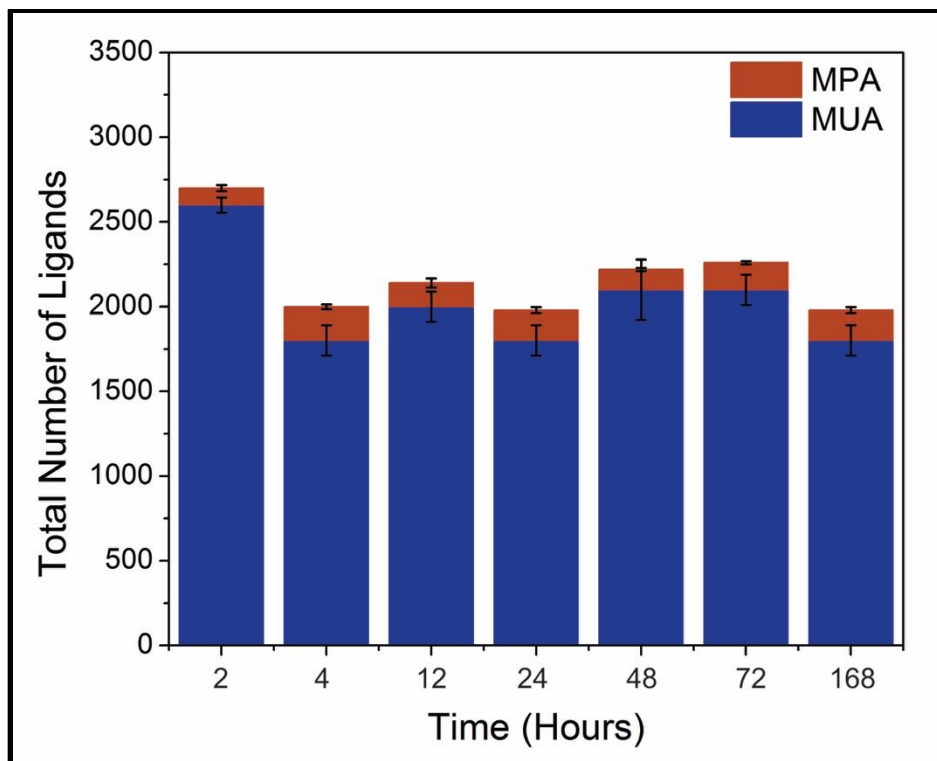


Figure 87. Graphs of the total number of ligands on MUA AuNPs backfilled with MPA as a function of time for 13 nm AuNPs, where the error bars represent the standard error of at least 5 trials. Results indicate that ligand loading reaches consistent values on the timescale of 2-3 hours under the conditions tested.

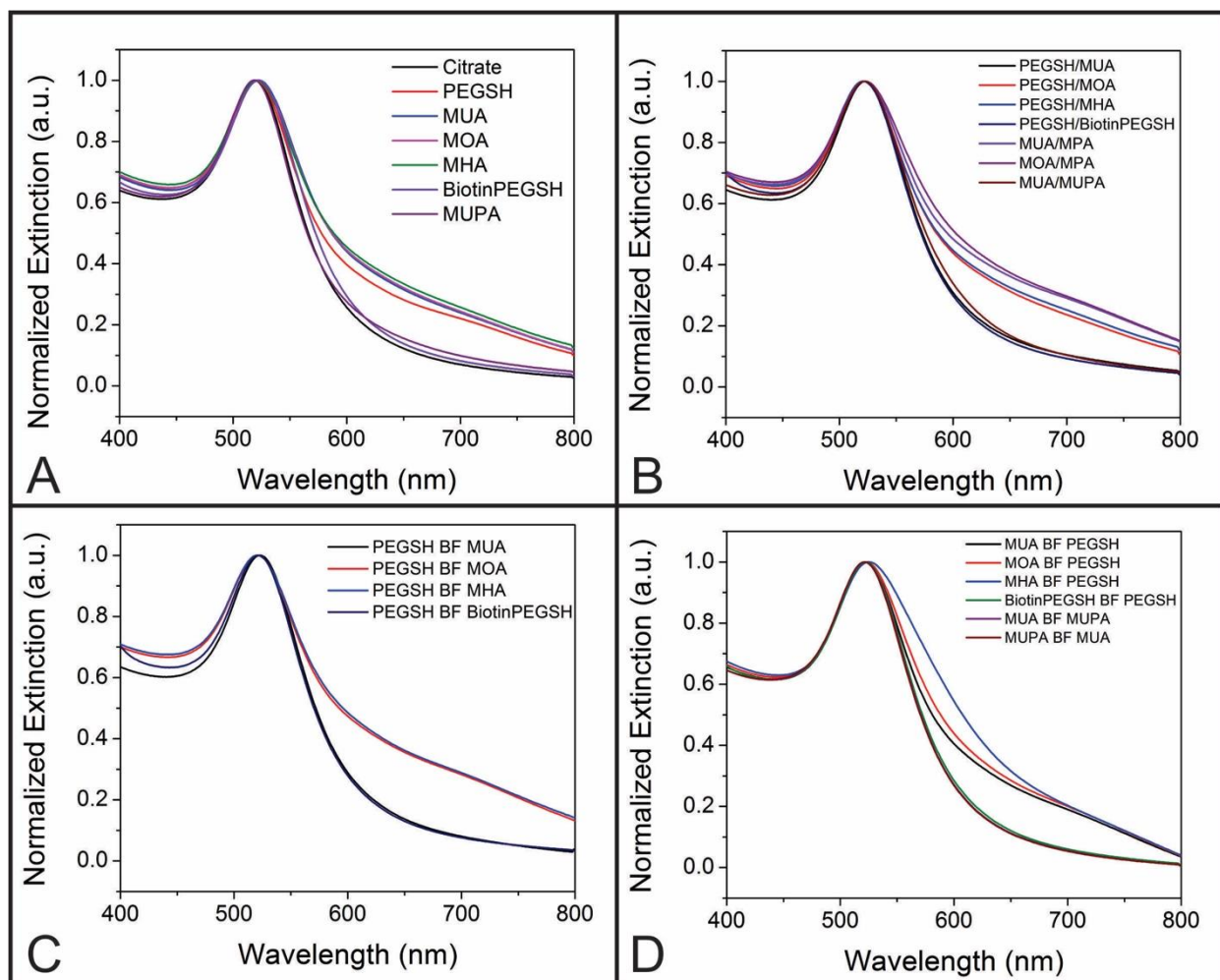


Figure 88. UV-vis-NIR spectra for all 13 nm AuNPs before and after ligand exchange from citrate to a thiolated ligand (A), after co-loading with two thiolated ligands (B), after backfilling PEGSH-capped particles with a secondary thiolated ligand (C), and after backfilling with PEGSH from other thiolated ligand-capped particles (D).

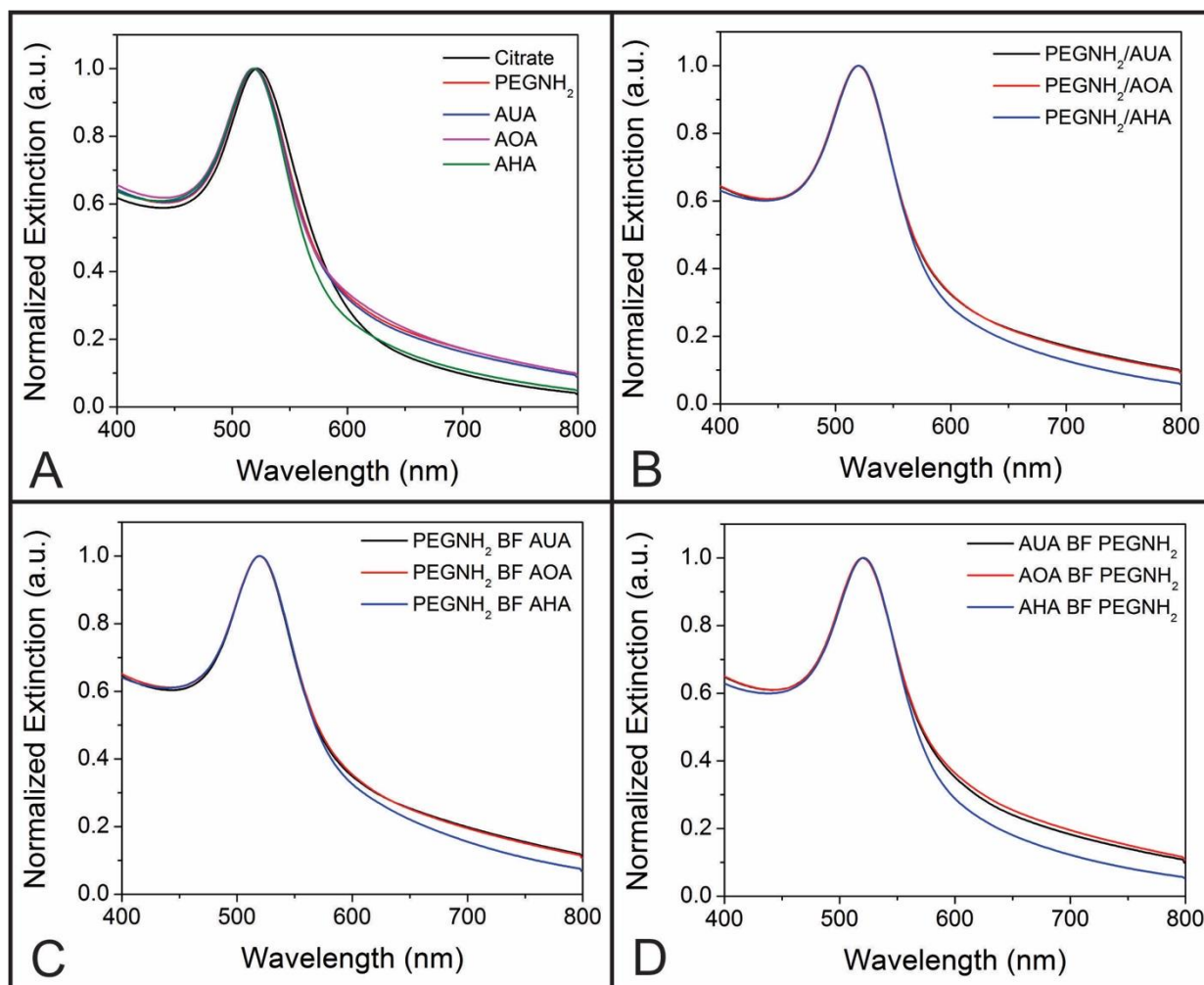


Figure 89. UV-vis-NIR spectra for all 13 nm AuNPs before and after ligand exchange from citrate to an aminated ligand (A), after co-loading with two aminated ligands (B), after backfilling PEGNH₂-capped particles with a secondary aminated ligand (C), and after backfilling with PEGNH₂ from other aminated ligand-capped particles (D).

APPENDIX C

REPRESENTATIVE ^1H NMR SPECTRA

Below are representative ^1H NMR spectra of the ligands after AuNP digestion. Spectra are taken in D_2O and at 298 K. In all cases, the indicated ligand peaks are compared to an ACN internal standard. Peaks from both the thiol and alcohol protons are not observed because they exchange with the deuterated medium.

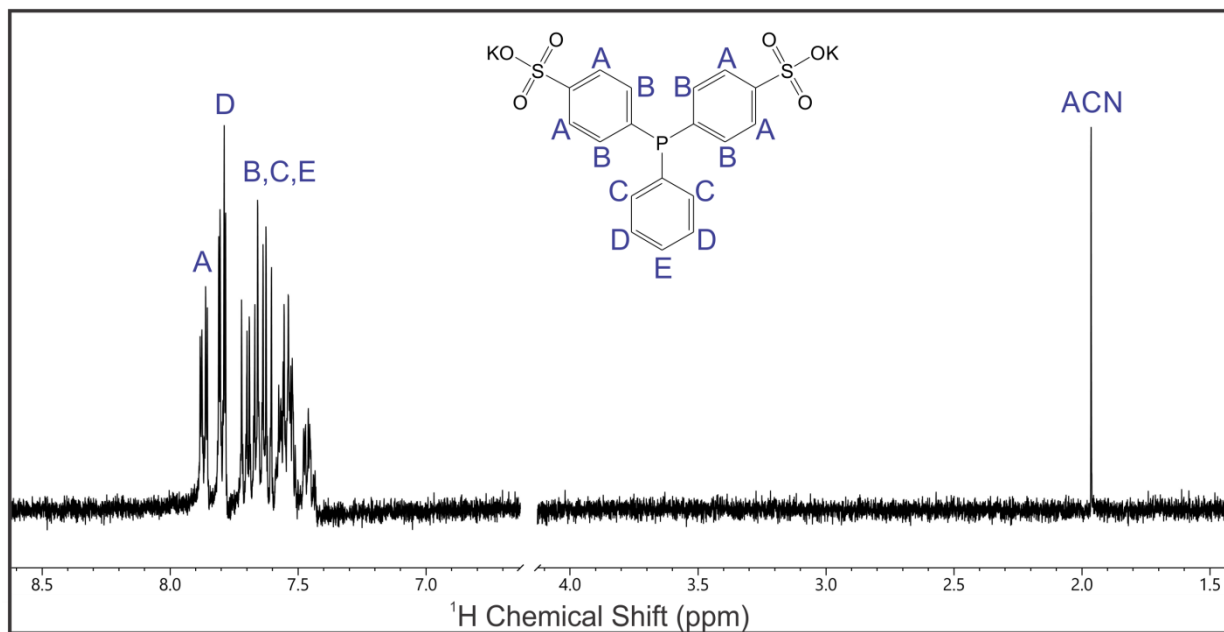


Figure 90. Representative ^1H NMR spectrum after digestion of BSPP-capped AuNPs. For calculation of ligand concentrations, the peak labeled BSPP is integrated and compared to the integrated intensity of the ACN peak.

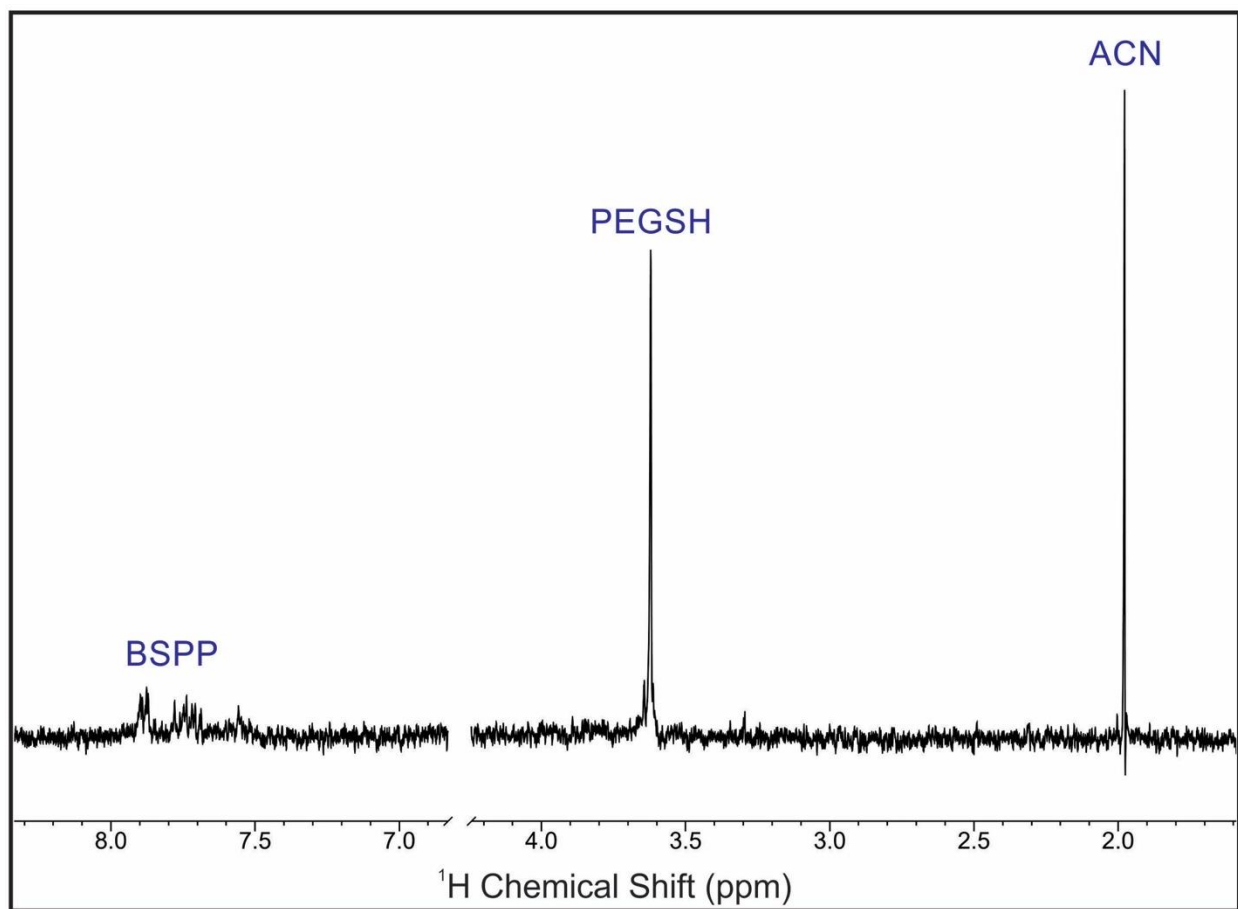


Figure 91. Representative ^1H NMR spectrum after digestion of BSPP and PEGSH co-loaded AuNPs. For calculation of ligand concentrations, the peaks labeled BSPP and PEGSH are integrated and compared to the integrated intensity of the ACN peak.

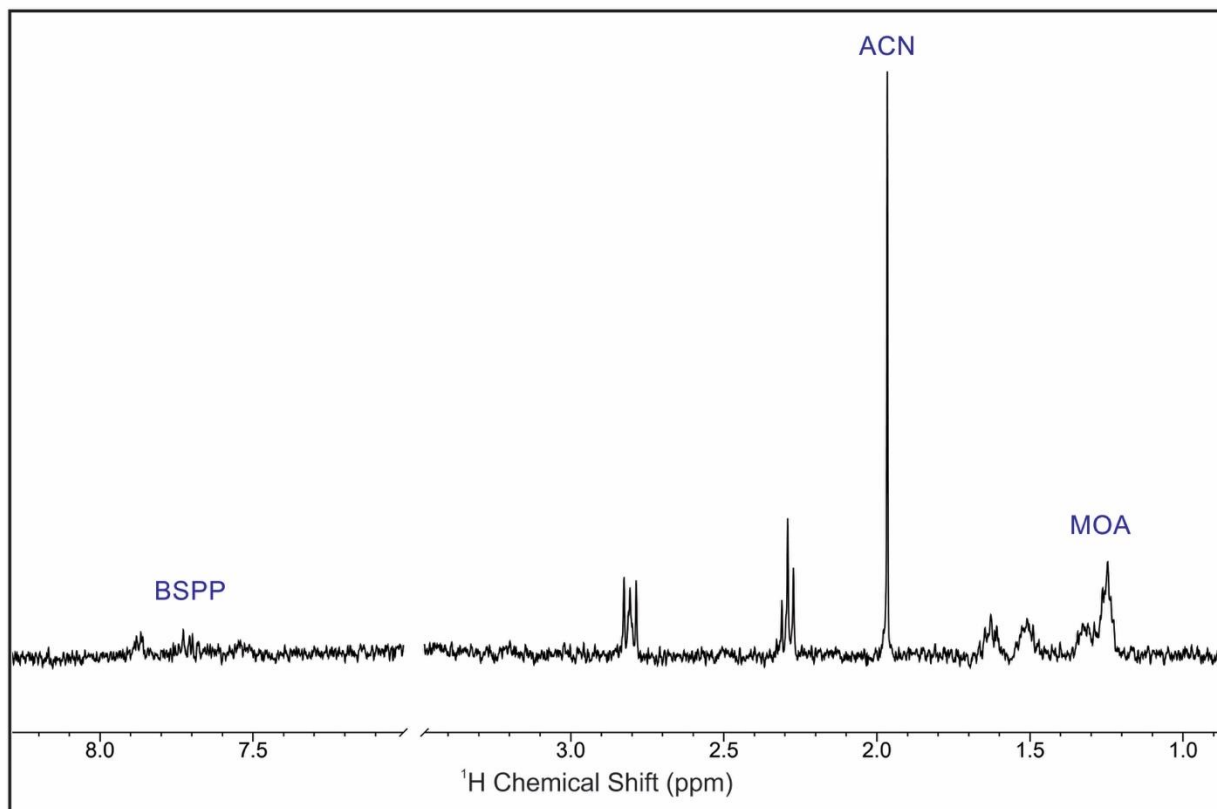


Figure 92. Representative ^1H NMR spectrum after digestion of BSPP and MOA co-loaded AuNPs. For calculation of ligand concentrations, the peaks labeled BSPP and MOA are integrated and compared to the integrated intensity of the ACN peak.

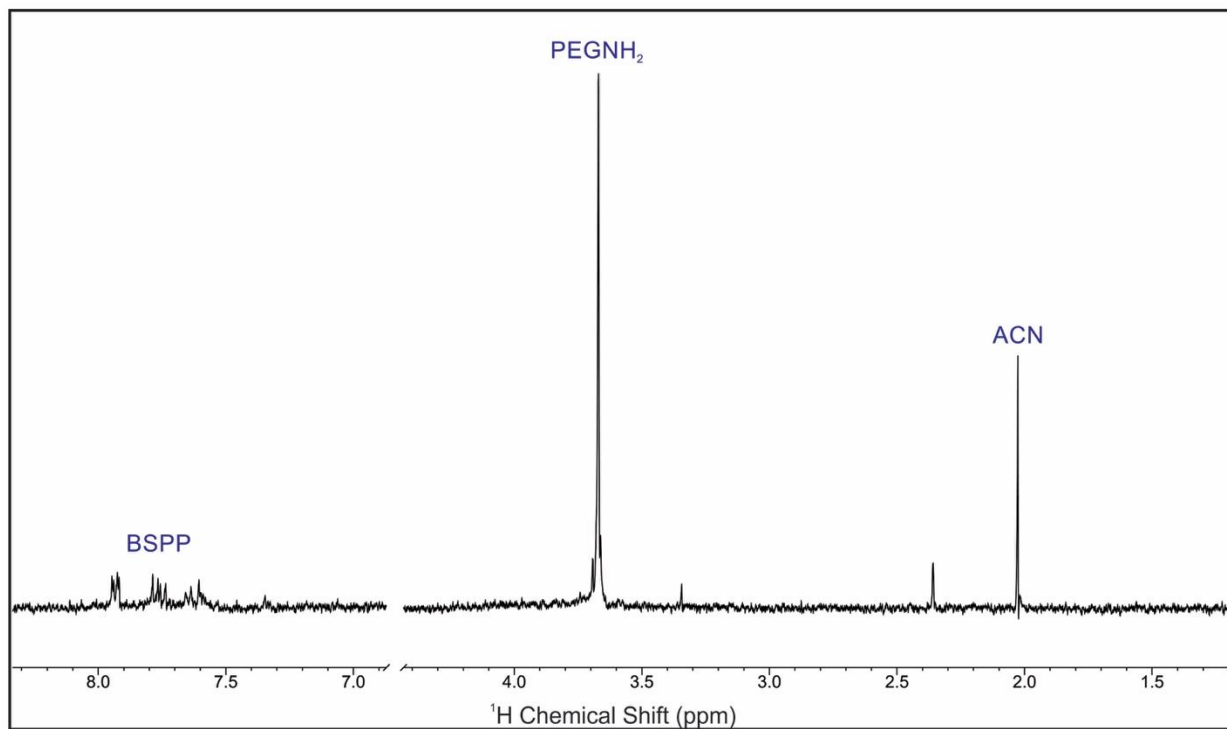


Figure 93. Representative ^1H NMR spectrum after digestion of BSPP and PEGNH₂ co-loaded AuNPs. For calculation of ligand concentrations, the peaks labeled BSPP and PEGNH₂ are integrated and compared to the integrated intensity of the ACN peak.

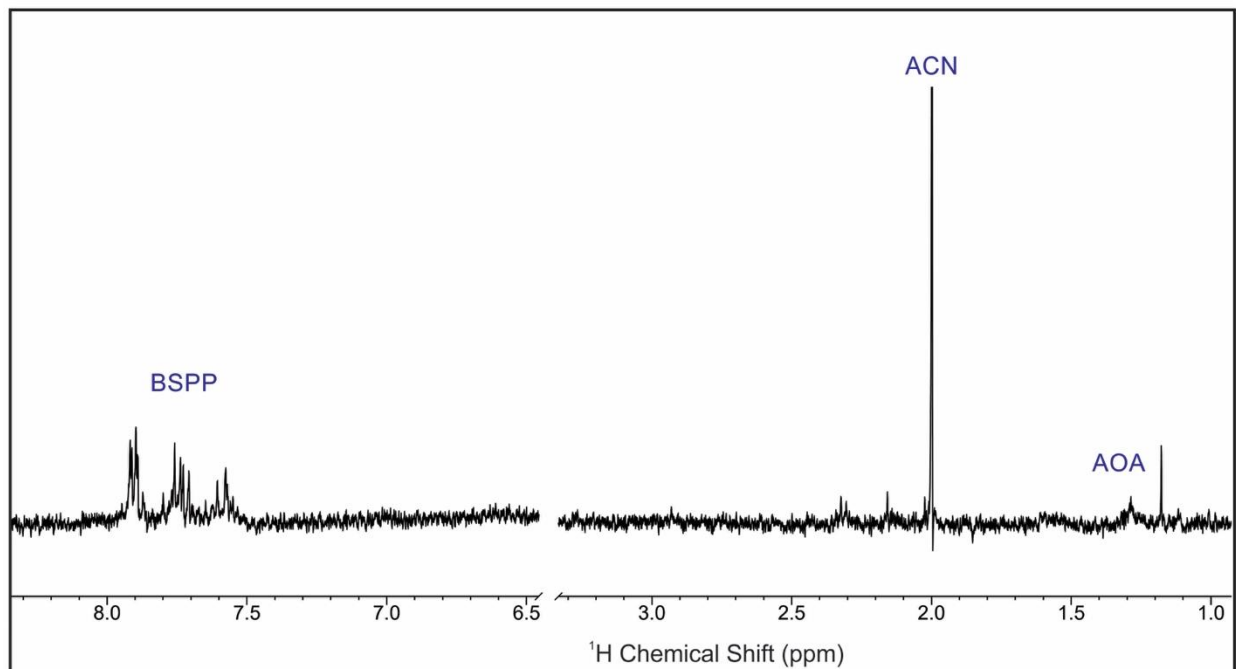


Figure 94. Representative ^1H NMR spectrum after digestion of BSPP and AOA co-loaded AuNPs. For calculation of ligand concentrations, the peaks labeled BSPP and AOA are integrated and compared to the integrated intensity of the ACN peak.

APPENDIX D

REPRESENTATIVE ^1H NMR SPECTRA

Below are representative ^1H NMR spectra acquired in D_2O of the ligands after digestion of AuNP conjugates by aqua regia. Spectra below are taken at 298 K. Ligand peaks are compared to an ACN internal standard, unless otherwise noted. In all cases, peaks from both the thiol and carboxylic acid protons are not observed because they exchange with the deuterated medium.

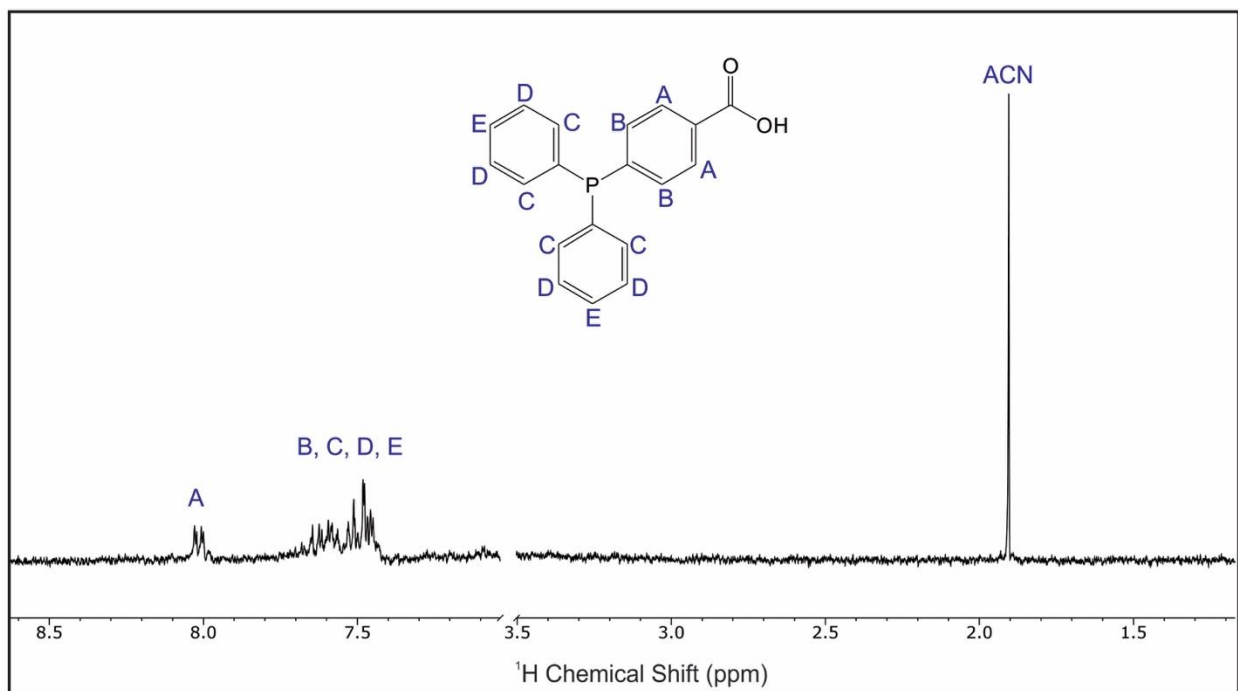


Figure 95. Representative ^1H NMR spectrum of 4-DPPBA after digestion of the AuNPs with its labeled structure corresponding to plotted ^1H NMR peak locations. For the calculation of 4-DPPBA concentration, Peaks A-E (due to peak overlap) are integrated and compared to the integrated intensity of the ACN peak.

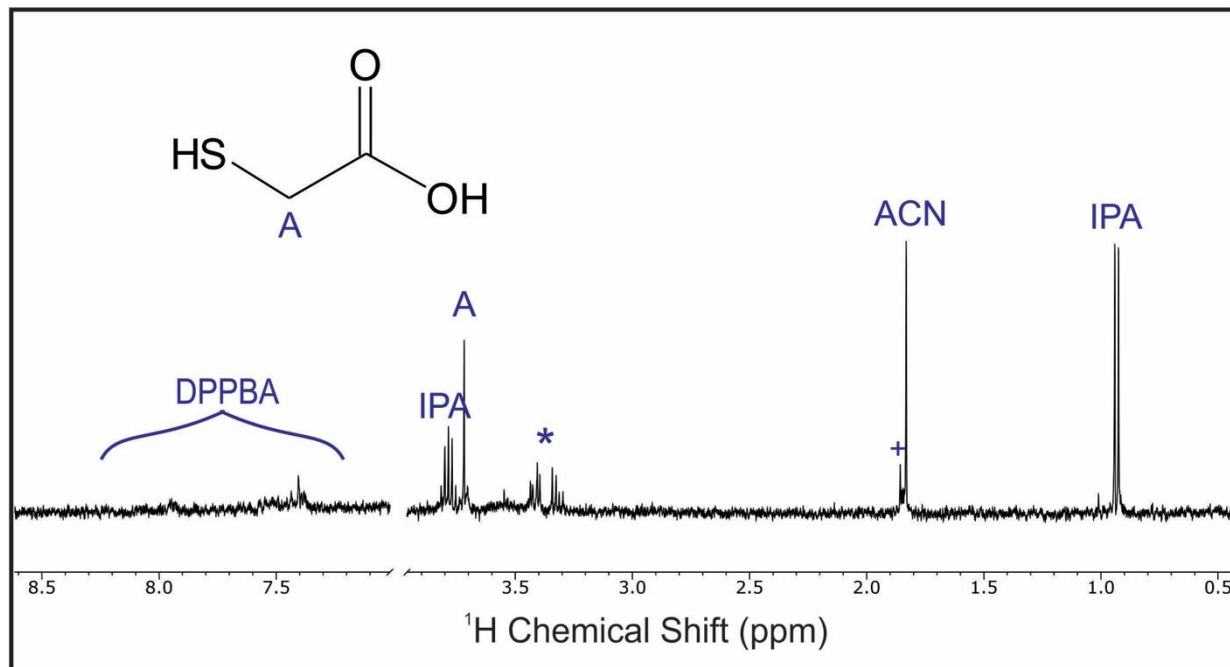


Figure 96. Representative ^1H NMR spectrum of TGA-exchanged AuNPs following digestion with aqua regia with its labeled structure corresponding to plotted ^1H NMR peak locations. Due to overlap of the impurity peak (+) with the ACN internal standard peak, isopropanol (IPA) is used as an internal standard. The impurity peak (*) is residual polymeric material (glycerol) from the molecular weight cut-off filters.

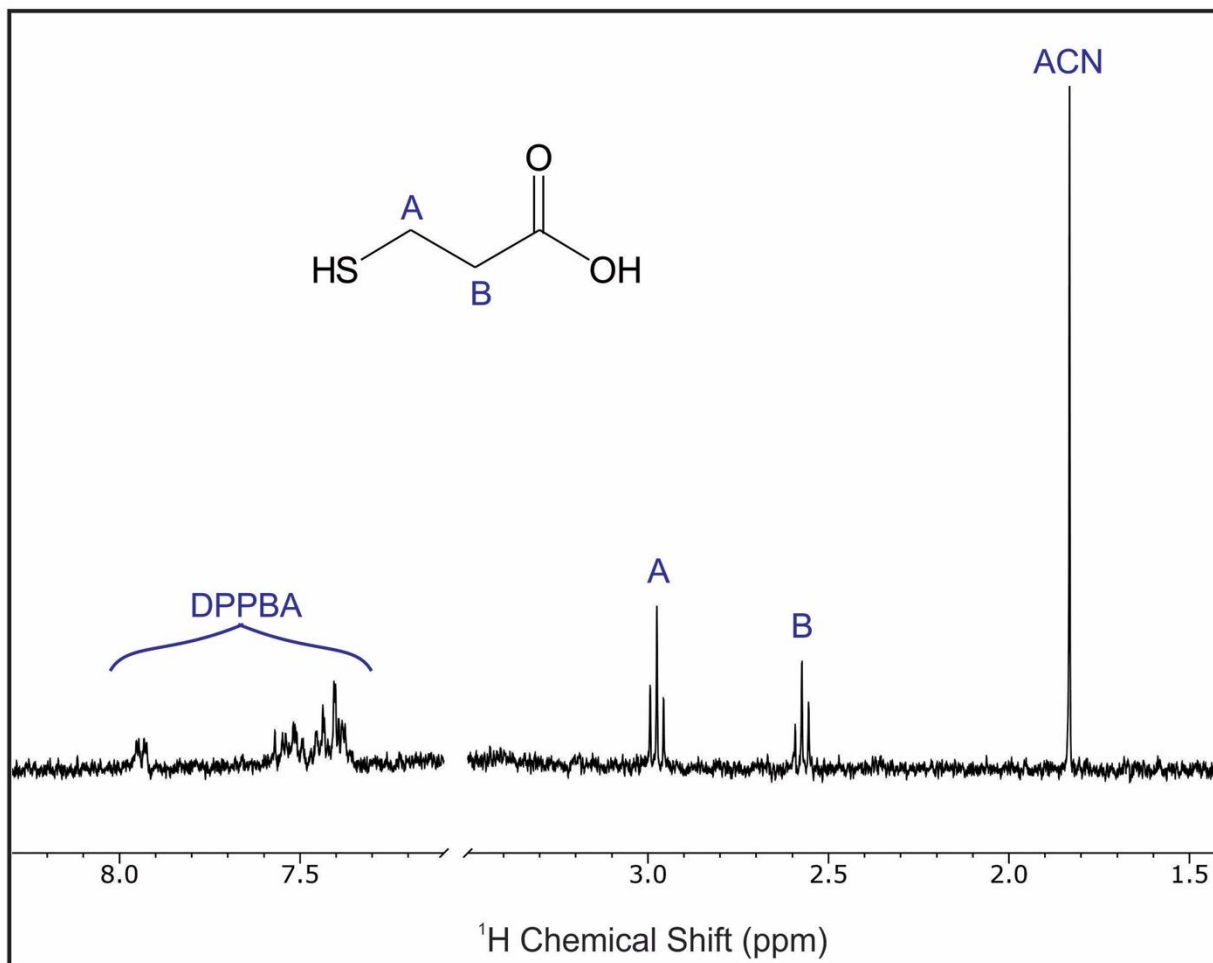


Figure 97. Representative ^1H NMR spectrum of MPA-exchanged AuNPs following digestion in aqua regia with its labeled structure corresponding to plotted ^1H NMR peak locations. For the calculation of MPA concentration, Peaks A and B are integrated and compared to the integrated intensity of the ACN peak.

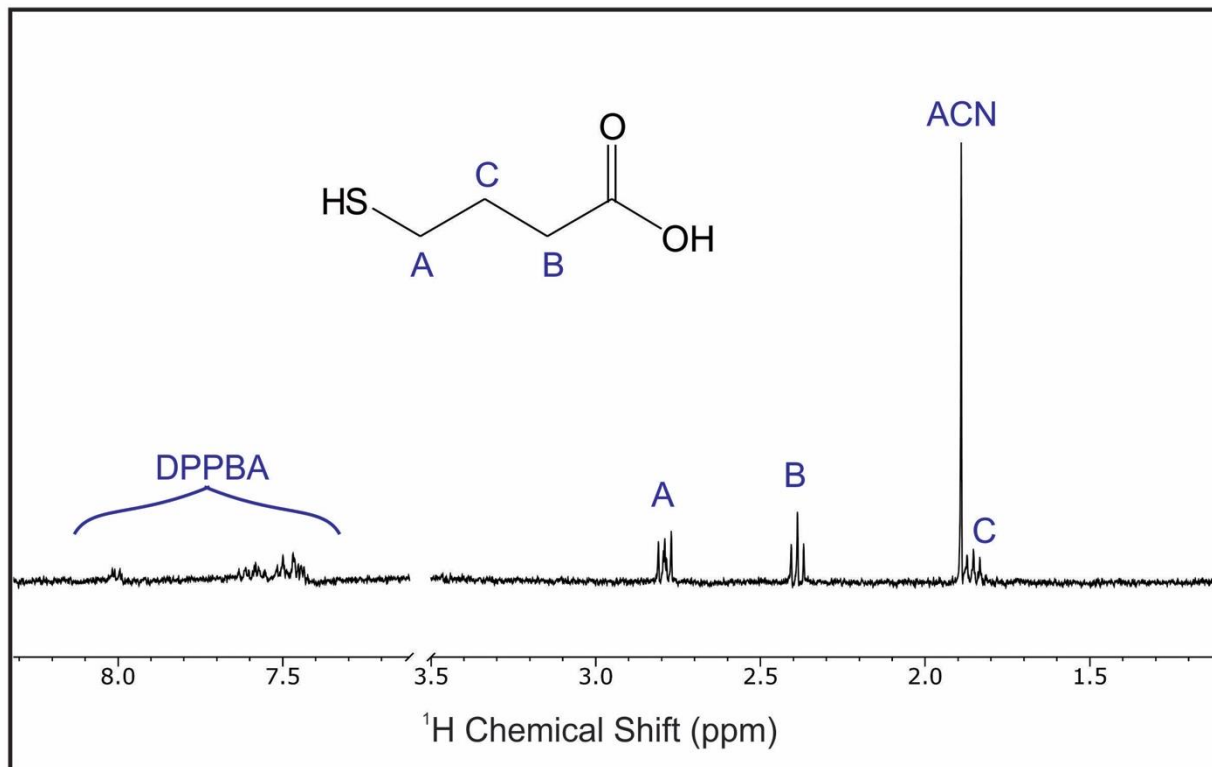


Figure 98. Representative ^1H NMR spectrum of MBuA-exchanged AuNPs following digestion in aqua regia with its labeled structure corresponding to plotted ^1H NMR peak locations. For the calculation of MBuA concentration, Peak B is integrated and compared to the integrated intensity of the ACN peak.

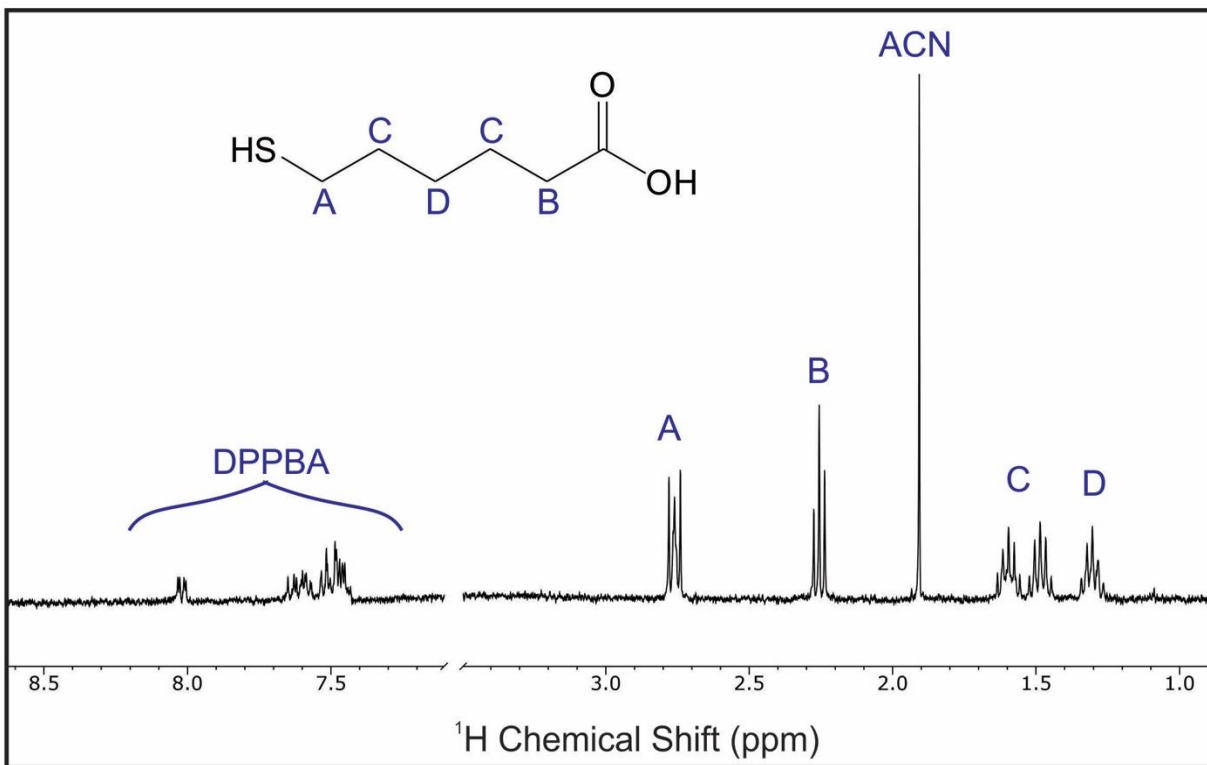


Figure 99. Representative ^1H NMR spectrum of MHA-exchanged AuNPs following digestion in aqua regia with its labeled structure corresponding to plotted ^1H NMR peak locations. For the calculation of MHA concentration, Peak B is integrated and compared to the integrated intensity of the ACN peak.

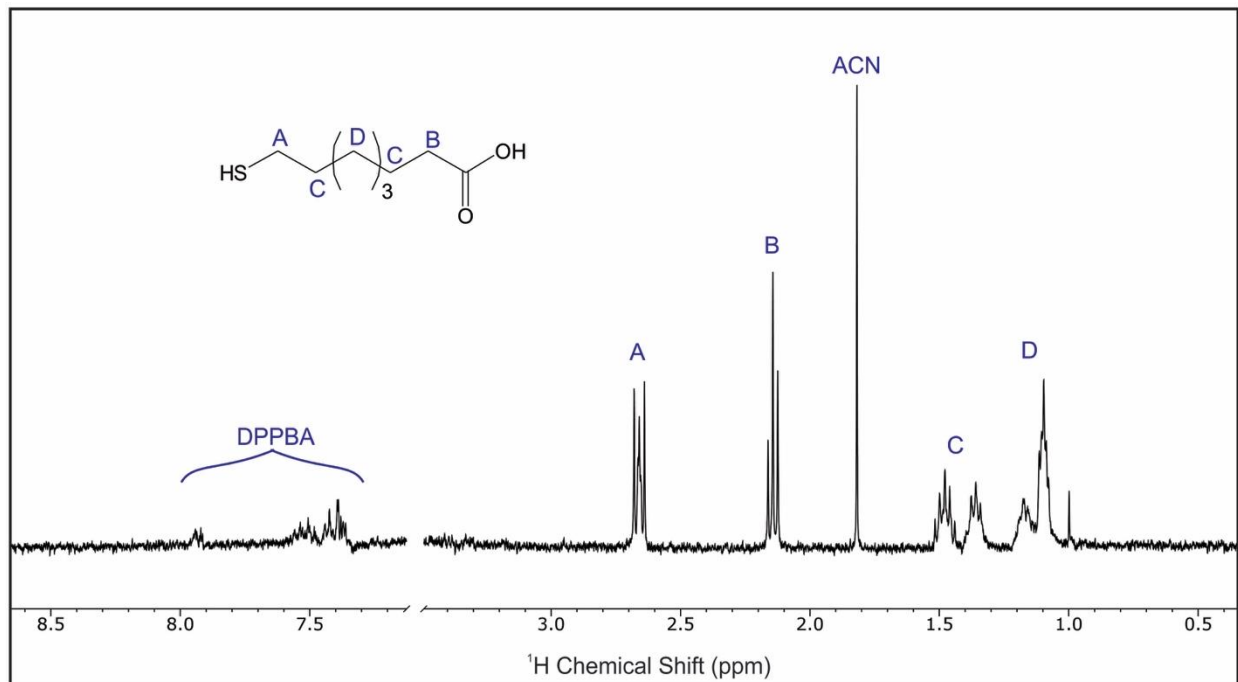


Figure 100. Representative ¹H NMR spectrum of MOA-exchanged AuNPs following digestion in aqua regia with its labeled structure corresponding to plotted ¹H NMR peak locations. For the calculation of MOA concentration, Peak D is integrated and compared to the integrated intensity of the ACN peak.

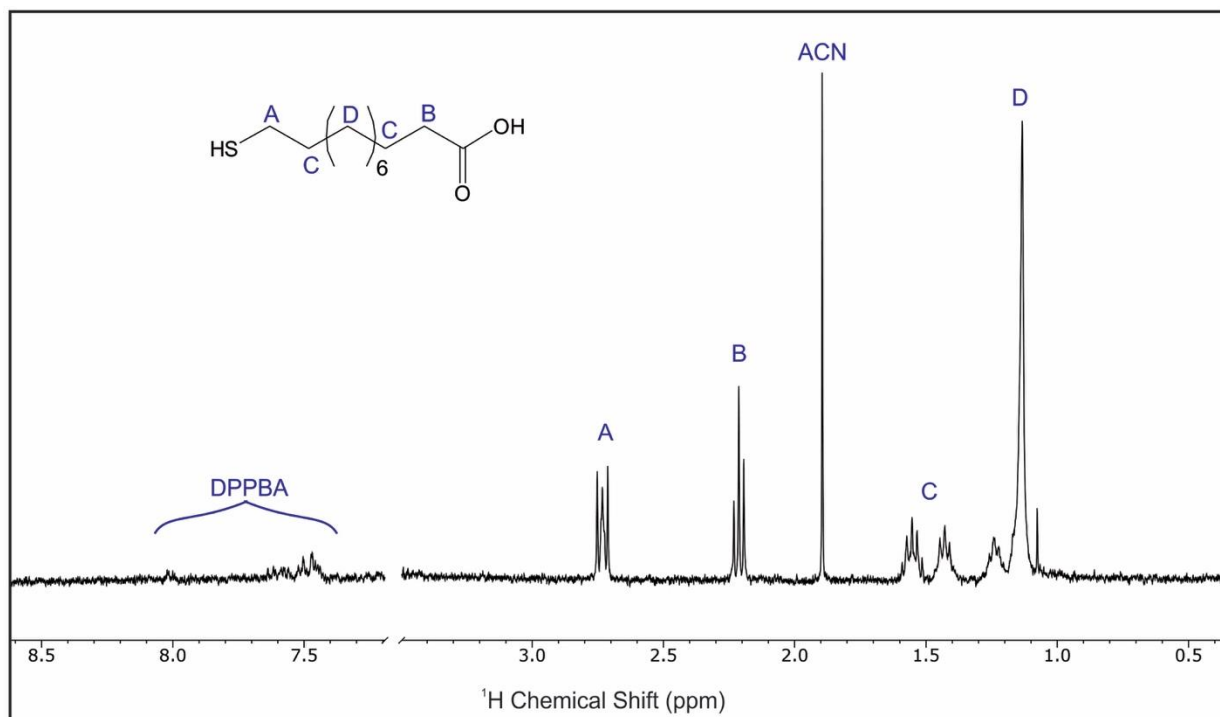


Figure 101. Representative ¹H NMR spectrum of MUA-exchanged AuNPs following digestion in aqua regia with its labeled structure corresponding to plotted ¹H NMR peak locations. For the calculation of MUA concentration, Peak D is integrated and compared to the integrated intensity of the ACN peak.

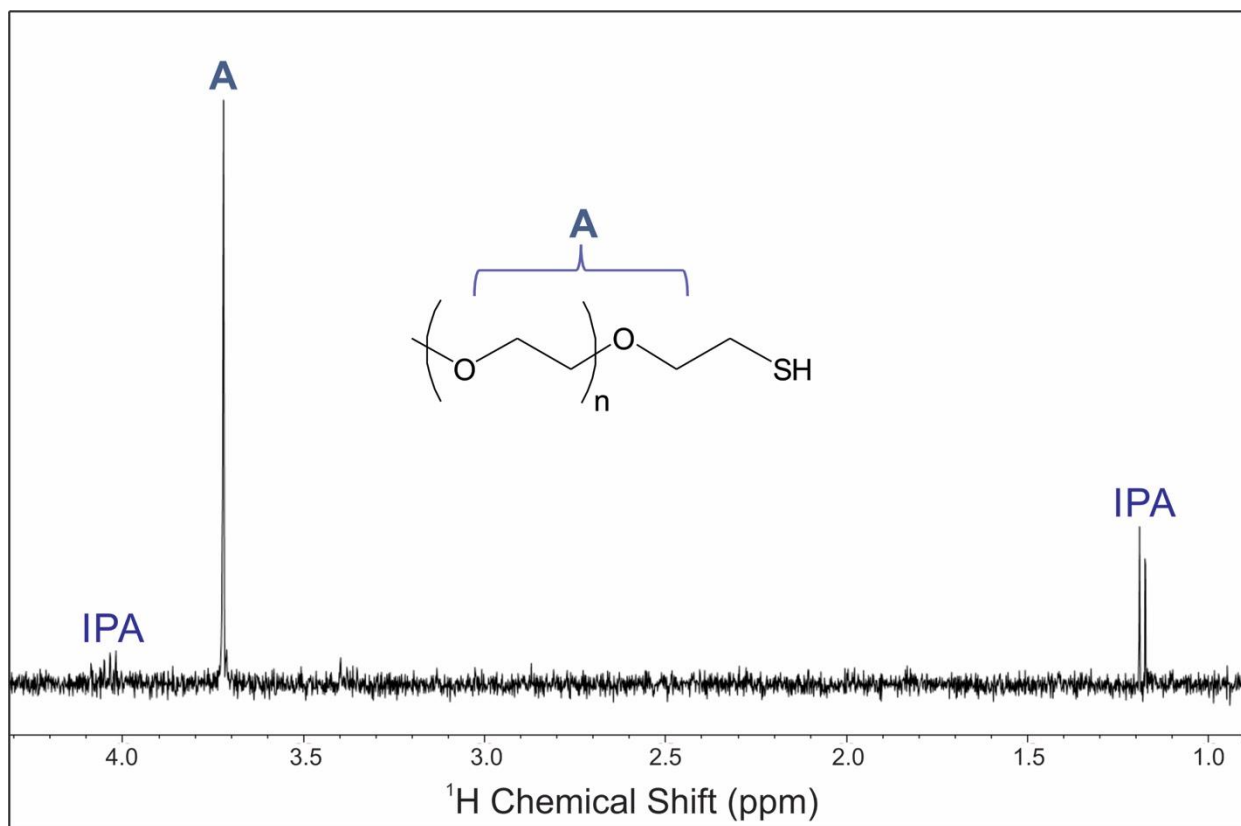


Figure 102. Representative ^1H NMR spectrum of PEGSH-exchanged AgNPs following particle digestion in nitric with its labeled structure corresponding to plotted ^1H NMR peak locations. For the calculation of PEGSH concentration, peak A is integrated and compared to the integrated intensity of the IPA doublet peak at 1.17 ppm.

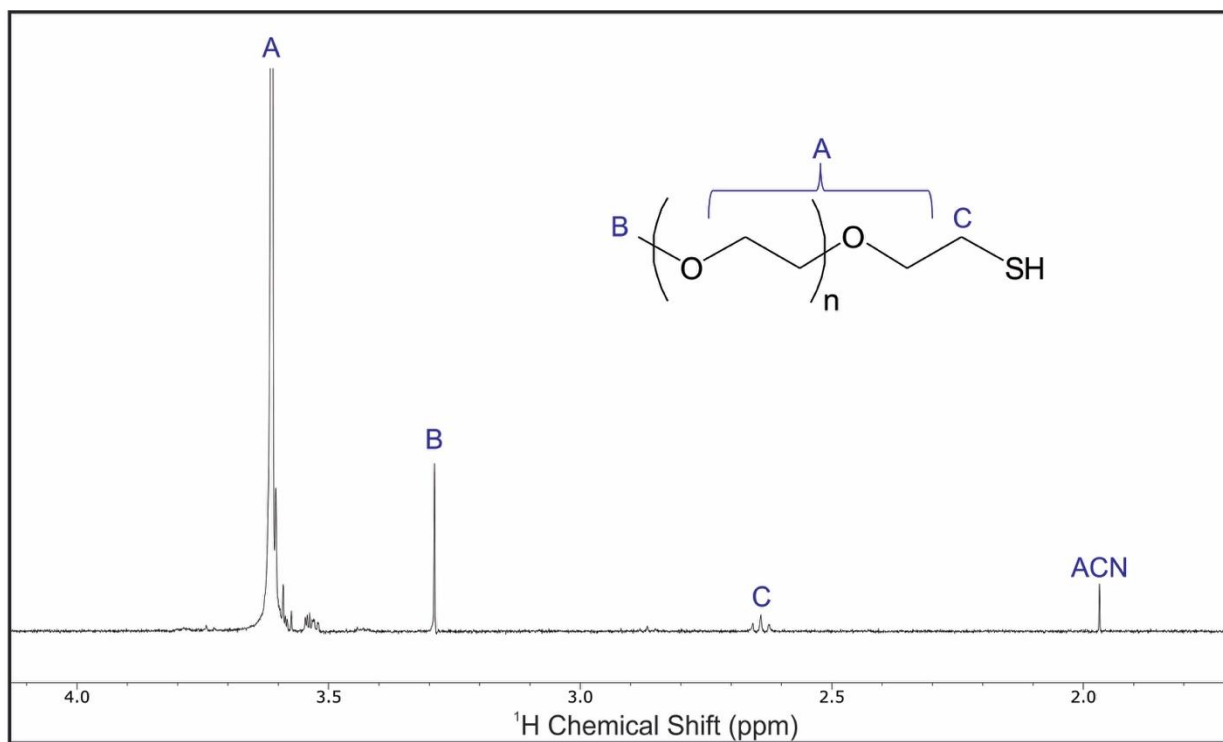


Figure 103. Representative ^1H NMR spectrum of PEGSH-exchanged AuNPs following particle digestion with its labeled structure corresponding to plotted ^1H NMR peak locations. For the calculation of PEGSH concentration, peak A is integrated and compared to the integrated intensity of the ACN peak.

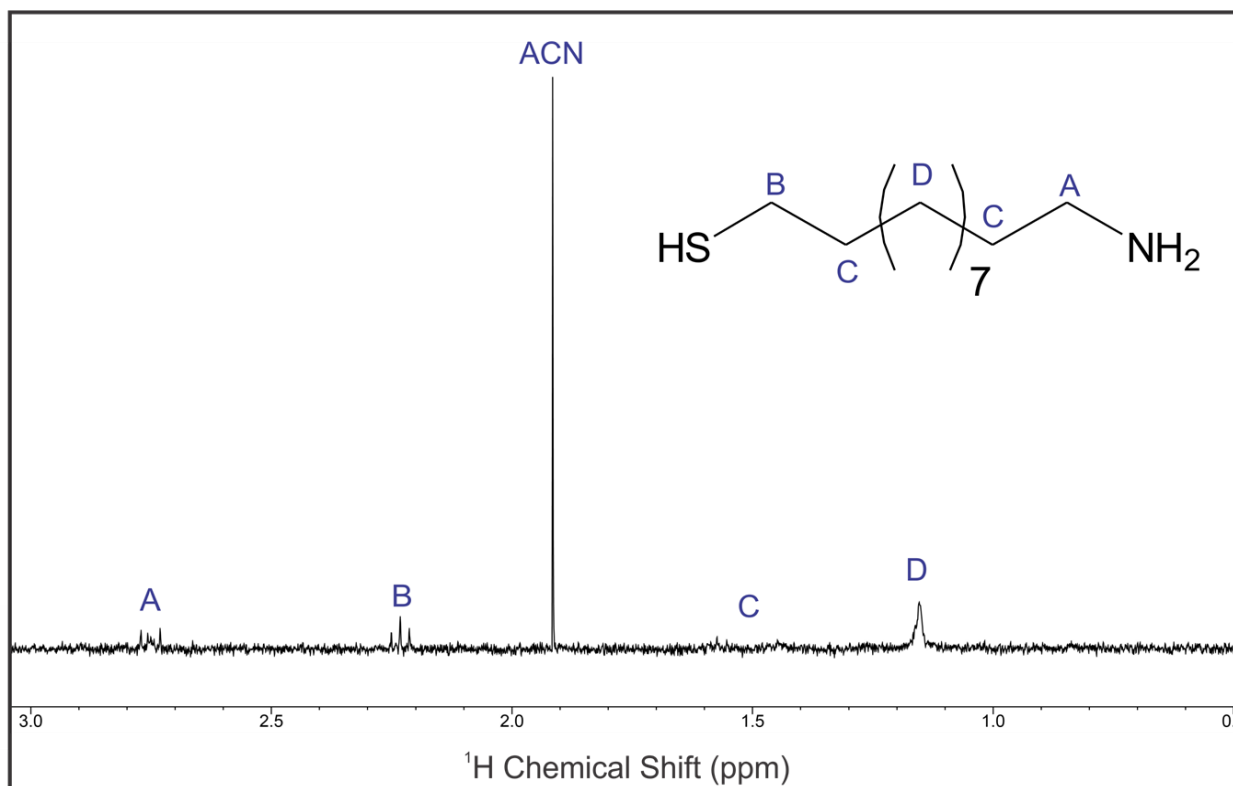


Figure 104. Representative ^1H NMR spectrum of AUT-exchanged Au prisms following digestion with aqua regia with its labeled structure corresponding to plotted ^1H NMR peak locations. For calculation of AUT concentration, Peak D is integrated and compared to the integrated intensity of the ACN peak.

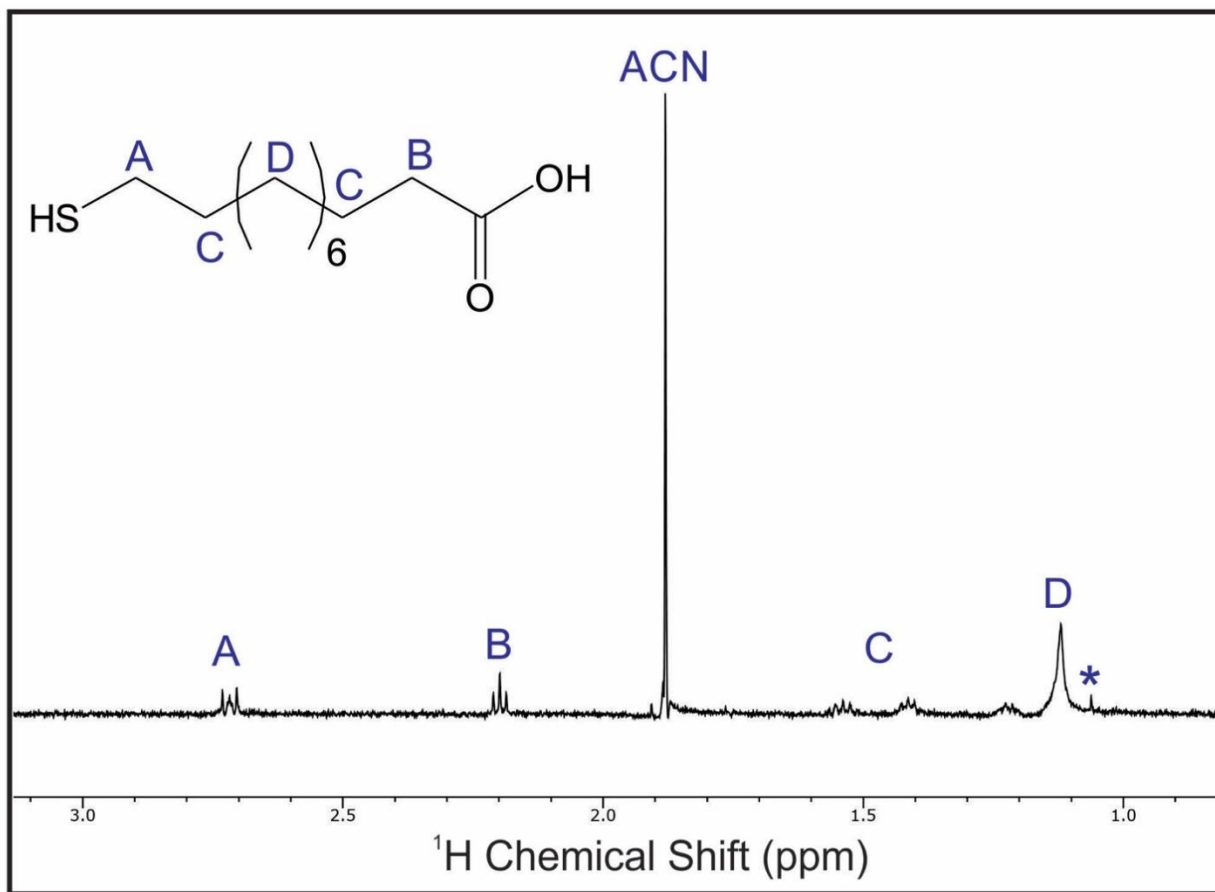


Figure 105. Representative ¹H NMR spectrum of MUA-exchanged Au prisms following digestion with aqua regia with its labeled structure corresponding to plotted ¹H NMR peak locations. The peak labelled with (*) indicates trace amounts of residual CTAB remaining after the ligand exchange. For calculation of MUA concentration, Peak B is integrated and compared to the integrated intensity of the ACN peak.

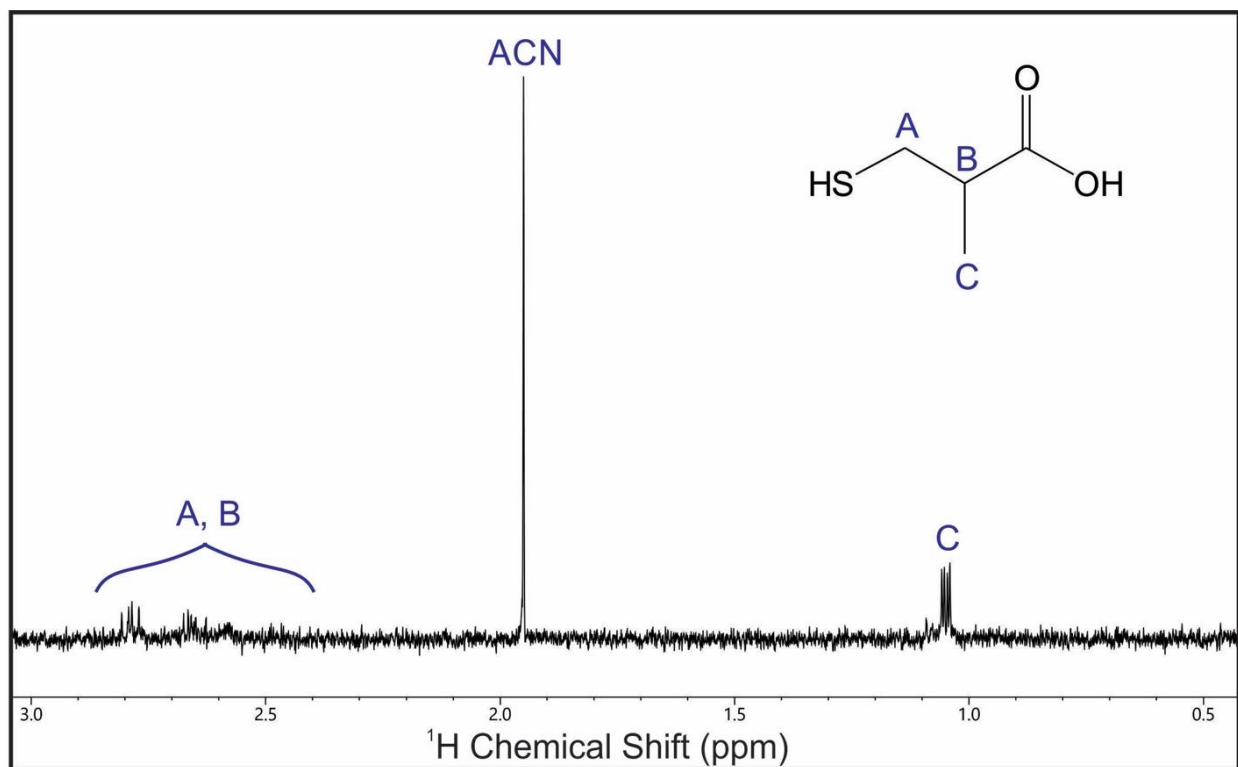


Figure 106. Representative ^1H NMR spectrum of MMPA-exchanged Au prisms following digestion with aqua regia with its labeled structure corresponding to plotted ^1H NMR peak locations. For calculation of MMPA concentration, Peak C is integrated and compared to the integrated intensity of the ACN peak.

BIBLIOGRAPHY

1. Puzder, A.; Williamson, A. J.; Zaitseva, N.; Galli, G.; Manna, L.; Alivisatos, A. P., *Nano Lett.* **2004**, *4*, 2361-2365.
2. Zeng, J.; Zheng, Y.; Rycenga, M.; Tao, J.; Li, Z.-Y.; Zhang, Q.; Zhu, Y.; Xia, Y., *J. Am. Chem. Soc.* **2010**, *132*, 8552-8553.
3. Grzelczak, M.; Perez-Juste, J.; Mulvaney, P.; Liz-Marzan, L. M., *Chem. Soc. Rev.* **2008**, *37*, 1783-1791.
4. Li, Y.; El-Sayed, M. A., *J. Phys. Chem. B* **2001**, *105*, 8938-8943.
5. Ott, L. S.; Finke, R. G., *Coord. Chem. Rev.* **2007**, *251*, 1075-1100.
6. Israelachvili, J., *Intermolecular and Surface Forces*. 3rd ed.; Elsevier: Burlington, MA, 2011.
7. Boles, M. A.; Ling, D.; Hyeon, T.; Talapin, D. V., *Nat. Mater.* **2016**, *15*, 141-153.
8. McArthur, E. A.; Morris-Cohen, A. J.; Knowles, K. E.; Weiss, E. A., *J. Phys. Chem. B* **2010**, *114*, 14514-14520.
9. Verma, A.; Stellacci, F., *Small* **2010**, *6*, 12-21.
10. Albanese, A.; Tang, P. S.; Chan, W. C., *Annu. Rev. Biomed. Eng.* **2012**, *14*, 1-16.
11. Feng, Z. V.; Gunsolus, I. L.; Qiu, T. A.; Hurley, K. R.; Nyberg, L. H.; Frew, H.; Johnson, K. P.; Vartanian, A. M.; Jacob, L. M.; Lohse, S. E., *Chem. Sci.* **2015**, *6*, 5186-5196.
12. Alkilany, A. M.; Nagaria, P. K.; Hexel, C. R.; Shaw, T. J.; Murphy, C. J.; Wyatt, M. D., *Small* **2009**, *5*, 701-708.
13. Lee, J.-S.; Bodnarchuk, M. I.; Shevchenko, E. V.; Talapin, D. V., *J. Am. Chem. Soc.* **2010**, *132*, 6382-6391.
14. Yu, W. W.; Chang, E.; Drezek, R.; Colvin, V. L., *Biochem. Biophys. Res. Commun.* **2006**, *348*, 781-786.

15. Love, J. C.; Estroff, L. A.; Kriebel, J. K.; Nuzzo, R. G.; Whitesides, G. M., *Chem. Rev.* **2005**, *105*, 1103-1170.
16. Prime, K. L.; Whitesides, G. M., *Science* **1991**, *252*, 1164-1167.
17. Laibinis, P. E.; Whitesides, G. M.; Allara, D. L.; Tao, Y. T.; Parikh, A. N.; Nuzzo, R. G., *J. Am. Chem. Soc.* **1991**, *113*, 7152-7167.
18. Ulman, A., *Chem. Rev.* **1996**, *96*, 1533-1554.
19. Sellers, H.; Ulman, A.; Shnidman, Y.; Eilers, J. E., *J. Am. Chem. Soc.* **1993**, *115*, 9389-9401.
20. Smith, R. K.; Lewis, P. A.; Weiss, P. S., *Prog. Surf. Sci.* **2004**, *75*, 1-68.
21. Häkkinen, H., *Nature Chem.* **2012**, *4*, 443-455.
22. Hassinen, A.; Moreels, I.; De Nolf, K.; Smet, P. F.; Martins, J. C.; Hens, Z., *J. Am. Chem. Soc.* **2012**, *134*, 20705-20712.
23. Tsai, D.-H.; Davila-Morris, M.; DelRio, F. W.; Guha, S.; Zachariah, M. R.; Hackley, V. A., *Langmuir* **2011**, *27*, 9302-9313.
24. Amin, V. A.; Aruda, K. O.; Lau, B.; Rasmussen, A. M.; Edme, K.; Weiss, E. A., *J. Phys. Chem. C* **2015**, *119*, 19423-19429.
25. Crawford, S. E.; Andolina, C. M.; Smith, A. M.; Marbella, L. E.; Johnston, K. A.; Straney, P. J.; Hartmann, M. J.; Millstone, J. E., *J. Am. Chem. Soc.* **2015**, *137*, 14423-14429.
26. Jokerst, J. V.; Lobovkina, T.; Zare, R. N.; Gambhir, S. S., *Nanomedicine-UK* **2011**, *6*, 715-728.
27. Cheng, T.-L.; Chuang, K.-H.; Chen, B.-M.; Roffler, S. R., *Bioconjugate Chem.* **2012**, *23*, 881-899.
28. Gavia, D. J.; Shon, Y.-S., *Langmuir* **2012**, *28*, 14502-14508.
29. He, G.; Song, Y.; Kang, X.; Chen, S., *Electrochim. Acta* **2013**, *94*, 98-103.
30. Ren, G.; Hu, D.; Cheng, E. W. C.; Vargas-Reus, M. A.; Reip, P.; Allaker, R. P., *Int. J. Antimicrob. Agents* **2009**, *33*, 587-590.
31. Esswein, A. J.; McMurdo, M. J.; Ross, P. N.; Bell, A. T.; Tilley, T. D., *J. Phys. Chem. C* **2009**, *113*, 15068-15072.
32. Lin, H.-F.; Liao, S.-C.; Hung, S.-W., *J. Photoch. Photobio. A* **2005**, *174*, 82-87.
33. Xing, Y., *J. Phys. Chem. B* **2004**, *108*, 19255-19259.

34. Trasatti, S.; Petrii, O., *Pure Appl. Chem.* **1991**, *63*, 711-734.
35. Haiss, W.; Thanh, N. T. K.; Aveyard, J.; Fernig, D. G., *Anal. Chem.* **2007**, *79*, 4215-4221.
36. Liu, X.; Atwater, M.; Wang, J.; Huo, Q., *Colloids Surf., B* **2007**, *58*, 3-7.
37. Chang, E.; Thekkek, N.; Yu, W. W.; Colvin, V. L.; Drezek, R., *Small* **2006**, *2*, 1412-1417.
38. Ballou, B.; Lagerholm, B. C.; Ernst, L. A.; Bruchez, M. P.; Waggoner, A. S., *Bioconjugate Chem.* **2004**, *15*, 79-86.
39. Hendel, T.; Wuthschick, M.; Kettemann, F.; Birnbaum, A.; Rademann, K.; Polte, J., *Anal. Chem.* **2014**, *86*, 11115-11124.
40. Scheffer, A.; Engelhard, C.; Sperling, M.; Buscher, W., *Anal. Bioanal. Chem.* **2008**, *390*, 249-252.
41. Mitrano, D. M.; Barber, A.; Bednar, A.; Westerhoff, P.; Higgins, C. P.; Ranville, J. F., *J. Anal. At. Spectrom.* **2012**, *27*, 1131-1142.
42. Oyewumi, M. O.; Yokel, R. A.; Jay, M.; Coakley, T.; Mumper, R. J., *J. Controlled Release* **2004**, *95*, 613-626.
43. Moreels, I.; Lambert, K.; De Muynck, D.; Vanhaecke, F.; Poelman, D.; Martins, J. C.; Allan, G.; Hens, Z., *Chem. Mater.* **2007**, *19*, 6101-6106.
44. Gießmann, U.; Greb, U., *Fresenius' J. Anal. Chem.* **1994**, *350*, 186-193.
45. Rempel, J. Y.; Trout, B. L.; Bawendi, M. G.; Jensen, K. F., *J. Phys. Chem. B* **2006**, *110*, 18007-18016.
46. Liu, K.; Zhao, N.; Kumacheva, E., *Chem. Soc. Rev.* **2011**, *40*, 656-671.
47. Liu, P.; Norskov, J. K., *Phys. Chem. Chem. Phys.* **2001**, *3*, 3814-3818.
48. Owen, J. S.; Park, J.; Trudeau, P.-E.; Alivisatos, A. P., *J. Am. Chem. Soc.* **2008**, *130*, 12279-12281.
49. Jasieniak, J.; Mulvaney, P., *J. Am. Chem. Soc.* **2007**, *129*, 2841-2848.
50. Liu, X.; Yu, M.; Kim, H.; Mameli, M.; Stellacci, F., *Nat. Commun.* **2012**, *3*, 1182.
51. Ha, J.-M.; Katz, A.; Drapailo, A. B.; Kalchenko, V. I., *J. Phys. Chem. C* **2009**, *113*, 1137-1142.
52. Wang, Y.; Zeiri, O.; Neyman, A.; Stellacci, F.; Weinstock, I. A., *ACS Nano* **2012**, *6*, 629-640.

53. Djebaili, T.; Richardi, J.; Abel, S.; Marchi, M., *J. Phys. Chem. C* **2015**, *119*, 21146-21154.
54. Smith, A. M.; Marbella, L. E.; Johnston, K. A.; Hartmann, M. J.; Crawford, S. E.; Kozycz, L. M.; Seferos, D. S.; Millstone, J. E., *Anal. Chem.* **2015**, *87*, 2771-2778.
55. Djebaili, T.; Richardi, J.; Abel, S.; Marchi, M., *J. Phys. Chem. C* **2013**, *117*, 17791-17800.
56. Hostetler, M. J.; Templeton, A. C.; Murray, R. W., *Langmuir* **1999**, *15*, 3782-3789.
57. Anderson, N. C.; Owen, J. S., *Chem. Mater.* **2013**, *25*, 69-76.
58. Wang, C.; Zhang, H.; Zhang, J.; Lv, N.; Li, M.; Sun, H.; Yang, B., *J. Phys. Chem. C* **2008**, *112*, 6330-6336.
59. Ionita, P.; Volkov, A.; Jeschke, G.; Chechik, V., *Anal. Chem.* **2008**, *80*, 95-106.
60. Wu, Z.; Jin, R., *Nano Lett.* **2010**, *10*, 2568-2573.
61. Ansar, S. M.; Haputhanthri, R.; Edmonds, B.; Liu, D.; Yu, L.; Sygula, A.; Zhang, D., *J. Phys. Chem. C* **2011**, *115*, 653-660.
62. Yavuz, M. S.; Cheng, Y.; Chen, J.; Cobley, C. M.; Zhang, Q.; Rycenga, M.; Xie, J.; Kim, C.; Song, K. H.; Schwartz, A. G.; Wang, L. V.; Xia, Y., *Nat. Mater.* **2009**, *8*, 935-939.
63. Rahme, K.; Chen, L.; Hobbs, R. G.; Morris, M. A.; O'Driscoll, C.; Holmes, J. D., *RSC Adv.* **2013**, *3*, 6085-6094.
64. Benoit, D. N.; Zhu, H.; Lilierose, M. H.; Verm, R. A.; Ali, N.; Morrison, A. N.; Fortner, J. D.; Avendano, C.; Colvin, V. L., *Anal. Chem.* **2012**, *84*, 9238-9245.
65. Woehrle, G. H.; Brown, L. O.; Hutchison, J. E., *J. Am. Chem. Soc.* **2005**, *127*, 2172-2183.
66. Badia, A.; Singh, S.; Demers, L.; Cuccia, L.; Brown, G. R.; Lennox, R. B., *Chem.-Eur. J* **1996**, *2*, 359-363.
67. Doane, T. L.; Cheng, Y.; Babar, A.; Hill, R. J.; Burda, C., *J. Am. Chem. Soc.* **2010**, *132*, 15624-15631.
68. Maccarini, M.; Briganti, G.; Rucareanu, S.; Lui, X.-D.; Sinibaldi, R.; Sztucki, M.; Lennox, R. B., *J. Phys. Chem. C* **2010**, *114*, 6937-6943.
69. Takae, S.; Akiyama, Y.; Otsuka, H.; Nakamura, T.; Nagasaki, Y.; Kataoka, K., *Biomacromolecules* **2005**, *6*, 818-824.
70. Corbierre, M. K.; Cameron, N. S.; Lennox, R. B., *Langmuir* **2004**, *20*, 2867-2873.

71. Corbierre, M. K.; Cameron, N. S.; Sutton, M.; Laaziri, K.; Lennox, R. B., *Langmuir* **2005**, *21*, 6063-6072.
72. Shan, J.; Nuopponen, M.; Jiang, H.; Kauppinen, E.; Tenhu, H., *Macromolecules* **2003**, *36*, 4526-4533.
73. Liang, M.; Lin, I.-C.; Whittaker, M. R.; Minchin, R. F.; Monteiro, M. J.; Toth, I., *ACS Nano* **2009**, *4*, 403-413.
74. Uz, M.; Bulmus, V.; Alsoy Altinkaya, S., *Langmuir* **2016**, *32*, 5997-6009.
75. Zheng, M.; Li, Z.; Huang, X., *Langmuir* **2004**, *20*, 4226-4235.
76. Sebby, K.; Mansfield, E., *Anal. Bioanal. Chem.* **2015**, *407*, 2913-2922.
77. Hostetler, M. J.; Wingate, J. E.; Zhong, C.-J.; Harris, J. E.; Vachet, R. W.; Clark, M. R.; Londono, J. D.; Green, S. J.; Stokes, J. J.; Wignall, G. D.; Glish, G. L.; Porter, M. D.; Evans, N. D.; Murray, R. W., *Langmuir* **1998**, *14*, 17-30.
78. Shon, Y.-S.; Gross, S. M.; Dawson, B.; Porter, M.; Murray, R. W., *Langmuir* **2000**, *16*, 6555-6561.
79. Wuelfing, W. P.; Gross, S. M.; Miles, D. T.; Murray, R. W., *J. Am. Chem. Soc.* **1998**, *120*, 12696-12697.
80. Terrill, R. H.; Postlethwaite, T. A.; Chen, C.-h.; Poon, C.-D.; Terzis, A.; Chen, A.; Hutchison, J. E.; Clark, M. R.; Wignall, G.; Londono, J. D.; Superfine, R.; Falvo, M.; Johnson, C. S.; Samulski, E. T.; Murray, R. W., *J. Am. Chem. Soc.* **1995**, *117*, 12537-12548.
81. Templeton, A. C.; Chen, S.; Gross, S. M.; Murray, R. W., *Langmuir* **1999**, *15*, 66-76.
82. Lin, I.-C.; Liang, M.; Liu, T.-Y.; Jia, Z.; Monteiro, M. J.; Toth, I., *Bioorg. Med. Chem.* **2012**, *20*, 6862-6869.
83. Guo, C.; Holland, G. P., *J. Phys. Chem. C* **2014**, *118*, 25792-25801.
84. Guo, C.; Holland, G. P., *J. Phys. Chem. C* **2015**, *119*, 25663-25672.
85. Schwaminger, S. P.; García, P. F.; Merck, G. K.; Bodensteiner, F. A.; Heissler, S.; Günther, S.; Berensmeier, S., *J. Phys. Chem. C* **2015**, *119*, 23032-23041.
86. Illum, L.; Church, A. E.; Butterworth, M. D.; Arien, A.; Whetstone, J.; Davis, S. S., *Pharm. Res.* **2001**, *18*, 640-645.
87. Butterworth, M. D.; Illum, L.; Davis, S. S., *Colloid Surf., A* **2001**, *179*, 93-102.
88. Amoli, B. M.; Gumfekar, S.; Hu, A.; Zhou, Y. N.; Zhao, B., *J. Mater. Chem.* **2012**, *22*, 20048-20056.

89. Zhou, Z.-Y.; Kang, X.; Song, Y.; Chen, S., *Chem. Commun.* **2011**, *47*, 6075-6077.
90. Cargnello, M.; Wieder, N. L.; Canton, P.; Montini, T.; Giambastiani, G.; Benedetti, A.; Gorte, R. J.; Fornasiero, P., *Chem. Mater.* **2011**, *23*, 3961-3969.
91. Sadeghmoghaddam, E.; Gaïeb, K.; Shon, Y.-S., *Appl. Catal., A* **2011**, *405*, 137-141.
92. Sadeghmoghaddam, E.; Lam, C.; Choi, D.; Shon, Y.-S., *J. Mater. Chem.* **2011**, *21*, 307-312.
93. Chen, W.; Zuckerman, N. B.; Kang, X.; Ghosh, D.; Konopelski, J. P.; Chen, S., *J. Phys. Chem. C* **2010**, *114*, 18146-18152.
94. Zhou, Z.-Y.; Kang, X.; Song, Y.; Chen, S., *Chem. Commun.* **2012**, *48*, 3391-3393.
95. Zhou, Z.-Y.; Ren, J.; Kang, X.; Song, Y.; Sun, S.-G.; Chen, S., *Phys. Chem. Chem. Phys.* **2012**, *14*, 1412-1417.
96. Mirkhalaf, F.; Paprotny, J.; Schiffrin, D. J., *J. Am. Chem. Soc.* **2006**, *128*, 7400-7401.
97. Demers, L. M.; Mirkin, C. A.; Mucic, R. C.; Reynolds, R. A.; Letsinger, R. L.; Elghanian, R.; Viswanadham, G., *Anal. Chem.* **2000**, *72*, 5535-5541.
98. Xia, X.; Yang, M.; Wang, Y.; Zheng, Y.; Li, Q.; Chen, J.; Xia, Y., *ACS Nano* **2012**, *6*, 512-522.
99. Yun, C. S.; Javier, A.; Jennings, T.; Fisher, M.; Hira, S.; Peterson, S.; Hopkins, B.; Reich, N. O.; Strouse, G. F., *J. Am. Chem. Soc.* **2005**, *127*, 3115-3119.
100. Hurst, S. J.; Lytton-Jean, A. K. R.; Mirkin, C. A., *Anal. Chem.* **2006**, *78*, 8313-8318.
101. Hill, H. D.; Millstone, J. E.; Banholzer, M. J.; Mirkin, C. A., *ACS Nano* **2009**, *3*, 418-424.
102. Li, Z.; Jin, R.; Mirkin, C. A.; Letsinger, R. L., *Nucleic Acids Res.* **2002**, *30*, 1558-1562.
103. Giljohann, D. A.; Seferos, D. S.; Patel, P. C.; Millstone, J. E.; Rosi, N. L.; Mirkin, C. A., *Nano Lett.* **2007**, *7*, 3818-3821.
104. Zhang, X.; Servos, M. R.; Liu, J., *J. Am. Chem. Soc.* **2012**, *134*, 9910-9913.
105. Maus, L.; Spatz, J. P.; Fiammengo, R., *Langmuir* **2009**, *25*, 7910-7917.
106. Patwardhan, S. V.; Emami, F. S.; Berry, R. J.; Jones, S. E.; Naik, R. R.; Deschaume, O.; Heinz, H.; Perry, C. C., *J. Am. Chem. Soc.* **2012**, *134*, 6244-6256.
107. Schroedter, A.; Weller, H., *Angew. Chem., Int. Ed.* **2002**, *41*, 3218-3221.
108. Chen, M. M. Y.; Katz, A., *Langmuir* **2002**, *18*, 2413-2420.

109. Xie, H.; Tkachenko, A. G.; Glomm, W. R.; Ryan, J. A.; Brennaman, M. K.; Papanikolas, J. M.; Franzen, S.; Feldheim, D. L., *Anal. Chem.* **2003**, *75*, 5797-5805.
110. Oh, E.; Susumu, K.; Blanco-Canosa, J.; Medintz, I.; Dawson, P.; Mattoussi, H., *Small* **2010**, *6*, 1273-1278.
111. Zhan, N.; Palui, G.; Merkl, J.-P.; Mattoussi, H., *J. Am. Chem. Soc.* **2016**, *138*, 3190-3201.
112. Ha, J.-M.; Solovyov, A.; Katz, A., *Langmuir* **2009**, *25*, 153-158.
113. Ha, J.-M.; Solovyov, A.; Katz, A., *Langmuir* **2009**, *25*, 10548-10553.
114. Ha, J.-M.; Solovyov, A.; Katz, A., *J. Phys. Chem. C* **2010**, *114*, 16060-16070.
115. Kumar, A.; Ma, H.; Zhang, X.; Huang, K.; Jin, S.; Liu, J.; Wei, T.; Cao, W.; Zou, G.; Liang, X.-J., *Biomaterials* **2012**, *33*, 1180-1189.
116. Lévy, R.; Thanh, N. T. K.; Doty, R. C.; Hussain, I.; Nichols, R. J.; Schiffrin, D. J.; Brust, M.; Fernig, D. G., *J. Am. Chem. Soc.* **2004**, *126*, 10076-10084.
117. Kira, A.; Kim, H.; Yasuda, K., *Langmuir* **2009**, *25*, 1285-1288.
118. Walkey, C. D.; Olsen, J. B.; Guo, H.; Emili, A.; Chan, W. C., *J. Am. Chem. Soc.* **2012**, *134*, 2139-2147.
119. Hinterwirth, H.; Kappel, S.; Waitz, T.; Prohaska, T.; Lindner, W.; Lämmerhofer, M., *ACS Nano* **2013**, *7*, 1129-1136.
120. Elzey, S.; Tsai, D.-H.; Rabb, S.; Yu, L.; Winchester, M.; Hackley, V., *Anal. Bioanal. Chem.* **2012**, *403*, 145-149.
121. Donakowski, M. D.; Godbe, J. M.; Sknepnek, R.; Knowles, K. E.; Olvera de la Cruz, M.; Weiss, E. A., *J. Phys. Chem. C* **2010**, *114*, 22526-22534.
122. Morris-Cohen, A. J.; Donakowski, M. D.; Knowles, K. E.; Weiss, E. A., *J. Phys. Chem. C* **2010**, *114*, 897-906.
123. Moreels, I.; Fritzing, B.; Martins, J. C.; Hens, Z., *J. Am. Chem. Soc.* **2008**, *130*, 15081-15086.
124. Badia, A.; Demers, L.; Dickinson, L.; Morin, F.; Lennox, R.; Reven, L., *J. Am. Chem. Soc.* **1997**, *119*, 11104-11105.
125. Ratcliffe, C. I.; Yu, K.; Ripmeester, J. A.; Zaman, M. B.; Badarau, C.; Singh, S., *Phys. Chem. Chem. Phys.* **2006**, *8*, 3510-3519.
126. Sachleben, J. R.; Wooten, E. W.; Emsley, L.; Pines, A.; Colvin, V. L.; Alivisatos, A. P., *Chem. Phys. Lett.* **1992**, *198*, 431-436.

127. Zelakiewicz, B. S.; Yonezawa, T.; Tong, Y., *J. Am. Chem. Soc.* **2004**, *126*, 8112-8113.
128. Sharma, R.; Holland, G. P.; Solomon, V. C.; Zimmermann, H.; Schiftenhaus, S.; Amin, S. A.; Buttry, D. A.; Yarger, J. L., *J. Phys. Chem. C* **2009**, *113*, 16387-16393.
129. Trébosc, J.; Wiench, J. W.; Huh, S.; Lin, V. S. Y.; Pruski, M., *J. Am. Chem. Soc.* **2005**, *127*, 3057-3068.
130. Johnston, K. A.; Smith, A. M.; Marbella, L. E.; Millstone, J. E., *Langmuir* **2016**, *32*, 3820-3826.
131. Anderson, N. C.; Hendricks, M. P.; Choi, J. J.; Owen, J. S., *J. Am. Chem. Soc.* **2013**, *135*, 18536-18548.
132. Harris, R. D.; Amin, V. A.; Lau, B.; Weiss, E. A., *ACS Nano* **2016**, *10*, 1395-403.
133. Hens, Z.; Moreels, I.; Martins, J. C., *Chem. Phys. Chem.* **2005**, *6*, 2578-2584.
134. Hens, Z.; Martins, J. C., *Chem. Mater.* **2013**, *25*, 1211-1221.
135. Vatassery, R.; Hinke, J. A.; Sanchez-Diaz, A.; Hue, R.; Mann, K. R.; Blank, D. A.; Gladfelter, W. L., *J. Phys. Chem. C* **2013**, *117*, 10708-10715.
136. Pauli, G. F.; Jaki, B. U.; Lankin, D. C., *J. Nat. Prod.* **2005**, *68*, 133-149.
137. Levitt, M. H., *Spin Dynamics: Basics of Nuclear Magnetic Resonance*. 2nd ed.; John Wiley & Sons Ltd: West Sussex, England, 2008.
138. Moreels, I.; Martins, J. C.; Hens, Z., *Chem. Phys. Chem.* **2006**, *7*, 1028-1031.
139. Fritzing, B.; Capek, R. K.; Lambert, K.; Martins, J. C.; Hens, Z., *J. Am. Chem. Soc.* **2010**, *132*, 10195-10201.
140. Rausch, M. D.; Mark, V., *J. Org. Chem.* **1963**, *28*, 3225-3228.
141. Lehman, S. E.; Tataurova, Y.; Mueller, P. S.; Mariappan, S. V. S.; Larsen, S. C., *J. Phys. Chem. C* **2014**, *118*, 29943-29951.
142. Valdez, C. N.; Schimpf, A. M.; Gamelin, D. R.; Mayer, J. M., *ACS Nano* **2014**, *8*, 9463-9470.
143. Becerra, L. R.; Murray, C. B.; Griffin, R. G.; Bawendi, M. G., *J. Chem. Phys.* **1994**, *100*, 3297-3300.
144. Zhang, D.; Ansar, S. M., *Anal. Chem.* **2010**, *82*, 5910-5914.
145. Levin, C. S.; Bishnoi, S. W.; Grady, N. K.; Halas, N. J., *Anal. Chem.* **2006**, *78*, 3277-3281.

146. Pease, L. F.; Tsai, D.-H.; Zangmeister, R. A.; Zachariah, M. R.; Tarlov, M. J., *J. Phys. Chem. C* **2007**, *111*, 17155-17157.
147. Tsai, D.-H.; DelRio, F. W.; MacCuspie, R. I.; Cho, T. J.; Zachariah, M. R.; Hackley, V. A., *Langmuir* **2010**, *26*, 10325-10333.
148. Guha, S.; Ma, X.; Tarlov, M. J.; Zachariah, M. R., *Anal. Chem.* **2012**, *84*, 6308-6311.
149. Latham, A. H.; Williams, M. E., *Langmuir* **2006**, *22*, 4319-4326.
150. Charron, G.; Hühn, D.; Perrier, A.; Cordier, L.; Pickett, C. J.; Nann, T.; Parak, W. J., *Langmuir* **2012**, *28*, 15141-15149.
151. Joseph, Y.; Besnard, I.; Rosenberger, M.; Guse, B.; Nothofer, H.-G.; Wessels, J. M.; Wild, U.; Knop-Gericke, A.; Su, D.; Schlögl, R., *J. Phys. Chem. B* **2003**, *107*, 7406-7413.
152. Zhang, H.; Yang, B., *Thin Solid Films* **2002**, *418*, 169-174.
153. Torelli, M. D.; Putans, R. A.; Tan, Y.; Lohse, S. E.; Murphy, C. J.; Hamers, R. J., *ACS Appl. Mater. Interfaces* **2015**, *7*, 1720-1725.
154. Ivanov, M. R.; Haes, A. J., *Anal. Chem.* **2012**, *84*, 1320-1326.
155. Volkert, A. A.; Subramaniam, V.; Ivanov, M. R.; Goodman, A. M.; Haes, A. J., *ACS Nano* **2011**, *5*, 4570-4580.
156. Techane, S. D.; Gamble, L. J.; Castner, D. G., *J. Phys. Chem. C* **2011**, *115*, 9432-9441.
157. Katari, J. E. B.; Colvin, V. L.; Alivisatos, A. P., *J. Phys. Chem.* **1994**, *98*, 4109-4117.
158. Lu, X.; Rycenga, M.; Skrabalak, S. E.; Wiley, B.; Xia, Y., *Annu. Rev. Phys. Chem.* **2009**, *60*, 167-192.
159. Personick, M. L.; Mirkin, C. A., *J. Am. Chem. Soc.* **2013**, *135*, 18238-18247.
160. García-Rodríguez, R.; Hendricks, M. P.; Cossairt, B. M.; Liu, H.; Owen, J. S., *Chem. Mater.* **2013**, *25*, 1233-1249.
161. McBride, J. R.; Pennycook, T. J.; Pennycook, S. J.; Rosenthal, S. J., *ACS Nano* **2013**, *7*, 8358-8365.
162. Willets, K. A.; Van Duyne, R. P., *Annu. Rev. Phys. Chem.* **2007**, *58*, 267-297.
163. Goodman, C. M.; McCusker, C. D.; Yilmaz, T.; Rotello, V. M., *Bioconjugate Chem.* **2004**, *15*, 897-900.
164. Murphy, C. J.; Gole, A. M.; Stone, J. W.; Sisco, P. N.; Alkilany, A. M.; Goldsmith, E. C.; Baxter, S. C., *Acc. Chem. Res.* **2008**, *41*, 1721-1730.

165. Samant, M. G.; Brown, C. A.; Gordon, J. G., *Langmuir* **1992**, *8*, 1615-1618.
166. Weare, W. W.; Reed, S. M.; Warner, M. G.; Hutchison, J. E., *J. Am. Chem. Soc.* **2000**, *122*, 12890-12891.
167. Crudden, C. M.; Horton, J. H.; Ebralidze, I. I.; Zenkina, O. V.; McLean, A. B.; Drevniok, B.; She, Z.; Kraatz, H.-B.; Mosey, N. J.; Seki, T.; Keske, E. C.; Leake, J. D.; Rousina-Webb, A.; Wu, G., *Nature Chem.* **2014**, *6*, 409-414.
168. Hinterwirth, H.; Kappel, S.; Waitz, T.; Prohaska, T.; Lindner, W.; Lammerhofer, M., *ACS Nano* **2013**, *7*, 1129-36.
169. Elzey, S.; Tsai, D. H.; Rabb, S. A.; Yu, L. L.; Winchester, M. R.; Hackley, V. A., *Anal. Bioanal. Chem.* **2012**, *403*, 145-9.
170. Lanterna, A. E.; Coronado, E. A.; Granados, A. M., *J. Phys. Chem. C* **2012**, *116*, 6520-6529.
171. Xia, X.; Yang, M.; Wang, Y.; Zheng, Y.; Li, Q.; Chen, J.; Xia, Y., *ACS Nano* **2011**, *6*, 512-522.
172. Obare, S. O.; Hollowell, R. E.; Murphy, C. J., *Langmuir* **2002**, *18*, 10407-10410.
173. Wang, Y.; Zeiri, O.; Neyman, A.; Stellacci, F.; Weinstock, I. A., *ACS Nano* **2011**, *6*, 629-640.
174. Badia, A.; Cuccia, L.; Demers, L.; Morin, F.; Lennox, R. B., *J. Am. Chem. Soc.* **1997**, *119*, 2682-2692.
175. Salorinne, K.; Lahtinen, T.; Malola, S.; Koivisto, J.; Hakkinen, H., *Nanoscale* **2014**, *6*, 7823-7826.
176. Lee, K.-H.; Lin, Y.-S.; Huang, P.-J., *J. Nanomater.* **2013**, *2013*, 8.
177. Morris-Cohen, A. J.; Donakowski, M. D.; Knowles, K. E.; Weiss, E. A., *J. Phys. Chem. C* **2009**, *114*, 897-906.
178. Kowarik, S.; Gerlach, A.; Sellner, S.; Schreiber, F.; Cavalcanti, L.; Konovalov, O., *Phys. Rev. Lett.* **2006**, *96*, 125504.
179. Bain, C. D.; Troughton, E. B.; Tao, Y. T.; Evall, J.; Whitesides, G. M.; Nuzzo, R. G., *J. Am. Chem. Soc.* **1989**, *111*, 321-335.
180. Frens, G., *Nat. Phys. Sci.* **1973**, *241*, 20-22.
181. Hill, H. D.; Mirkin, C. A., *Nat. Protoc.* **2006**, *1*, 324-336.
182. Bioconjugation Protocols: Strategies and Methods. In *Methods in Molecular Biology* 283, Niemeyer, C. M., Ed. Humana Press: Totowa, N. J., 2004.

183. Hanwell, M. D.; Curtis, D. E.; Lonie, D. C.; Vandermeersch, T.; Zurek, E.; Hutchison, G. R., *J. Cheminformatics* **2012**, *4*, 17.
184. Rowland, R. S.; Taylor, R., *J. Phys. Chem.* **1996**, *100*, 7384-7391.
185. Fritzing, B.; Moreels, I.; Lommens, P.; Koole, R.; Hens, Z.; Martins, J. C., *J. Am. Chem. Soc.* **2009**, *131*, 3024-3032.
186. Morris-Cohen, A. J.; Malicki, M.; Peterson, M. D.; Slavin, J. W. J.; Weiss, E. A., *Chem. Mater.* **2012**, *25*, 1155-1165.
187. Turkevich, J.; Stevenson, P. C.; Hillier, J., *Discuss. Faraday Soc.* **1951**, *11*, 55-75.
188. Badia, A.; Demers, L.; Dickinson, L.; Morin, F. G.; Lennox, R. B.; Reven, L., *J. Am. Chem. Soc.* **1997**, *119*, 11104-11105.
189. Solomon, I., *Phys. Rev.* **1955**, *99*, 559-565.
190. Bloembergen, N., *J. Chem. Phys.* **1957**, *27*, 572-573.
191. Song, Y.; Harper, A. S.; Murray, R. W., *Langmuir* **2005**, *21*, 5492-5500.
192. Badia, A.; Gao, W.; Singh, S.; Demers, L.; Cuccia, L.; Reven, L., *Langmuir* **1996**, *12*, 1262-1269.
193. Schmitt, H.; Badia, A.; Dickinson, L.; Reven, L.; Lennox, R. B., *Adv. Mater. (Weinheim, Ger.)* **1998**, *10*, 475-480.
194. Harris, D. C., *Quantitative Chemical Analysis*. 7th ed.; W. H. Freeman and Company: New York, 2007.
195. Bain, C. D.; Evall, J.; Whitesides, G. M., *J. Am. Chem. Soc.* **1989**, *111*, 7155-7164.
196. Shuster, M. J.; Vaish, A.; Gilbert, M. L.; Martinez-Rivera, M.; Nezarati, R. M.; Weiss, P. S.; Andrews, A. M., *J. Phys. Chem. C* **2011**, *115*, 24778-24787.
197. Karakoti, A. S.; Das, S.; Thevuthasan, S.; Seal, S., *Angew. Chem. Int. Edit.* **2011**, *50*, 1980-1994.
198. *Poly(Ethylene Glycol) Chemistry: Biotechnical and Biomedical Applications*. Plenum Press: New York, 1992; p 385.
199. Folkers, J. P.; Laibinis, P. E.; Whitesides, G. M., *Langmuir* **1992**, *8*, 1330-1341.
200. Stranick, S. J.; Parikh, A. N.; Tao, Y. T.; Allara, D. L.; Weiss, P. S., *J. Phys. Chem.* **1994**, *98*, 7636-7646.
201. Zhou, F.; Huck, W. T. S., *Phys. Chem. Chem. Phys.* **2006**, *8*, 3815-3823.

202. Dreaden, E. C.; Alkilany, A. M.; Huang, X.; Murphy, C. J.; El-Sayed, M. A., *Chem. Soc. Rev.* **2012**, *41*, 2740-2779.
203. Daniel, M.-C.; Astruc, D., *Chem. Rev.* **2004**, *104*, 293-346.
204. Sperling, R. A.; Gil, P. R.; Zhang, F.; Zanella, M.; Parak, W. J., *Chem. Soc. Rev.* **2008**, *37*, 1896-1908.
205. Ghosh, P.; Han, G.; De, M.; Kim, C. K.; Rotello, V. M., *Adv. Drug Delivery Rev.* **2008**, *60*, 1307-1315.
206. Liu, Y.; Shipton, M. K.; Ryan, J.; Kaufman, E. D.; Franzen, S.; Feldheim, D. L., *Anal. Chem.* **2007**, *79*, 2221-2229.
207. Poirier, G. E.; Pylant, E. D., *Science* **1996**, *272*, 1145-1148.
208. Nuzzo, R. G.; Zegarski, B. R.; Dubois, L. H., *J. Am. Chem. Soc.* **1987**, *109*, 733-740.
209. Pong, B.-K.; Lee, J.-Y.; Trout, B. L., *Langmuir* **2005**, *21*, 11599-11603.
210. Wetterer, S. M.; Lavrich, D. J.; Cummings, T.; Bernasek, S. L.; Scoles, G., *J. Phys. Chem. B* **1998**, *102*, 9266-9275.
211. Grönbeck, H.; Curioni, A.; Andreoni, W., *J. Am. Chem. Soc.* **2000**, *122*, 3839-3842.
212. Daraee, H.; Eatemadi, A.; Abbasi, E.; Fekri Aval, S.; Kouhi, M.; Akbarzadeh, A., *Artif. Cells Nanomed. Biotechnol.* **2016**, *44*, 410-422.
213. Chithrani, B. D.; Ghazani, A. A.; Chan, W. C. W., *Nano Lett.* **2006**, *6*, 662-668.
214. Turner, M.; Golovko, V. B.; Vaughan, O. P. H.; Abdulkin, P.; Berenguer-Murcia, A.; Tikhov, M. S.; Johnson, B. F. G.; Lambert, R. M., *Nature* **2008**, *454*, 981-983.
215. Mitsudome, T.; Kaneda, K., *Green Chem.* **2013**, *15*, 2636-2654.
216. Smith, A. M.; Johnston, K. A.; Marbella, L. E.; Millstone, J. E., **2017**, In preparation.
217. Goldmann, C.; Ribot, F.; Peiretti, L. F.; Quaino, P.; Tielens, F.; Sanchez, C.; Chanéac, C.; Portehault, D., *Small* **2017**, 1604028-n/a.
218. Brust, M.; Fink, J.; Bethell, D.; Schiffrin, D. J.; Kiely, C., *J. Chem. Soc., Chem. Commun.* **1995**, 1655-1656.
219. Kumar, A.; Mandal, S.; Selvakannan, P. R.; Pasricha, R.; Mandale, A. B.; Sastry, M., *Langmuir* **2003**, *19*, 6277-6282.
220. Aslam, M.; Fu, L.; Su, M.; Vijayamohanan, K.; Dravid, V. P., *J. Mater. Chem.* **2004**, *14*, 1795-1797.

221. Schroedter, A.; Weller, H., *Angew. Chem. Int. Edit.* **2002**, *41*, 3218-3221.
222. Zhong, J.; Qu, J.; Ye, F.; Wang, C.; Meng, L.; Yang, J., *J. Colloid Interface Sci.* **2011**, *361*, 59-63.
223. Lipka, J.; Semmler-Behnke, M.; Sperling, R. A.; Wenk, A.; Takenaka, S.; Schleh, C.; Kissel, T.; Parak, W. J.; Kreyling, W. G., *Biomaterials* **2010**, *31*, 6574-6581.
224. Claridge, S. A.; Goh, S. L.; Fréchet, J. M. J.; Williams, S. C.; Micheel, C. M.; Alivisatos, A. P., *Chem. Mater.* **2005**, *17*, 1628-1635.
225. Prabhu, K. R.; Pillarsetty, N.; Gali, H.; Katti, K. V., *J. Am. Chem. Soc.* **2000**, *122*, 1554-1555.
226. Ghosh, A.; Basak, S.; Wunsch, B. H.; Kumar, R.; Stellacci, F., *Angew. Chem., Int. Ed.* **2011**, *50*, 7900-7905.
227. Siriwardana, K.; LaCour, A.; Zhang, D., *J. Phys. Chem. C* **2016**, *120*, 6900-6905.
228. Saha, K.; Agasti, S. S.; Kim, C.; Li, X.; Rotello, V. M., *Chem. Rev.* **2012**, *112*, 2739-2779.
229. Malinsky, M. D.; Kelly, K. L.; Schatz, G. C.; Van Duyne, R. P., *J. Am. Chem. Soc.* **2001**, *123*, 1471-1482.
230. Hrapovic, S.; Liu, Y.; Male, K. B.; Luong, J. H. T., *Anal. Chem.* **2004**, *76*, 1083-1088.
231. Gupta, A. K.; Gupta, M., *Biomaterials* **2005**, *26*, 3995-4021.
232. Dykman, L.; Khlebtsov, N., *Chem. Soc. Rev.* **2012**, *41*, 2256-2282.
233. Thanh, N. T. K.; Green, L. A. W., *Nano Today* **2010**, *5*, 213-230.
234. Mirkin, C. A.; Letsinger, R. L.; Mucic, R. C.; Storhoff, J. J., *Nature* **1996**, *382*, 607.
235. Brust, M.; Walker, M.; Bethell, D.; Schiffrin, D. J.; Whyman, R., *J. Chem. Soc., Chem. Commun.* **1994**, 801-802.
236. Sondi, I.; Salopek-Sondi, B., *J. Colloid Interface Sci.* **2004**, *275*, 177-182.
237. Kim, J. S.; Kuk, E.; Yu, K. N.; Kim, J.-H.; Park, S. J.; Lee, H. J.; Kim, S. H.; Park, Y. K.; Park, Y. H.; Hwang, C.-Y.; Kim, Y.-K.; Lee, Y.-S.; Jeong, D. H.; Cho, M.-H., *Nanomed.-Nanotechnol.* **2007**, *3*, 95-101.
238. Narayanan, R.; El-Sayed, M. A., *J. Am. Chem. Soc.* **2003**, *125*, 8340-8347.
239. Astruc, D., *Inorg. Chem.* **2007**, *46*, 1884-1894.
240. Nikoobakht, B.; El-Sayed, M. A., *Chem. Mater.* **2003**, *15*, 1957-1962.

241. Vayssieres, L., *Adv. Mater. (Weinheim, Ger.)* **2003**, *15*, 464-466.
242. Métraux, G. S.; Mirkin, C. A., *Adv. Mater. (Weinheim, Ger.)* **2005**, *17*, 412-415.
243. Millstone, J. E.; Hurst, S. J.; Métraux, G. S.; Cutler, J. I.; Mirkin, C. A., *Small* **2009**, *5*, 646-664.
244. Pandian Senthil, K.; Isabel, P.-S.; Benito, R.-G.; Abajo, F. J. G. d.; Luis, M. L.-M., *Nanotechnology* **2008**, *19*, 015606.
245. Huang, X.; El-Sayed, I. H.; Qian, W.; El-Sayed, M. A., *J. Am. Chem. Soc.* **2006**, *128*, 2115-2120.
246. Guo, Z.; Fan, X.; Liu, L.; Bian, Z.; Gu, C.; Zhang, Y.; Gu, N.; Yang, D.; Zhang, J., *J. Colloid Interface Sci.* **2010**, *348*, 29-36.
247. Guerrero-Martínez, A.; Barbosa, S.; Pastoriza-Santos, I.; Liz-Marzán, L. M., *Curr. Opin. Colloid Interface Sci.* **2011**, *16*, 118-127.
248. Kane, V.; Mulvaney, P., *Langmuir* **1998**, *14*, 3303-3311.
249. Bastús, N. G.; Merkoçi, F.; Piella, J.; Puentes, V., *Chem. Mater.* **2014**, *26*, 2836-2846.
250. Liu, X.; Yin, Y.; Gao, C., *Langmuir* **2013**, *29*, 10559-10565.
251. Millstone, J. E.; Wei, W.; Jones, M. R.; Yoo, H.; Mirkin, C. A., *Nano Lett.* **2008**, *8*, 2526-2529.
252. Panáček, A.; Kvítek, L.; Pucek, R.; Kolář, M.; Večeřová, R.; Pizúrová, N.; Sharma, V. K.; Nevěčná, T. j.; Zbořil, R., *J. Phys. Chem. B* **2006**, *110*, 16248-16253.
253. Xiu, Z.-m.; Zhang, Q.-b.; Puppala, H. L.; Colvin, V. L.; Alvarez, P. J., *Nano Lett.* **2012**, *12*, 4271-4275.
254. Maurer-Jones, M. A.; Mousavi, M. P.; Chen, L. D.; Bühlmann, P.; Haynes, C. L., *Chem. Sci.* **2013**, *4*, 2564-2572.
255. Christopher, P.; Xin, H.; Linic, S., *Nature Chem.* **2011**, *3*, 467-472.
256. Mitsudome, T.; Mikami, Y.; Funai, H.; Mizugaki, T.; Jitsukawa, K.; Kaneda, K., *Angew. Chem.* **2008**, *120*, 144-147.
257. Gao, C.; Lu, Z.; Liu, Y.; Zhang, Q.; Chi, M.; Cheng, Q.; Yin, Y., *Angew. Chem. Int. Edit.* **2012**, *51*, 5629-5633.
258. McFarland, A. D.; Van Duyne, R. P., *Nano Lett.* **2003**, *3*, 1057-1062.
259. Straney, P. J.; Andolina, C. M.; Millstone, J. E., *Langmuir* **2013**, *29*, 4396-4403.

260. Shankar, S. S.; Rai, A.; Ankamwar, B.; Singh, A.; Ahmad, A.; Sastry, M., *Nat. Mater.* **2004**, *3*, 482-488.
261. Kumar, P. S.; Pastoriza-Santos, I.; Rodríguez-González, B.; de Abajo, F. J. G.; Liz-Marzán, L. M., *Nanotechnology* **2007**, *19*, 015606.
262. Salem, A. K.; Searson, P. C.; Leong, K. W., *Nat. Mater.* **2003**, *2*, 668-671.
263. Jones, M. R.; Millstone, J. E.; Giljohann, D. A.; Seferos, D. S.; Young, K. L.; Mirkin, C. A., *ChemPhysChem* **2009**, *10*, 1461-1465.
264. Lyons, P. E.; De, S.; Elias, J.; Schamel, M.; Philippe, L.; Bellew, A. T.; Boland, J. J.; Coleman, J. N., *J. Phys., Lett.* **2011**, *2*, 3058-3062.
265. Straney, P. J.; Marbella, L. E.; Andolina, C. M.; Nuhfer, N. T.; Millstone, J. E., *J. Am. Chem. Soc.* **2014**, *136*, 7873-7876.
266. Straney, P. J.; Diemler, N. A.; Smith, A. M.; Gilliam, M. S.; Eddinger, Z. A.; Millstone, J. E., **2017**, In preparation.